Enhancing Heat Transfer in Processing Systems Using Swirl Tube Technology

Xingyu Feng, BEng

Thesis submitted to the University of Nottingham

for the degree of Doctor of Philosophy

Sep, 2024

ABSTRACT

This thesis elucidates the fundamental principles underlying the improvement of the thermal performance of a heat-transfer unit through the introduction of a swirl flow generated by a 4-lobed swirl tube. This research conducts a comprehensive literature review on thermal enhancement methods, investigation techniques, and undertakes two sets of numerical and experimental studies involving a 4-lobed swirl tube in a heat exchanger and a solar water heater.

The literature review classifies and systematically analyzes diverse thermal enhancement methods for tube flows. It also summarises commonly-employed numerical and experimental techniques for investigating these methods, facilitating researchers' method-selection process. Moreover, it compiles the Nusselt number and friction factor correlations relevant to the enhancement methods, which is of great value to the scientific and industrial communities. It is concluded that some thermal enhancement methods, such as the twisted tape method, are often accompanied by a significant amount of pressure drop, potentially nullifying the energy gain from heat transfer enhancement.

Numerical studies on the 4-lobed swirl tube explore and evaluate the thermal performance of different tube configurations. The regularly-spaced 4-lobed swirl tube is proposed as a means to achieve higher heat-transfer enhancement with a moderate pressure drop. A double-pipe heat-exchanger experiment is carried out, and the 3D-printing method is adopted to fabricate 4-lobed swirl tubes with different geometries. The thermal enhancement capability of the 4-lobed swirl tube is verified. Among all configurations, the 4-lobed swirl tube with a pitch-to-diameter ratio of 4 exhibits the highest overall performance, with values ranging from 1.12 to 1.09.

The thermal enhancement effect of the regularly-spaced 4-lobed swirl tube in a simplified solar water heater (SWH) is numerically investigated. The regularly-spaced lobed tube demonstrates superior thermal performance compared to the regularly-spaced twisted- tape tube. Based on the previous findings, a solar water heater equipped with regularly-spaced 4-lobed swirl tubes is constructed and compared with a circular SWH. The swirl-tube-

equipped SWH shows greater efficiency in turbulent-flow regions. However, in laminar-flow regions, the efficiency of these configurations decreases. The solar water heater with inserted swirl tubes shows approximately a 3% higher efficiency than the circular one, highlighting the potential of this method in real-world applications.

ACKNOWLEDGEMENTS

I would like to thank the University of Nottingham's graduate school for the scholarship I received to complete this PhD and the LDS Innovation Fellowship for funding the experimental rigs.

I owe a great debt of gratitude to my supervisors, Prof. Nick Miles, Prof. Philip Hall and Dr Zheng Wang for their precious support, supervision, guidance, encouragement, suggestions and invaluable input to this research.

I extend my gratitude to:

Qing Zhao and Zijun Han for their support and help with rig installation.

Prof. Jun He for his valuable input and critical evaluation of my work and Dr Guozhen Li for his support with the experimental rig and CFD simulations.

My friends Jiarui Gao, Qi Yang, Yubang Shen for their advice on CFD simulations.

My friend Yitao Zheng, Mingkai Li, Shuhan Wang and Runda Xue make difficult situations easier and dull moments more enjoyable.

Finally, I am especially grateful to my parents, my wife Ran Tao, my aunts and my grandparents for their love, support and understanding.

TABLE OF CONTENTS

LIST OF FIGURES

LIST OF TABLES

NOMENCLATURE

Nomenclature

A

Heat transfer area, m^2

c_p

Specific heat capacity, $J/(kg \cdot K)$

D_h

Hydraulic diameter, m

f

Friction factor

h

Heat transfer coefficient, $W/(m^2 \cdot K)$

I

Turbulence intensity

L

Effective length of test tube, m

l

Length of swirl tube, m

m

Mass flow rate, kg/s

Nu

Nusselt number

PEC

Performance evaluation criteria

Pr

Prandtl number

Δp

Pressure drop, Pa

P

wetted perimeter in m

PD

Pitch to diameter ratio

Q_{heat}

Heat transfer rate, W

Q_s

Heat transfer rate for swirl tube, W

Q_c

Heat transfer rate for circular tube, W

Q_{pump}

energy consumption for pump, W

q

Heat flux, W/m^3

R

Radius of the core, m

Re

Reynolds number

r

Radius of the lobe, m

r_s

Radical coordinate, m

Ra

Surface average roughness

S

cross-sectional area of the tube in m^2

SN

Swirl intensity

T

Temperature, K

ΔT

Temperature difference between inlet and outlet

∇T

Temperature gradient, K

ΔT_{LMTD}

logarithmic mean temperature, K

U

Overall heat transfer coefficient, $W/m^2 \cdot K$

$\vec{U}$

Velocity vector field, m/s

u

Velocity, m/s

u, v, w

Velocity vector on x, y and z direction, m/s

x, y, z

Cartesian coordinates, m

Greek symbols

β

swirl decay rate

μ

dynamic viscosity, $Pa \cdot s$

μ_t

eddy viscosity, $Pa \cdot s$

ρ

density, kg/m^3

λ

thermal conductivity, $W/(m \cdot K)$

θ

synergy angle, ^{o}

ε

Relative roughness

τ

Shear stress

δ_t

thermal boundary layer

η_h

Thermal efficiency of heat exchanger

$\eta_h{}'$

Effective thermal efficiency of heat exchanger

η_s

Thermal efficiency of solar water heater

$\eta_s{}'$

Effective thermal efficiency of solar water heater

Subscripts

ave

average

c

circular tube

in

inlet

out

outlet

s

shell side

t

tube side

w

tube wall

CHAPTER 1: INTRODUCTION

1.1 General Introduction

Heat exchangers constitute one of the most important and ubiquitous unit operations across numerous industrial sectors, where they are utilised to regulate temperature through either heating or cooling. The global market for heat exchangers was estimated to be $23.0 billion in 2024 and is expected to reach nearly $32.3 billion by 2029 (MarketsandMarkets, 2024). One of the primary driving factors for this upward trend is the rapid development and industrialization in countries such as China. However, insufficient awareness about the importance of energy efficiency and recovery can be an obstacle to market growth. In 2017, Luo et al. (2017) suggested that the industrial waste heat in northern China that can be utilised for domestic heating was 2.93 exajoules, which was equivalent to the heat generated by 100 million tons of standard coal. Thus, any small improvements in the performance of heat exchangers can have a significant and positive influence.

Heat transfer mechanisms can be categorised into three types: conduction, convection and radiative heat transfer. Conduction predominantly occurs in solids or stationary fluids due to microscopic collisions of particles and radical movements of electrons. Convective heat transfer occurs spontaneously due to fluid motions, which can be further distinguished into free and forced convection. Free convection happens when the density of the fluid changes due to temperature variation and fluid movement occurs due to buoyancy force. Forced convection occurs when an internal source, such as a pump, induces fluid to flow through the surface. Radiative heat transfer is an electromagnetic wave emitted from matter with a temperature above absolute zero.

In heat exchanger applications, conductivity and convection are the primary considerations, as the emission process is often neglected (Bejan and Kraus, 2003). Due to the enhanced heat transfer coefficient associated with fluid movement, convection typically exhibits a higher heat transfer rate than conduction. Consequently, convection is preferred in engineering applications. Researchers have investigated various methods to enhance the forced convective heat transfer under the same flow velocity, including, rotating tubes, magnetic fields, nanoparticles and twisted tape (Huang et al., 2017, Manglik, 2003, Rohsenow et al., 1998). A prominent technique is the swirl tube, which generates vortices as the fluid passes through the tube geometry. These methods can be divided into active and passive methods. The active methods typically require an external power source while passive methods do not need such source.

Swirl tubes have been investigated at the University of Nottingham, UK since 1993. An initial focus was on enhancing the efficiency of slurry transport. This was achieved by generating swirl motion from various lobed tube shapes. Further optimisation was performed on the lobed number, pitch-to-diameter ratio, pipe length, and development of a transition part between the lobed tube and circular tubes (Ariyaratne, 2005, Fokeer, 2006, Ganeshalingam, 2002, George, 2008, Raylor, 1998). In addition to slurry transport, potential applications have recently been examined. For instance, Li (2016) demonstrated through both experiments and simulations that the installation of an optimised 4-lobed swirl tube would enhance the clean-in-place efficiency.

Another potential application of swirl tubes is heat exchangers. The introduction of swirl tubes increases flow turbulence and enhances heat transfer through convection. Numerous experimental and numerical studies have been conducted to investigate the swirl effects generated by various heat transfer methods. For instance, Eiamsa-ard and Seemawute (2012) presented numerical and experimental studies on swirl flows created by inserting twisted tapes. They discovered that the heat transfer ratio doubled when the twisted ratio was 5. One common performance metric in heat transfer studies is the Performance Evaluation Criteria (PEC). PEC can be defined as the ratio of the heat transfer enhancement factor to the friction penalty factor. When the value of PEC is greater than 1, it indicates that the heat transfer enhancement achieved outweighs the penalty in terms of increased friction. Jafari et al. (2017a) developed a 3-lobed swirl generator for heat transfer enhancements. They concluded that by inserting it, the PEC would vary from 1.25 to 1.55 depending on the geometry of the swirl generators. The primary novelty of this thesis lies in its investigation of the heat transfer effect of a 4-lobed swirl tube, which has been created and optimised by researchers at the University of Nottingham. Given that no previous research has explored this specific configuration, this study aims to fill a significant gap in the existing literature on swirl flow heat transfer devices. By conducting a comprehensive analysis of the heat transfer characteristics and performance evaluation of this 4-lobed swirl tube, new insights into the design and optimisation of heat transfer systems using such geometries will be provided.

Furthermore, the swirl tube possesses distinct advantages compared with other methods in heat exchangers. It is superior in its simplicity to the active method and can be readily applied to existing heat exchangers, as installing additional surfaces (fins and twisted tapes) reduces the flow area inside the tube, increasing the susceptibility to debris accumulation. Moreover, adding a swirl tube improves the heat transfer rate and addressed the fouling problem. Fouling reduces the heat exchanger’s thermal efficiency, thereby increasing the demand for cooling water. To remove the fouling, periodic cleaning through water or chemical washing is essential. The additional surface from the fins and twisted tapes further increases the fouling opportunities, necessitating more frequent cleaning. These additional cleaning procedures increase the consumption of washing water and cleaning time. However, the 4-lobed swirl tube can increase the wall shear stress, thereby facilitating the removal of fouling (Li et al., 2015).

Given these advantages, the objective of this investigation is to examine the thermal potential of a 4-lobed swirl tube to enhance the heat transfer coefficient compared with a conventional circular tube. Furthermore, swirl effectiveness criteria, which evaluate swirl effectiveness and pressure drop, are utilised in previous research to optimise the swirl tube geometry (Li, 2016). Although swirl effectiveness is appropriate for slurry transport and clean-in-place applications, heat transfer coefficient and pressure drop should be the primary considerations for heat exchangers. The influence of the swirl effect on both the temperature and velocity fields should be evaluated to obtain a more comprehensive understanding. Consequently, the PEC factor, which considers both heat transfer coefficient and pressure drop, may be more suitable for heat exchanger optimisation (Chhabra and Shankar, 2017). The field synergy principle (Guo et al., 1998) is also applied to investigate the temperature and velocity fields developed by the swirl generator for the first time.

1.2 Aims and Objectives

The primary objective of this study is to investigate the thermal enhancement effect of swirl flow generated by a 4-lobed swirl tube and its potential for implementation in existing heat exchanger devices. The specific objectives are as follows:

- Conduct a comprehensive literature review on heat transfer enhancement methods, with particular emphasis on lobed tubes, swirl flow applications in heat transfer, and the experimental and modeling methodologies used in existing literature.
- Develop steady-state Computational Fluid Dynamics (CFD) model to evaluate the performance enhancement of a 4-lobed swirl tube compared with a circular tube.
- Evaluate different 3D configurations of the 4-lobed swirl tube and assess their thermal effects when integrated into heat exchangers.
- Analyse the relationship between heat transfer coefficient and the decay of swirl intensity, as well as the differences in flow characteristics between continuous and decaying swirl flow.
- Perform experiments to validate the CFD simulations and verify the thermal enhancement predictions.
- Optimise the geometric parameters (e.g., pitch-to-diameter ratio) of the 4-lobed swirl tube to maximise thermal enhancement and minimise pressure loss.
- Conduct combined numerical simulations and experimental investigations to evaluate the thermal enhancement capability of the 4-lobed swirl tube in solar water heater applications.

1.3 Thesis Outline

This thesis is comprised of seven chapters. The following section provides a concise description of each chapter.

Chapter 1 presents general background information, the rationale for the study, research aims and objectives, and the thesis structure.

Chapter 2 offers a literature review encompassing prevalent types of heat exchangers, various proposed thermal enhancement techniques, and corresponding numerical and experimental investigation approaches. This chapter summarises and compares the Nusselt number and friction factor correlations for different thermal enhancement methods. The critical evaluation criteria and terms pertaining to swirl flow performance are elucidated.

Chapter 3 describes the calculation and geometry creation of the 4-lobed swirl tube. The requisite information and procedures for creating a 4-lobed swirl tube are included.

Chapter 4 focuses on the computational fluid dynamics methodology for modelling heat transfer in a swirl flow. Subsequently, the effect of different 4-lobed swirl tube arrangements on thermal performance is studied. Finally, a regularly spaced 4-lobed swirl tube is proposed based on the preceding results.

Chapter 5 addresses the construction of a double-pipe heat exchanger incorporating a 4-lobed swirl tube to generate a decaying swirl flow. A 3D-printing method is employed to produce swirl tubes with different PD ratios. The results validate the numerical simulations.

Chapter 6 examines the potential application of the 4-lobed swirl tube and twisted tape in a solar water heater. Swirl generators and twisted tapes are periodically installed within the solar water heater to enhance thermal efficiency. This chapter further demonstrates the thermal performance of a regularly spaced 4-lobed swirl tube within a solar water heater. The temperature, pressure drop, and thermal efficiency of the solar water heater are investigated.

Chapter 7 summarises the results of the numerical and experimental research, and discusses the implications of this study. Future research opportunities are proposed.

CHAPTER 2: LITERATURE REVIEW

2.1 Introduction

A heat exchanger is a device capable of transferring heat between two media, such as fluid-to-fluid. Various heat exchangers have been developed to perform distinct functions in chemical engineering, power generation, waste heat recovery, and air conditioning. One study highlighted that the maximum amount of recoverable waste heat is equal to 20 billion tons of standard coal in China in 2020 (Liu et al., 2024a). Therefore, even minor enhancements in the performance of heat exchangers could have a substantial impact. Techniques to enhance heat transfer coefficient within heat exchanger tubes are highly desirable.

The quest to improve the efficiency of heat exchangers began 160 years ago with Joule (1861). He conducted a comprehensive study that provided a solid basis for understanding the effect of various condenser tube designs and materials on thermal enhancement (Bejan and Kraus, 2003). Following Joule's lead, researchers have devised various thermal enhancement techniques, generally classified as active or passive, depending on whether they require external power. Active methods provide more control over the enhancement of heat transfer, although they are more complex, more expensive, and less frequently used than passive ones (Léal et al., 2013). Swirl flow devices, such as twisted tapes and lobed tubes, have attracted attention for their simplicity of integration into current systems and their comparably low-pressure drops (Liu and Sakr, 2013, Hasanpour et al., 2014).

This review encompasses relevant topics on heat exchangers, various thermal enhancement techniques, and their associated numerical and experimental approaches. It discusses the swirl intensity and field synergy principle, which are two prevalent analytical concepts for examining the thermal enhancement mechanisms in swirl flows. Furthermore, this review outlines notable numerical models and experimental techniques. The reviewed thermal enhancement techniques are evaluated and compared based on their heat transfer coefficient, pressure drop penalties, and practical applicability.

2.2 Heat Exchangers

Heat exchangers are essential components in modern industrial settings due to the critical need for heating and cooling. A range of heat exchanger types has been developed to address diverse applications. The most prevalent varieties include double-pipe heat exchangers, shell and tube heat exchangers, condensers, and boilers (Nitsche and Gbadamosi, 2015). While the first two (double-pipe and shell-and-tube heat exchangers) are typically associated with single-phase flow, the latter two (condensers and boilers) involve phase change processes.

Double Pipe Heat Exchanger

A schematic of the double-pipe heat exchanger is shown in Figure 2.2-1. Two fluids with different temperatures flow into the tube and shell sides, and heat is transferred through the tube wall. This type of heat exchanger is the simplest because it involves an inner tube and an outer shell. Owing to its simplicity, a double-pipe heat exchanger is inexpensive to construct and maintain (Omidi et al., 2017). Despite its low efficiency and large space requirement, this type of heat exchanger remains widely used due to its simplicity and cost-effectiveness (Tavousi et al., 2023).

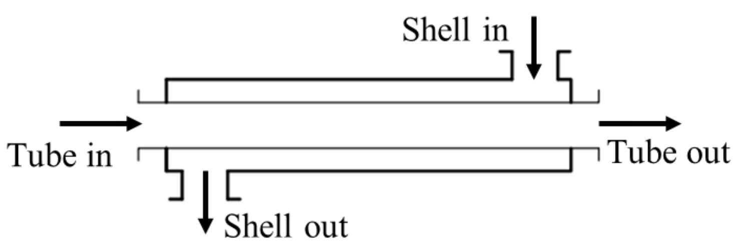

Figure 2.2-1. Schematic of double pipe heat exchanger.

Shell and Tube Heat Exchanger

The most common type of heat exchanger applied in large chemical processes is the shell and tube heat exchanger (Kuppan, 2013). Instead of only one tube inside the shell, a bundle of tubes is placed to increase the heat transfer area. The tube-side fluid flows axially through the tubes, while the shell-side fluid moves horizontally across the shell (guided by baffles). The cylindrical shell design ensures uniform stress distribution under high pressure, and its simple geometry facilitates manufacturing, making it ideal for high-pressure applications. Baffles are often installed in the shell side to enhance turbulence as shown in Figure 2.2-2.

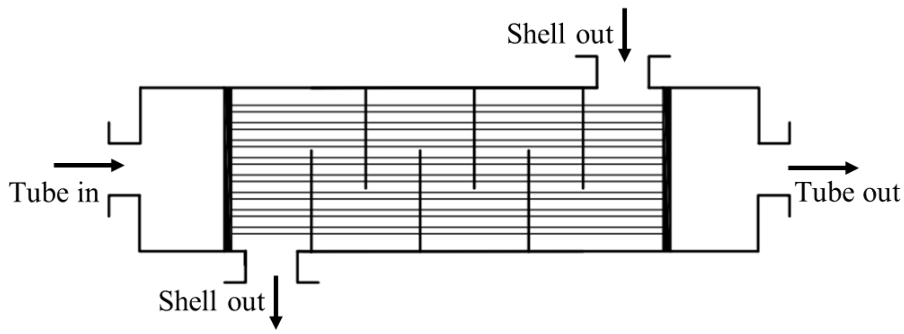

Figure 2.2-2. Schematic of straight-tube heat exchanger.

Another popular variation on the shell and tube heat exchanger is the U shape version (see Figure 2.2-3). The tube-side fluid passes through the shell twice through a U-bend and exits the heat exchanger on the same side as the inlet. This U-shaped heat exchanger, in comparison with a straight-tube one, provides an even larger heat transfer area within the same volume of space (Stewart, 2013).

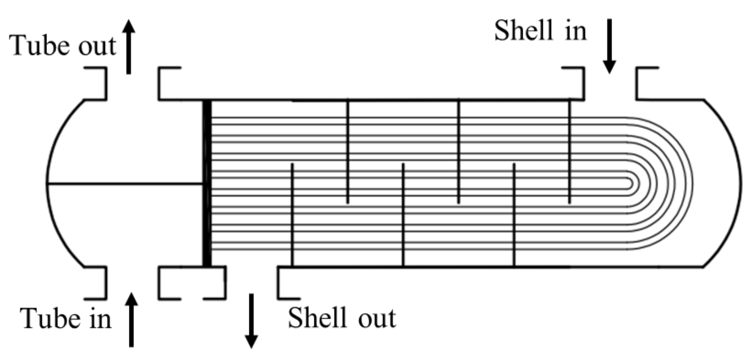

Figure 2.2-3. Schematic of U-shape heat exchanger.

Phase Change Heat Exchangers

Unlike single-phase heat exchangers, condensers and boilers involve phase change processes: boiling a liquid to vaporise it or condensing a vapour to liquefy it. This type of heat exchanger involves a phase change, that is: boiling a liquid to vaporise it or condensing a vapour to liquefy it. In fossil fuel and nuclear power plants, a reboiler heat exchanger is used to generate steam to push turbines (Moeck and Mcmorran, 1977). A conventional diagram of a boiler is shown in Figure 2.2-4.

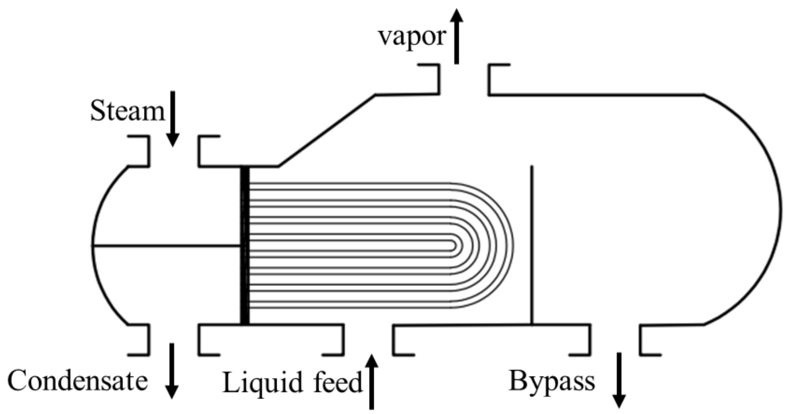

Figure 2.2-4. Schematic of boiler heat exchanger.

2.3 Thermal Enhancement Methods

Numerous thermal enhancement techniques have been developed in the past decade to enhance the heat transfer coefficient of various heat exchangers. These methods yield varying degrees of thermal enhancement, depending on whether they apply to single-phase or two-phase flows, for example, boiling and condensation in two-phase systems. However, given the extensive research in this field and to maintain focus, this section will specifically concentrate on popular thermal enhancement methods for single-phase flows.

2.3.1 Method Classification

Thermal enhancement methods can be broadly divided into three types, active, passive, and combined methods (Bergles, 1998). These methods are generally developed to reduce the thermal resistance in double pipe and shell and tube heat exchangers. They achieve this by increasing the convective heat transfer coefficient (Webb and Kim, 2004). The active methods typically require an external power source to enhance heat transfer, while passive methods rely on modifying the geometry or surface characteristics of the heat exchanger without the need for additional power. Combined methods integrate active and passive techniques to synergistically enhance heat transfer. By clearly understanding these different categories, researchers and engineers can make clearer decisions when selecting the most suitable thermal enhancement method for a specific application.

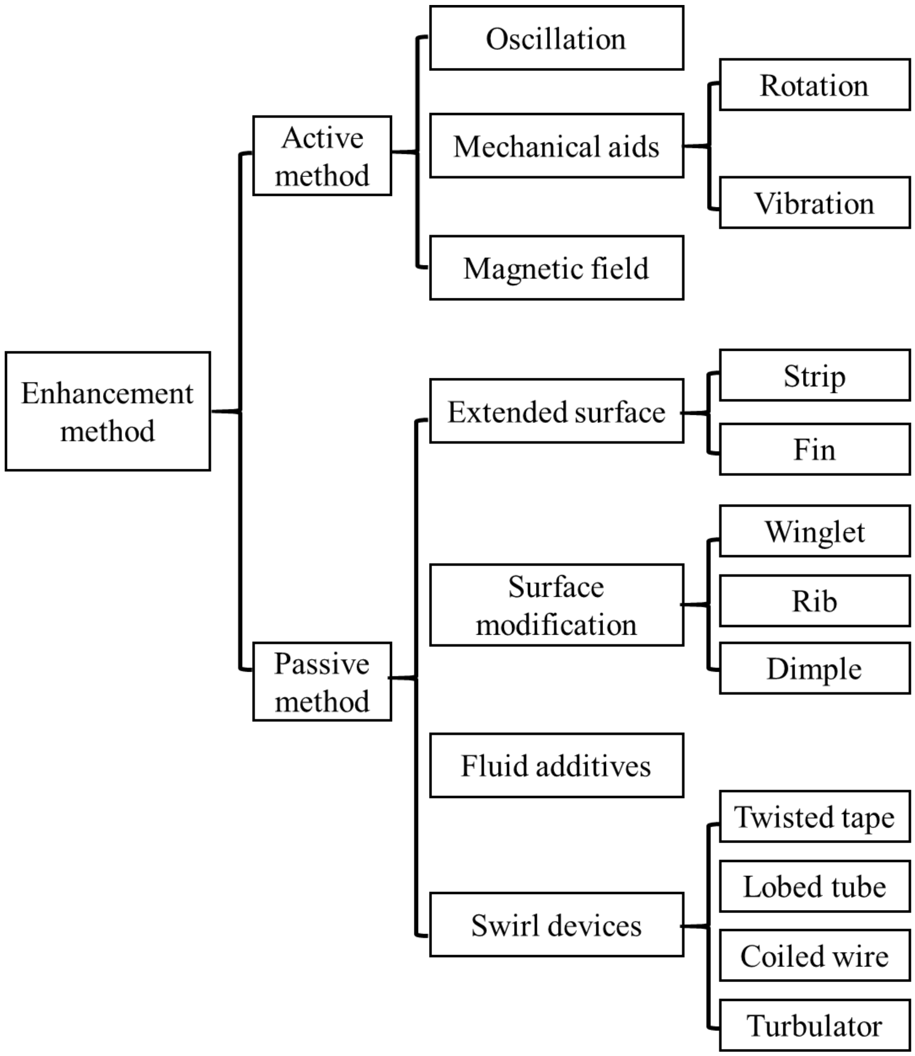

Figure 2.3-1. Classification of thermal enhancement methods.

The utilisation of active methods in various practical domains is limited by the challenge of installing an external power supply. As a result, these methods do not possess the same potential as passive methods. (Sheikholeslami et al., 2015, Li et al., 2022a, Bergles, 1998). Popular active methods include the following.

Mechanical aids: The fluid is stirred either by surface rotation or mechanical means. Examples include rotating the tube surface and rotating the twisted tape inside the tube.

Magnetic fields: Magnetic fields are generated from DC or AC sources and can only be applied in heat transfer processes involving conducting fluids. Greater bulk fluid mixing can be promoted in the vicinity of the heat transfer surface.

Oscillation: Either a low- or high-frequency vibration is created at the flow inlet, resulting in a higher convective heat transfer rate.

Some passive methods usually alter the geometries and surfaces of the flow tube, whereas others incorporate additives, such as nanoparticles, into the base fluid. However, passive methods sometimes dramatically augment the pressure drop across the tube to enhance the rate of heat transfer, which increases the requirement of the pumping system (Sheikholeslami et al., 2015, Maradiya et al., 2018, Wang et al., 2020, Mousa et al., 2021, Li et al., 2022a). Popular passive methods include the following.

Extended surface: Surfaces such as fins, louvred strips and winglets are added to the heat exchanger to increase the effective heat transfer area and flow turbulence.

Fluid additives: These additives mostly refer to nanoparticles, which have high thermal conductivity and mobility. The heat transfer ability of the base fluid increases by dispersing these particles uniformly within the base fluid.

Surface modification: Rough surface configurations can range from sand-grain roughness to discrete protuberances such as corrugated tubes and ribs. The purpose of these configurations is to promote turbulence near the tube surface.

Swirl flow devices: These devices create rotation and secondary flow in the fluid through either geometric arrangements or inserts such as twisted tape, wire coils, and lobed tubes.

In addition to the individual use of active and passive methods, researchers have also attempted to employ multiple techniques simultaneously, in a practice known as the compound method. Moreover, some researchers have noted that the passive methods generally appear more attractive overall when compared to the active approaches, owing to their simplicity (Hasanpour et al., 2014, Manglik, 2003, Rohsenow et al., 1998).

2.3.2 Definition of Terms

To understand and compare the overall performance of each thermal enhancement technique, the following terms are commonly used in the literature.

Hydraulic diameter

The hydraulic diameter of a tube is defined as (Nesbitt, 2006)

$$D_h = \frac{4S}{P} \tag{2.3-1}$$

where D_h denotes the hydraulic diameter in m; S denotes the cross-sectional area of the tube in m^2; P denotes the wetted perimeter in m.

Reynolds number

The Reynolds number can be calculated based on the following equation

$$Re = \frac{\rho u D_h}{\mu} \tag{2.3-2}$$

where μ is the viscosity of the fluid in $Pa \cdot s$, ρ is the density in kg/m^3, u is the average velocity in m/s, D_h is the hydraulic diameter of the pipe in m.

Heat transfer rate

$$Q_{heat} = mc_p(T_{out} - T_{in}) \tag{2.3-3}$$

Where Q_{heat} is the heat exchanger heat transfer rate in W, m is the mass flow rate in kg/s, c_p is the heat capacity in $J/(kg \cdot K)$, T_{out} is the outlet temperature in K, T_{in} is the inlet temperature in K.

Heat transfer coefficient

The heat transfer coefficient is a quantitative evaluation of the convective heat transfer between the fluid medium and the tube wall. This number is the core of heat exchanger design and also determines the performance of the heat exchangers (Nitsche and Gbadamosi, 2015). The heat transfer coefficient h can be calculated using the following equation:

$$h = \frac{Q_{heat}}{A(T_w - T_f)} \tag{2.3-4}$$

where A is the surface area for heat transfer in m^2; h is the heat transfer coefficient in $W \cdot m^{-2} \cdot K^{-1}$; T_f is the average temperature of the fluid at the inlet and the outlet ($T_f = \frac{T_{out}+T_{in}}{2}$) in K; T_w is the temperature of the wall surface in K; Q_{heat} is the heat transfer rate in W.

Heat exchanger energy efficiency

Moreover, the energy efficiency can also be compared by using the ratio between energy absorbed by the swirl heat exchanger Q_s and circular heat exchanger Q_c.

$$\eta_h = \frac{Q_s}{Q_c} \tag{2.3-5}$$

Pumping power energy

The energy input from the pump can be calculated by following equations (Singh and Vardhan, 2021).

$$Q_{pump} = \frac{V_{fluid}\, \Delta p}{C} \tag{2.3-6}$$

where V_{fluid} is the volumetric flow rate of the fluid in m^3/s, C is a conversion factor that accounts for the net conversion efficiency from thermal power unit to mechanical power, Δp is the pressure drop in Pa, C is recommended as 0.18 (Gupta and Kaushik, 2009).

$$\eta_h{}' = \frac{Q_s - Q_{spump}}{Q_c - Q_{cpump}} \tag{2.3-7}$$

Nusselt number

In certain circumstances, Dimensionless numbers are preferred in heat transfer analysis as they simplify complex relationships by reducing variables. The Nusselt number is a dimensionless parameter used to quantify the enhancement of convective heat transfer due to flow geometry modification. It is introduced to describe the increased heat transfer coefficient resulting from changes in the flow geometries, where a higher Nusselt number indicates an enhancement in the heat transfer rate. This dimensionless number is widely used to characterise the heat transfer coefficient of a heat exchanger and is defined as the ratio of the overall heat transfer coefficient (convection+conduction) to conductive heat transfer at the fluid boundary (Welty, 2001).

$$Nu = \frac{hD_h}{\lambda} \tag{2.3-8}$$

where D_h is the hydraulic diameter in m, λ is the thermal conductivity in $\mathrm{W} \cdot m^{-1} \cdot K^{-1}$.

Prandtl number

The Prandtl number is a dimensionless quantity, named after the German physicist Ludwig Prandtl, which represents the ratio of momentum diffusivity to thermal diffusivity (Welty, 2001). The Prandtl number is defined as:

$$Pr = \frac{c_p\mu}{\lambda} \tag{2.3-9}$$

Where c_p is the heat capacity of the fluid in $J/(kg \cdot K)$,

Friction factor

Changes in the geometry of the working medium frequently lead to greater pumping power being required to push the fluid through the pipe. Therefore, it is necessary to evaluate the pumping cost as well. To enable better comparison of the pumping costs for different geometries, a dimensionless number, the friction factor, is introduced (Welty, 2001). Under the same flow condition, a higher friction factor relates to a higher pumping cost.

$$f = \frac{\Delta p}{(L/D_h)(\rho u^2/2)} \tag{2.3-10}$$

Where D_h is the hydraulic diameter in m, Δp is the pressure drop in Pa, L is the tube length in m, ρ is the density of the fluid in $kg \cdot m^{-3}$, u is the velocity in m/s

Performance evaluation criteria (PEC)

The Nusselt number alone, however, cannot fully describe the improvement in heat exchange, as geometrical alterations often involve higher pumping power. Therefore, it is essential to consider the total inputs and outputs of the system. The performance evaluation factor can be used to compare the heat transfer coefficient of the modified tube with that of a circular tube. This considers both the energy gained from the modified tube and the energy lost owing to the increased pressure drop. The 1/3 is mainly based on experiment and experience (Webb, 1981).

$$PEC = \frac{Nu_t/Nu_c}{(f_t/f_c)^{1/3}} \tag{2.3-11}$$

where Nu_t stands for the Nusselt number for the modified tube, Nu_c stands for the Nusselt number for the circular tube, f_t stands for the friction factor for the modified tube, f_c stands for the friction factor for the circular tube.

A PEC factor smaller than 1 indicates that the overall energy recovered by modifying a tube is lower than that of a circular tube owing to the frictional resistance. A factor higher than 1 suggests that a modified tube would have improved energy transfer performance compared to a circular tube. In addition, due to the nature of PEC as a ratio of ratios involving Nu_t/Nu_c and f_t/f_c, even small errors in the values can lead to a compounded error in the calculated PEC value. This highlights the importance of accurate measurement and calculation of the evaluation parameters.

2.3.3 Active Methods

2.3.3.1 Mechanical Aids (rotation, vibration)

The mechanical stirring action significantly enhances the heat transfer performance. With the stirring effect from a mechanical aid, the fluid in that region moves along the stirring surface owing to shear stress. This movement causes an increase in the tangential velocity of the fluid, creating a vortex in the flow field. The stirring effect leads to fluid rotation, which encourages better fluid mixing and results in a higher heat transfer rate.

In addition to mechanical stirring, rotating surfaces also play a crucial role in heat-transfer processes. Rotating surfaces, such as gas turbine rotor blades, are common in cooling processes. The research on the relationship between rotation and heat transfer has a long history. For instance, McElhiney and Preckshot (1977) stated that in the case of laminar flow within a rotating circular tube, the heat transfer enhancement could reach up to 350%. Morris and Rahmat-Abadi (1996) conducted experiments to study the thermal effect of orthogonally rotating internal ribs inside a tube. Their findings indicated that the rib geometries induced a heat transfer enhancement of over 300% compared to a smooth tube.

With these foundations, researchers have investigated various rotating surfaces for stirring different base fluids. Qiu et al. (2013) conducted an experimental study on the thermal effect of rotating a square U-duct with a Reynolds number ranging from 10,000 to 70,000. They found that rotation was most pronounced in the bending and turning areas. Consequently, the Nusselt number exhibited the greatest increase in this region.

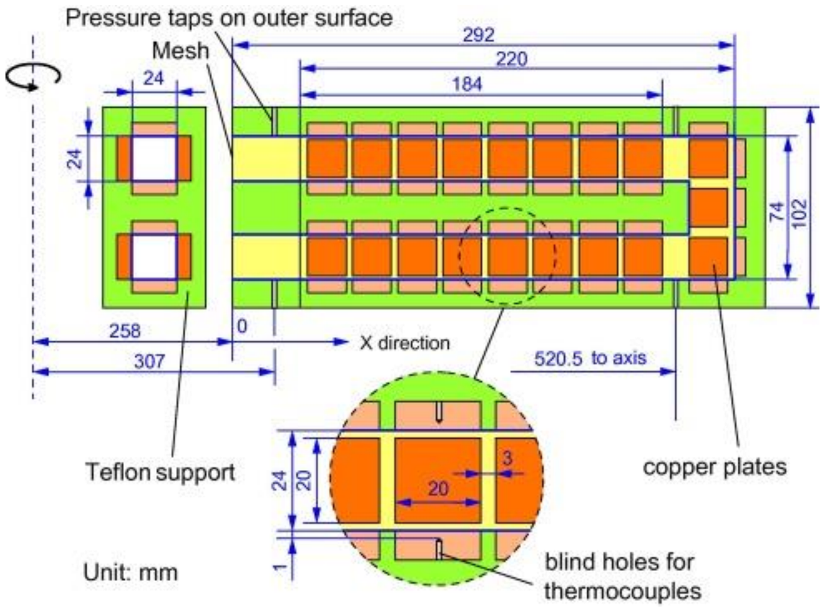

Figure 2.3-2. Schematic of U-shaped rectangular duct (Qiu et al., 2013).

Abou-Ziyan et al. (2016) combined fin and inner tube rotations experimentally. Compared to a circular stationary tube, the overall Nusselt number increased by 7.5 times with the inner tube rotation and helical fins. In addition, due to the driving effect of rotation, the pressure drops of the fins under rotating conditions were lower than those under stationary conditions. However, considering the complex structure and operation requirements of these rotation devices, they might be difficult to apply to existing systems.

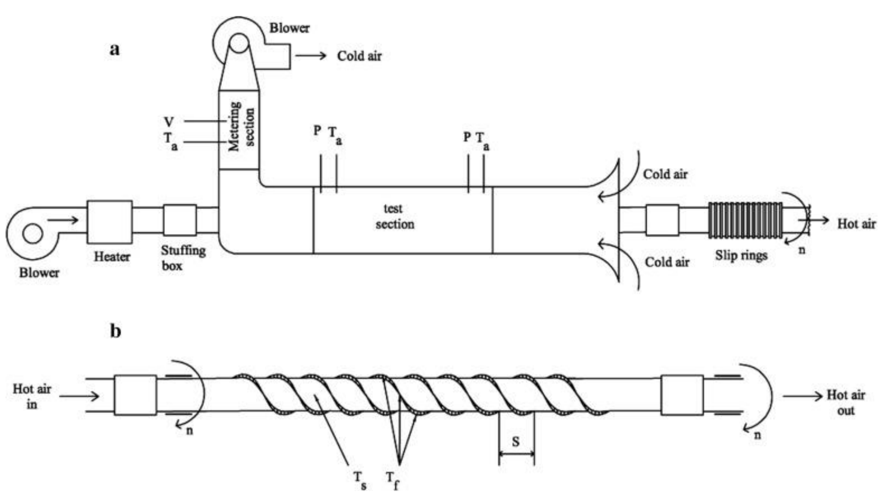

Figure 2.3-3. The schematic diagram for tube rotation with fins (Abou-Ziyan et al., 2016).

In addition, heat transfer enhancement can be achieved by applying surface vibration to the tube wall through electrodynamic vibrators (Hosseinian and Meghdadi Isfahani, 2018). The maximum increase of 97% was observed for the heat transfer coefficient at the largest vibration level (9 $m \cdot s^{-2}$) during the experiments. Mashoofi Maleki et al. (2023) installed a stretched vibrating string in experiments inside a heated tube. They soldered a permanent magnet onto the string. A magnetic field is imposed on this magnet to achieve string vibration. The greatest thermal enhancement factor at 1.5 was attained when the magnet was placed at 0.77 times the length of the tube (from the entrance of the tube). Although increasing heat transfer through the utilisation of mechanical power has significant potential, it is one of the most challenging techniques to implement in the industry because of the requirement for moving elements (Mousa et al., 2021). These moving parts may make the equipment more vulnerable to fatigue and failure, and require an additional power supply to operate, thereby increasing the operational costs.

2.3.3.2 Applying Magnetic Fields

Magnetic fields can interact with ferrofluid-type fluids, and they may also have interactions with some other fluids with magnetic properties. The application of external magnetic fields can accelerate the movement of ferrofluid-type fluids inside the duct. This disrupts the thermal boundary layer. The thermal enhancement capability of combining a magnetic fluid and magnetic field was demonstrated through visual observations by Nakatsuka et al. (2002). Further investigations have focused on the location and strength of the magnetic field, as well as the exploration of different base fluids to maximise the thermal enhancement effect.

Building on the previous research on the interaction between magnetic fields and fluids, Li and Xuan (2009) performed experiments in the presence of a magnetic field with different strengths and directions as shown in Figure 2.3-4. They reported that the control of the heat transfer process can be achieved by altering either the direction or magnitude c of the external magnetic field. For instance, when a magnetic field gradient is applied along with the flow direction, the heat transfer process is considerably enhanced.

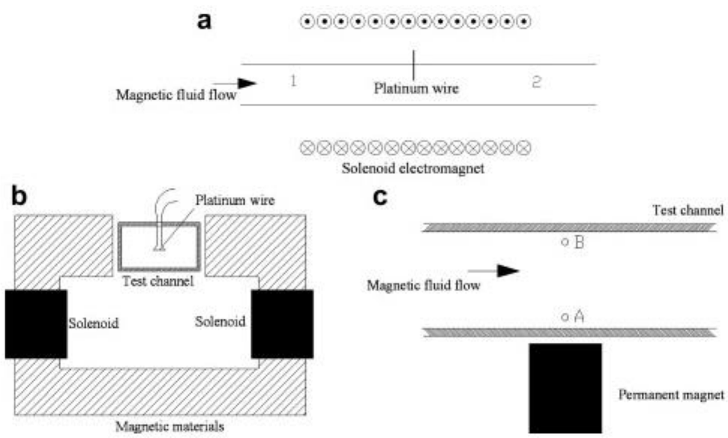

Figure 2.3-4. Schematics of magnetic field systems (a) Solenoid electromagnet (parallel field); (b) Electromagnet (perpendicular field); (c) Permanent magnet (perpendicular field) (Li and Xuan, 2009).

Naphon and Wiriyasart (2018) combined pulsating flow, TiO_2 nanofluids, fin tubes and magnetic fields to investigate the thermal enhancement effect. Twelve magnetic bars were equally spaced on the magnetic layer, as shown in Figure 2.3-5. The continuous nanofluid flow with a magnetic field yielded a Nusselt number 6.2% higher than that without a magnetic field effect.

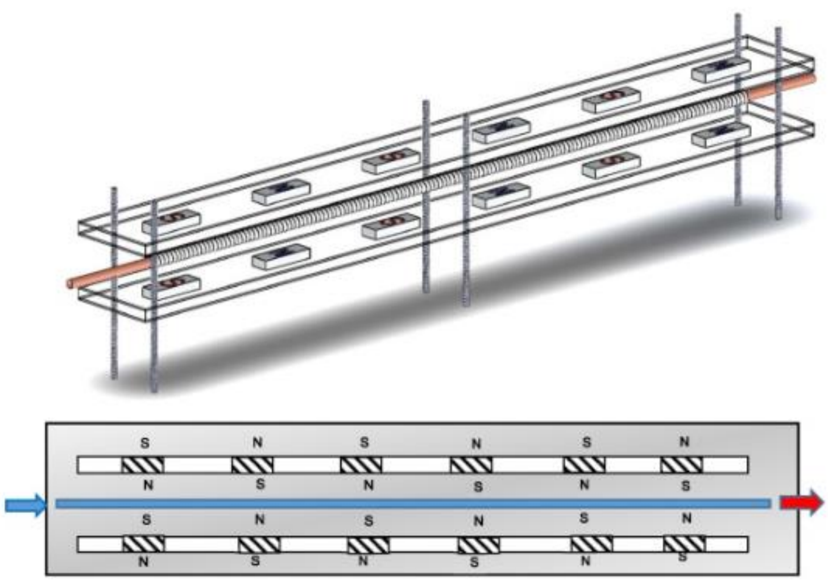

Figure 2.3-5. Schematic diagram of magnetic bar arrangements. (Naphon and Wiriyasart, 2018).

Fan et al. (2020) analysed the thermal-hydraulic performance of $Fe_3O_4 - H_2O - AG$ nanofluids in corrugated tubes with different turbulators. They concluded that the heat transfer characteristic of a bilateral staggered magnetic field was 5.8% higher than that of a unilateral field. Furthermore, combining nanofluids, corrugated tubes, perforated turbulators, and magnetic fields has a positive effect on the heat transfer performance.

Bezaatpour and Goharkhah (2020) performed simulations to apply an external magnetic field to a mini double-pipe heat exchanger to generate a swirl flow. The results suggested that the application of the magnetic field improved the heat transfer rate by up to 320%, with only a slight increase in the pressure drop. Temperature streamlines were used to illustrate the generation of swirl flow from magnetic fields, as shown in Figure 2.3-6.

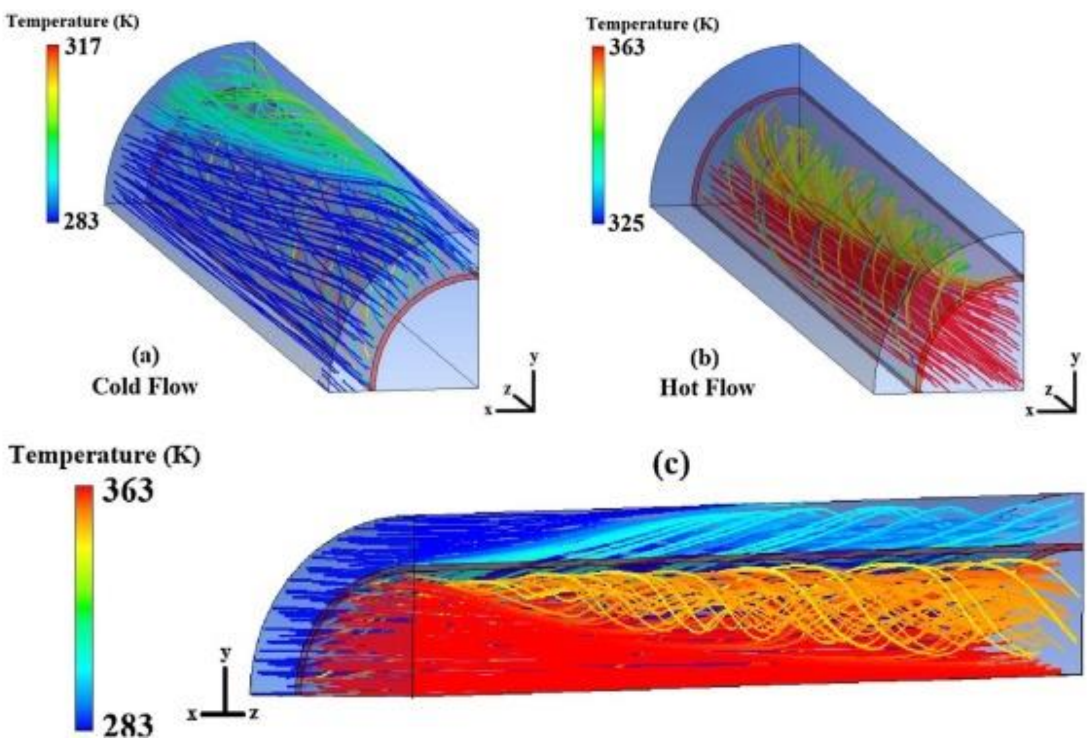

Figure 2.3-6. Temperature streamlines of (a) cold flow, (b) hot flow, and (c) cold and hot flow along the heat exchangers (Bezaatpour and Goharkhah, 2020).

The primary advantage of these active techniques, including magnetic fields, is their capacity to regulate the level of heat transfer improvement while in operation by varying the magnetic field strength. The extent of adjustment that can be achieved through passive methods is not comparable to that of active methods, as the latter involves geometrical modifications which are often less flexible and cannot be easily adjusted during operation. It is possible to control the amount of heat transfer enhancement by changing the magnetic intensity even during operations, which is not possible with passive techniques. However, the primary limitation of magnetic field applications is the necessity for ferro-type fluids. Without such fluids, the interaction between the magnetic field and the fluid, which is crucial for heat-transfer control, cannot be effectively established.

2.3.3.3 Flow Oscillation

Flow oscillation is widespread and is exemplified by the pumping of blood flow in the heart. It is also known as pulsating flow and has been utilised in various industrial fields, such as thermal energy engineering, chemical engineering, and electronic engineering (Ye et al., 2021). This oscillating or pulsating flow, which is imparted at the flow inlet by a pump or valve, disturbs the thermal boundary layer by inducing flow instability. The alternating acceleration and deceleration of the flow facilitates the transfer of heat from the near-wall region to the mainstream, thereby enhancing the heat transfer coefficient.

Elshafei et al. (2008) conducted experimental studies on pulsating turbulent air flow in a pipe heated at a uniform heat flux. The local Nusselt number variation was more pronounced in the entrance region. The highest thermal enhancement was approximately 9% at a Reynolds number of 37,100 and a frequency of 13.3 Hz. Khosravi-Bizhaem et al. (2019) experimentally studied the effects of a pulsating flow on heat transfer and pressure drop in helically coiled tubes. It was found that the pressure fluctuations decreased when the pulsating frequency increased and the average value for pressure loss was 3-7% higher than that of the steady flow. Davletshin et al. (2020) explored the heat transfer characteristic of a steady and pulsating airflow passing through a spanwise rib. Compared to steady-state flow, pulsating flow improved the heat transfer rate, especially in the area along the wake behind the rib. While the pulsating flows applied by the researchers above were all unidirectional–moving in a single direction–reciprocating flow is a pulsating flow that can switch the flow direction periodically. Yuan et al. (2020) studied experimentally the thermal effects and associated bubble behaviour of a high-frequency, reciprocating flow on a silicon chip in a rectangular flow channel. As shown in Figure 2.3-7, this flow pattern was achieved by installing four solenoid valves. The heat flux for the reciprocating flow was 42.3% higher than that for the steady flow.

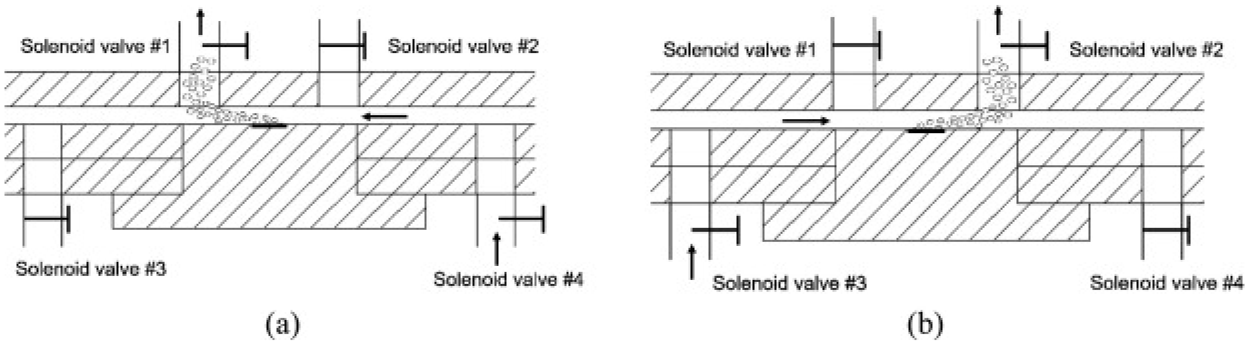

Figure 2.3-7. Schematic diagram of reciprocating flow and bubbling characteristics of the chips. (Yuan et al., 2020).

Guo et al. (2020) numerically investigated the effect of pulsating flow on the helical coiled tube and observed a stronger counter-rotating vortex structure formed in the axial direction of the coils. At a pulsation frequency of 9 Hz, the heat transfer coefficient was enhanced by a factor ranging approximately from 1.18 to 1.35 compared to the non-pulsating condition.

Ye et al. (2021) reviewed the thermal enhancement ability of pulsating flow. They concluded that for a single-phase pulsating flow, the highest thermal enhancement was around 20%. However, they also pointed out that some studies (Mehta and Khandekar, 2015, Yuan et al., 2016) drew a different conclusion in that a pulsating flow weakens or provides little thermal enhancement. Simulating pulsating flow in turbulent regions is extremely challenging. Current numerical investigations are mostly limited to single-phase laminar flow. Consequently, the enhancement mechanism of pulsating flow, especially in turbulent regions, remains poorly understood. To resolve this discrepancy in research findings, further investigations are necessary to explore the underlying mechanisms of pulsating flow.

Researchers have tended to investigate vortices produced by pulsating flows through different obstacles. Since pulsating flow is already ubiquitous in modern industries, the application of pulsating flow is easier compared with the other two active methods. However, the equipment required to generate pulsating flow is costly. Moreover, due to the oscillatory nature of the flow, the equipment is more susceptible to fatigue caused by vibration (Ye et al., 2021).

2.3.4 Passive Methods

2.3.4.1 Extended Surfaces (fins, strips, winglets and rings)

These extended surfaces cannot only induce additional turbulence but also enlarge the effective heat transfer area. Nevertheless, these additional surfaces often lead to high pumping power costs.

Fins

Fins are employed as a universally accepted method in industrial applications.

El Maakoul et al. (2017) numerically studied the heat transfer performance of an air-to-water double pipe heat exchanger. Fins were installed on the inner tube of the gas side as shown in Figure 2.3-8. They concluded that a higher thermal performance was achieved with helical fins than with longitudinal fins. The optimal fin spacing was determined to be 0.1. Compared with longitudinal fins, this fin spacing resulted in a 36% higher heat transfer rate and a 54% higher pressure drop.

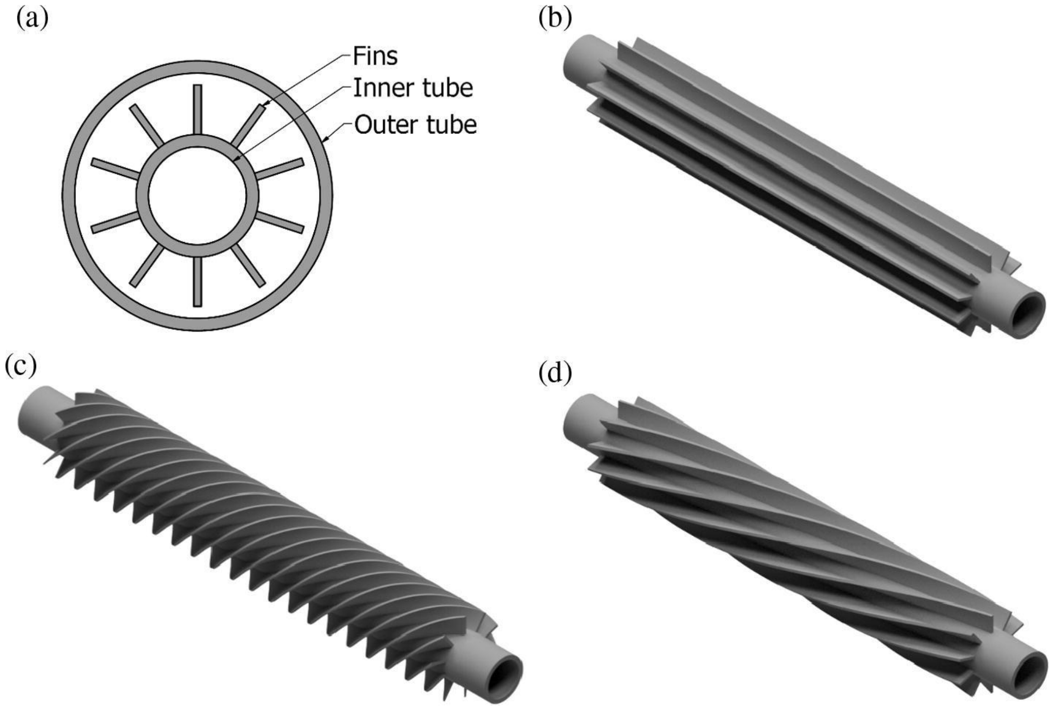

Figure 2.3-8. Geometries of double pipe heat exchangers with fins (a) cross-sectional view of the double pipe heat exchanger. (b) longitudinal fins (c) helical fins with a fin spacing of 0.2m (d) helical fins with a fin spacing of 0.05m (El Maakoul et al., 2017).

Tuncer et al. (2021) conducted numerical and experimental research to explore the effect of adding longitudinal fins to a shell and helically coiled tube heat exchanger. The addition of longitudinal fins to this type of heat exchanger led to an average 10% increase in the overall heat transfer coefficient. Eiamsa-ard et al. (2023) combined the thermal effects of helical fins and 2-lobed tube. They achieved the highest PEC factor of 1.32.

Strips

Eiamsa-ard et al. (2008) conducted experiments using louvred strips within a circular tube, with Reynolds numbers ranging from 6,000 to 42,000. The orientations of the forward and backward configurations are shown in Figure 2.3-9. Here, the forward and backward configurations refer to the different installation directions of the louvred strips relative to the fluid flow. Compared with a circular tube, the Nusselt number and friction factor for forward louvred strips increased by 284% and 413% respectively.

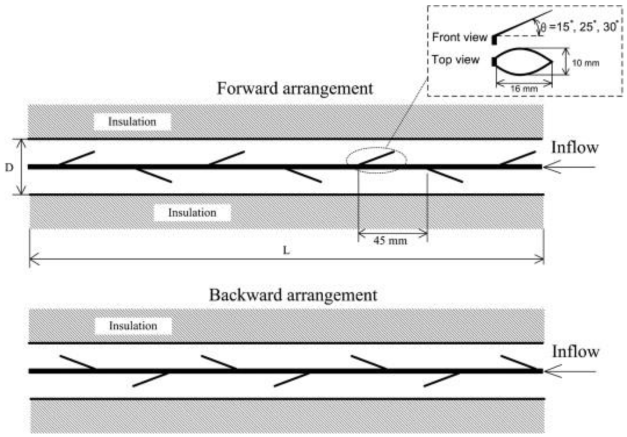

Figure 2.3-9. Louvred strip inserted tube. (Eiamsa-ard et al., 2008).

Nakhchi et al. (2020) simulated a perforated louvred strip with different slant angles to analyse the thermal performance. By adjusting the slant angle from 15° to 25°, the average PEC factor increased from 1.5 to 1.8. However, the friction factor for slant angles of 15° and 25° was 81% and 400% higher, respectively, than that of a smooth circular tube. This significant increase in the friction factor implies a greater pressure drop and thus higher pumping power requirements. The researchers should weigh the benefits of the increased PEC factor against the drawback of the higher friction factor when considering the practical application of such perforated louvred strips with different slant angles.

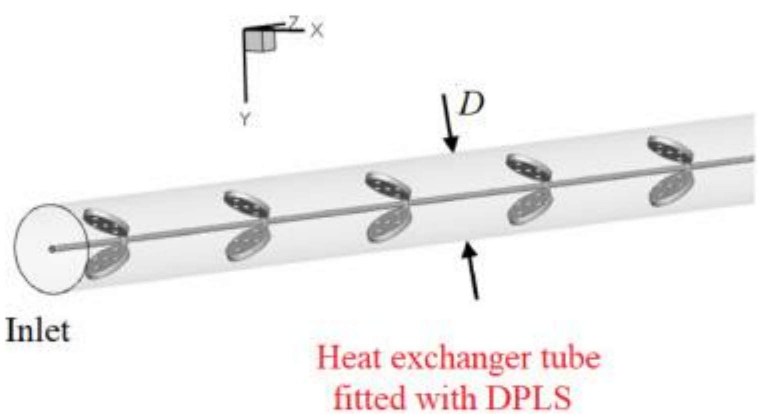

Figure 2.3-10. Double perforated louvred strips (DPLS) (Nakhchi et al., 2020).

Winglets

Sun et al. (2020) performed both simulations and experiments to study the thermal performance of multiple rectangular winglets in circular tubes. It has been noted that the quantity of vortices produced is directly proportional to the winglet count. However, some cases suggested that the overall performance may not increase with the number of winglets. The highest PEC factor of 1.27 was obtained at a winglet number of 8.

Figure 2.3-11. Multiple rectangular winglet vortex generators (N=number of winglet vortex) (Sun et al., 2020).

Promvonge and Skullong (2020) conducted an experimental study to evaluate the overall performance of V-shaped winglets. Both the Nusselt number and friction factor increased considerably with increasing winglet height and decreasing winglet distance. The Nusselt number and friction factor were 3.1-4.58 times and 8.12-32.05 times higher than the plain tube. The highest PEC value was achieved at 2. This result implies that although increasing the winglet height and decreasing the winglet distance can enhance heat transfer, there is a trade-off between heat-transfer improvement and pressure-drop increase.

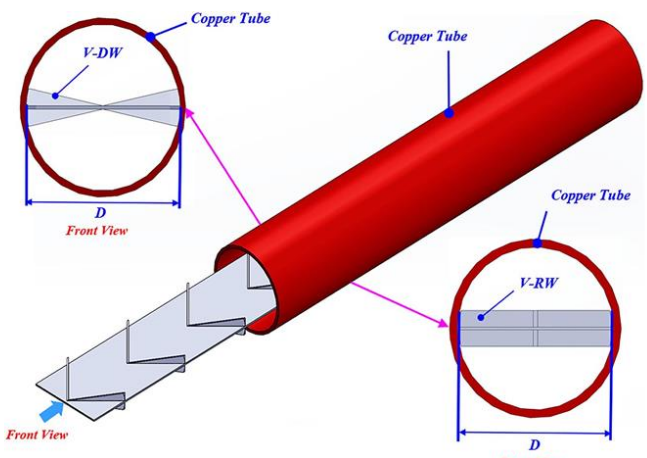

Figure 2.3-12. V-shaped winglet vortex generator (Promvonge and Skullong, 2020).

Rings

Kongkaitpaiboon et al. (2010) experimentally investigated the heat transfer and pressure drop in a circular tube with circular ring coils. The heat transfer rate of the tubes equipped with ring turbulators increased from approximately 57% to 195% with Reynolds numbers ranging from 4,000 to 20,000. With the optimal geometries, the highest PEC value of 1.07 was achieved at the lowest Reynolds numbers.

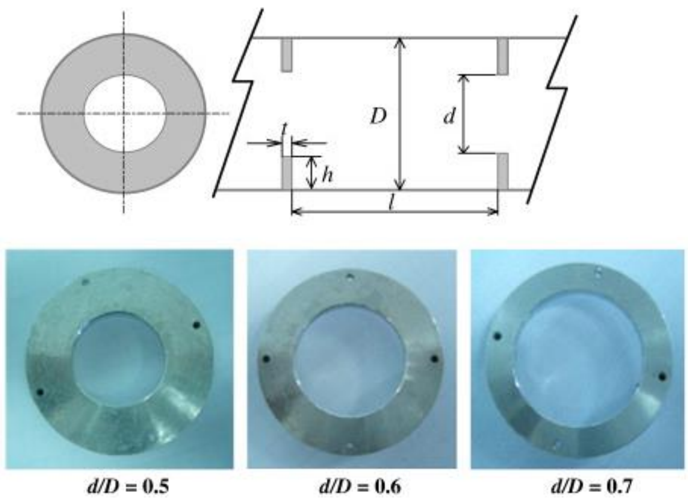

Figure 2.3-13. Circular ring turbulators (Kongkaitpaiboon et al., 2010).

Ibrahim et al. (2019) carried out a computational investigation on the heat transfer enhancement of inserting conical rings inside tubes. Different types of ring arrays were inserted as shown in Figure 2.3-14. The PEC factor decreased with increasing Reynolds number and the divergent arrays, with a pitch-to-diameter ratio of 0.4, improved by 29.1% compared with a smooth circular tube overall at a Reynolds number of 6,000.

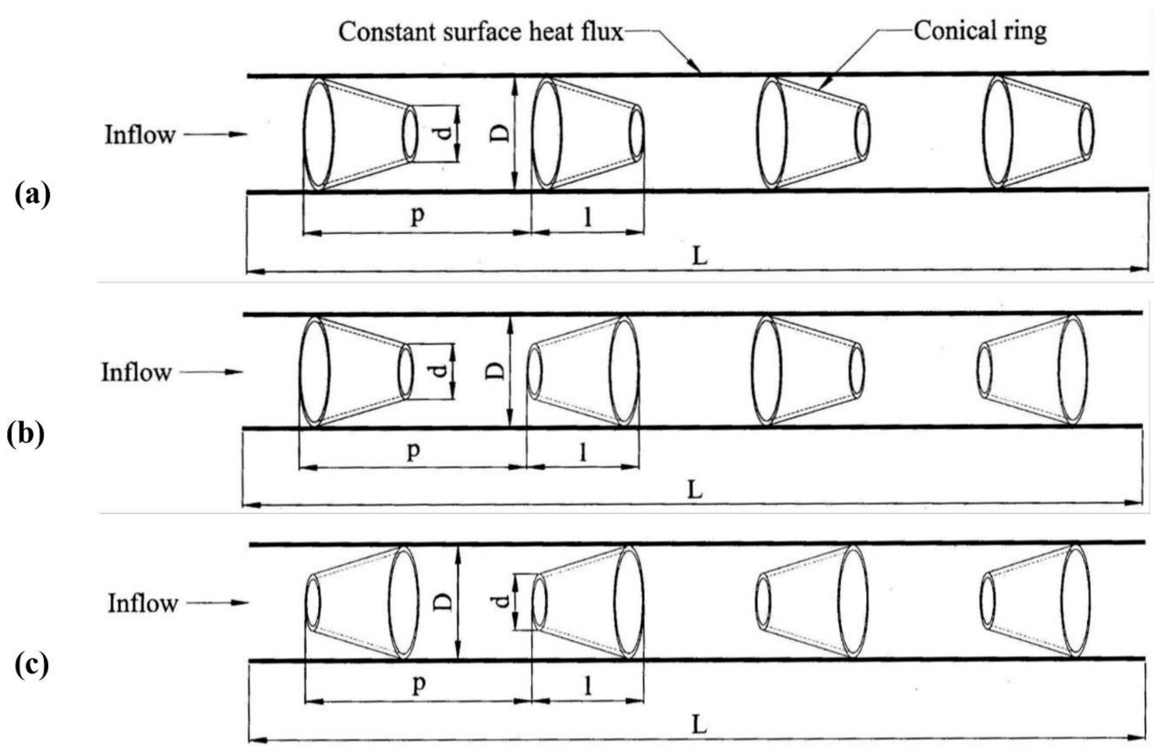

Figure 2.3-14. Various conical ring arrays (a) Convergent arrays (b) Convergent-divergent arrays (c) Divergent arrays. (Ibrahim et al., 2019).

Based on the above-reviewed literature, it is evident that the addition of fins and strips can substantially enhance the heat transfer rate. Moreover, by adjusting the geometrical parameters of these fins and strips, the degree of thermal enhancement can be effectively controlled.

However, it is crucial to note that the installation of fins and strips also leads to a considerable increase in pressure drops. For instance, in some of the studies mentioned earlier, the pressure drop increased by 413% when fins were installed, which could potentially have a negative impact on the overall energy efficiency of the system.

2.3.4.2 Additives for Liquids (nanoparticles)

Unlike other methods that enhance turbulence to improve heat transfer, the addition of nanoparticles augments the thermal conductivity of the working medium.

In 1993, Masuda et al. (1993) added Al_2O_3 and TiO_2 to water and found that at a concentration of 4.3%, the thermal conductivity increased by 32% and 11%, respectively. These results indicated that nanofluids could be used to enhance convective heat transfer. Pak and Cho (1998) verified this concept by experimenting with these two nanoparticles. They concluded that, for a fixed Reynolds number, the increment in the heat transfer coefficient for Al_2O_3 particles was 45% at a concentration of 1.3% and increased to 75% when the concentration changed to 2.8%. However, when the fluid velocity was fixed, the Reynolds number of the nanofluid was only 36.2% of that of pure water. This difference in Reynolds number is because the addition of nanoparticles changes the density and viscosity of the fluid. When comparing under a fixed-velocity condition, the heat transfer coefficient of the nanofluid was 12% lower than that of pure water. They also pointed out that selecting particles with high thermal conductivity and an appropriate particle size is crucial. Therefore, when using nanofluids to improve thermal performance, it is necessary to compare the performance under both fixed-velocity and fixed-Reynolds number conditions.

Hemmat Esfe et al. (2014) experimentally tested the thermal enhancement of COOH-functionalized double-walled carbon nanotube nanoparticles. Compared with pure water, this mixture achieved an average heat transfer enhancement of 25%. The effect of stable TiO_2-water nanofluids was experimentally investigated at mass fractions of 0.1 wt% to 0.5 wt% in triangular and circular tubes. It was concluded that nanofluids improved the heat transfer coefficient with an acceptable augmentation of the friction factor in triangular tubes (Qi et al., 2018a).

In addition, Wu et al. (2013) experimentally investigated the heat transfer characteristics of an alumina nanofluid over a weight fraction range of 0.8% to 7.0% on helically coiled tubes. The data illustrated that the enhancement by using nanofluid on the heat transfer coefficient and pressure drop was negligible. The effect of nanofluids in a plate heat exchanger was examined by Zamzamian et al. (2011) using aluminium oxide and copper oxide-ethylene glycol nanofluids. They suggested that a higher temperature and nanoparticle concentration would result in a larger heat transfer coefficient. In addition, Esfahani and Languri (2017) showed that a graphene oxide concentration between 0.01%

and 0.1% led to a 9% to 20% increase in thermal conductivity compared to pure water. Hosseinian et al. (2018) investigated the mechanical vibrations method with a MWCNT-water nanofluid. The results suggested that the optimal condition can increase the heat transfer coefficient by 100% at a mass fraction of 0.04% and at the highest vibration level. Ghasemiasl et al. (2023) summarised the different types of nanoparticles investigated by numerous researchers as shown in Figure 2.3-15. The most common type of nanoparticle investigated from 2017 to 2023 was Al_2O_3, mainly owing to its good dispersion rate and low cost.

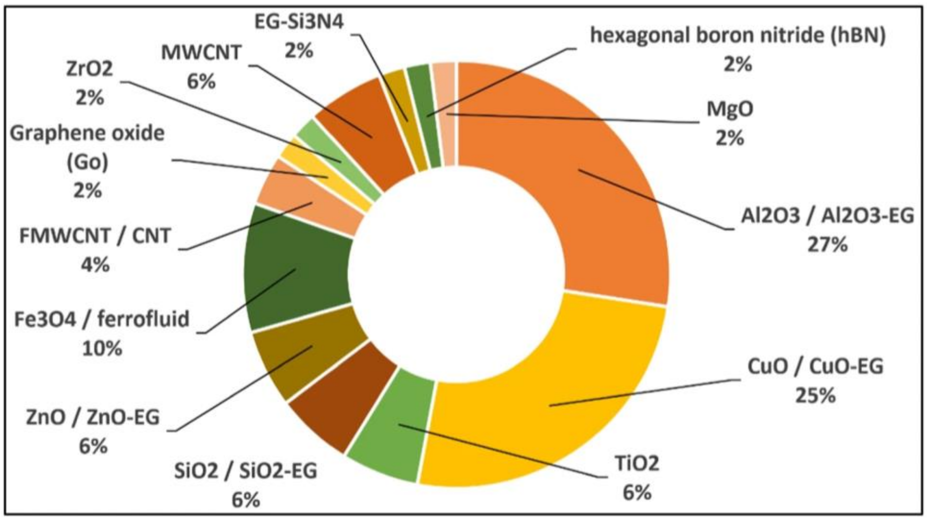

Figure 2.3-15. Research focus on nanoparticle types between 2017-2023. (Ghasemiasl et al., 2023).

In general, the addition of nanoparticles increases the heat transfer coefficient, and the extent of this enhancement can be adjusted by changing the nanoparticle concentration. However, nanoparticles cannot be used in boiler applications where fluid purity is critical because agglomeration and sedimentation of nanoparticles can aggravate fouling issues (Awais et al., 2021). Moreover, when evaluating the thermal performance of nanofluids, it is important to compare the results under both fixed-velocity and fixed-Reynolds number conditions to obtain a comprehensive understanding.

2.3.4.3 Surface Modification (corrugated tube, dimples)

Modification of the tube surface can enhance the heat transfer rate by increasing the contact area and surface roughness. Moreover, this irregular surface can create turbulence near the wall region. Researchers often attempt to increase the surface roughness by adding corrugations and dimples to the tube wall.

Corrugated tube

Pethkool et al. (2011) investigated the thermal enhancement effect of a corrugated tube. The geometric shape of the corrugated tube is shown in Figure 2.3-16. The highest PEC value was 2.33 at the lowest Reynolds number. This might be because at low Reynolds numbers, the increase in pressure drop caused by the corrugated structure is relatively small compared to the enhancement in heat transfer. The Nusselt number and friction factor were 3.01 times and 2.14 times higher than those of the smooth tube.

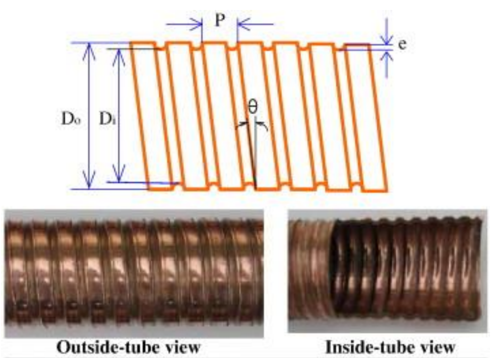

Figure 2.3-16. Configuration of a corrugated tube (Pethkool et al., 2011).

Sadighi Dizaji et al. (2015) studied the PEC for different arrangements of the corrugated tubes in a double-pipe heat exchanger (see Figure 2.3-17). They concluded that the arrangement type case f had a significant effect on the overall PEC values, with the highest PEC factor being 1.2 at a Reynolds number of 18,000.

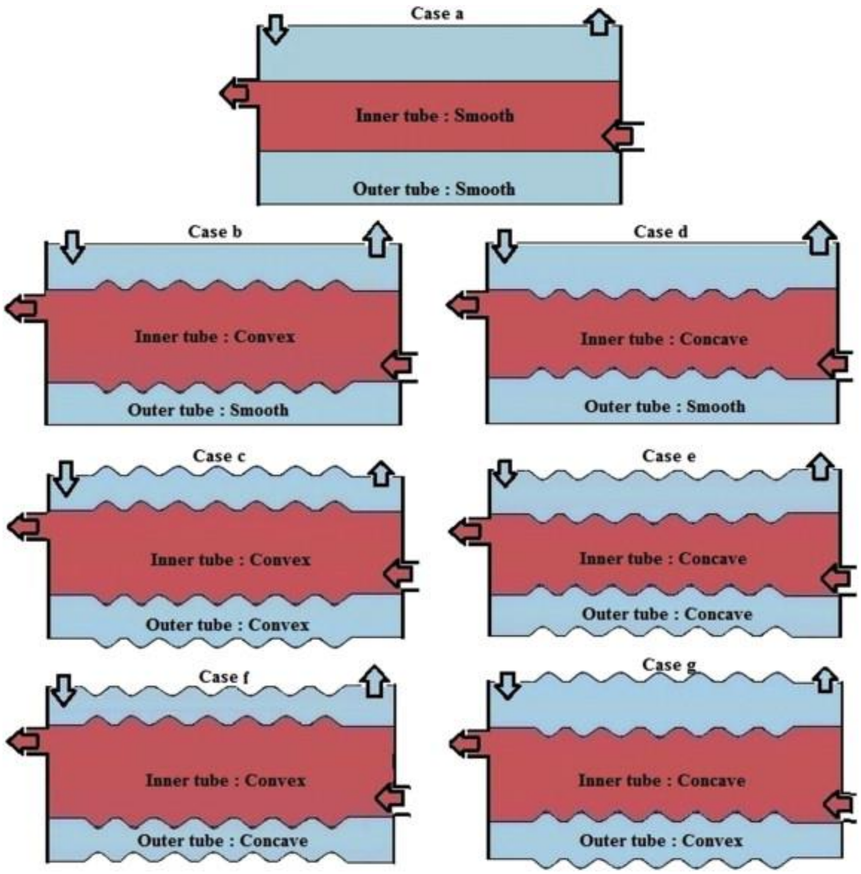

Figure 2.3-17. Arrangement for corrugated double pipe heat exchanger. (Sadighi Dizaji et al., 2015).

Hu et al. (2022) compared the thermal performance of three types of corrugated tubes (outward corrugated tubes, helically corrugated tubes and transversely corrugated tubes). The helically corrugated tubes have the highest PEC value at around 1.09 with a pressure drop ratio increased by around 3.

Dimples

In addition to the research on corrugated tubes, the study of surface modifications also extends to dimples. Xie et al. (2022) studied the influence of staggered and helical dimples on heat exchangers. The helical dimples had a better overall thermal performance than the staggered ones. The Nusselt number and friction factor increased with dimple depth and radius and decreased with spiral pitch and transverse length. This implies that proper adjustment of dimple geometric parameters can effectively enhance heat transfer coefficient.

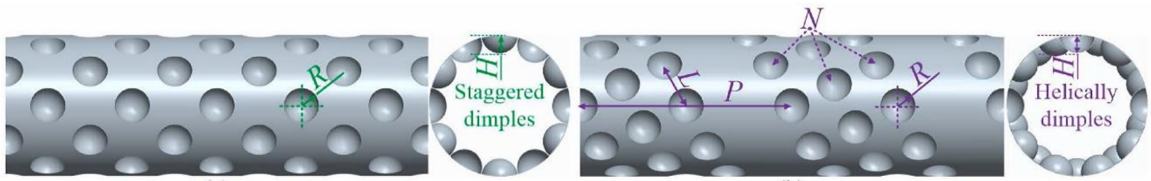

Figure 2.3-18. Dimples arrangements (Xie et al., 2022).

Kaood et al. (2022) simulated the thermal performance of conical tubes with dimples as shown in Figure 2.3-19. Overall, the convergent dimple tubes exhibited better thermal performance than the divergent dimple tubes. They concluded that the convergent dimpled tube with a diameter ratio of 1.5 presented the highest PEC value at 1.3 at the lowest Reynolds number.

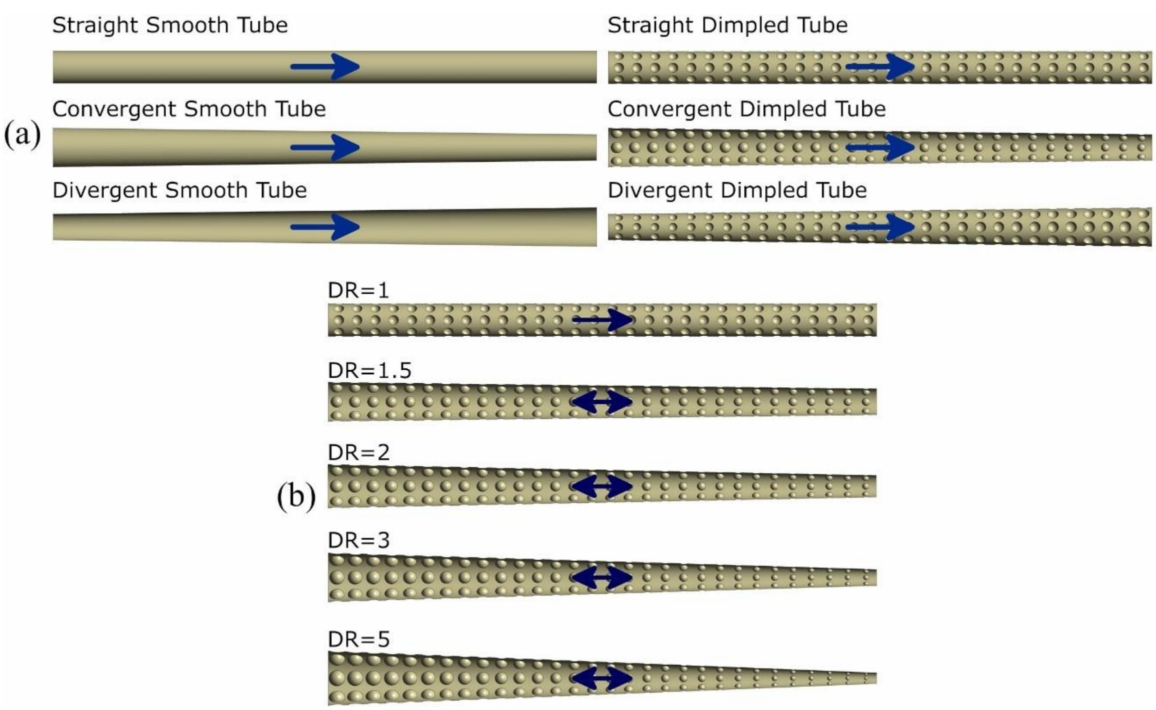

Figure 2.3-19. (a) Straight and conical tubes with and without dimples. (b) Conical tubes with different diameter ratios (DR) (Kaood et al., 2022).

Wang et al. (2022) attempted to combine a 3-lobed tube and dimples. They concluded that this combination had a positive influence on the overall thermal performance. The Nusselt number and friction factor increased by 26.7% and 20.0%, respectively, when the Reynolds number was equal to 2,000 compared to the 3-lobed tube without dimples.

The ability of surface modification to enhance heat transfer has been extensively demonstrated in the literature. Corrugated tubes and dimples, in particular, are cost-effective and easy to manufacture, making them attractive options for heat-transfer applications. However, it is unclear whether these dimple structures affect certain physical properties of the tube, such as their mechanical strength, shape stability, or fatigue resistance. Further research is needed to comprehensively evaluate the impact of dimple structures on the long-term performance and integrity of the tube.

2.3.4.4 Swirl Flow Devices (wire coiled, twisted tape, lobed tube and turbine)

Swirl flow devices, such as twisted tape and lobed tubes, can generate swirl flow through their unique geometries.

Wire coiled

Gunes et al. (2010) presented an experimental study of the thermal performance in a tube inserted with coiled wires as shown in Figure 2.3-20. The highest PEC value of 1.5 was achieved and the pressure drop increased by around 8 times.

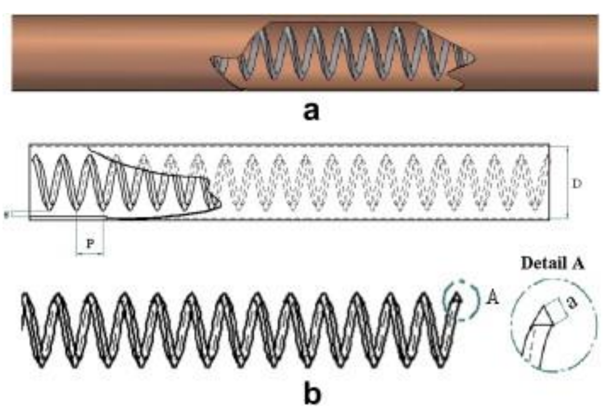

Figure 2.3-20. (a) The inserted coiled wire in the tube. (b) coiled wire overview (Gunes et al., 2010).

Keklikcioglu and Ozceyhan (2016) also investigated the heat transfer effect of inserting a coiled wire and concluded that the maximum PEC value was observed at the lowest Reynolds number of 3,429. They further inserted three different types of coiled wires, regularly spaced (Keklikcioglu and Ozceyhan, 2021), as shown in Figure 2.3-21. The diverging type of coiled wire had the highest PEC value at 1.6 with a friction factor ratio around 2.5. This indicates that while the diverging coiled wire can significantly enhance heat transfer (as reflected by the high PEC value), it also leads to a relatively large increase in the friction factor, which implies a higher pressure drop.

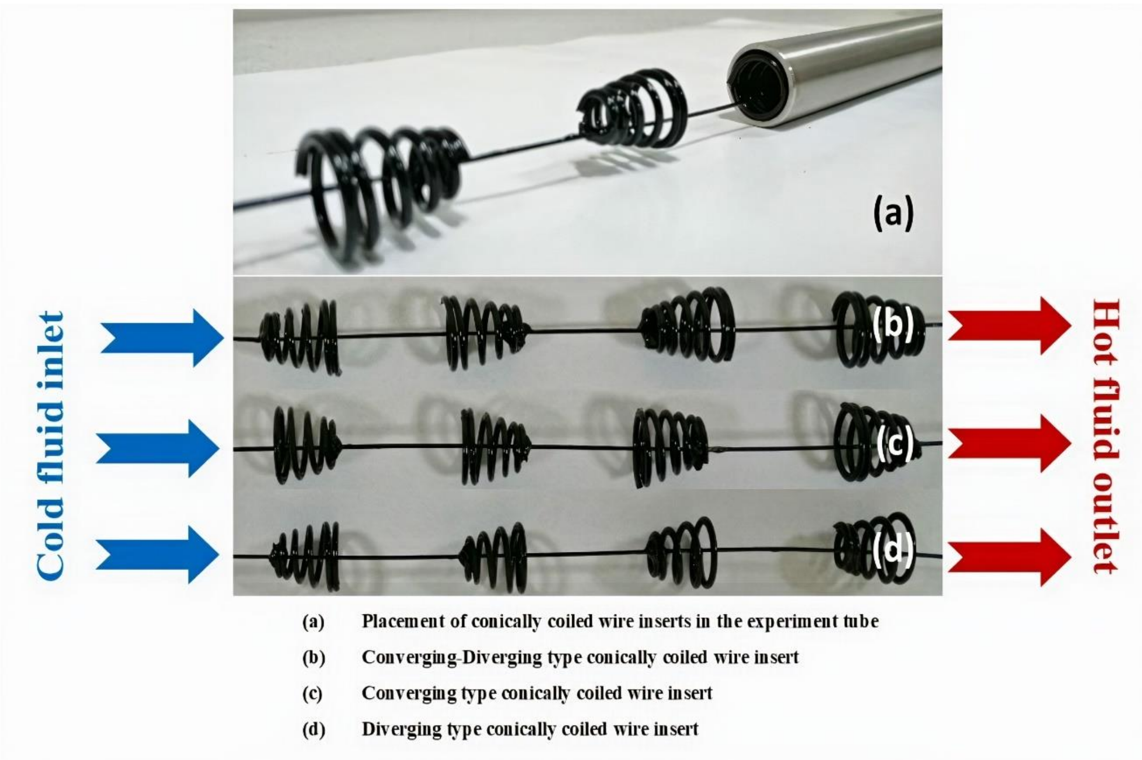

Figure 2.3-21. Regularly spaced coiled wires (Keklikcioglu and Ozceyhan, 2021).

Twisted tape

The twisted tape has been proven effective and applicable in many application areas (Keklikcioglu and Ozceyhan, 2018). However, sometimes it requires a greater amount of pumping power to achieve the desired improvement. This was noted by Liu and Sakr (2013) who inserted a full-length twisted tape into a tube; the pressure drop was 1.85 times greater than that of the circular tube. Such high-pressure drop issues increased the difficulty of installing these devices into existing systems. Therefore, efficiently enhancing the heat transfer rate, with a modest increase in pressure drop, requires further investigation (Li et al., 2022a).

Eiamsa-ard and Seemawute (2012) presented numerical and experimental studies on both continuous and decaying swirl flows generated by inserting twisted tapes. Although over a Reynolds number range of 4,000 to 10,000, the PEC factor for the decaying swirl flow was poorer than the continuous one, with Reynolds numbers greater than 10,000, the PEC factor for the decaying swirl flow surpassed that of the continuous flow at twisted ratios of 4 and 5.

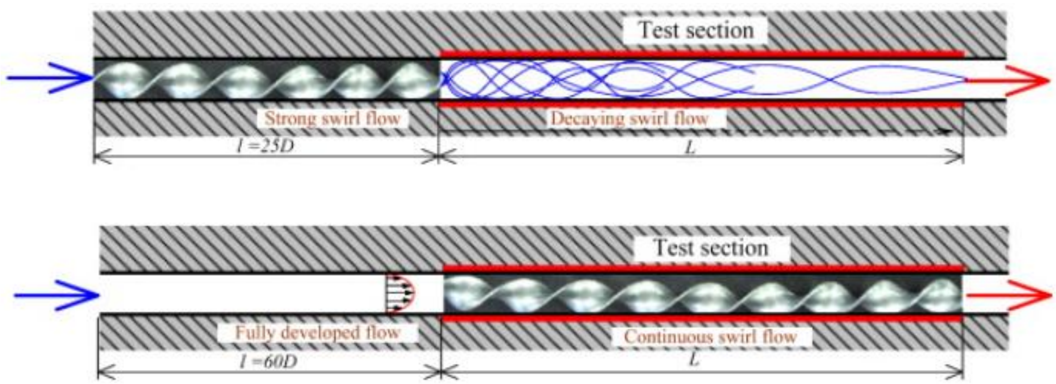

Figure 2.3-22. Continuous and decaying swirl flow generated by twisted tape (Eiamsa-ard et al., 2012).

Wang et al. (2011) adopted regularly spaced short-length twisted tape rather than full-length tape. They determined that when the Reynolds number ranged from 10,000 to 20,200, the greatest PEC was 1.08. However, the friction factor ratio remained higher than 1.8. This indicates that while the short-length twisted tapes can enhance heat transfer to a certain extent, they also lead to a relatively large increase in pressure drop. Du and Hong (2020) further modified the shape of a regularly spaced short-length twisted tape and combined it with a transverse rib tube. Though this combination achieved an overall enhancement of 1.00-1.26, the friction factor ratio increased by approximately 5.97 to 15.31.

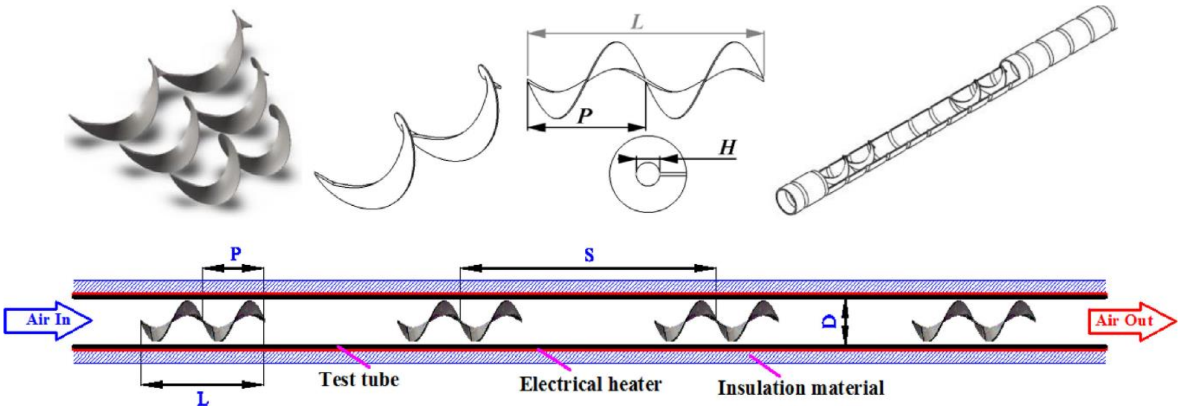

Figure 2.3-23. Regularly spaced short-length twisted tape (Du and Hong, 2020).

Numerous attempts have been made to modify the twisted tape surface, such as peripherally-cut twisted tapes, delta-winglet twisted tape, cut twisted tape and perforations in twisted tape, as summarised by various researchers (Bucak and Yılmaz, 2020, Zhang et al., 2016, Shelare et al., 2022).

In addition to modifying the tape surface, Chokphoemphun et al. (2015) presented experimental results on the effect of heat transfer and pressure drop by adding multiple twisted tapes into a circular tube as shown in Figure 2.3-24. Increasing the number of twisted tapes also increased the heat transfer rate and pressure drop. The quadruple counter twisted tape provided the highest PEC factor ranging from 1.11 to 1.33. However, its pressure drop was 3.61-4.06 higher than that of a circular tube.

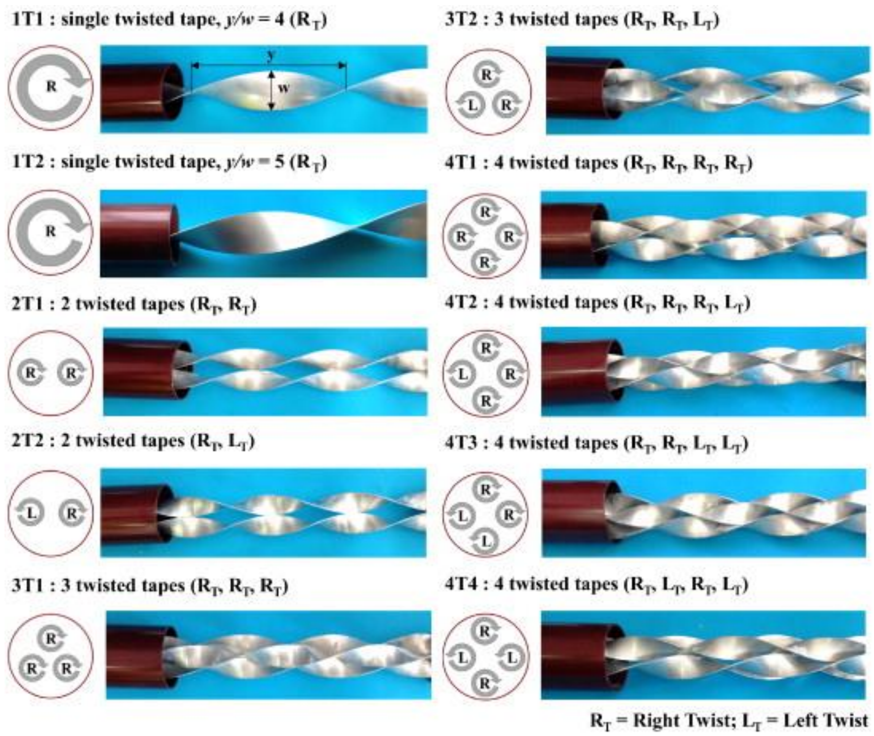

Figure 2.3-24. Test tube inserted with different numbers of twisted tapes (Chokphoemphun et al., 2015).

Furthermore, Samruaisin et al. (2018) explored the thermal enhancement and flow resistance behaviours of a circular tube with regularly spaced quadruple twisted tape. The Nusselt number and friction factor decreased when the distance between the twisted tapes decreased. A maximum PEC factor of 1.27 was achieved at the smallest distance between each twisted tape. Qi et al. (2018b) conducted experiments on self-rotating twisted tape and TiO_2-H_2O nanofluids. The results showed an excellent enhancement in the heat transfer of 101.6% compared with that in a circular tube. Zhang et al. (2021) used a self-rotating short-length twisted tape and concluded that the self-rotating tape generated higher performance compared with the stationary one. The self-rotation can disrupt the boundary layer more effectively, enhancing heat transfer while keeping the pressure-drop increase within a certain range. Xiao et al. (2024) numerically and experimentally investigated the thermal effect of inserting an assembled self-rotating twisted tape into a tube. They concluded that by self-rotation the PEC value was 36% higher than that of the stationary one.

Overall, these studies show a trend of continuous improvement in the design and application of twisted tapes, from single tapes to multi-tapes and self-rotating tapes, aiming to achieve better heat-transfer performance with reasonable pressure-drop levels.

Lobed tube

The lobed tube is the most visually distinctive of all tube designs. Yang et al. (2011) carried out experiments on a two-lobed swirl tube, also known as a twisted oval tube. They found that increasing the twisted ratio of the tube resulted in higher heat transfer coefficients and greater pressure drops. This phenomenon can be attributed to the fact that a higher twisted ratio leads to a more complex flow pattern inside the tube.

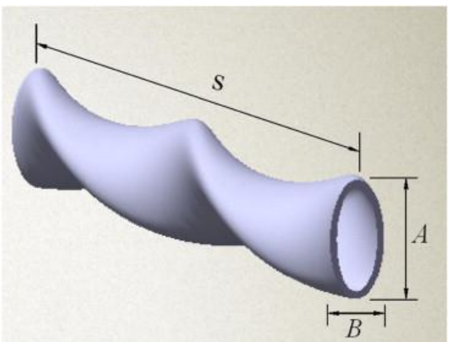

Figure 2.3-25. Twisted oval tube (Yang et al., 2011).

The mechanism of thermal enhancement by an oval tube was investigated by Tan et al. (2012). They conducted experiments and simulations to demonstrate the influence of the geometrical shape of the 2-lobed tube. By analysing the flow velocity and temperature distribution, the existence of a secondary flow inside the tube was observed, which better revealed the hidden mechanism underlying the heat enhancement of the twisted tube design.

In addition, Tan et al. (2013) and Li et al. (2018) attempted to apply an oval tube to an actual shell and tube heat exchanger The performance of the oval tube increased by 25.5%-33.3% compared to that of the circular tube. Luo and Song (2021) carried out simulation work on two counter-2-lobed tubes with air as the working medium. They found that a strong longitudinal vortex was generated in this type of geometry. As a result, the Nusselt number increased by 157% and the friction factor increased by 118% compared to a smooth circular tube. Furthermore, Tang et al. (2015) provided a newly developed 3-lobed tube for a heat exchanger and compared its thermal performance with oval and circular tubes. It was noted that the 3-lobed tubes provided a higher heat transfer and pressure drop compared with those of the other two by using synergy principle analysis (a theory that analyses the synergy relationship between the velocity field and the temperature gradient field to evaluate heat transfer performance).

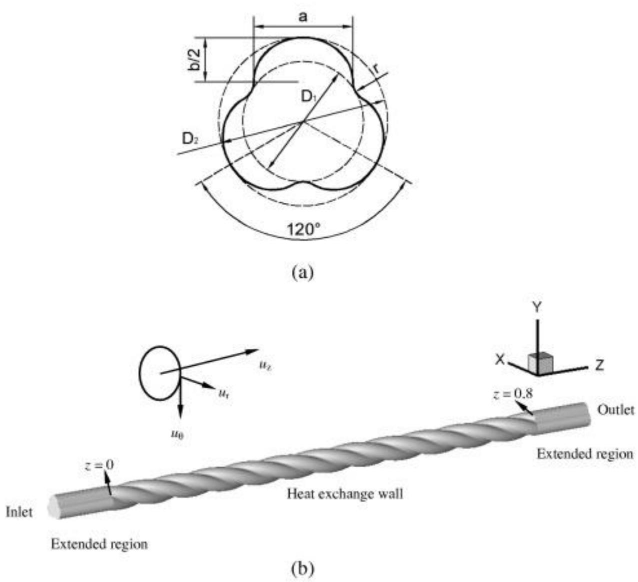

Figure 2.3-26. 3-lobed tube (Tang et al., 2015).

Jafari et al. (2017a) conducted simulation and experiments to evaluate the thermal and pumping power effect of a three-lobed swirl generator. The heat transfer enhancement ranged from 125-155% by different types of swirl generators. The strongest swirl was observed after exiting the swirl-inducing pipe and decayed exponentially afterwards. They then extended their work to a 4-lobed (Jafari et al., 2017c) and a 5-lobed swirl generator (Jafari et al., 2017b) under the same experimental conditions. With a friction factor ratio of less than 152%, the overall heat transfer performance for the 4- and 5-lobed generators increased by 1.3 to 1.65 and 1.25 to 1.52, respectively. Therefore, instead of an entire section of the lobed tube, a lobed swirl generator may provide a better overall performance with an acceptable pressure drop. However, they only used a constant wall flux as the experimental condition instead of a double-pipe heat exchanger. Hemmat Esfe et al. (2018) performed a numerical study on a three-lobed tube inserted with twisted tape. The pitch ratio and baffle width to tube diameter were taken as two parameters for evaluation. The Nusselt number and friction factor increased with the augmentation of those two parameters. Arjmandi et al. (2020) carried out a numerical simulation with a combined vortex generator and twisted tape. The results indicated that reducing the distance of each turbulator would lead to a thermal efficiency increase of up to five times compared to a circular one. The thermal potential of a twisted oval tube combined with a wire coil was also studied numerically (Yu et al., 2020). They performed such an alteration with different cross-sections (i.e., circular, square and equilateral triangles) with a square cross-section giving the maximum enhancement for Nu at 57.5%. In addition, Omidi et al. (2019) numerically studied the thermal effect of a 3-lobed tube with a Y tape inserted. The results indicated that the Y-tape would provide higher heat transfer performance but also higher pressure drops than a single 3-lobed tube.

Overall, these studies show a continuous exploration of different tube enhancement techniques, including swirl generators, oval tube 3-lobed tube, and combinations of various structures.

Other devices

Kurtbaş et al. (2009) used a novel conical injector swirl generator to enhance the thermal performance. They achieved a PEC value ranging from 2.3 to 1.4 with Reynolds numbers ranging from 10,000 to 35,000.

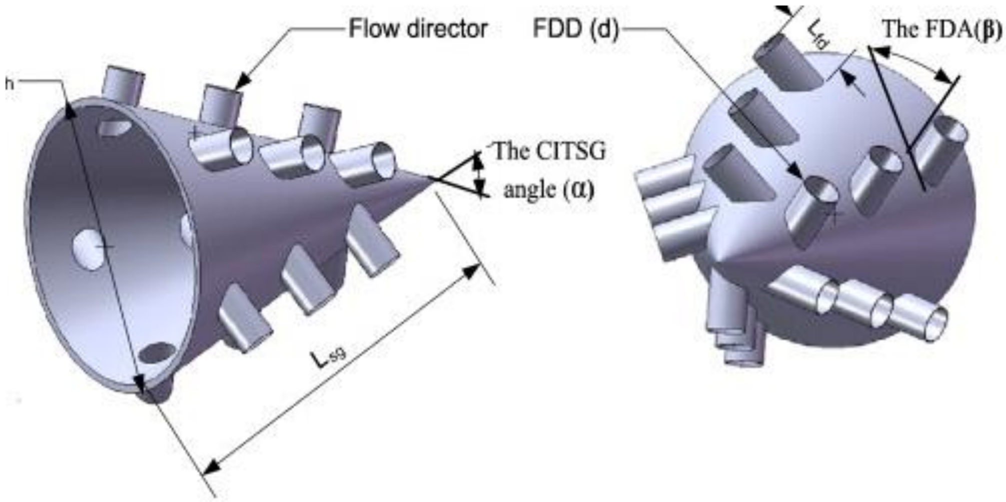

Figure 2.3-27. Detailed figure of the conical injector swirl generator (Kurtbaş et al., 2009).

Zohir et al. (2011) examined the impact of installing a freely rotating propeller, reporting that the heat transfer coefficient increased by around 1.69 times, and the pressure drop tripled. Bilen et al. (2022) experimentally and numerically studied a decaying swirl flow generated by a swirl generator. Compared to a system without the swirl generator, the enhancement in the heat transfer coefficient ranged from 10% to 41%. However, due to a high-pressure drop penalty (an increase of 130%-576% compared to the system without the swirl generator), the maximum PEC value was approximately 0.83.

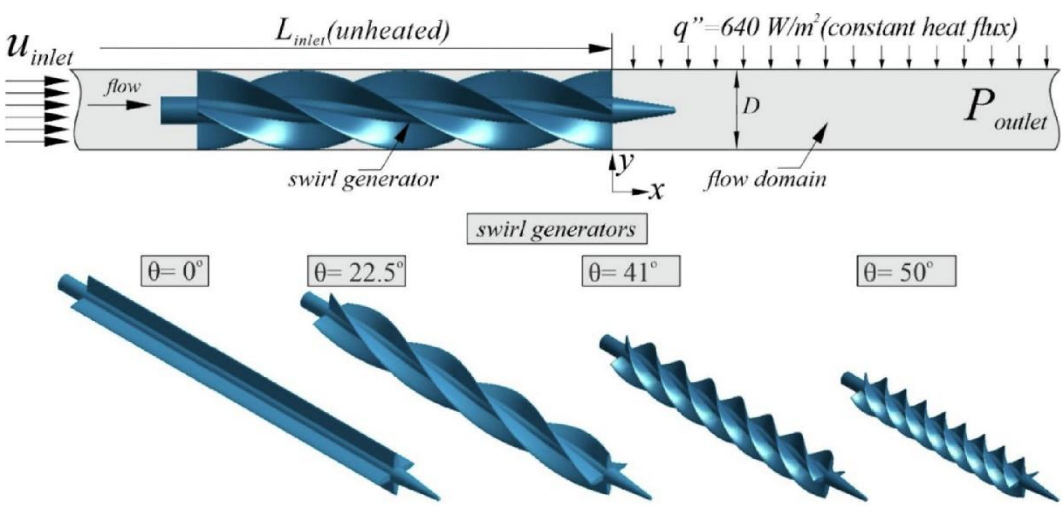

Figure 2.3-28. Schematic view of the inserted swirl generator with different rotation angles (Bilen et al., 2022).

Hangi et al. (2022) numerically investigated the thermal influence of inserting a freely rotating turbine-shaped swirl generator. Although the S-type generator had the highest enhancement in the heat transfer coefficient, the highest PEC factor of 1.4 belonged to the TzT type, which had the lowest pressure drop penalty of approximately 1.6 times that of a smooth tube.

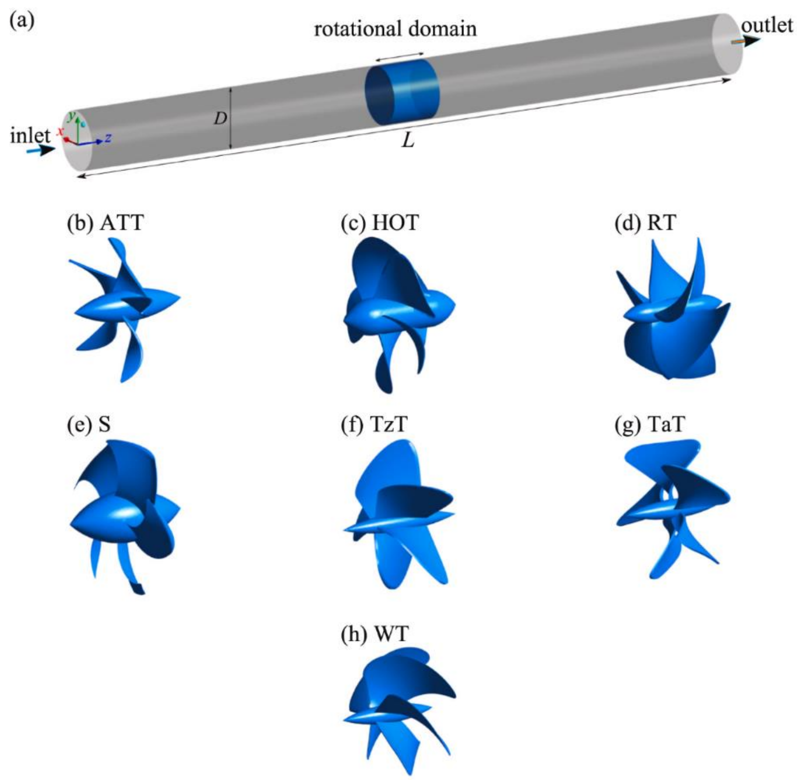

Figure 2.3-29. Different types of swirl generators (Hangi et al., 2022).

In conclusion, these swirl devices can considerably enhance the heat transfer rate by introducing a swirling flow. Similar to all the passive methods, these devices are superior in their simplicity and ease of installation. However, devices such as twisted tape that involve inserting material can significantly increase the pumping power cost to achieve the desired improvement. For instance, by inserting a full-length twisted tape, the pressure drop was more than 1.85 times higher than that of an empty tube (Liu and Sakr, 2013). These additional surfaces may be susceptible to fouling and difficult to clean. In contrast, lobed tubes could provide a relatively lower pressure drop, and inserting a “swirl generator” could achieve the same PEC value in comparison to the entire length of a lobed tube.

2.3.5 Critical Evaluation Parameters

Based on the above literature review, the critical evaluation parameters for the thermal enhancement methods have been summarised. As can be seen in Table 2.3-1, passive heat transfer enhancement methods such as winglets and rings typically result in pressure drop increases that, in most cases, exceed heat transfer enhancements. For example, conical ring turbulators (Ibrahim et al., 2019) induce pressure losses up to 52,000%—an order of magnitude higher than their 420% heat transfer enhancement—rendering them impractical for low-energy systems. A notable exception is rotating tube systems, where moving components can reduce flow resistance. However, evaluating these systems requires considering both the pressure drop reduction and the energy input required for rotation when assessing overall energy efficiency.

Geometric parameter sensitivity emerges as a critical design criterion. For passive methods, pitch and spacing ratios are commonly used for different types of thermal enhancement methods and often a smaller pitch leads to higher thermal enhancement and pressure drop, highlighting the necessity of multi-factor optimisation in design. Dynamic parameters in active systems, such as rotating speeds or magnetic field strengths, offer adjustable performance but introduce operational complexity.

A combination strategies, such as rotating tube with twisted tape (Xiao et al., 2024) demonstrate potential to balance heat transfer gains with manageable pressure penalties. However, such innovations must confront practical constraints, including maintenance demands for moving components in active systems and manufacturability of complex passive geometries. Ultimately, the selection of enhancement techniques should integrate context-specific efficiency metrics, such as the ratio of heat transfer gain to pressure loss (e.g., PEC factors), alongside operational boundaries like fluid type, Reynolds number, and allowable energy expenditure, to ensure optimal design across industrial, thermal, and energy applications.

Table 2.3-1. Critical parameters for the thermal enhancement methods.

Research	Critical Parameters	Thermal enhancement	Pressure loss
Rotating pipe with helical fins (Abou-Ziyan et al., 2016)	Inner tube rotation speed (0 to 400 RPM) Fin spacing 75mm	+730% to +750%	-25% to -30%
Tube vibration (Hosseinian and Meghdadi Isfahani, 2018)	Vibration level (3 m/s^2 to 9m/s^2)	+10% to 21%	-
Magnetic field (Bezaatpour and Goharkhah, 2020)	Magnetic field strength (0 to 1600G) 3% Fe3O4 nanoparticles	+60% to +216%	+50% to +120%
Pulsating flow (Khosravi-Bizhaem et al., 2019)	Pulsating flow frequency (0Hz to 10Hz)	0% to +19%	+3% to +7%
Helical fins (El Maakoul et al., 2017)	Helical fins spacing (0.2m to 0.05m)	+14% to +83%	+130% to 670%
louvered strip (Nakhchi et al., 2020)	Strips angle (15^o to 25^o)	+26% to +56%	+80% to +300%
Winglet (Sun et al., 2020)	Pitch ratio (1.57 to 4.71) Winglet number (4 to 8) Height ratio (0.05 to 0.2)	+15% to +132%	+46% to +1,063%
Conical rings (Ibrahim et al., 2019)	Diameter ratio (0.3 to 0.7) Ring orientations	+100% to +420%	+1,000% to +52,000%
Corrugated tube (Hu et al., 2022)	Corrugation height (0.02 to 0.04) Corrugation pitch (0.6 to 0.8)	+43.7% to +60%	+57.6% to 167%
Twisted tape (Du and Hong, 2020)	Distance ratio (5.7 to 14.2) Pitch length ratio (1.03 to 1.7)	+110% to + 175%	+500% to +1,490%
Lobed tube(Tang et al., 2015)	Lobe number (2 to 6) Twisted pitch ratio (2.5 to 12.5)	+4.8% to +25.3%	+8.5% to +22.8%

Furthermore, a comparison table between the passive and active methods are added in Table 2.3-2.

Table 2.3-2. General comparison between the passive methods and the active methods.

Comparison Dimensions	Passive Methods (e.g., Winglets, Rings)	Active Methods (e.g., Rotating Tubes)
Energy Requirement	None (rely on flow characteristics changes)	Required (e.g., motor-driven pipe rotation)
Pressure Impact	Typically, significant increase in pressure drop (higher flow resistance)	Potential reduction in pressure drop (flow boundary layer disruption by moving components)
Heat transfer coefficient	Limited enhancement (restricted by passive structures)	More significant enhancement (active flow intervention)
Application Scenarios	Low-energy systems, conventional operating conditions	High-load systems, scenarios allowing energy input
Maintenance Complexity	Low (no moving parts)	High (requires maintenance of rotating components)
Comprehensive Energy Evaluation	Only pressure drop vs. heat transfer ratio needs consideration	Requires simultaneous evaluation of pressure drop reduction and energy cost

2.4 Numerical Investigation Techniques

2.4.1 Two Popular Investigation Principles

In addition to using surface Nusselt number, velocity streamlines, and turbulence kinetic energy, the thermal enhancement mechanism can be further investigated using swirl intensity and the field synergy principle. The swirl intensity primarily focuses on the flow characteristics, while the field synergy principle reveals the connection between the flow velocity field and heat transfer enhancement.

2.4.1.1 Swirl Intensity

Swirl intensity is commonly used to describe swirl flow behaviours. The strength of the swirl in a swirl tube is widely described by the swirl number, SN, which is also known as the swirl intensity. It was defined as the ratio between pipe radial and axial momentum flux. (Li and Tomita, 1994)

$$SN = \frac{\int_0^R v_t v_x {r_s}^2 dr_s}{R \int_0^R {v_x}^2 r_s dr_s} \tag{2.3-12}$$

where v_t is the tangential velocity in m/s, v_x is the axial velocity in m/s,r_s is the radial coordinate in m, R is the radius of the pipe in m.

A swirl decay law has been proposed by several researchers to study the relationship between swirl intensity and decay distance, which indicates that the swirl intensity varies exponentially with distance in the flow direction (Rocklage-Marliani et al., 2003).

$$SN = S_{N0} e^{-\beta \frac{x}{D}} \tag{2.3-13}$$

where SN_0 is the initial swirl intensity, x is the decay distance in m, D is the pipe diameter in m, β is the swirl decay rate, which is a dimensionless number.

2.4.1.2 Field Synergy Principle

The field synergy principle, developed by Guo et al. (1998), has been widely applied in recent years by researchers to investigate the mechanism of thermal enhancement (Zhao et al., 2020). This principle establishes that the heat transfer rate is related to the intersectional angle, or synergy angle, between the velocity vector and temperature gradient. A smaller angle indicates a higher heat transfer rate.

Yang et al. (2011) applied the field synergy principle to elucidate the mechanism of heat enhancement in their experiment with a 2-lobed tube. They further discovered that a lower twisted ratio led to both a higher thermal enhancement and a lower average synergy angle, corroborating this principle. Tang et al. (2015) conducted a study on a newly designed three-lobed tube and compared its performance with a two-lobed tube. Simulations were used to calculate the synergy principle, which showed that the average angle for the three-lobed tube was lower than that for the two-lobed tube. This result was consistent with the observation that the three-lobed tube performed better than the oval tube. In addition, Guo et al. (2005) determined the local synergy angle for a helical screw tape inside a circular pipe. The pattern of the local synergy angle matched the local heat transfer coefficient, suggesting that a larger angle led to a lower coefficient.

In principle, convective heat transfer is considered a form of conduction heat transfer, but with the additional factor of fluid movement. For a three-dimensional flow of water in a tube, the viscosity is assumed to be constant. The energy equation of the 3-D boundary can be written as (Zhao et al., 2020):

$$\rho c_p\left(u\frac{\partial T}{\partial x}+v\frac{\partial T}{\partial y}+w\frac{\partial T}{\partial z}\right)=\frac{\partial}{\partial y}\left[\lambda\frac{\partial T}{\partial x}\right]+\frac{\partial}{\partial y}\left[\lambda\frac{\partial T}{\partial y}\right]+\frac{\partial}{\partial y}\left[\lambda\frac{\partial T}{\partial z}\right] \qquad (2.3\text{-}14)$$

where ρ is the density of the fluid, c_p is the heat capacity, u, v, and w are x, y and z components of the velocity field, T is the temperature, λ is the thermal conductivity.

Considering only the conductive component perpendicular to the heat transfer surface and disregarding axial heat conduction within the fluid (Guo et al., 2005), the above equation can be integrated over the thermal boundary layer δ_t (thermal boundary layer thickness).

$$\int_0^{\delta_t}\rho c_p\left(u\frac{\partial T}{\partial x}+v\frac{\partial T}{\partial y}+w\frac{\partial T}{\partial z}\right)dy=-\int_0^{\delta_t}\lambda\frac{\partial T}{\partial y}dy=q_w \qquad (2.3\text{-}15)$$

Outside the thermal boundary, the condition can be written as:

$$\left.\frac{\partial T}{\partial y}\right|_{\delta_t}=0 \qquad (2.3\text{-}16)$$

$$u\frac{\partial T}{\partial x}+v\frac{\partial T}{\partial y}+w\frac{\partial T}{\partial z}=\vec{U}\cdot\nabla T \qquad (2.3\text{-}17)$$

With the above condition, Equation (2.3-15) can be calculated as:

$$\int_0^{\delta_t} \rho c_p (\vec{U} \cdot \nabla T) dy = \lambda \frac{\partial T}{\partial y}\bigg|_{y=0} = q_w \tag{2.3-18}$$

Furthermore, it can be mathematically obtained that:

$$\vec{U} \cdot \nabla T = |\vec{U}||\nabla T| cos\theta \tag{2.3-19}$$

Substituting equation (2.3-19) into equation (2.3-18) gives:

$$\int_0^{\delta_t} \rho c_p (|\vec{U}||\nabla T| cos\theta) dy = q_w \tag{2.3-20}$$

From Equation (2.3-20), it can be observed that a smaller synergy angle θ will lead to a higher heat transfer rate. Thus, one can quantify the heat transfer enhancement effect by calculating the synergy angle.

The local synergy angle θ can be calculated by:

$$\theta = cos^{-1} \frac{u \frac{\partial T}{\partial x} + v \frac{\partial T}{\partial y} + w \frac{\partial T}{\partial z}}{|\vec{U}||\nabla T|} \tag{2.3-21}$$

Thus, the volume-averaged intersectional angle θ_{ave} can be derived from:

$$\theta_{ave} = \frac{\sum \theta dv}{\sum dv} \tag{2.3-22}$$

where dv is each domain of calculating the local intersectional angle.

As previously discussed, the swirl intensity mainly provides insights into the characteristics of swirl flow, with a primary focus on fluid motion. While swirl intensity quantifies rotational flow dynamics, the field synergy principle offers a complementary perspective by linking velocity-temperature gradient interactions, together providing a holistic framework for analysing thermal enhancement mechanisms. However, to gain a comprehensive understanding of the heat-transfer enhancement mechanism, the field synergy principle is employed in further research. It offers a distinct perspective by exploring the relationship between the velocity vector and the temperature gradient.

2.4.2 Choosing Turbulence Models

The turbulence models widely used today, such as $k-\varepsilon$, $k-\omega$ and SST $k-\omega$ models, are based on the Reynolds-averaged Navier-Stokes equations (Fluent, 2011). The key difference is that the $k-\ \varepsilon$ model employs an empirical damping function in the viscous sublayer, necessitating a relatively larger y^+ value ($y^+\geq30$) compared to the $k-\ \omega$ model ($y^+\leq1$). This is because the $k-\ \omega$ model is designed to better capture the near-wall flow characteristics with a smaller y^+ requirement.

However, the $k-\ \varepsilon$ model has limitations. When it faces with adverse pressure gradients, which can reverse the flow boundary layer direction and lead to flow recirculation, the empirical equation unreliable and results in inaccuracies. Among the various $k-\ \varepsilon$ models, the realisable $k-\ \varepsilon$ model is one of the most widely used simulation models in industrial applications (Menter et al., 2021).

In contrast, the k- ω model utilises a denser, near-wall mesh to capture the near-wall sublayer, thereby overcoming the issue present in the $k-\varepsilon$ model. Nevertheless, researchers claim that the $k-\omega$ model has relatively strict requirements for inlet turbulence settings (Fluent, 2023, Fluent, 2011). For example, small errors in the inlet turbulence intensity and length scale can lead to significant deviations in the simulation results and overestimation of the flow turbulence. To address the limitations, the SST $k-\omega$ model was developed (Menter, 1994). This model combines the advantages of the $k-\varepsilon$ model in the free stream region and the $k-\ \omega$ model in the viscous sublayer region. This approach better captures the tangential shear stress near the wall surface compared to the other models while being less sensitive to inlet conditions. Due to these characteristics, the SST $k-\omega$ model is widely used in aerodynamic flows involving adverse pressure gradients and separation from smooth surfaces.

Researchers have conducted investigations on the accuracy level of the different models. In previous studies of a 4-lobed swirl generator, both Ariyaratne (2005) and (Li, 2016) used the $k-\varepsilon$ model to model turbulence with an acceptable difference between simulation and experimental result. However, their model did not include an energy conservation equation. The following researchers compared the accuracy of different turbulence models for simulating heat exchangers. They concluded that the SST $k-\omega$ model is the most suitable one in lobed tube simulation, as it provides more accurate predictions of heat transfer and fluid flow characteristics in such geometries. Therefore, the SST $k-\omega$ model is used in further investigations.

Table 2.3-3. Model's accuracy for lobed tubes.

	RNG $k-\varepsilon$	SST $k-\omega$	realizable $k-\varepsilon$	standard $k-\varepsilon$	standard $k-\omega$
Guo et al. (2010)	δ_{Nu}=20% δ_f=35%	δ_{Nu}=12% δ_f=26%	-	-	-
Tang et al. (2015)	δ_{Nu}=35% δ_f=7.2%	δ_{Nu}=2.7% δ_f=4.6%	δ_{Nu}=21% δ_f=7.2%	-	δ_{Nu}=5% δ_f=2.3%
Abe et al. (2021)	-	δ_{Nu}=10%	δ_{Nu}=30%	-	-
. Li et al. (2022b)	δ_{Nu}=6.7% δ_f=21%	δ_{Nu}=6.4% δ_f=9.7%	δ_{Nu}=6.8% δ_f=13.5%	δ_{Nu}=6.5% δ_f=9.9%	δ_{Nu}=6.6% δ_f=13.5%
(Liaw et al., 2023)	-	δ_{Nu}=2% δ_f=2%	δ_{Nu}=3% δ_f=1%	-	-
(Liu et al., 2024b)	δ_{Nu}=26.2% δ_f=17.9%	δ_{Nu}=6.7% δ_f=2.9%	δ_{Nu}=12.5% δ_f=9.4%	-	δ_{Nu}=7.5% δ_f=3.2%

2.4.3 Setting Thermal Boundary Conditions.

ANSYS CFD offers versatile options for fluid heat transfer modelling. It can calculate the heat transfer within a single flow region by setting the wall boundary condition, or model the heat transfer in two separate fluid regions, such as a double pipe heat exchanger. To investigate the impact of thermal boundary conditions on the heat transfer coefficient, Taylor et al. (1990) conducted experiments in a turbulent flow region, considering both constant wall temperature and constant heat flux conditions. They concluded that in the turbulent region, changing the wall boundary condition has little effect on the heat transfer coefficient.

Rohsenow et al. (1998) pointed out three thermal boundary conditions for heat exchanger simulation: constant wall temperature in both the axial and peripheral directions; constant wall heat flux in the axial direction while the wall temperature is constant in the peripheral direction (here, the wall heat flux refers to the amount of heat transferred per unit time through a unit wall area, and the wall temperature is the average temperature of the wall); constant wall heat flux in both the axial and peripheral directions. They further revealed that for laminar flow, the heat transfer rate was sensitive to the thermal boundary condition. However, in turbulent flow, different thermal boundary conditions did not lead to significant differences. This is because in the turbulent state, the strong mixing of the fluid weakens the influence of the wall boundary conditions. Therefore, based on this characteristic, instead of constructing the entire experimental rig, the simulation boundary condition can be simplified by setting the tube wall temperature to a constant value. The rationality of this simplification lies in the fact that the influence of boundary conditions on heat transfer is relatively small in turbulent flow, and the simplified setting will not cause large deviations in the results.

Some researchers who investigated the thermal effect of a lobed tube in the turbulent region did not simulate the entire double-pipe heat exchanger. Instead, they only constructed a single pipe and set the pipe wall at either a constant wall temperature or a constant wall heat flux. (Biegger et al., 2015, Li et al., 2021, Omidi et al., 2019, Tan et al., 2012, Tang et al., 2015, Wu et al., 2018, Yu et al., 2020, Liaw et al., 2023). These researchers verified the reliability of the constant temperature and constant wall flux approach through experiments. Specifically, they compared the results under the simplified simulation conditions with the actual experimental data. Thus, such simplification will be used in the numerical investigations.

2.5 Experimental Investigation Techniques

To systematically compare the heat transfer enhancement rate for each technique, an analytical method can be employed involving the solution of a system of mass, momentum and energy conservation equations. However, this approach is only practical for simple geometries and often under specific assumptions. Since most heat transfer enhancement techniques utilise complicated geometries that produce intricate flow fields, a systematic comparison cannot be achieved through analytical methods (Fernández-Seara et al., 2007).

As previously defined, two dimensionless coefficients, the Nusselt number, and friction factor, can be used systematically to compare the overall performance. The friction factor can be directly obtained by measuring the pressure drop, Δp, across the flow region.

Therefore, obtaining the Nusselt number from the heat transfer coefficient, h, is a critical part of the heat transfer experiment. Researchers have developed numerous correlations for Nusselt number to assess the factors calculated from circular pipes, utilising the Sieder-Tate (2.5-1) and Gnielinski Equations (2.5-2) (Gnielinski, 2013).

The analytical friction factors for the circular pipe were also compared with those obtained by Petukhov (2.5-3) and, Blasius as defined in Equations (2.5-4) (Welty, 2001). The Sieder-Tate (2.5-1) accounts for the effect of viscosity difference, while the Gnielinski (2.5-2) couples heat transfer and friction factor to account for turbulent momentum and heat transport. For the friction factor, f, the Petukhov (2.5-3) and Blasius (2.5-4) apply to smooth pipes.

$$Nu_c = 0.027Re^{4/5}Pr^{1/3}(\frac{\mu_{av}}{\mu_s})^{0.14} \tag{2.5-1}$$

$$Nu_c = \frac{(f/8)(Re-1000)Pr}{1+12.7(f/8)^{0.5}(Pr^{\frac{2}{3}}-1)} \tag{2.5-2}$$

$$f_c = (0.79lnRe - 1.64))^{-2} \tag{2.5-3}$$

$$f_c = 0.316Re^{-0.25} \tag{2.5-4}$$

where μ_{av} is the average viscosity and μ_s is the viscosity at the wall.

2.5.1 Single Tube Method

Some heat transfer enhancement techniques are too intricate to be implemented within a double-pipe heat exchanger. Instead, researchers have chosen to use a single tube, which enables the direct measurement of the surface temperature (Suresh et al., 2012, Qi et al., 2018a, Jafari et al., 2017a, Samruaisin et al., 2019). This tube was encircled using a helical coil heater to provide a heating source. The wall temperature was typically measured directly by affixing multiple thermocouples to the surface of the tube. To reduce the heat loss to the surroundings, insulation layers were employed around the test tube.

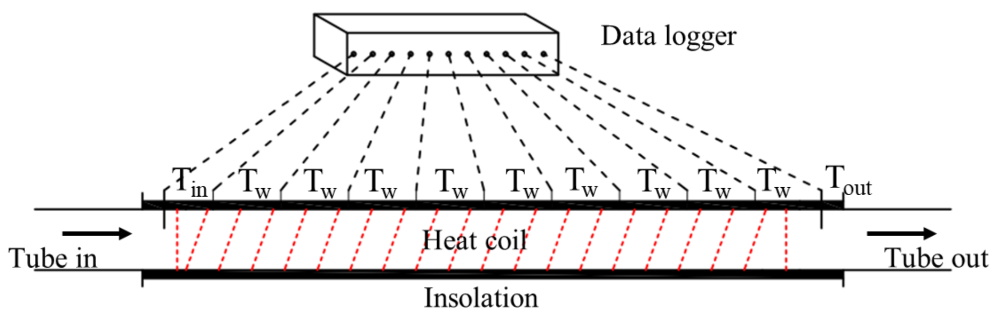

Figure 2.5-1. Sample experimental setup for measuring surface temperature.

The general procedure to obtain the heat transfer coefficient is illustrated below:

Firstly, the average temperature on the tube wall is calculated (assume eight thermal couples are used):

$$\bar{T}_w = \sum_{i=1,n}^{n} T_{w,i}/8 \tag{2.5-5}$$

The overall heat transfer rate $\dot{Q}$ can be calculated from the following equations:

$$\dot{Q} = mc_p(T_{out} - T_{in}) \tag{2.5-6}$$

where m is the mass flow rate in kg/s, c_p is the heat capacity of the fluid in $J/(kg \cdot K)$, T_{out} and T_{in} are the outlet and inlet temperatures in K.

The heat generated by electricity is calculated with the following equation.

$$Q = VI \tag{2.5-7}$$

where V and I are the voltage and electric current, respectively.

Multiple sets of experimental setups can be used to obtain the mass flow rate, wall temperature, and inlet and outlet temperatures. From these data, the heat transfer coefficient can be calculated using in Equation (2.3-4).

This experimental method has been favoured by many researchers investigating various thermal enhancement techniques, such as lobed tube swirl generators (Jafari et al., 2017a), and regularly spaced twisted tapes (Samruaisin et al., 2019). Although this approach is more convenient than constructing a double-pipe heat exchanger, as the heat transfer coefficient can be calculated directly, it may not accurately represent the thermal performance of the enhancement in actual working conditions. Therefore, a double pipe method is developed.

2.5.2 Double Tube Method (Wilson plot method)

To obtain heat transfer coefficient, the surface temperature of the inner tube is required. However, it can be challenging to measure the surface temperature in a double-pipe heat exchanger during the experiment. An indirect method, known as the Wilson plot technique, was developed to evaluate the convective heat transfer coefficient in a shell and tube heat exchanger (Fernández-Seara et al., 2007). The general idea of this approach is to separate the overall heat transfer coefficient, U, into the convective coefficients of the tube and shell sides, and the remaining heat transfer resistance in the heat exchange process. A conventional double-pipe heat exchanger experiment is depicted in Figure 2.5-2, where the inlet and outlet temperatures at the shell and tube sides, respectively, are monitored.

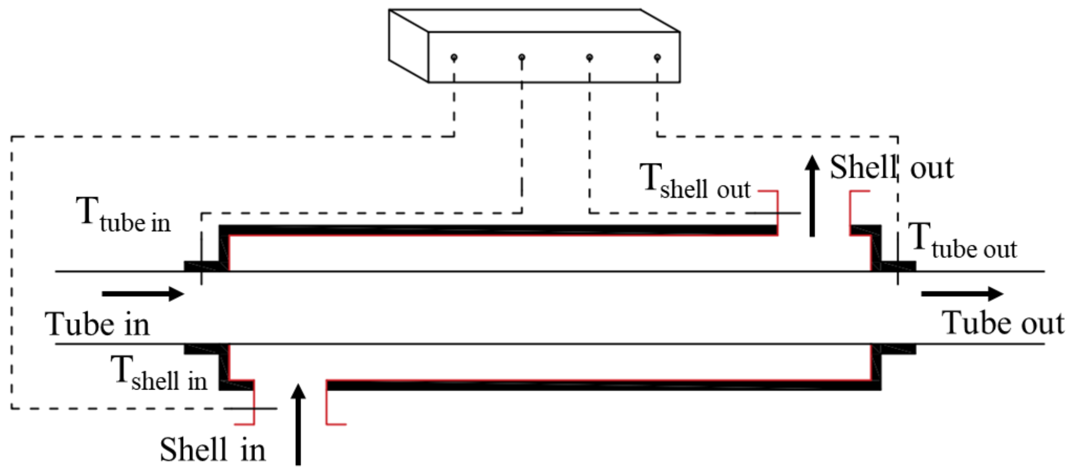

Figure 2.5-2. Double pipe heat exchanger experimental set up.

The overall heat transfer coefficient U can be obtained through the following procedures.

Firstly, heat transfer rates of the tube side, Q_t, and the shell side, Q_s, are calculated from the following equations,

$$Q_t = m_t c_{p,t}(T_{t,out} - T_{t,in}) \quad (2.5\text{-}8)$$

$$Q_s = m_s c_{p,s}(T_{s,in} - T_{s,out}) \quad (2.5\text{-}9)$$

where the m_t and m_s are the mass flow rate of the tube and shell sides in kg/s, $c_{p,t}$ and $c_{p,s}$ are the heat capacity of the tube and shell sides in $J/(kg \cdot K)$, $T_{t,out}$ and $T_{s,out}$ are the outlet temperature at the tube and shell sides and $T_{t,in}$ and $T_{s,in}$ are the inlet temperature at the tube and shell sides in K.

The average heat transfer rate between the shell and tube sides is calculated from,

$$Q_{av} = \frac{Q_t + Q_s}{2} = UA\Delta T_{LMTD} \quad (2.5\text{-}10)$$

where U is the overall heat transfer coefficient in $W/(m^2 \cdot K)$, A the heat transfer area in m^2 and ΔT_{LMTD} the logarithmic mean temperature in K. The logarithmic mean temperature difference between the inlet and outlet of the swirl tube can be calculated based on:

$$\Delta T_{LMTD} = \frac{\left(T_{s,out} - T_{t,in}\right) - (T_{s,in} - T_{t,out})}{ln\frac{T_{s,out} - T_{t,in}}{T_{s,in} - T_{t,out}}} \tag{2.5-11}$$

The overall heat transfer coefficient can be expressed as the sum of the convective heat transfer coefficient of the shell side h_s, the convective heat transfer coefficient of the tube side h_t and the fouling resistance R_f and wall resistance R_w.

$$\frac{1}{U} = \frac{1}{h_s} + R_w + R_f + \frac{d_{w,o}}{h_t d_{w,i}} \tag{2.5-12}$$

where h_t and h_s are the heat transfer coefficients for the tube and shell sides in $W/(m^2 \cdot K)$, R_w is the wall resistance in $(m^2 \cdot K)$/W, R_f is the fouling resistance in in $(m^2 \cdot K)$/W, $d_{w,o}$ and $d_{w,i}$ is the tube side outer and inner diameters in m.

The wall resistance can be expressed as:

$$R_w = \frac{\ln({}^{d_{w,o}}\!/_{d_{w,i}})}{2\pi\lambda_w L} \tag{2.5-13}$$

where λ_w is the wall thermal conductivity in $\mathrm{W}/(m \cdot K)$, L is the tube length in m.

Fouling resistance is typically neglected because the equipment is usually thoroughly cleaned before the experimental runs. During the experiments, the shell side flow rate should be fixed to its maximum value and the tube side flow rate should change gradually. If the mass flow rate of the shell side is fixed as a constant, then the alteration of the overall heat transfer coefficient will be caused mainly by the variation in the tube side heat transfer coefficient, while the change in the rest of the heat transfer coefficient is negligible (Fernández-Seara et al., 2007). Therefore, by neglecting the fouling resistance, the wall resistance and shell side coefficient can be considered constant.

$$C_1 = \frac{1}{h_s} + R_w \tag{2.5-14}$$

where C_1 is a constant named shell and wall resistance.

Furthermore, researchers have discovered that the heat transfer coefficient, h_t , is influenced not only by the flow velocity but also by the properties of the fluid. These equations related the Nusselt number to the Reynolds number and Prandtl number in a general form, which has been proven to be effective in describing the heat transfer under different flow rates. Reynolds and Prandtl numbers are used in the general correlation equations for forced convection (Dittus and Boelter, 1985, Sieder and Tate, 1936, Welty, 2008).:

$$Nu = aRe^b Pr^c \tag{2.5-15}$$

where a and b are constants, the Reynolds number is calculated from $Re = \frac{\rho u D_h}{\mu}$, the Nusselt number Nu is $Nu = \frac{hD_h}{\lambda}$ and the Prandtl number is $Pr = \frac{\mu c_p}{\lambda}$.

The overall heat transfer coefficient U can be calculated in terms of the individual heat transfer coefficients.

$$\frac{1}{U} = \frac{1}{h_s} + R_w + R_f + \frac{d_{w,o}}{a\lambda} Re_i^{-b} Pr^{-0.4} \tag{2.5-16}$$

where h_s are the heat transfer coefficient for shell sides in $W/(m^2 \cdot K)$, R_w is the wall resistance, R_f is the fouling resistance and $d_{w,o}$ and $d_{w,i}$ are the tube side outer and inner diameters in m.

To determine the constants a and b, the flow rate of the hot water on the shell side should be fixed at its maximum value and the temperature variation of the inlet and outlet hot water should be small, ensuring that the heat transfer coefficient h_s on the shell side is almost unchanged. Since the internal surfaces of the pipes are carefully washed before the experiment, R_f is neglected. The above equation can be simplified to:

$$\frac{1}{U} = C_1 + C_2 Re_i^{-b} \tag{2.5-17}$$

where C_1, C_2 are constants and $C_1 = \frac{1}{h_s} + R_w$ and $C_2 = \frac{d_{w,o} Pr^{-0.4}}{a\lambda_i}$.

Through the experiment, a set of data regarded to Re and U can be obtained. A regression analysis can be applied to calculate those constants. The final calculated value can be checked with a modification of the Equation (2.5-17)

$$ln\left[\frac{C_2 U}{1 - UC_1}\right] = bln(Re) \tag{2.5-18}$$

This general form incorporates the change in fluid properties under different temperatures, which provides a more accurate prediction of the heat transfer coefficient calculations. Based on this equation, a general correlation for circular pipe can be summarised (Dittus and Boelter, 1985).

$$Nu_c = 0.023 Re^{0.8} Pr^{0.4} \tag{2.5-19}$$

Moreover, in most cases, the shell side heat transfer coefficient remained largely unchanged between the different stages of the calculation process. Researchers can predict this coefficient based on the above correlation, enabling them to estimate the constant C_1 within the correlation.

In addition, Sieres and Campo (2018) highlighted that traditional Wilson plots neglect data point uncertainties. Therefore, they proposed a non-linear weighted regression method in which each data point was evaluated to be inversely proportional to the square value of the experimental uncertainty.

$$\chi^2 = \sum_{i=1}^{N} \left[\frac{\frac{1}{U} - C_1 - C_2 Re_i^{-b}}{\delta_i}\right]^2 \tag{2.5-20}$$

Based on the above equation, constants C_1, C_2 and b can be determined when χ is at a minimum value. The weighting factor δ_i is the combined uncertainty of the experimental data δ_y and the input value, such as the Reynolds number, δ_x

$$ {\delta_i}^2 = {\delta_y}^2 + {\delta_x}^2 \qquad (2.5\text{-}21) $$

Compared to the single-tube method, this method is more complex and incurs higher labour costs; however, it can accurately represent the performance of the enhancement method in the working scenario. Furthermore, it can be applied to other types of heat exchangers, such as shell and tube designs and boilers. In this research, the double pipe method is selected and used.

2.6 Proposed Correlation and comparisons

To conduct numerical investigations on different thermal enhancement methods, the validation of the numerical model is critical to verify to the reliability of the model. Correlations of the Nusselt number and friction factor for different enhancement methods are summarised for this purpose. Correlations that studied laminar flow (Khosravi-Bizhaem et al., 2019), only include the Nusselt number correlation (Goshayeshi et al., 2016), or do not include the Prandtl number (Hu et al., 2022, Sun et al., 2020, Arjmandi et al., 2020, Qi et al., 2018a) are not included. To compare the performance among methods, the Gnielinski equation and Petukhov equation are used to calculate the Nusselt number and friction factor for a circular tube. The Prandtl number is set as 5.77 and the method reported in the literature with the optimal PEC value for comparable flow conditions is selected. The correlations are shown below:

Delta Winglet (Promvonge and Skullong, 2020)

$$ Nu = 0.155Re^{0.767}Pr^{0.4}(Pitch\ ratio)^{0.135}(Blokage\ ratio)^{-0.169} \qquad (2.5\text{-}22) $$

$$ f = 2.106Re^{-0.056}(Pitch\ ratio)^{0.438}(Blokage\ ratio)^{-0.472} \qquad (2.5\text{-}23) $$

Circular rings (Kongkaitpaiboon et al., 2010)

$$Nu = 0.354Re^{0.697}Pr^{0.4}(Diameter\ ratio)^{-0.555}(Pitch\ ratio)^{-0.598} \quad (2.5\text{-}24)$$

$$f = 0.715Re^{-0.081}(Diameter\ ratio)^{-4.775}(Pitch\ ratio)^{-0.846} \quad (2.5\text{-}25)$$

Corrugated tube (Pethkool et al., 2011)

$$Nu = 1.579Re^{0.639}Pr^{0.3}(Rib\ height\ ratio)^{0.46}(Pitch\ ratio)^{0.35} \quad (2.5\text{-}26)$$

$$f = 1.15Re^{-0.239}(Rib\ height\ ratio)^{0.179}(Pitch\ ratio)^{0.164} \quad (2.5\text{-}27)$$

Regularly placed coiled wire (Gunes et al., 2010)

$$Nu = 0.077156Re^{0.716692}Pr^{0.4}(Pitch\ ratio)^{-0.253417} \quad (2.5\text{-}28)$$

$$(Distance/Diameter)^{-0.124382}$$

$$f = 3.970492Re^{-0.367485}(Pitch\ ratio)^{-0.31182}$$

$$(Distance/Diameter)^{-0.157719} \quad (2.5\text{-}29)$$

Coiled wire (Keklikcioglu and Ozceyhan, 2016)

$$Nu = 1.087Re^{0.569}Pr^{0.4}(Pitch\ ratio)^{-0.33}$$

$$(Distance\ ratio)^{-0.152} \quad (2.5\text{-}30)$$

$$f = 6.423Re^{-0.301}(Pitch\ ratio)^{-0.587}$$

$$(Distance\ ratio)^{-0.106} \quad (2.5\text{-}31)$$

Regularly placed helical tapes (Du and Hong, 2020)

$$Nu = 0.0412Re^{0.86224}Pr^{0.4}(Pitch\ ratio)^{-0.11395}$$

$$(Distance\ ratio)^{-0.17507} \quad (2.5\text{-}32)$$

$$f = 39.17661Re^{-0.39561}(Pitch\ ratio)^{-1.07246}$$

$$(Distance\ ratio)^{-0.37832} \quad (2.5\text{-}33)$$

Multiple twisted tape (Chokphoemphun et al., 2015)

$$Nu = 0.092Re^{0.65}Pr^{0.4}(tape\ number)^{0.46} \tag{2.5-34}$$

$$f = 0.791Re^{-0.33}(tape\ number)^{0.873} \tag{2.5-35}$$

Regularly-placed quadruple twisted tape (Samruaisin et al., 2018)

$$Nu = 0.565Re^{0.543}Pr^{0.4}(Distance\ ratio)^{-0.053} \tag{2.5-36}$$

$$f = 1.93Re^{-0.24}(Distance\ ratio)^{-0.041} \tag{2.5-37}$$

Self-rotating twisted tape (Zhang et al., 2021)

$$Nu = 0.02785Re^{0.7748}Pr^{0.3}(1 + length\ ratio)^{0.6139} \tag{2.5-38}$$

$$f = 3.4143Re^{-0.4168}(0.06517 + length\ ratio)^{0.2867} \tag{2.5-39}$$

2-lobed tube (Yang et al., 2011)

$$Nu = 0.3496Re^{0.615}Pr^{\frac{1}{3}}(Aspect\ ratio)^{0.490}(Twist\ ratio)^{-0.394} \tag{2.5-40}$$

$$f = 1.529Re^{-0.35}(Aspect\ ratio)^{1.686}(Twist\ ratio)^{-0.366} \tag{2.5-41}$$

Full-length twisted tape (Eiamsa-ard et al., 2014),

$$Nu = 0.144Re^{0.697}Pr^{0.4}(Twist\ ratio)^{-0.228} \tag{2.5-42}$$

$$f = 3.044Re^{-0.225}(Twist\ ratio)^{-0.556} \tag{2.5-43}$$

The corresponding geometrical parameters and the calculated Nusselt number ratio and friction factor ratio are shown in Table 2.5-1.

Table 2.5-1. Nusselt number ratio and friction factor ratio for optimal geometrical parameters.

Literature	Geometrical parameters	Nu ratio	f ratio
Delta Winglet (Promvonge and Skullong, 2020)	$Pitch\ ratio = 1$ $Blokage\ ratio = 0.15$	4.89-6.32	45.5-52.5
Circular rings (Kongkaitpaiboon et al., 2010)	$Diameter\ ratio = 0.7$ $Pitch\ ratio = 6$	1.85-2.14	13.10-15.64
Corrugated tube (Pethkool et al., 2011)	$Rib\ height\ ratio = 0.27$ $Pitch\ ratio = 0.06$	2.06-2.22	2.24-2.03
Regularly placed coiled wire (Gunes et al., 2010)	$Pitch\ ratio = 1$ $Distance\ ratio = 1/56$	1.89-2.24	9.67-7.03
Coiled wire (Keklikcioglu and Ozceyhan, 2016)	$Pitch\ ratio = 1$ $Distance\ ratio = 1/56$	8.36-7.66	22.51-18.35
Regularly placed helical tapes (Du and Hong, 2020)	$Pitch\ ratio = 1.72$ $Distance\ ratio = 5.69$	1.48-2.26	11.47-7.94
Multiple twisted tape (Chokphoemphun et al., 2015)	$tape\ number = 4$	1.46-1.59	4.72-3.67
Regularly-placed quadruple twisted tape (Samruaisin et al., 2018)	$Distance\ ratio = 0.5$	1.97-1.75	7.68-6.96
self-rotating twisted tape (Zhang et al., 2021)	$length\ ratio = 1$	0.88-1.15	2.94-1.96
2-lobed tube (Yang et al., 2011)	$Aspect\ ratio = 1.6$ $Twist\ ratio = 5.47$	1.64-1.12	2.32-2.09
Full length twisted tape (Eiamsa-ard et al., 2014),	$Twist\ ratio = 6$	1.20-1.37	4.95-4.60

The calculated PEC value between different thermal enhancement methods is shown in Figure 2.5-3.

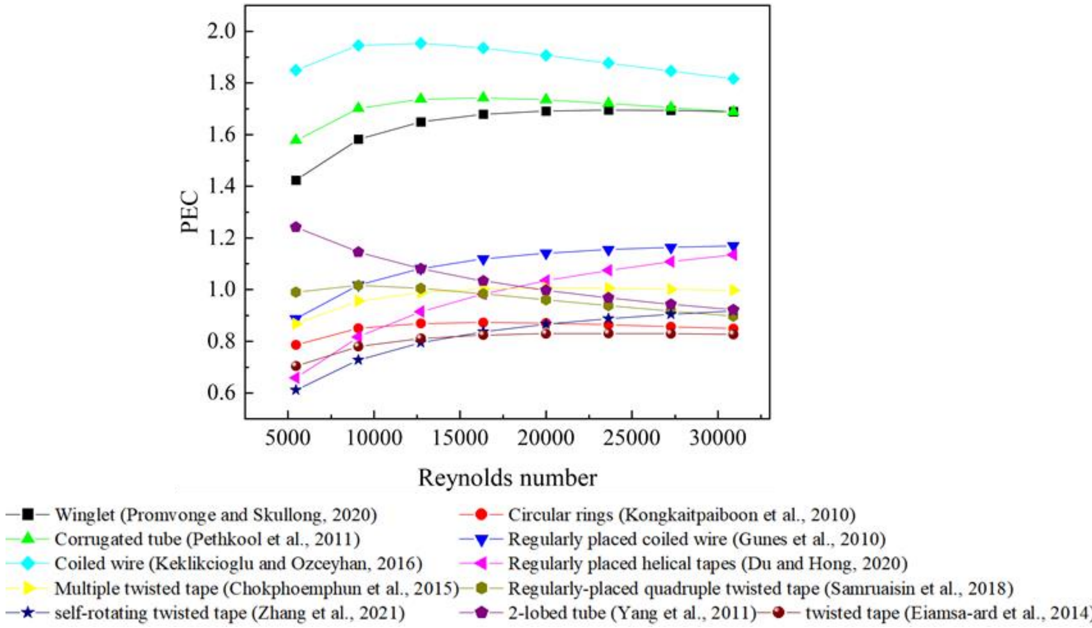

Figure 2.5-3.Comparison between different thermal enhancement methods (Gunes et al., 2010, Kongkaitpaiboon et al., 2010, Pethkool et al., 2011, Yang et al., 2011, Eiamsa-ard et al., 2014, Chokphoemphun et al., 2015, Keklikcioglu and Ozceyhan, 2016, Samruaisin et al., 2018, Du and Hong, 2020, Promvonge and Skullong, 2020, Zhang et al., 2021).

Among all configurations, the coiled wire (Keklikcioglu and Ozceyhan, 2016) has the highest PEC value at around 1.9 with a friction factor ratio ranging from 12.0 to 14.7. Such a high-pressure drop increases the requirement for pumping power. The corrugated tube (Pethkool et al., 2011) achieves the second-highest PEC value (1.7) and features a lower friction factor ratio of around 2.3 compared to the coiled wire, which seems more applicable in engineering applications. The long-twisted tape (Eiamsa-ard et al., 2014) has the lowest PEC value (0.8) on average. Additionally, the friction factor ratio for most of the methods is higher than 4 apart from the corrugated tube, the 2-lobed tube and self-rotating tube. Further research may consider using corrugated tube and lobed tube to improve thermal performance with a moderate pressure drop.

2.7 Conclusions

- Various types of heat exchangers, thermal enhancement methods and relevant terms and equations for evaluating heat transfer performance are discussed.
- Active thermal enhancement methods pose challenges. It is difficult to systematically evaluate whether the energy input and increased friction resistance will offset the enhanced heat transfer rate. Moreover, integrating active devices like vibration pumps into existing processes often requires significant modifications to the system, which are costly and time-consuming.
- Passive thermal enhancement techniques, such as inserting twisted tapes or altering tube geometries, are easier to install compared to active methods. However, they also bring issues. The extra surfaces created by twisted tapes or wires can cause severe fouling problems and increase the difficulty in cleaning. Additionally, in boilers, where high-purity heat transfer media are required, nanofluids cannot be used as a thermal enhancement approach.
- Two techniques of swirl intensity and the field synergy principle, which are used to investigate the swirl flow thermal enhancement mechanism, are demonstrated.
- The experimental methods for measuring the heat transfer coefficient and pressure loss of the heat exchanger are outlined.
- Nusselt number and friction factor correlations for enhancement methods are summarised, and their thermal performance is compared using PEC values. A critical finding is that thermal enhancement often comes at the cost of substantial pressure drops, which may offset the energy gains from improved heat transfer.

CHAPTER 3: MODELLING METHODOLOGY

3.1 Introduction

The swirl effect induced by the swirl tube has been continuously investigated at the University of Nottingham for the last 20 years. Ganeshalingam (2002) conducted a comparative analysis of various cross-sectional shapes of the swirl tube and determined that the 4-lobed cross-section was optimal based on Swirl Effectiveness (the ratio between swirl intensity and pressure loss). Ariyaratne (2005) designed the transition pipe between the circular and lobed sections by using numerical flow simulations. The purpose of this transition pipe was to mitigate pressure drops and enhance the swirl inducing ability of the pipe. Li (2016) also constructed numerical models and further optimised the tube geometry by reducing the total tube length from 600mm to 400mm. He concluded that a 400mm swirl tube was more efficient in generating swirl flow.

Computational fluid dynamics (CFD) is a group of techniques that help a computer generate a numerical fluid flow simulation. The physical behaviour of a given fluid can be established using three fundamental equations: (i) the Continuity equation; (ii) the Momentum equation and (iii) the Energy equation. These fundamental equations can be used to describe the heat transfer problem in a swirl tube (Fluent, 2020).

This chapter will concisely elucidate the fundamental calculation and design procedure of a 200mm long swirl tube and the computational methods. Various geometrical arrangements and variations of the 4-lobed swirl tube are also presented in this chapter This chapter will delineate the fundamental equations in CFD modelling and essential procedures in Fluent to investigate the thermal performance of the swirl tube.

3.2 Geometry Calculation

Figure 3.2-1 shows the optimised 400mm long, 4-lobed swirl generator developed by Li (2016). This apparatus is comprised of two transition components and a swirl component. The transition section connects circular and swirl sections. As the rotation angle for each lobe is fixed at 360° (90° for the first transition section, 180° for the swirl section, and 90° for the second transition section), the lengths of the three pipes vary by the different PD (pitch to diameter ratio) ratios.

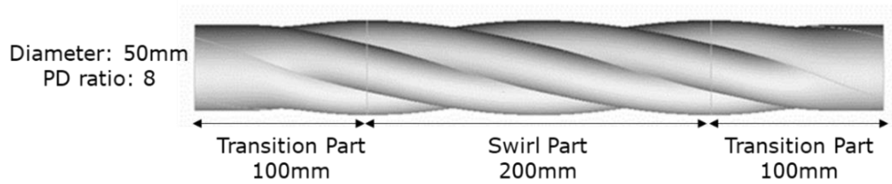

Figure 3.2-1. The optimised 4-lobed swirl tube (Li, 2016).

The shape of the transition part has been elucidated by Ariyaratne (2005). As no further research was conducted based on the shape of the transition part in this study, it will not be explored in more detail. The computational methodologies for both the transition and swirl components of the 4-lobed tube were comprehensively delineated by Li (2016), and this section provides only a concise overview of the calculation procedure

3.2.1 Swirl tube Calculation

Figure 3.2-2 illustrates the cross-sectional area of the swirl tube (black line) and connected circular tube (red line). The cross-sectional area between the swirl tube and connected circular tube is equal. The purpose of this is to maintain the same flow area between the circular and swirl tubes.

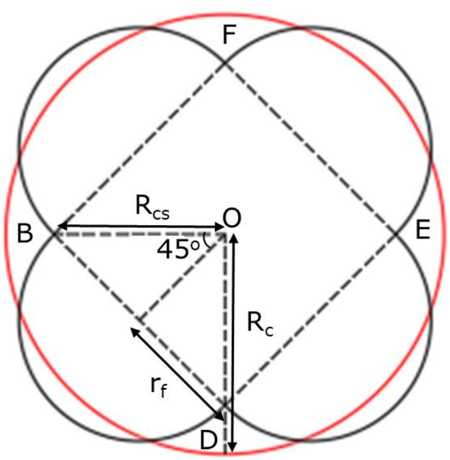

Figure 3.2-2. Cross-sectional area of the swirl part.

The calculation process for the transition part is summarised below:

1. **Calculate the lobe radius r_f:** Calculate the lobe radius r_f for a fully developed swirl tube based on the radius of the circular tube R_c since the cross-sectional areas between the two are the same.

$$Area\ of\ the\ swirl\ part = area\ of\ the\ square\ (ABCD) + \ area\ of\ 4\ lobes$$
$$= \ Area\ of\ the\ circular\ pipe$$

$$4{r_f}^2 + 2\pi {r_f}^2 = \pi {R_c}^2$$

$$r_f = \sqrt{\frac{\pi {R_c}^2}{4 + 2\pi}}$$

2. **Calculate the tube length:** Calculate the tube length based on a pitch-to-diameter (PD) ratio of 8 so that the twisted degree is consistent throughout the swirl tube.

$$Twisted\ ratio = \frac{360°}{PD \times d} = \frac{360°}{8 \times 0.05m} = 900degree/m$$

The length for a 4-lobed pipe, twisted to $360°$ is:

$$L = \frac{1m}{900degree/m} \times 360° = 0.4m$$

where d is the equivalent diameter of the pipe.

3. **Calculate the core length r_{cs}:** Calculate the core length r_{cs} in Figure 3.2-2

$$R_{cs} = \frac{r_f}{sin(45^o)} = \sqrt{2}r_f$$

3.2.2 Transition Pipe Calculation

The calculation procedure for transition pipes is shown below:

1. **Introduce the angle:** Let γ be introduced as the angle of rotation when lobes develop from circular ($\gamma = 45°$) to 4-lobed shapes ($\gamma = 90°$). The cross-sectional area of the transition pipe at $\gamma = 65^o$ is illustrated in Figure 3.2-3.

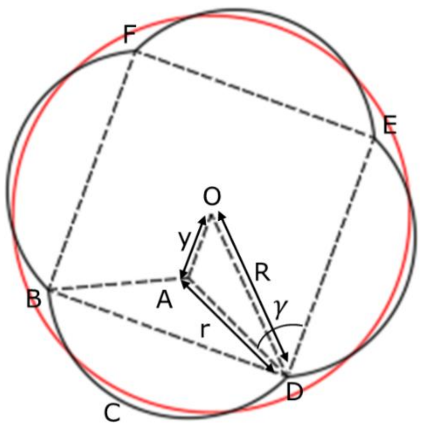

Figure 3.2-3. Cross-sectional area of transition pipe at $\gamma = 65°$.

where r is the lobe radius of the transition pipe.

where R is the core radius of the transition pipe.

where y is the distance from the lobe centre to the tube centre O.

where γ is the angle between line AD and line DE.

2. **Calculate the areas:** Based on Figure 3.2-3, the area of segmental lobes (BCD) and area of square (BDEF) can be calculated as:

$$Area\ of\ BCD = area\ of\ ABCD - area\ of\ ABD$$

$$Area\ of\ BCD = \frac{1}{2}r^2 \times 2\gamma - rcos\gamma \times rsin\gamma$$

$$Area\ of\ BCD = r^2\ (\gamma - \frac{1}{2}sin2\gamma)$$

$$Area\ of\ BDEF = 2R^2 \tag{3.2-1}$$

3. **Introduce f and f_1:** Introduce f and f_1 to simplify the calculation of $Area\ of\ BCD$ and $Area\ of\ BDEF$.

$$f = (\gamma - \frac{1}{2}sin2\gamma)$$

So,

$$Area\ of\ BCD = fr^2 \qquad (3.2\text{-}2)$$

Apply sine rule for triangle ABO,

$$\frac{R}{\sin(180^o - \gamma)} = \frac{y}{\sin(\gamma - 45^o)}$$

With simplification,

$$y = \frac{1}{\sqrt{2}}\left(1 - \frac{1}{tan\gamma}\right)R$$

$$f_1 = \frac{1}{\sqrt{2}}\left(1 - \frac{1}{tan\gamma}\right)$$

Therefore,

$$y = f_1R \qquad (3.2\text{-}3)$$

4. **Apply the cosine rule in triangle ABO**:

$$r^2 = R^2 + y^2 - 2Rycos45^o = R^2 + y^2 - \sqrt{2}Ry$$

By replacing y with equation (3.2-3)

$$r^2 = R^2 + {f_1}^2R^2 - \sqrt{2}f_1R^2$$

5. **Equate the cross-sectional areas**: When lobes develop, the cross-sectional areas between the developing lobe and the circular tube (with a radius of R_c) should also be the same. Therefore, the following equations were derived.

$$Area\ of\ circular\ tube = \pi {R_c}^2$$

$$\pi {R_c}^2 = Area\ of\ 4\ segmental\ lobes\ (BCD) + Area\ of\ square\ BDEF$$

By substitution equations (3.2-1) and (3.2-2)

$$\pi {R_c}^2 = 4fr^2 + 2R^2$$

Replacing r^2 with $R^2 + y^2 - \sqrt{2}Ry$

$$\pi {R_c}^2 = 4f(R^2 + {f_1}^2 R^2 - \sqrt{2} f_1 R^2) + 2R^2$$

$$\pi {R_c}^2 = R^2(4f + 4f{f_1}^2 - 4\sqrt{2} f f_1 + 2)$$

$$R = R_c \sqrt{\frac{\pi}{4f + 4f{f_1}^2 - 4\sqrt{2} f f_1 + 2}} \qquad (3.2\text{-}4)$$

6. **Calculate the lobe area for each intermediate stage (LA_i)**: Calculate the lobe area for each intermediate stage (LA_i) based on f, R and r. The lobe area at the intermediate stage (LA_i) is depicted in black and shown in Figure 3.2-4.

Given that the cross-sectional areas between the developing lobe and the circular tube (with a radius of R_c) are equivalent,

$$lobe\ area\ (LA_i) = Area\ of\ circular\ tube - Area\ of\ intermediate\ circle$$

$$lobe\ area\ (LA_i) = \pi {R_c}^2 - \pi R^2 \qquad (3.2\text{-}5)$$

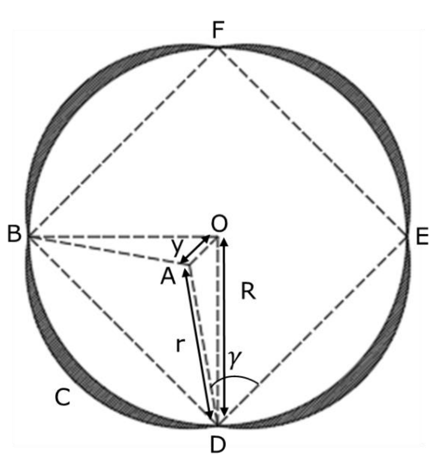

Figure 3.2-4. Total lobe area at the intermediate stage at $\gamma = 65°$.

7. **Characterise the rotation process**: In addition to the morphology of the intermediate lobes, the rotation process from the circular cross-section to the 4-lobed cross-section can be characterised by various transition functions. Ariyaratne (2005) conducted a numerical comparison of different transition functions that described this rotation and ascertained that a beta transition function and cosine function were optimal for inducing swirl flow.

Introduce a transition function β:

$$\beta = [\frac{\frac{LA_i}{\pi R^2 - LA_i}}{\frac{LA_{FD}}{\pi R^2 - LA_{FD}}}]^{0.5} \tag{3.2-6}$$

where LA_i is the lobe area at the intermediate stage.

where LA_{FD} is the lobe area of fully developed swirl tube,

$$LA_{FD} = \pi {R_c}^2 - \pi {R_{cs}}^2$$

where R_{cs} is the minimum core radius of the circular section of the fully developed swirl tube.

8. **Define the angle and length ratio**: Define the intermediate twisted angle and the length ratio ($\frac{x}{L}$) of each intermediate lobe.

The length ratio is defined as a cosine function of β,

$$\frac{x}{L} = \frac{cos^{-1}(1 - 2\beta)}{\pi} \tag{3.2-7}$$

where x is the intermediate length between the centre of the intermediate lobe and the starting point of the transition.

where L is the total length of the transition part.

The intermediate twisted angle can be calculated by,

$$Twisted[0, 90°] = \frac{x}{L} \times 90° \times Twisted\ direction \tag{3.2-8}$$

where $Twisted\ direction$ is -1 (for clockwise rotation)

9. **Calculate the shape, location and twisted angle**: For each number of γ, the shape of the intermediate lobe can be calculated by y and R using equations (3.2-3) and (3.2-4), the location and the twisted angle are based on the length ratio ($\frac{x}{L}$) using equation (3.2-7) and (3.2-8). A sample calculation at $\gamma = 65°$ is shown in Appendix 1.2 Sample Calculation for Transition Part.

10. **Tabulate the calculated data**: Tabulate calculated data at each stage of γ as it increases from 5° to 90°. The development of 4-lobed transition is given in Appendix 1.3 Transition Development of the 4-Lobed Pipe.

3.2.3 Information for the 4-Lobed Swirl tube

Through the transition-pipe calculation procedure, a table for the 4-lobed transition pipe was generated, as presented in Appendix 1.4 Table for 4-lobed Swirl Tube. The swirl component can be fabricated in SolidWorks to the generation of the transition component using the data from this table. The critical information about the 4-lobed swirl tube is summarised below:

Table 3.2-1. Critical information about the 4-lobed swirl tube.

Information	Dimension	Description
Lobe number	4	
Transition length	100mm	One lobe rotated 90 degrees
Swirl length	200mm	One lobe rotated 180 degrees
Total length	400mm	Transition + Swirl + Transition
Equivalent inner diameter	50mm	
Pitch-to-diameter ratio	8	
Twisted degrees	900^{o}	Twisted degrees per metre
r_f	13.8mm	Minimum lobe radius
R_{cs}	19.5mm	Minimum core radius
LA_{FD}	763.9mm^2	Lobe area (fully developed)

3.3 Geometric Design

SolidWorks was employed to generate the transition pipe and swirl tube models. It is a powerful 3D CAD software that can effectively handle a large number of components, making it convenient for assembling and simulating complex pipe systems.

The creation of the transition pipe was initially attempted with the loft feature. This feature facilitates the generation of a solid part within the space between multiple cross-sections. Each cross-section was created based on a constant γ interval of 5 °.

- Create the X-Y sketch plane for the intermediate lobes and define the distance between each plane on the Z-axis according to the calculation results.
- Create each intermediate lobe accordingly based on the core radius of the transition pipe (R) and the distance from the lobe centre to the tube centre O (y).
- Rotate each intermediate lobe based on the twisted angle.

To capture the steeper cross-section transition in the initial 5° (45 °≤ γ ≤ 50°) and the final 5° (85 °≤ γ ≤ 90°) more accurately, Li (2016) incorporated eight additional intermediate sections. Furthermore, an additional cross section was added at γ=45.1° to capture the transition trajectory. These additional 9 cross-sections are indicated by red circles, as shown in Figure 3.2-5.

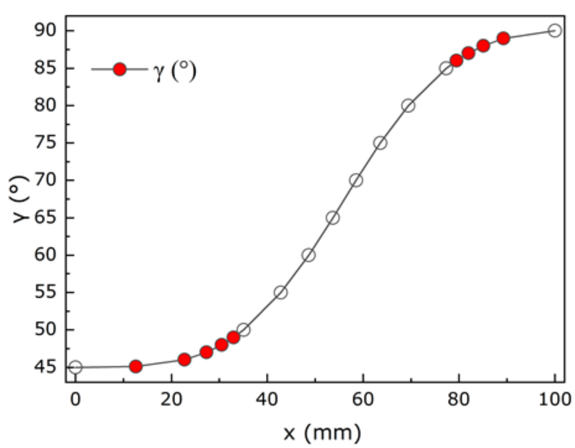

Figure 3.2-5. Graph of γ verses distance between sketches.

19 sections used to loft into the transition pipe are shown in Figure 3.2-6 (a). 4 curves and

4 intersection points were created in SolidWorks following the same procedure described previously. Therefore, the transition trajectory can be traced by selecting the 4 points in each sketch. The final loft result is shown in Figure 3.2-6 (b).

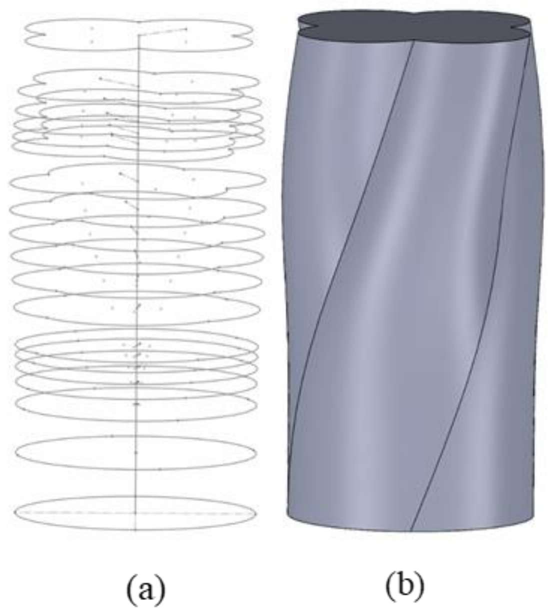

Figure 3.2-6. Demonstration of loft feature in SolidWorks. (a) 19 sections were used to loft into the transition pipe. (b) Created pipe.

The 200mm long swirl part can be achieved through the application of boss-extrude and flex features.

- Apply the boss-extrude feature on the fully developed lobe. Set the extruded length as 200mm. The extrude results are shown below:

Figure 3.2-7. Boss-extrude results.

- Apply the flex feature with a twisted degree at 180 degrees. The flex results are shown below:

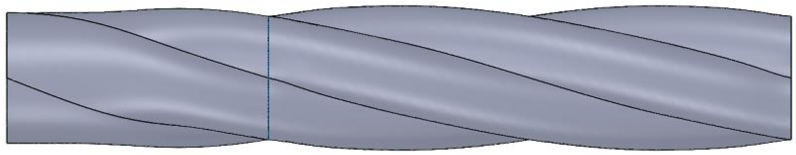

Figure 3.2-8. Flex feature results.

The other transition part can be created by moving and rotating the created transition part in the Body-Move/Copy feature. The final PD8 4-lobed swirl tube is shown below:

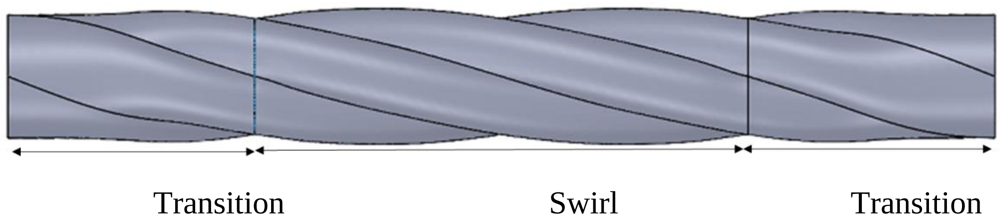

Figure 3.2-9. Created PD8 4-lobed swirl tube.

Swirl tubes with different PD ratios can be created by reducing the total tube length with scale function. Note that the PD ratio for transition and swirl sections is the same and the shape of the cross-section at each end are circular. The created pipe is the same as shown in Figure 3.2-1

3.4 Fluid Dynamic Models

Continuity Equation

The continuity equation is derived based on the principle of mass conservation. The rate of mass change within a fluid element is equivalent to the net mass flow rate of the fluid element across its surface

$$\frac{\partial \rho}{\partial t} + \nabla \cdot (\rho \vec{U}) = 0 \tag{3.4-1}$$

where $\frac{\partial \rho}{\partial t}$ is the rate of mass change in the fluid element; $\nabla \cdot (\rho \vec{U})$ is the mass convection in the fluid element.

Momentum Equation

The momentum equation is derived from Newton's second law of motion. The rate of momentum change in the fluid element is equal to the total force applied to the fluid element.

$$\frac{\partial(\rho\vec{U})}{\partial t} + \nabla\cdot(\rho\vec{U}\vec{U}) = \rho\vec{f} + (-\nabla p + \nabla\cdot\tau) \tag{3.4-2}$$

where $\frac{\partial(\rho\vec{U})}{\partial t}$ is the change of momentum with time; $\nabla\cdot(\rho\vec{U}\vec{U})$ is momentum convection; $\rho\vec{f}$ is the body forces such as gravity; $(-\nabla p + \nabla\cdot\tau)$ is the pressure force and shear stress.

Energy Equation

The energy equation is derived from the first law of thermodynamics. The rate of energy change of the fluid element is equal to the sum of the net heat flux into the element and the rate of work done on the element due to the total forces.

$$\frac{\partial(\rho E)}{\partial t} + \nabla\cdot(\vec{U}\rho E) = -\nabla\cdot q + \nabla\cdot(\tau\vec{U} - p\vec{U}) + \rho g\cdot\vec{U} \tag{3.4-3}$$

where $\frac{\partial(\rho E)}{\partial t}$ is the rate of energy change with time; $\nabla\cdot(\vec{U}\rho E)$ is the convection energy transfer; $\nabla\cdot q$ is the energy due to conduction and diffusion; $\nabla\cdot(\tau\vec{U} - p\vec{U})$ is the energy due to pressure force and shear stress; E is the total energy and is the sum of internal energy and kinetic energy.

Compared with experiment-based methods, Computational Fluid Dynamics (CFD) offers noteworthy advantages in investigating fluid flow. For instance, it provides insights into the effects of design modifications on flow patterns with reduced cost and time expenditure. Furthermore, ANSYS Fluent, an industry-leading CFD software based on three fundamental equations, is renowned for its modelling capabilities and accuracy. ANSYS Fluent utilises the finite volume method to solve the governing equations pertaining to the physical behaviour of a given fluid.

3.5 RANS Averaging Modelling

In fluid mechanics, the Reynolds number (Re) is a dimensionless quantity that predicts flow patterns by measuring the ratio between inertial and viscous forces. At a low Re, the flow tends to be laminar and the fluid flows in parallel layers without disrupting each layer. A high Re tends to result in a turbulent flow comprising multiple scales of eddies and disorder with random and unsteady velocity fluctuations. To model this chaotic movement, the Reynolds-averaged Navier–Stokes equations (RANS) is proposed. RANS is time-averaged equations, particularly applicable to turbulent flows. Based on this concept, different turbulence models are proposed, for instance, the $k-\varepsilon$ model, $k-\omega$ model and SST $k-\omega$ model. These models are utilised in Fluent and are briefly discussed in the following sections.

In Reynolds averaging, the solution variable such as the velocity component in the Navier-Stokes equations is divided into the time-averaged and fluctuating components. The decomposition for the velocity component is given below (Fluent, 2020):

$$u_i = \overline{u_i} + {u_i}' \qquad (3.5\text{-}1)$$

where $\overline{u_i}$ and ${u_i}'$ are the mean and fluctuating velocity components.

For pressure and other scalar components:

$$\varphi_i = \overline{\varphi_i} + {\varphi_i}' \qquad (3.5\text{-}2)$$

where φ is a scalar such as pressure and energy.

The above expressions are substituted into the continuity and momentum equations. The incompressible Reynolds-averaged Navier Stokes Equations (RANS) can be written as:

$$\frac{\partial(\rho\overline{u_i})}{\partial t} + \frac{\partial}{\partial x_j}\left(\rho\overline{u_i}\overline{u_j}\right) = -\frac{\partial p}{\partial x_i} + \frac{\partial}{\partial x_j}\left[\mu\left(\frac{\partial\overline{u_i}}{\partial x_j} + \frac{\partial\overline{u_j}}{\partial x_i}\right)\right] - \rho\overline{u_i'u_j'} \qquad (3.5\text{-}3)$$

The Reynolds stresses term $-\rho\overline{u_i'u_j'}$ is the result of Reynolds-averaging and must be modelled to solve the RANS. A common method is to use the Boussinesq hypothesis (Fluent, 2020):

$$-\rho\overline{u_i'u_j'} = \mu_t(\frac{\partial \overline{u_i}}{\partial x_j} + \frac{\partial \overline{u_j}}{\partial x_i}) \tag{3.5-4}$$

where μ_t is the eddy viscosity, which characterizes the transport and dissipation of energy in the small-scale vortices. The eddy viscosity is assumed to be isotropic. Based on this assumption, different models such as the $k - \varepsilon$ (Launder and Spalding, 1972) and $k - \omega$ models (Wilcox, 2008) are proposed to model the nonlinear Reynolds stress term.”

3.5.1 SST $k - w$ Model

However, the $k - \varepsilon$ and $k - \omega$ models exhibit limitations in turbulent flow simulation as discussed previously (Menter, 1994, Menter et al., 2003).

- The numerical results for the $k - \varepsilon$ model in the near-wall region lack reliability, especially for adverse pressure gradient flows.
- The $k - \omega$ model has a strong sensitivity to the freestream value of ω specified at the inlet.

Therefore, Menter (1994) proposed an alternative model for maintaining the reliability of the $k - \omega$ model in the near-wall region while leveraging freestream independence of the $k - \varepsilon$ model in the inlet. This model is referred to as the shear-stress transport (SST) $k - \omega$ model.

In the standard $k - \varepsilon$ model proposed by Launder and Spalding (1972), the eddy viscosity is based on the turbulence kinetic energy (k) and its dissipation rate (ε).

$$\mu_t = c_\mu \frac{\rho k^2}{\varepsilon} \tag{3.5-5}$$

where c_μ is an empirical coefficient.

k is characterized by the measured root-mean-square of the velocity fluctuations while ε is the rate of dissipation of turbulent kinetic energy, representing the conversion of turbulent kinetic energy into internal energy due to viscous effects.

The transport equation for k and ε is derived by assuming that the flow is fully turbulent and ignoring the molecular viscosity effects. For k:

$$\frac{\partial(\rho k)}{\partial t}+\frac{\partial(\rho k u_j)}{\partial x_j}=\frac{\partial}{\partial x_j}\left[\left(\mu+\frac{\mu_t}{\sigma_k}\right)\frac{\partial k}{\partial x_j}\right]+P_k-\rho\varepsilon \tag{3.5-6}$$

And for ε:

$$\frac{\partial(\rho \varepsilon)}{\partial t}+\frac{\partial(\rho \varepsilon u_j)}{\partial x_j}=\frac{\partial}{\partial x_j}\left[\left(\mu+\frac{\mu_t}{\sigma_\varepsilon}\right)\frac{\partial \varepsilon}{\partial x_j}\right]+C_{\varepsilon 1}\frac{\varepsilon}{k}P_k-C_{\varepsilon 2}\rho\frac{\varepsilon^2}{k} \tag{3.5-7}$$

The equations mean:

Rate of change of k or ε + Transfer of k or ε due to convection = Transfer of k or ε due to diffusion + the production of k or ε due to mean velocity gradient– The destruction of k or ε.

In the above two equations, c_μ, σ_k, σ_ε, $C_{\varepsilon 1}$, and $C_{\varepsilon 2}$ are empirical coefficients.

Substituting $\varepsilon = c_\mu k\omega$ into the ε equation:

$$\begin{aligned}\frac{\partial(\rho \omega)}{\partial t}&+\frac{\partial(\rho \omega u_j)}{\partial x_j}\\&=\frac{\partial}{\partial x_j}\left[\left(\mu+\frac{\mu_t}{\sigma_\omega}\right)\frac{\partial \omega}{\partial x_j}\right]+C_{\omega 1}\frac{\omega}{k}P_k-C_{\omega 2}\rho\omega^2+\frac{2\rho}{\sigma_\omega\omega}\frac{\partial k}{\partial x_j}\frac{\partial \omega}{\partial x_j}\end{aligned} \tag{3.5-8}$$

Note that the coefficients differ from those in the previous equations. The additional term is called the cross-diffusion term and results from substitution.

As for the original $k-\omega$ model (Menter, 1994), the turbulent kinetic energy (k):

$$\frac{\partial(\rho k)}{\partial t}+\frac{\partial(\rho k u_j)}{\partial x_j}=\frac{\partial}{\partial x_j}\left[\left(\mu+\frac{\mu_t}{\sigma_k}\right)\frac{\partial k}{\partial x_j}\right]+P_k-\rho c_\mu k\omega \qquad (3.5\text{-}9)$$

And for ω :

$$\frac{\partial(\rho\omega)}{\partial t}+\frac{\partial(\rho\omega u_j)}{\partial x_j}=\frac{\partial}{\partial x_j}\left[\left(\mu+\frac{\mu_t}{\sigma_\omega}\right)\frac{\partial\omega}{\partial x_j}\right]+C_{\omega 1}\frac{\omega}{k}P_k-C_{\omega 2}\rho\omega^2 \qquad (3.5\text{-}10)$$

By using a blending function F_1, the dissipation equation of the $k-\omega$ model and the substituted $k-\varepsilon$ model can be blended, which is known as the SST $k-\omega$ model.

For ω:

$$\frac{\partial(\rho\omega)}{\partial t}+\frac{\partial(\rho\omega u_j)}{\partial x_j}=\frac{\partial}{\partial x_j}\left[\left(\mu+\frac{\mu_t}{\sigma_\omega}\right)\frac{\partial\omega}{\partial x_j}\right]+C_{\omega 1}\frac{\omega}{k}P_k-C_{\omega 2}\rho\omega^2+2(1-F_1)\rho CD \qquad (3.5\text{-}11)$$

$$CD=\frac{1}{\sigma_\omega\omega}\frac{\partial k}{\partial x_j}\frac{\partial\omega}{\partial x_j} \qquad (3.5\text{-}12)$$

With the blending function, $k-\varepsilon$ model is applied away from the wall and $k-\omega$ model is used in the near wall region.

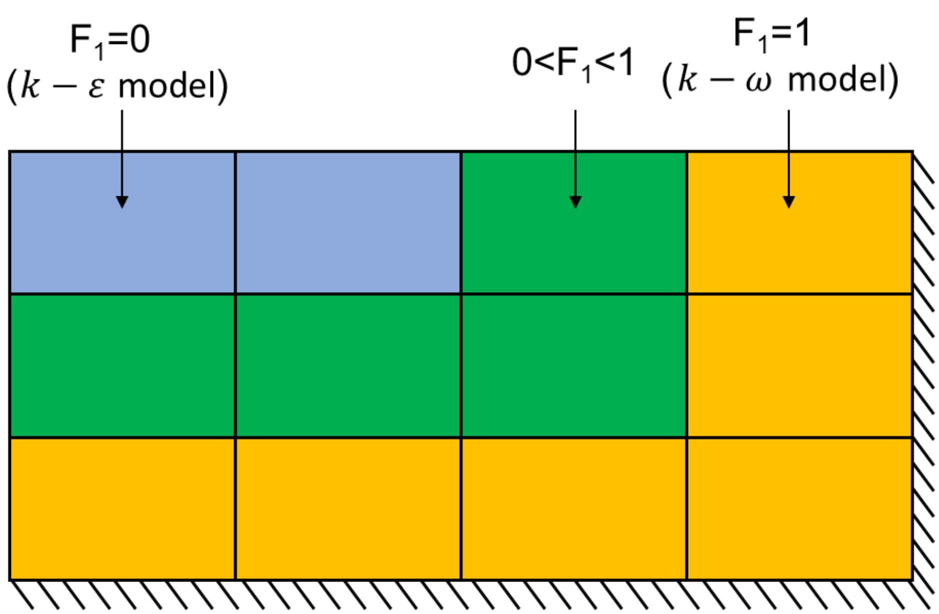

Figure 3.5-1. The blending function F_1.

Noticed that the coefficients for the two models are different as shown in the table below:

Table 3.5-1. coefficient for SST model (ANSYS, 2021).

SST	$\boldsymbol{C_{\omega 1}}$	$\boldsymbol{C_{\omega 2}}$	$\boldsymbol{\sigma_k}$	$\boldsymbol{\sigma_\omega}$	$\boldsymbol{c_\mu}$
$\boldsymbol{k-\varepsilon}$ model	5/9	3/40	1/0.85	2	0.09
$\boldsymbol{k-\omega}$ model	0.44	0.0828	1	1.17	0.09

At the intermediate region ($\boldsymbol{0 < F_1 < 1}$):

$$coef = (1 - F_1)coef_{k-\omega} + F_1 coef_{k-\varepsilon} \tag{3.5-13}$$

The eddy viscosity is calculated by:

$$\mu_t = \rho \frac{k}{max(\omega, \frac{F_2 S}{0.31})} \tag{3.5-14}$$

where S is the absolute value of vorticity and F_2 is another blending function.

The function F_2 is employed to mitigate the overprediction of the wall shear stress. In the SST $k - \omega$ model, both F_1 and F_2 are empirically calibrated through testing with multiple experimental results. The detailed information about the two blending functions can be found in Menter's work and ANSYS's relevant documentation (Menter, 1994, ANSYS, 2021). Since SST model incorporates advantages from both the $k - \varepsilon$ and $k - \omega$ models, it is recommended for a wide range of industrial applications with high accuracy by Fluent (ANSYS, 2022).

3.5.2 Numerical Schemes

In ANSYS Fluent, the governing integral equations for the conservation of mass and momentum are solved by a control-volume-based technique. When appropriate, the equations for energy and other scalars such as turbulence are also solved using this technique. The steps include:

- Division of the domain into discrete control volumes using a computational grid, which is also known as the meshing process.
- Integration of the governing equations over the individual control volumes to construct algebraic equations for the discrete dependent variables (“unknowns”) such as velocities, pressure, temperature, and conserved scalars.
- Linearisation of the discretised equations and solution of the resultant linear equation system to yield updated values of the dependent variables.

3.5.2.1 Solver

ANSYS Fluent provides two numerical methods for solving fluid flow problems: a pressure-based solver and a density-based solver. The pressure-based solver is typically employed for low-speed incompressible flows, whereas the density-based solver is primarily utilised for high-speed compressible flows. Although both pressure- and density-based solvers have been developed for a wide range of flow conditions, a pressure-based solver was selected for this study owing to the assumption of fluid incompressibility.

Among the available solvers for the pressure-based approach, Fluent offers a segregated algorithm and coupled algorithm for a pressure-based solver. In the segregated algorithm, the governing equations are solved sequentially, whereas in the coupled algorithm, the continuity and momentum equations are solved simultaneously. The overall steps of the two solvers are as follows:

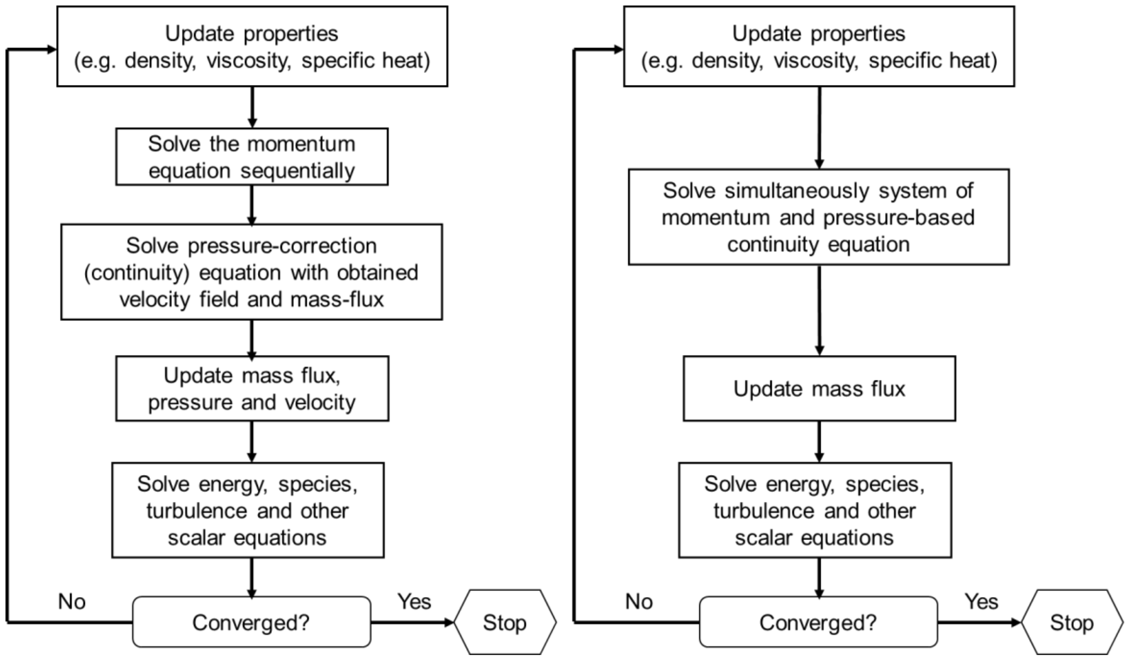

Figure 3.5-2. Overview of the pressure-based solution methods.

The coupled algorithm has a significantly higher solution convergence rate, especially for compressible flows and complex geometries, compared to the segregated algorithm (Alonzo-García et al., 2016).Nevertheless, the memory usage for the coupled algorithm also increases considerably (Li, 2016). However, due to its lower memory usage compared to the coupled algorithm, the segregated algorithm was selected despite its slower convergence rate.

For segregated algorithms, Fluent provides the following options: SIMPLE, SIMPLEC and PISO. Since PISO is recommended for transient calculations (Li, 2016), SIMPLEC algorithm was selected.

3.5.2.2 Numerical Spatial Discretization

For the finite volume method (FVM), the flow variables φ such as pressure, temperature and velocity are computed and stored at the cell centroid (P and N) as shown in the below figure (Fluent, 2020, Jasak, 1996).

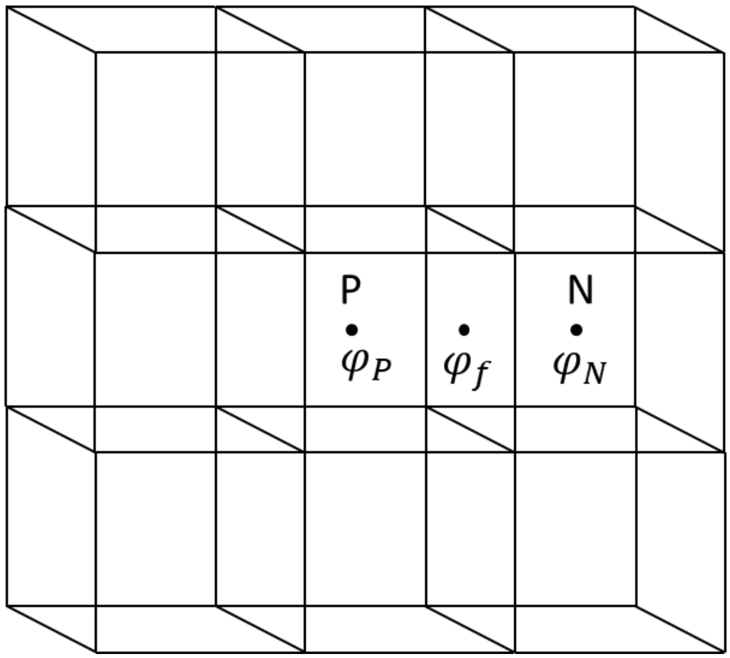

Figure 3.5-3. 3-dimensional mesh in FVM.

For a scalar (φ) equation (such as those for continuity, momentum and energy), a general form is:

$$\frac{\partial(\rho\varphi)}{\partial t} + \nabla \cdot \left(\rho\vec{U}\varphi\right) = \nabla \cdot (\Gamma\nabla\varphi) + S \tag{3.5-15}$$

In other words, the equation means that the change of the scalar with time + the convection term = the gradient term + the source term.

For incompressible and steady-state flow, integrating the above scalar equation across the cell (P) gives:

$$\int \nabla \cdot \left(\rho\vec{U}\varphi\right)dV = \int \nabla \cdot (\Gamma\nabla\varphi)dV + \int SdV \tag{3.5-16}$$

To solve this, the value φ_f on the interface between cells P and N and the gradient $\nabla\varphi$ must be found. The overall process is known as the spatial discretization process.

To implement the finite volume method effectively, specific schemes are needed to handle the interpolation of values on cell interfaces and the calculation of gradients. The value φ_f

can be interpolated from the cell centre values φ_P and φ_N, Fluent provides several schemes: first-order upwind, second-order upwind, QUICK and third-order MUSCL. Fluent states that the first order scheme will yield better convergence than the second-order while yielding less accurate results, especially on triangular meshes. Though the QUICK and third-order MUSCL schemes may provide superior accuracy compared to the second-order scheme for rotating or swirling flow, the second-order scheme is deemed sufficient and is utilised in the simulation (ANSYS, 2022).

The following gradient evaluation methods are provided to calculate the gradient $\nabla\varphi$: the green-gauss cell-based, the green-gauss node-based and the least squares cell-based. Fluent suggests that the accuracy of the least squares cell-based is comparable to that of the green-gauss node-based methods. Both are more accurate than the green-gauss cell-based method, especially for irregular unstructured meshes. As the computational cost for the least squares cell-based method is lower than that of the green-gauss node-based method, it is selected.

3.6 CFD Model Formulation

The CFD modelling process and corresponding software used in this study are shown in Figure 3.6-1. The geometry creation section is outlined in the previous chapter and this section focuses on the Fluent settings part of the CFD modelling

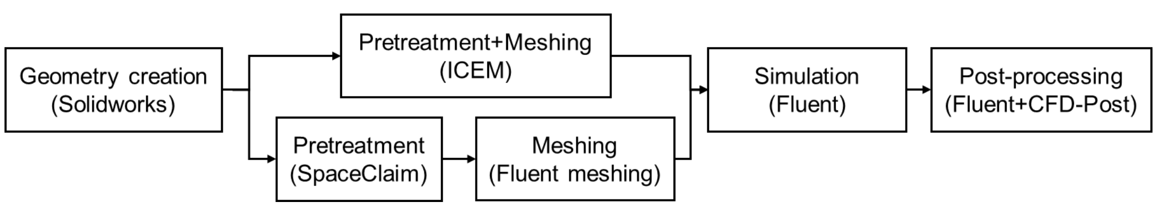

Figure 3.6-1. CFD modelling process.

3.6.1 Assumptions

Before the CFD modelling, the following assumptions are made to reduce the complexity of the flow problem:

- The flow consists of water only.

- The flow is in a steady state and incompressible.
- The effect of radiation is ignored.
- The water properties are considered constant.
- No heat loss occurs through the boundary.

3.6.2 Flow Region and Boundary Condition

The geometrical configuration of the 4-lobed swirl tube was varied to enable the comparison and evaluation of different configurations. The flow region in this study usually consists of the following parts, the wall-in, wall-out and wall-heat regions as shown in Figure 3.6-2. The wall-in and out regions are designed to develop the flow viscous boundary layer, while the wall-heat region is where heat transfer occurs.

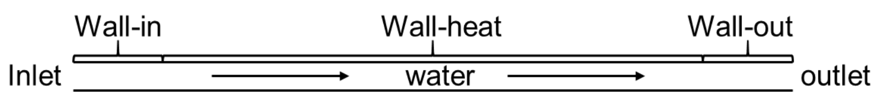

Figure 3.6-2. Flow region and boundaries.

Fluent offers two types of wall-heat boundary conditions: constant wall temperature and wall heat flux (Rohsenow et al., 1998). Simulations were conducted to evaluate the accuracy of the two boundary conditions as shown in Figure 3.6-3. Gnielinski equation is used to calculate the Nusselt number and Petukhov equation is used to calculate the friction factor, which is demonstrated in Chapter 2 section 5. For the Nusselt number, the average deviations for wall heat flux and constant wall temperature were 8.1% and 3.2% respectively. For the friction factor, the average deviation for both settings is 1.4%. Since the constant wall temperature condition exhibited a smaller discrepancy between simulation results and literature values for the Nusselt number, it was used in further simulations.

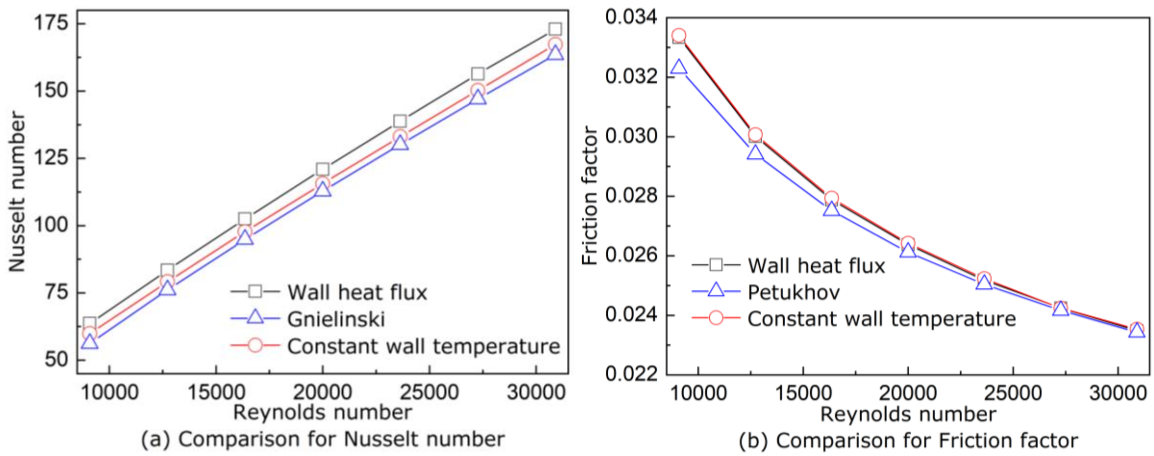

Figure 3.6-3. Evaluation of wall boundary conditions between the wall heat flux=5000W/m^2 and the wall temperature=350K.

The boundary conditions at the inlet, outlet and heat exchanger wall regions in the cylindrical coordinate system are listed below:

- Inlet boundary condition: $u_r = u_\theta = 0$, $u_z = U_{in}$, $T_{in} = 300K$, turbulence intensity=I
- Outlet boundary condition: $\frac{\partial u_z}{\partial z} = \frac{\partial u_r}{\partial z} = \frac{\partial u_\theta}{\partial z} = 0$, $\frac{\partial T}{\partial z} = 0$, $p = 0$, turbulence intensity=I
- Heated wall condition: $u_r = u_\theta = u_z = 0, T_{wall} = 350K$
- Adiabatic wall condition: $u_r = u_\theta = u_z = 0, Heat\ flux = 0$

The turbulence intensity, I, is calculated from the Reynolds number as follows (ANSYS, 2022)

$$I = 0.16Re^{-\frac{1}{8}} \tag{3.6-1}$$

Since the temperature difference between the inlet and the outlet was minor, the effect of thermal radiation and viscous heating can be neglected (Tang et al., 2015). Thus, the thermal properties of water in this simulation were set as constant and the quantities are listed in Table 3.6-1.

Table 3.6-1. Water properties.

Density ρ kg/m^3	Thermal conductivity k $W/(m \cdot K)$	Heat capacity c_p $J/(kg \cdot K)$	Viscosity μ $Pa \cdot s$
998	0.6472	4179	0.000549

The SIMPLEC (Zeng and Tao, 2003) was employed for pressure-velocity coupling and the second-order upwind scheme was used for the viscous terms.

The tube geometries were generated in SolidWorks. Figure 3.6-4 illustrates cross-sectional views of the 4-lobed tube with varying PD ratios. The 4-lobed swirl tube comprises two transition sections and one swirl section, with the transition sections connecting the circular and swirl components. The core radius, R, measures 7.8mm, while the lobe radius, r, is 5.52mm, ensuring that the cross-sectional area of the 4-lobed swirl tube is equivalent to that of a 20mm circular pipe, thus maintaining consistency with the experimental setup.

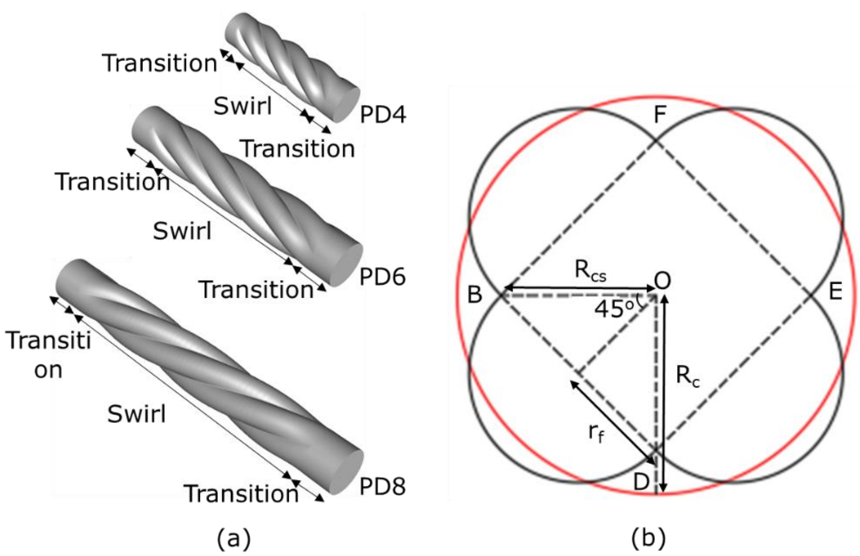

Figure 3.6-4. 4-lobed swirl tubes. (a) swirl tube with different PD ratios; (b) cross-section of the swirl tube.

Various lobed tube configurations with different PD ratios were constructed for a series of investigations. The PD8 swirl tube is depicted here merely for illustrative purposes. The initial group (Group 1) primarily aims to evaluate the decaying swirl flow, as illustrated in Figure 3.6-5.

Figure 3.6-5. Group 1 configuration that investigates the decaying swirl flow.

The second group (Group 2) is to evaluate the thermal performance of different tube arrangements as shown in Figure 3.6-6. The effective length is reduced to 48D so that twelve PD4 swirl tubes, eight PD6 swirl tubes and six PD8 swirl tubes can be connected in sequence without further modification on the tube geometry.

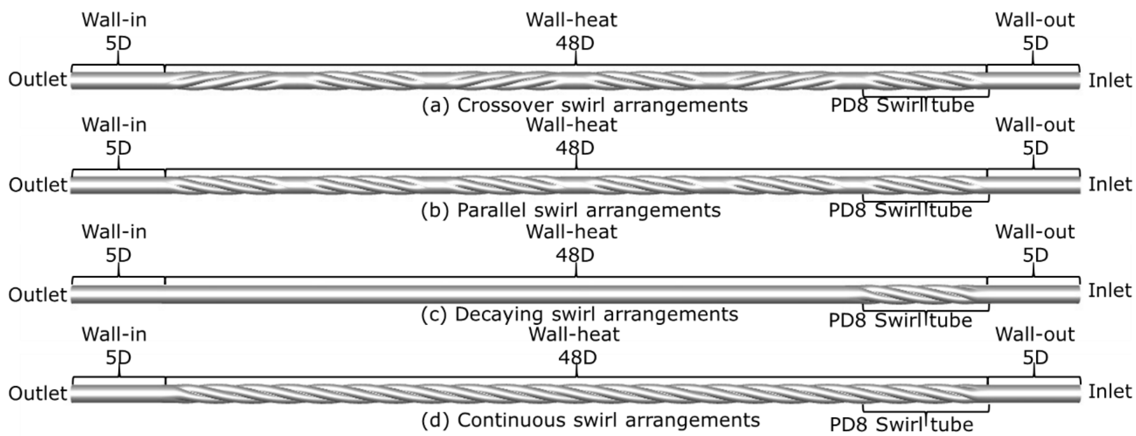

Figure 3.6-6. Group 2 configuration that investigates the different tube arrangements.

It is essential to simulate the Nusselt number and friction factor values of a circular tube, and these values serve as a benchmark for the PEC values. The entrance region facilitates the development of the flow boundary layer. Consequently, the inlet region was initially set to 20D for the investigation of the decaying swirl flow. However, when the length of the wall heat section was reduced to 48D in the second group, it was found that the deviation between simulation results and the literature correlations increased when the inlet region length remained at 20D for both the Nusselt number and the friction factor. To mitigate this discrepancy, the lengths of the inlet and outlet regions were adjusted to 5D based on the literature (Tang et al., 2015).

A comparison of the Nusselt number and friction factor for different inlet and outlet region lengths is shown in Figure 3.6-7. The numerical results for different lengths were compared with the empirical correlations (Gnielinski and Petukhov equations). The average deviations for the 20D+100D configuration were 1.5% and 1.4% for the Nusselt number and friction factor, respectively. For the 20D+48D and 5D+48D+5D configurations, the average deviations were 10.8% and 2.4% for the Nusselt number, and 3.6% and 2.8% for the friction factor, respectively. Therefore, when the heating section was 100D, the inlet region was established as 20D. When the heating section was reduced to 48D, the inlet region correspondingly reduced to 5D.

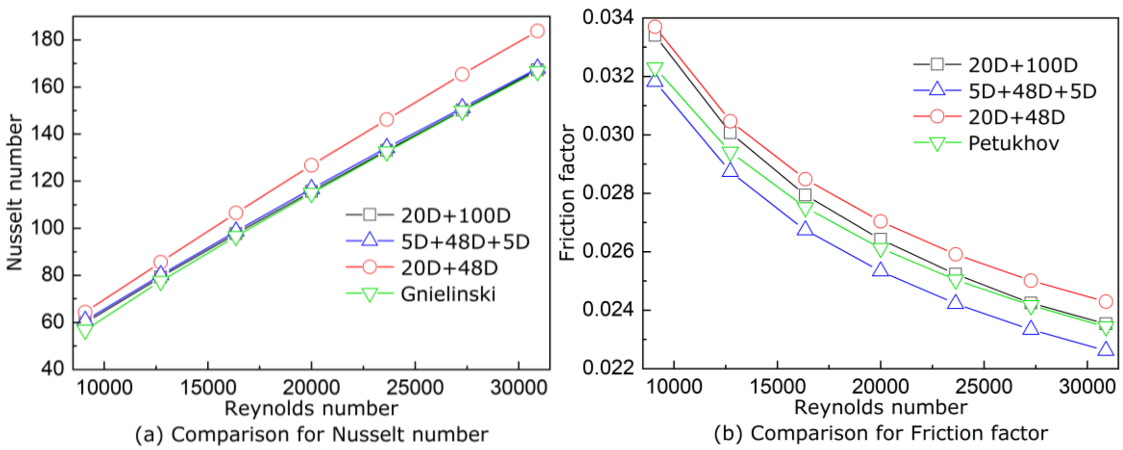

Figure 3.6-7. Comparison of inlet, heat and outlet region length for Nusselt number and friction factor for circular tubes.

3.6.3 Hexahedral Mesh

After defining the boundary conditions, the next crucial step in the CFD modelling process is the discretization of the flow region into a mesh. To numerically solve the governing equations, the flow region including all boundaries must be discretised into a finite number of control volumes, which is known as the mesh. For 3D meshes, tetrahedron, hexahedral and polyhedral meshes are acceptable in Fluent (ANSYS, 2022). In this study, hexahedral and polyhedral meshes are utilised to conduct the investigation. The hexahedral mesh in the above flow domain was generated by ICEM, a meshing software used by Li (2016), while the polyhedral mesh was utilised for the investigation of the solar water heaters and constructed by Fluent meshing, which will be discussed in section 6.4

For the SST $k - \omega$ model used in this study, the near-wall mesh size is critical to fully capture the thermal and turbulence boundary layers. The near-wall mesh is usually defined by the y^+ value and should be around 1 as recommended by ANSYS (2022). The $y^+=1$ is achieved by adjusting the first layer height to around 0.03m in ICEM settings.

To minimise the errors associated with the mesh density, a mesh independence test was conducted by altering the node numbers for two groups of configurations accordingly. In Table 3.6-2, the predicted value of the heat transfer rate, outlet mass-average temperature, and inlet mass-average pressure were compared until they were not affected by the node numbers. Three meshes with different cell numbers of 7,811,730, 9,476,330, and 10,784,230 were constructed and the layout for the 9,476,330 cell mesh is shown in Table 3.6-2. Three identical cases were run employing the three meshes respectively with the Reynolds number at 12,700. The difference between the results obtained by the last two mesh densities was below 1%. Thus, cell number 9,476,330 was mesh-independent and was utilised in subsequent simulations.

Table 3.6-2. Mesh independence test with PD8 Re at 12,700 for group 1.

Number of cells	Heat transfer rate W	Outlet temperature ^{o}C	Inlet pressure Pa
7,811,730	32,021.6 (-0.054%)	327.5 (-0.3%)	47.6 (-4.8%)
9,476,330	32,037.4 (-0.05%)	328.7 (0%)	50.0 (0%)
10,784,230	32,039.0	328.7	50.0

The mesh test for Group 2, which investigates different lobed tube arrangements, is presented in Table 3.6-3. The Reynolds number, calculated from the inlet condition, ranged from 9,089 to 30,903 in the numerical simulation. To assess the reliability of the numerical work, a mesh independence test was conducted on four meshes with different numbers of cells, before the formal simulation. As the mesh density increased, the relative differences in Nu and f between each mesh system decreased. The difference between 3,766,266 and

4,381,485 was smaller than 1%. Considering both computational accuracy and time efficiency, a mesh setting of 3,766,266 was utilised to construct the other meshes.

Table 3.6-3. Mesh independence test with PD8 decaying swirl flow and Re at 16,360 for group 2.

Number of cells	Average Nu	R_{Nu}	f	R_f
2,491,140	103.0	5.95%	0.0310	6.49%
3,090,848	106.6	2.36%	0.0325	1.63%
3,766,266	108.2	0.88%	0.0330	0.27%
4,381,485	109.1	Baseline	0.0331	Baseline

The hexahedral mesh overview and mesh quality are presented in Figure 3.6-8. The cell equiangular skewness and cell orthogonal quality are two important criteria for evaluating mesh quality. For the orthogonal quality, the worst cells will have a value closer to 0, and the best cells will have a value closer to 1. For skewness, a value of 0 indicates the best cells, whereas 1 indicates the worst cells. As can be seen in Figure 3.6-8, the minimum orthogonal quality and the maximum skewness value for the PD8 swirl tube are 0.45 and 0.66, respectively, suggesting a good mesh quality (orthogonal quality> 0.1 is generally acceptable). These values were all near the lobed region owing to the sharp edges.

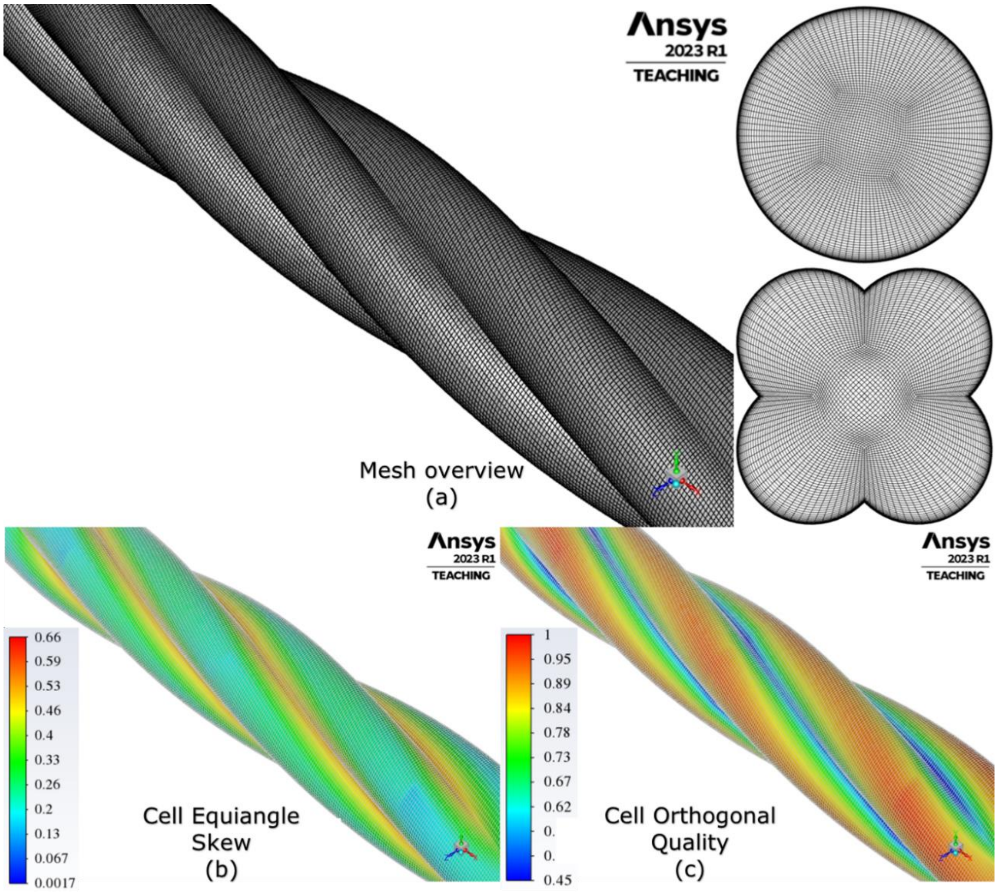

Figure 3.6-8. Mesh overview and mesh quality.

3.6.4 Judging Convergence

To assess convergence, the criteria for residuals were established to be 10^{-8}. The static pressure at the inlet, heat flux across the wall, and temperature at the outlet were monitored throughout the calculation and utilised to evaluate convergence. Figure 3.6-9 illustrates the residuals for a PD8 100D decaying swirl flow simulation model.

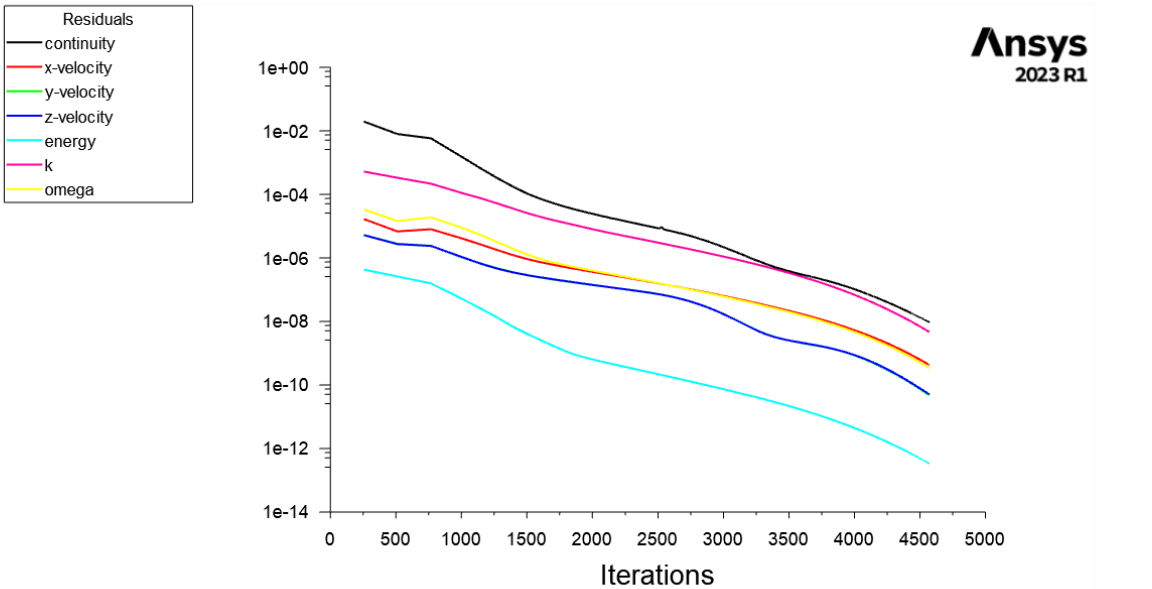

Figure 3.6-9. Scaled residuals for a PD8 100D simulation model.

In instances where the residuals do not decrease below the established criteria of 10^{-8}, the aforementioned representative flow variables may be utilised to assess convergence when these values cease to fluctuate with subsequent iterations.

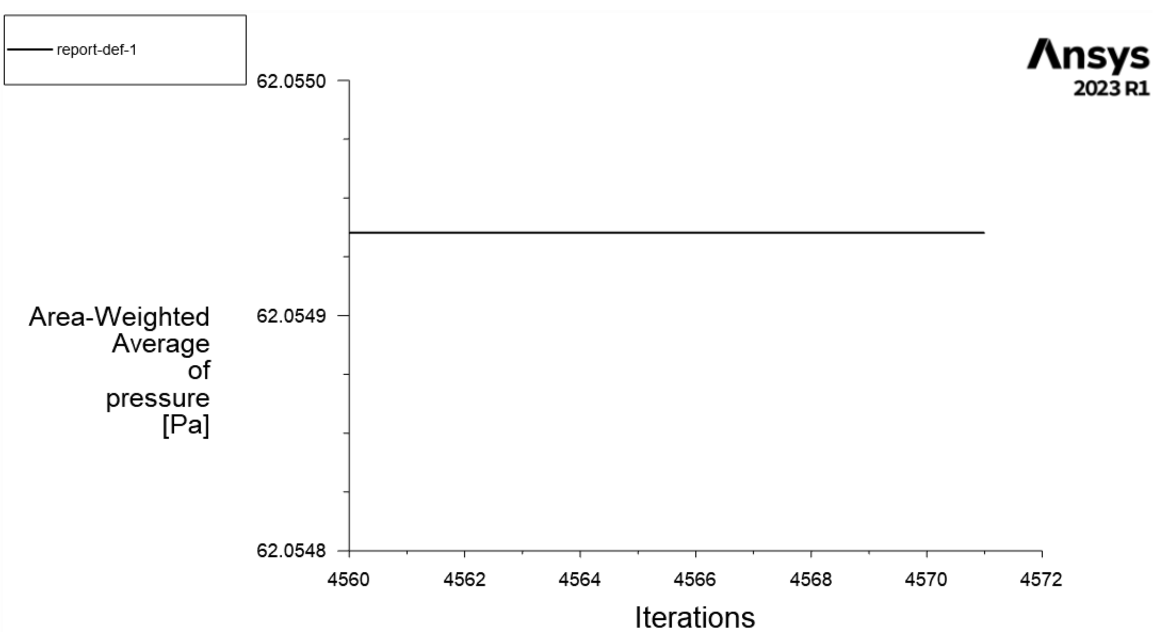

Figure 3.6-10. Variation of area-weighted static pressure at the inlet.

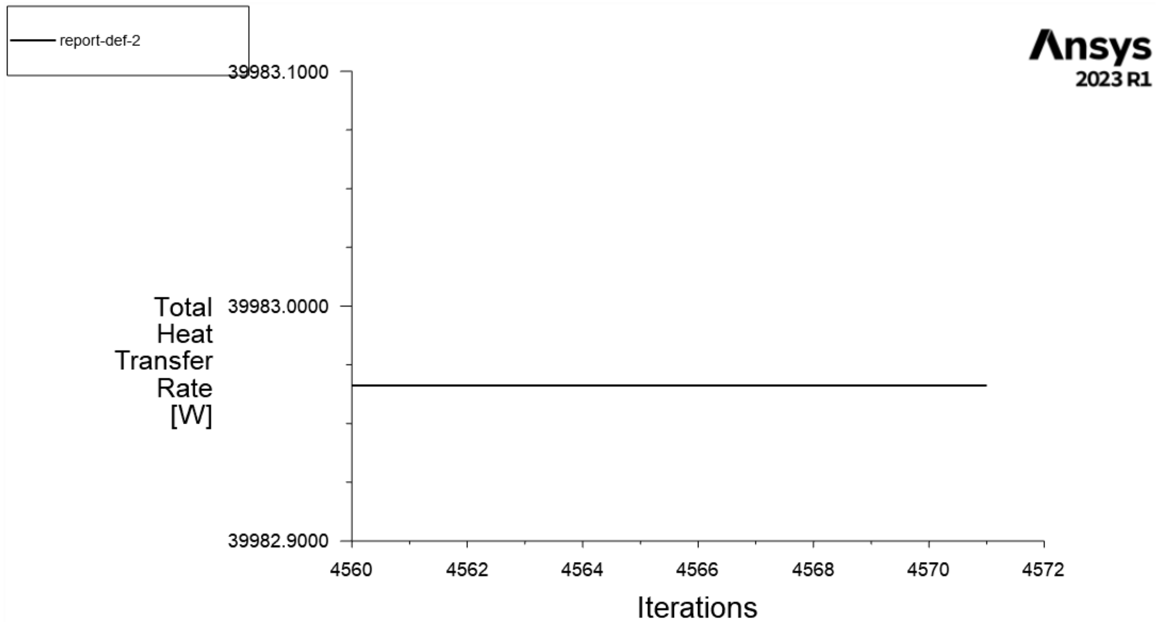

Figure 3.6-11. Variation of total heat transfer rate across the tube wall.

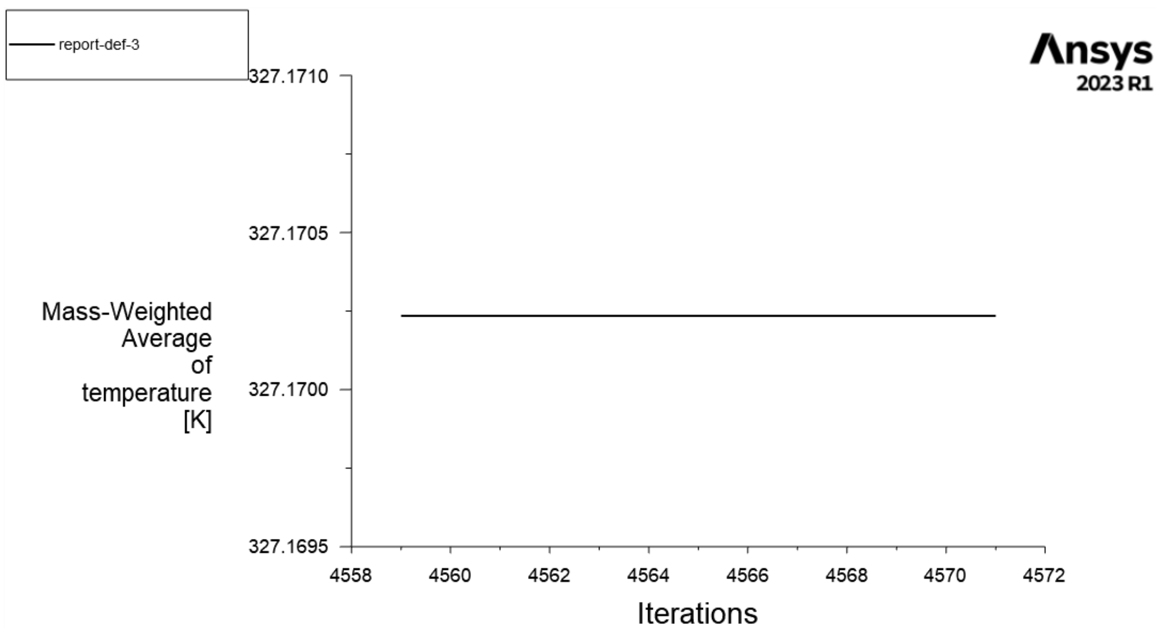

Figure 3.6-12. Variation of mass-weighted average temperature at the outlet.

During investigation, it was observed that such a low convergence residual, 10^{-8}, would increase the convergence time and cost. Consequently, for some cases with high mesh cell numbers, the residual was increased to 10^{-6}.

3.7 Conclusions

- The computational procedures for both the transition tube and the swirl tube are clearly described.
- The creation procedure of the 400mm long PD8 4-lobed swirl tube using SolidWorks is presented.
- The principles and methods of CFD simulation using ANSYS Fluent are introduced in this chapter.
- The numerical theories, including the governing equations, turbulence model, solver, and numerical discretization schemes applied, are elucidated.
- The numerical model employed to simulate the 4-lobed swirl tube is introduced. The assumptions, configurations of the fluid regions, and specification of the boundary conditions are delineated in detail.
- The hexahedral mesh used in the model and its mesh quality are described.
- Residuals and monitored variables during the simulation to assess convergence are presented.

CHAPTER 4: NUMERICAL INVESTIGATION OF THE 4-LOBED SWIRL TUBE

4.1 Introduction

This chapter presents two parts of a numerical investigation of a 4-lobed swirl tube. The first part focuses on the mechanism of the decaying swirl flow and the thermal enhancement performance of the decaying swirl flow with different downstream circular pipe lengths. The second part aims to investigate the thermal performance of the 4-lobed swirl tube under different tube arrangements and with regularly-inserted 4-lobed swirl tubes.

4.2 Simulation in Decaying Swirl Flow

In the initial phase of the numerical studies, the effects of including or excluding the 4-lobed tube in the heat exchanger were examined. For this purpose, two configurations were created, the ex-swirl and in-swirl configurations. For the ex-swirl configuration, the swirl tube is not included in the heat exchanger. For the in-swirl configuration, the swirl tube is included in the heat exchanger. The pipe geometry and boundary conditions used in the simulation are described below and illustrated in Figure 4.2-1. In both configurations, the geometry comprised three sections: pre-swirl, swirl, and post-swirl sections, which are consistent with previous research (Li et al., 2015). The circular tube has an inner diameter of 0.02m. The inlet velocity varied from 0.15m/s to 0.85m/s.

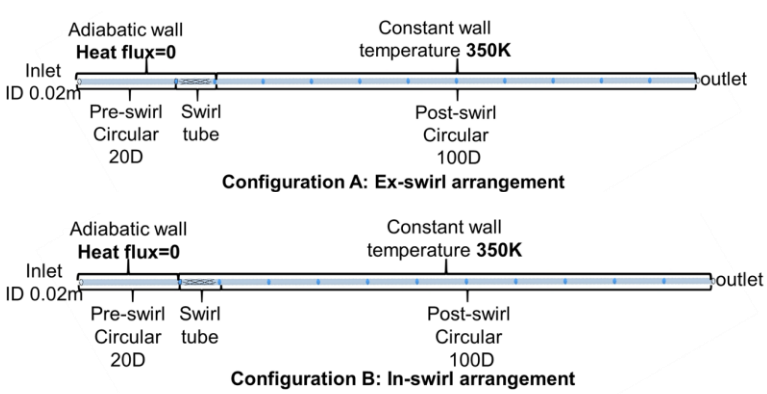

Figure 4.2-1. Pipe geometry and arrangement for simulation.

To simplify the simulation, heat transfer was achieved by establishing the wall temperature at 350K (Tang et al., 2015, Tan et al., 2012). The distinction between the two configurations is as follows.

Configuration A – the swirl tube is not included in the heat exchanger and the wall boundary conditions are: pre-swirl section (circular tube) – heat flux = 0; swirl section (swirl tube) –heat flux = 0; post-swirl section (circular tube) – 350K. This configuration is called the ex-swirl.

Configuration B – the swirl tube is included in the heat exchanger and the wall boundary conditions are: pre-swirl section (circular tube) – heat flux = 0; swirl section (swirl tube) – 350K; post-swirl section (circular tube) – 350K. This configuration is called the in-swirl.

4.3 Results and Discussion

4.3.1 Effect of PD Ratio and Tube Location

A circular tube with the same setting as Figure 4.2-1 configuration A was simulated and utilised as the benchmark for PEC calculations. To evaluate the effect of the pitch-to-diameter ratio (PD ratio) on the thermal performance of the swirl generator, three different PD ratios were examined for configurations A and B, resulting in six configurations, as illustrated in Table 4.3-1. The *Nu* and *f* ratios were employed to demonstrate the difference between each arrangement. A detailed illustration of the calculation of Nusselt number and friction factor is shown in Appendix 1.5 Calculation for Nusselt number from Simulation Results.

Table 4.3-1. Coding for Swirl Tube Inclusion and Pitch-to-Diameter (PD) Ratios.

Swirl tube included <u>or</u> excluded as part of the heat transfer component	Pitch-to-Diameter (PD) Ratio	Code
excluded	8	PD8 ex-swirl
	6	PD6 ex-swirl
	4	PD4 ex-swirl
included	8	PD8 in-swirl
	6	PD6 in-swirl
	4	PD4 in-swirl

The ratio of the Nu of the swirl tube (Nu_s) to the Nu of the circular tube (Nu_c) against Reynolds number is plotted in Figure 4.3-1.

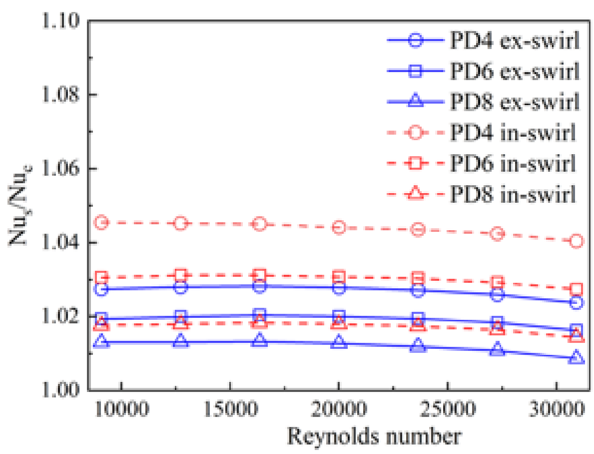

Figure 4.3-1. Plot of Nusselt number ratio and Reynolds number for different geometries.

All geometries exhibited a Nusselt number ratio higher than 1, which indicated the thermal enhancement ability of the swirl generator. Although the ratio of Nu_s/Nu_c did not vary significantly over this Reynolds number range that was covered for both in-swirl and ex-swirl cases, there was a slight decrease when the Reynolds number was greater than 20,000. It was clear from the figure that, firstly the Nu_s/Nu_c ratios in-swirl configurations were generally larger than those for ex-swirl configuration for all PD ratios, and secondly, a decreasing pipe sections (with a lower PD ratio) led to higher Nu_s/Nu_c ratios. This was because lower PD ratio can create higher turbulence and mixing effect resulting higher heat transfer enhancement. Though it is possible to further reduce the PD ratio to 2, it is not attempted because such low PD ratio may increase the difficulty in actually manufacturing such tube. On the contrary, a very large PD ratio is a lobed straight tube. It therefore indicated that an in-swirl arrangement was more appropriate in heat transfer applications. The largest temperature difference observed between the inlet and outlet was around 30 degrees Celsius at the lowest flow rate. In this study, it was assumed that the viscosity and density are constant for simplification based on previous research (Tang et al., 2015). For further studies, the effect of temperature change on fluid properties such as viscosity and density should be considered.

The variation of the friction factor ratio, f_s/f_c, (ratio of the friction factor of a swirl tube section to that of a circular pipe section) is plotted in Figure 4.3-2 for various arrangements.

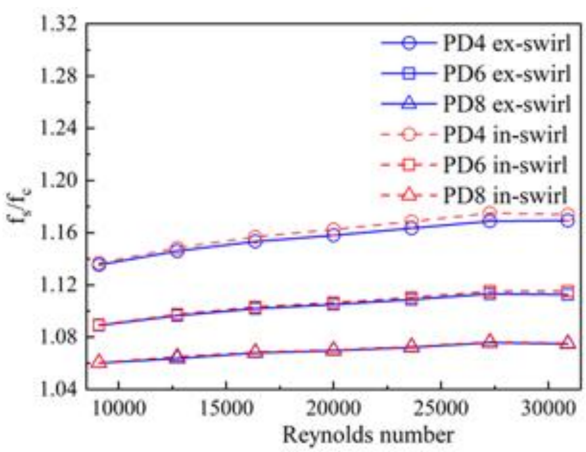

Figure 4.3-2. Plot of Friction factor ratio and Reynolds number for different geometries.

The f_s/f_c greater than 1 indicated a higher pumping power cost for swirl sections in comparison to a circular pipe section. As observed in Figure 4.3-2, for all PD ratio swirl tubes, including or excluding the swirl part, the ratio exceeded 1 and gradually increased with increasing Reynolds number. The swirl tube with a PD ratio of 4 created the highest friction factor ratio for both in-swirl and ex-swirl configurations. Nevertheless, the f_s/f_c for all the arrangements was considerably lower than that of full-length twisted tape (Liu and Sakr, 2013).

Figure 4.3-3 presents the PEC factor (the ratio of the energy recovered due to heat transfer to the energy consumed due to a higher pressure drop) with different Reynolds numbers for all swirl generators.

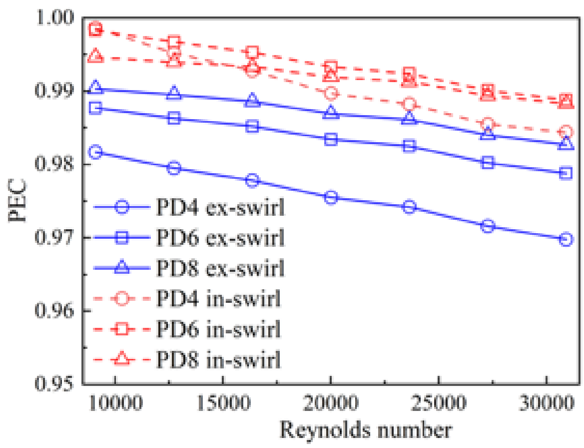

Figure 4.3-3. Plot of PEC and Reynolds number for different geometries.

The performance evaluation criterion (PEC) for all swirl tubes was lower than 1, indicating that the higher pressure drops caused by the swirl tubes outweigh the heat transfer enhancement compared to that of the circular tube. The highest PEC factor was around 0.995 at a Reynolds number of 9,000 for a PD6 in-swirl tube arrangement. As observed in Figure 4.3-1, the Nu_s/Nu_c ratio was higher than 1, which indicated the positive thermal enhancement capability for all swirl tube geometries in comparison to the circular pipe section. However, this thermal enhancement was cancelled out, as shown in Figure 4.3-3, by the requisite pumping power. It can be concluded that incorporating the swirl tube as a component of the heat transfer apparatus was advantageous from a heat transfer perspective; however, the 2m length of the post-swirl circular pipe was excessive, as the swirl effect diminished with increasing downstream distance, nullifying most of the heat exchange benefits. Therefore, further investigations on the length of the post-swirl tube was investigated so as to optimise the design and guide the experimental studies.

4.3.2 Effect of Different Lengths of Post-Swirl tube

To investigate the effect of the post-swirl tube length on the overall performance, a series of simulations were conducted with post-swirl circular pipe lengths varying from 40 to 80 times the pipe diameter. Given that the diameter of the pipe was 0.02m, the attached pipe lengths were characterised by the length to pipe diameter ratio (x/D) and ranged from 0.8m (40D), 1.2m (60D), to 1.6m (80D). In addition, the performance of a PD ratio of 10 was examined. The PEC factors for various PD ratios and post-swirl tube lengths across a range of Reynolds numbers are shown in Figure 4.3-4.

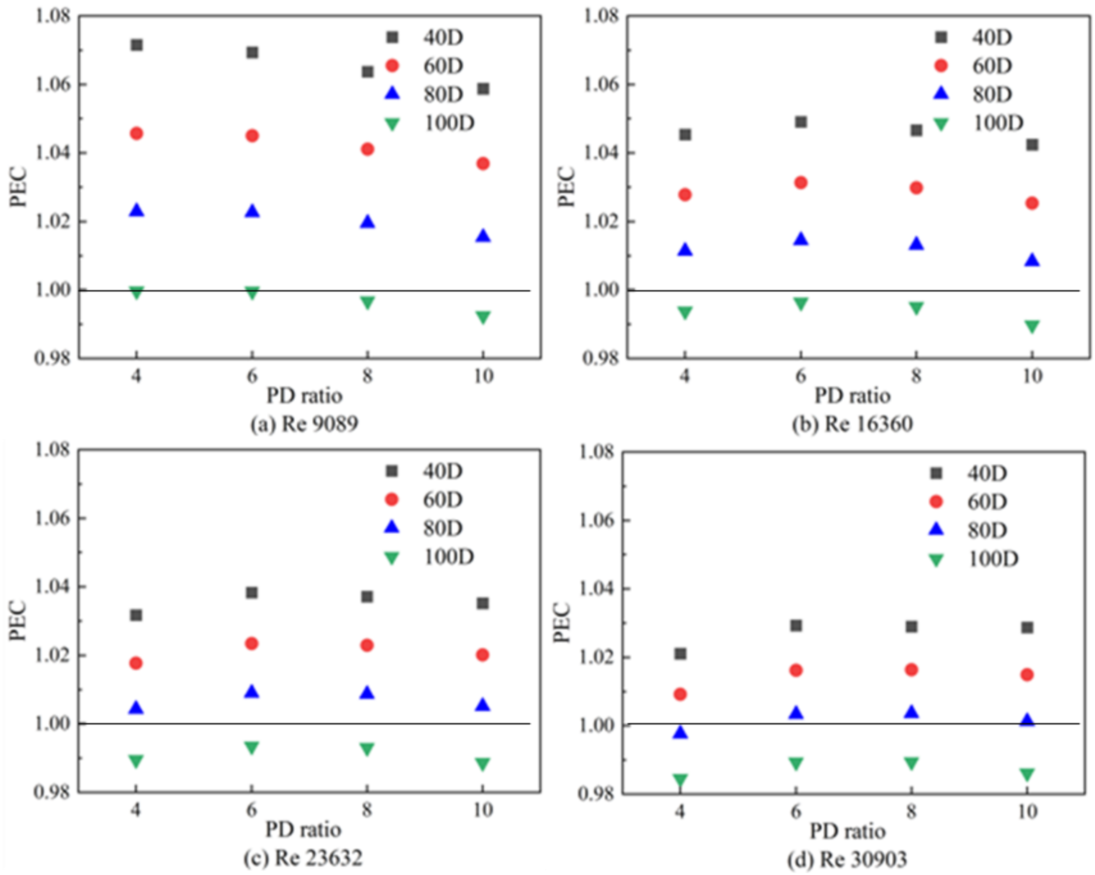

Figure 4.3-4. Plot of PEC and PD ratio for different post-swirl tube lengths.

It was observed that post-swirl circular pipe sections with lengths below 80D resulted in a PEC factor exceeding 1. For all PD ratio swirl tubes, a maximum PEC value of 1.07 was achieved with post-swirl circular pipe lengths of 40D at a Reynolds number of 9,089. The findings indicated that the optimal PD ratio varied with the Reynolds number. At higher Reynolds numbers, it was approximately six, while at lower Reynolds numbers, it was four. Consequently, to maximise the PEC factor for the swirl tube (the ratio of energy recovered from heat transfer to energy consumed by increased pressure drop), it was necessary to operate with shorter lengths of post-swirl circular pipe sections and at lower Reynolds numbers (i.e. lower flowrates/fluid velocities). These two aspects are important considerations when optimising swirl tubes. Considering these factors, there may be a potential benefit in having regularly spaced swirl tubes. However, the relationship between these factors and the regularly-spaced swirl tube needs further investigation, which will be discussed in further chapters.

4.3.3 Flow Behaviour Analysis

To visualize the thermal enhancement effect of installing a swirl tube, the cross-sectional tangential velocity vector and isotherm lines for a PD8 in-swirl configuration was selected as an example to demonstrate the field synergy principle. The cross-sectional views are situated at the entrance, middle and exit of the swirl tube, and 10 D downstream of the swirl tube as shown in Figure 4.3-5.

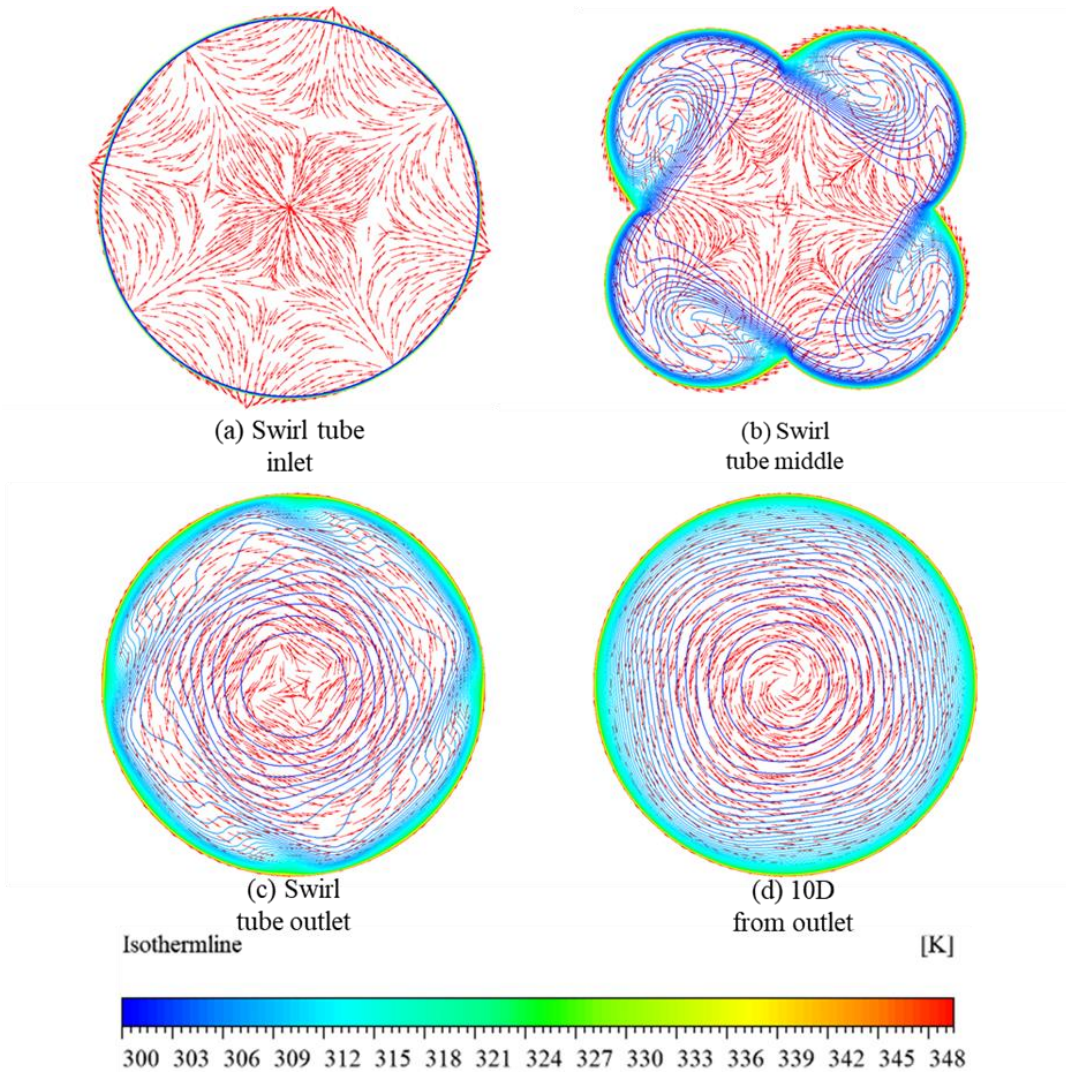

Figure 4.3-5. Counter plot for isotherm line and velocity vector at Reynolds number of 16,360.

The velocity vector is normalized for presentation. The lobed tube induces a re-distribution of the velocity field at the inlet due to the modification of the pipe geometry. Vortices were generated at the centre of each semicircle of the four lobes within the swirl tube, redistributing the temperature and velocity field as they rotated around the vortices' centres. This increased the heat transfer as the direction of the velocity vector became perpendicular to the isotherm line, leading to a decrease in the synergy angle. Considering these observations, the application of the field synergy principle facilitated a more comprehensive understanding of the mechanism underlying the heat transfer rate enhancement with swirl tubes (Guo et al., 2005). Although the distribution of the temperature and velocity fields at the swirl tube exit still indicated increased heat transfer, it dissipated rapidly as the distance from the swirl tube increased. At 10D downstream of the swirl tube exit, the velocity vector was increasingly parallel to the isotherm line, implying a diminishing heat transfer enhancement effect.

Figure 4.3-6 compares the average synergy angle for different Reynolds numbers between different tube arrangements over the complete length of the pipe section.

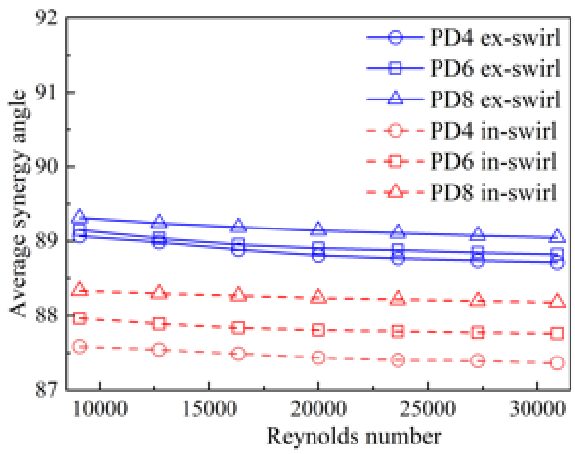

Figure 4.3-6. Average synergy angle for all tube arrangements over the complete length of the pipe section.

In summary, a small synergy angle suggests a high Nusselt number (Guo et al., 2005). The synergy angle is around 89° for ex-swirl sections, and 88° for in-swirl arrangements. The reason for this is that the heat-transfer effect is more pronounced in the swirl tube region as it is where turbulence is created. This observation aligns with our previous findings, which demonstrated that the in-swirl configuration yields a higher Nusselt number. In general, a slight reduction in the synergy angle was observed with increasing Reynolds number across all PD ratio swirl tube sections. The smallest synergy angles were achieved with the in-swirl arrangement of the PD4 swirl tube. In this case, the smaller twisted ratio resulted in a smaller average synergy angle, thereby enhancing heat transfer. This phenomenon was consistent with the variation in the Nusselt number ratio in Figure 4.3-1, which decreases with a reduction in the twisted ratio.

The local synergy angle variation within and downstream of the swirl tube for various PD ratios for the in-swirl arrangement is shown in Figure 4.3-7

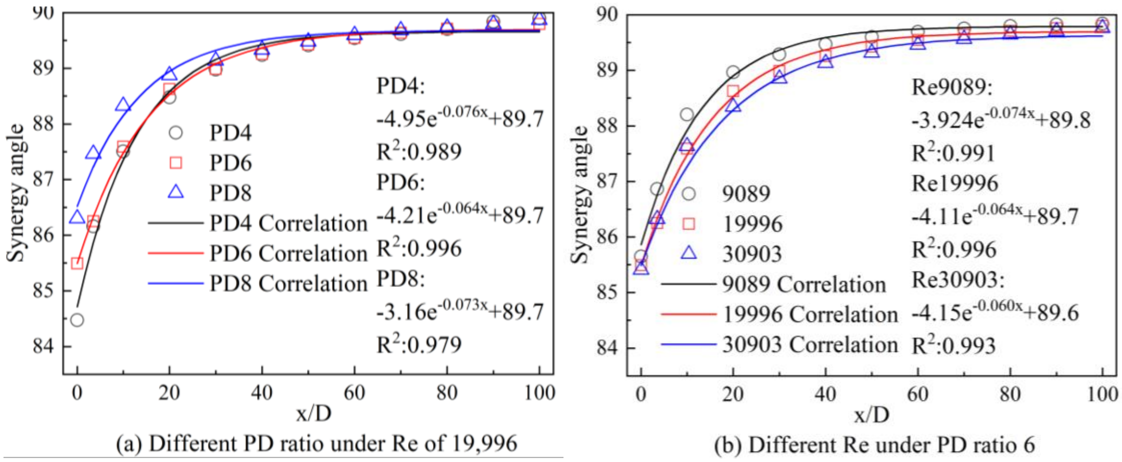

Figure 4.3-7. Local synergy angle variation for in-swirl arrangement at (a) different PD ratio under Reynolds number of 19,996, (b) different Reynolds number under PD ratio 6.

For all swirl tubes with different PD ratios, the lowest angle was observed at the outlet of the swirl tube which rose steeply from 0 to 20D and then began flattening out further downstream to around 90°. In general, lower PD ratios and higher fluid velocities resulted in reduced synergy angles. Irrespective of the configuration, the swirl effect on the thermal enhancement disappeared at around 60D to 80D downstream after it approached the synergy angle for the normal circular pipe. This phenomenon elucidated the reason for the increased Nu observed in Figure 4.3-4 when the post swirl length was reduced.

Moreover, the synergy angle variation downstream of the post-swirl tube for the in-swirl arrangement seemed to fit an exponential trend similar to the swirl intensity. Such correlation is proposed with the ideal of swirl intensity correlations (2.3-13). An attempt was made to fit an exponential correlation between distance and local synergy angle.

$$\theta = -\Delta\theta e^{-\gamma\frac{x}{D}} + \theta_c \qquad (4.3\text{-}1)$$

Where θ is the local synergy angle, $\Delta\theta$ is the difference between θ_0 and θ_c when $\frac{x}{D} = 0$, γ is the decaying swirl rate coefficient related to synergy angle.

The fitted curves at different PD ratios and Reynolds numbers are presented in Figure 4.3-7. This correlation generally predicted the variation of synergy angle. θ_c, $\Delta\theta$ and γ were all negatively correlated with the Reynolds number. Conversely, only $\Delta\theta$ decreases with Reynolds number, whereas θ_c was not related to the PD ratio and γ reaches its highest value at PD6. Generally, θ_c represented synergy angle for a develops flow in a circular pipe under identical flow conditions. A higher $\Delta\theta$ indicated a lower initial synergy angle and a lower γ suggested that the swirl effect on the thermal enhancement persisted for a longer duration. Based on these coefficients, a lower PD ratio and a higher Reynolds number related to a lower $\Delta\theta$, indicating a higher heat transfer rate. PD6 gave the lowest γ value across all three ratios, which explains why PD6 has the highest PEC value in Figure 4.3-3. Increasing the Reynolds number leads to a lower θ_c, $\Delta\theta$ and γ, suggesting a higher heat transfer rate. However, further investigations are necessary to determine whether this correlation can accurately describe the synergy angle variations related to decaying swirl flow generated by other thermal enhancement devices.

4.4 Simulations in Tube Arrangements

In the second part of the numerical studies, different tube arrangements with PD ratios of 8, 6 and 4 were constructed to compare the hydrothermal performance. Four types of arrangements, using only PD8 as an example, are shown in Figure 4.4-1 for demonstration. To ensure the formation of a fully developed flow at the inlet of the continuous swirl tube, the upstream and downstream sections of the circular tube were extended by 5D (five times the diameter). The total length of the heated part was consistent. Because there is a length difference between each PD ratio, the number of tubes for different PD values is different for crossover and parallel arrangements. Specifically, for these two arrangements, 6 PD8 tubes, 8 PD6 tubes, and 12 PD4 tubes are created. The purpose of having these different numbers of tubes for different PD values is to ensure that the total length of the tubes is identical across all configurations

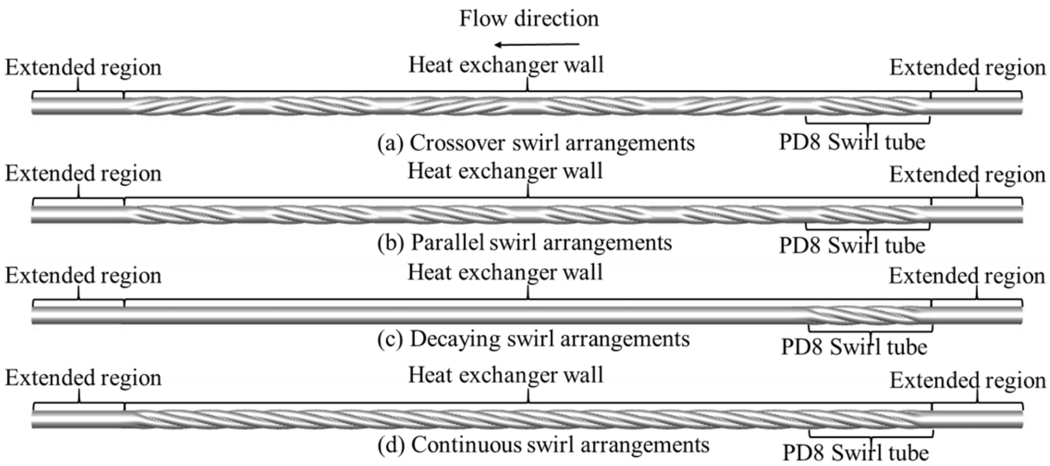

Figure 4.4-1. Views of different tube arrangements at PD8.

4.5 Results and Discussion

4.5.1 Effect of Different Tube Arrangements

The simulation data regarding the temperature difference ΔT between the inlet and outlet, heat exchanger energy efficiency η_h defined in equation (2.3-5) and effective efficiency $\eta_h{}'$ defined in equation (2.3-7) are presented in Table 4.5-1 and Table 4.5-2. Among all the arrangements, the crossover arrangement exhibits the highest ΔT and energy efficiency. In contrast, the decaying arrangement has the lowest ΔT and the energy efficiency η_h.

Furthermore, as the Reynolds number increases, the discrepancy between the energy efficiency η_h and effective efficiency $\eta_h{}'$ for crossover arrangement grows. Regarding other arrangements, particularly for decaying one, the change in the two efficiencies is not pronounced. This indicates that the impact of pressure drop becomes more evident at higher flow rates, especially for the crossover arrangement, while the pressure-drop penalty for the decaying flow is not that significant compared with the crossover one. In addition, for all arrangements, a lower PD ratio results in a higher temperature difference. This is because a lower PD ratio induces greater turbulence within the flow.

Table 4.5-1. Performance summary for continuous and decaying arrangements

Reynolds number	PD ratio	Continuous			Decaying		
		ΔT	η_h	$\eta_h{}'$	ΔT (°C)	η_h	$\eta_h{}'$
9,089	PD8	18.642	1.221	1.221	16.152	1.059	1.059
19,996	PD8	16.478	1.213	1.211	14.348	1.057	1.056
30,903	PD8	15.563	1.208	1.207	13.541	1.053	1.053
9,089	PD6	19.918	1.304	1.304	16.677	1.094	1.093
19,996	PD6	17.348	1.271	1.270	14.835	1.092	1.090
30,903	PD6	16.303	1.270	1.266	14.020	1.089	1.086
9,089	PD4	21.995	1.440	1.439	17.046	1.131	1.129
19,996	PD4	19.052	1.395	1.392	15.270	1.120	1.119
30,903	PD4	17.896	1.391	1.384	14.507	1.117	1.115

Table 4.5-2. Performance summary for crossover and parallel arrangements.

Reynolds number	PD ratio	Crossover			Parallel		
		ΔT	η_h	$\eta_h{}'$	ΔT (°C)	η_h	$\eta_h{}'$
9,089	PD8	20.326	1.331	1.330	19.300	1.264	1.263
19,996	PD8	18.166	1.333	1.327	16.606	1.221	1.216
30,903	PD8	17.167	1.342	1.326	15.512	1.217	1.207
9,089	PD6	22.360	1.463	1.462	20.957	1.372	1.371
19,996	PD6	19.620	1.438	1.429	17.746	1.303	1.298
30,903	PD6	18.450	1.436	1.414	16.521	1.294	1.282
9,089	PD4	25.450	1.664	1.661	26.373	1.537	1.535
19,996	PD4	21.884	1.598	1.583	20.015	1.468	1.461
30,903	PD4	20.320	1.568	1.530	18.405	1.438	1.421

Figure 4.5-1 plots the ratio of Nu of the swirl tube to that of the circular tube versus the Reynolds number for various arrangements. All the swirl arrangements yielded a Nu ratio higher than 1 indicating that the heat transfer coefficient of all arrangements exceeded that of the circular tube. The numerical results demonstrated that for all arrangements, the Nu ratio decreased as Reynolds number increased and PD ratios decreased. The crossover arrangement exhibited the highest Nu ratio, while the decaying arrangement exhibited the

lowest Nu ratio. This phenomenon can be attributed to the disruption of both the thermal and velocity boundary layers due to the connection of multiple swirl tubes and the reduction in the PD ratio. For all arrangements, an increase was observed when the PD ratio decreased from 6 to 4. The highest Nu ratio is from 1.71 to 1.57 for the PD4 crossover configuration and the lowest Nu ratio ranged from 1.11 to 1.09 for the PD8 decaying configuration across all Reynolds numbers.

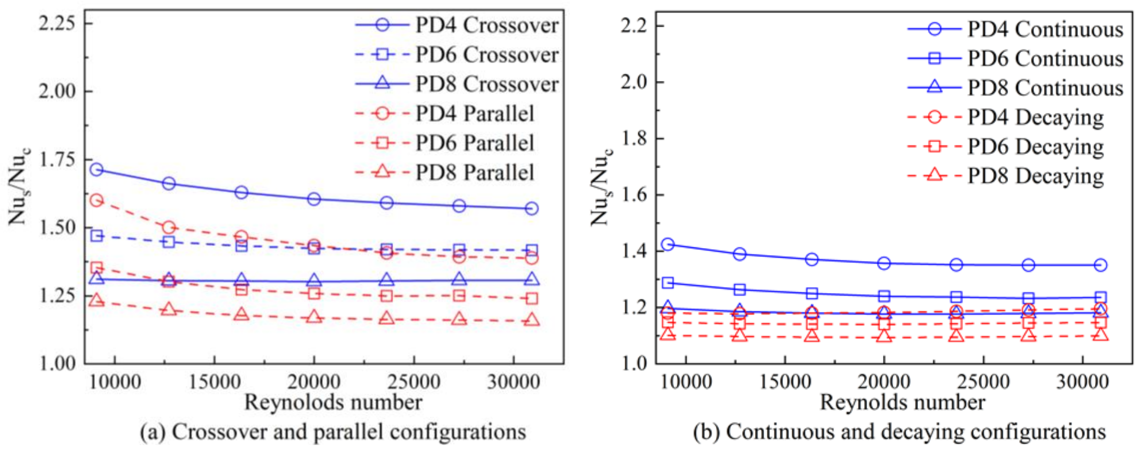

Figure 4.5-1. Plot of Nusselt number ratio and Reynolds number for different arrangements. (a) crossover and parallel configurations; (b) continuous and decaying configurations.

The variation of the friction factor ratio, f_s/f_c, (ratio of the friction factor of a swirl tube to that of a circular tube) for different arrangements is presented in Figure 4.5-2. All the swirl configurations exhibited a friction factor ratio higher than 1, indicating that all arrangements possess a higher flow resistance in comparison to the regular circular tube. According to the numerical results, the f ratio demonstrated a tendency to increase with an increase of Re and a reduction of the PD ratio for all swirl arrangements. Similar to Nu ratio, the crossover arrangement exhibited the highest f ratio, whereas the decaying configuration demonstrated the lowest f ratio. Though inserting several swirl tubes disrupted the boundary layer, they also generated higher flow resistance. Such a high-pressure drop negates any improved heat transfer benefits when these devices are implemented into existing systems The highest f ratio is from 4.81 to 6.07 for PD4 crossover and the lowest f ratio is from 1.22 to 1.25 across all Reynolds numbers.

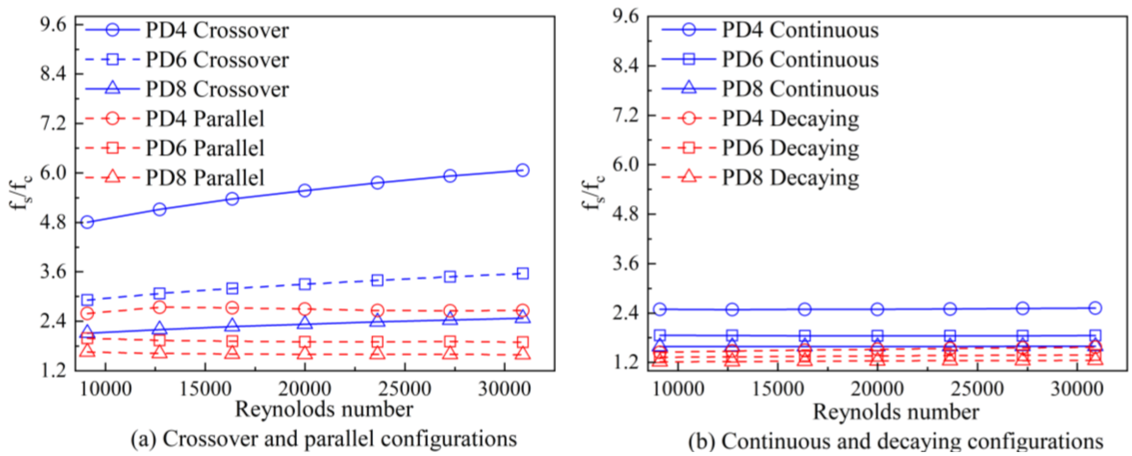

Figure 4.5-2. Plot of friction factor ratio and Reynolds number for different arrangements. (a) crossover and parallel arrangements; (b) continuous and decaying configurations.

The PEC factor (the ratio of the energy recovered due to heat transfer to the energy consumed due to a higher pressure drop) with different Reynolds numbers for different arrangements is plotted in Figure 4.5-3. The scale between the two figures differs to facilitate a better distinction of variation. When the PEC factor exceeded 1, the overall performance of the devices surpassed that of the circular tubes. Only parallel and decaying arrangements exhibited a PEC factor higher than 1 for all PD ratios and Reynolds numbers investigated. Crossover and continuous arrangements demonstrate a PEC factor lower than 1, particularly at high Reynolds numbers. Generally, PD4 for all arrangements exhibited a steep reduction as the Reynolds number increased. This phenomenon is likely attributable to the increased pressure drop caused by the swirl tubes outweighing the heat transfer enhancement component compared to that of the circular tube. The continuous swirl flow consistently demonstrated higher thermal enhancement and pressure drop than the decaying swirl flow, which aligns with the findings reported by Eiamsa-ard and Seemawute (2012) wherein the short-length twisted tape provided lower heat transfer and pressure drop than the full-length twisted tape.

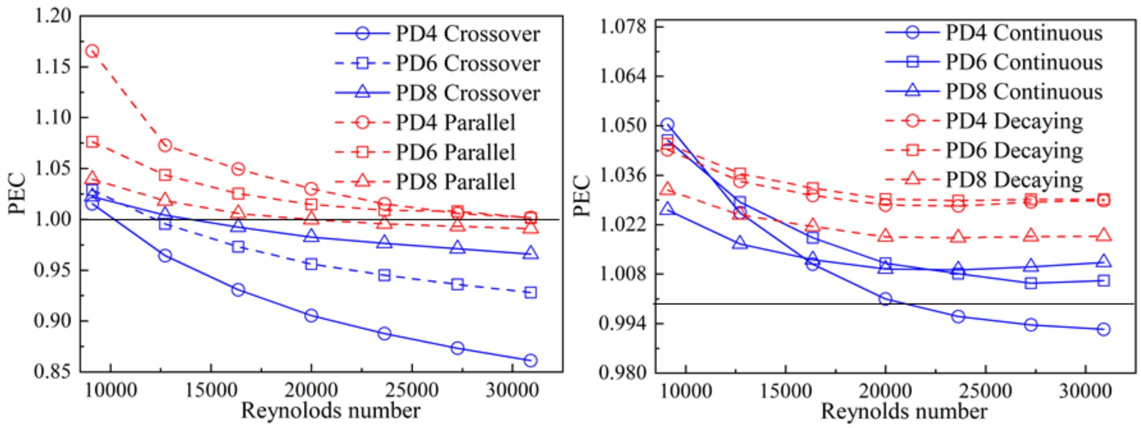

(a) Crossover and parallel configurations

(b) Continuous and decaying configurations

Figure 4.5-3. Plot of PEC and Reynolds numbers for different arrangements. (a) crossover and parallel arrangements; (b) continuous and decaying arrangements.

Furthermore, in Figure 4.5-3 (a), the PD4 crossover exhibits the lowest PEC values, ranging from 1.02 to 0.86, whereas the PD4 parallel configuration demonstrates the highest PEC values, ranging from 1.17 to 1, particularly at low Reynolds numbers. In Figure 4.5-3 (b), the PD6 decaying arrangement presents the largest values, ranging from 1.04 to 1.03. Regarding the continuous arrangement, PD4 exhibited the highest PEC value at a Reynolds number of 9,089, followed by PD6, which demonstrated the highest values over the Reynolds number range from 12,724 to 20,000. At Reynolds numbers exceeding 20,000, PD8 continuously surpasses PD6 and attains the highest values. These variations in the PEC values were primarily attributable to changes in the friction ratio.

4.5.2 Streamline and Local Nusselt Number Analysis

To better understand the thermal enhancement mechanism in swirl tubes, the flow streamlines and tube surface Nusselt numbers are considered valuable for describing the local velocity fields and temperature distributions. The three-dimensional streamline views for different tube arrangements in this study are depicted in Figure 4.5-4. These swirl tubes generate vortices within the lobed region and in the near-wall region. For Figure 4.5-4 (a) and (b), the flow structure twists as the swirl direction changes, reversing the vortex direction. Small-scale vortices are also generated, particularly in the transition region for crossover arrangements, which is comparable to a 3-lobed swirl tube (Tang et al., 2015). As shown in Figure 4.5-4 (c) and (d), although vortices are also generated within the swirl tube, the streamlines are uniform compared to those in the parallel and crossover arrangements. Moreover, the vortices gradually dissipate after exiting the swirl tube, as reported in a previous study also conducted at the University of Nottingham (Li et al., 2017). Additionally, these vortices can significantly enhance the heat transfer rate because they promote fluid mixing and disrupt the boundary layer. However, a larger pressure drop was also created along the flow direction owing to the substantial change in flow velocity. Therefore, the degree of thermal enhancement and flow resistance is proportional to the number of vortices, which explains the differences in the Nu ratio in Figure 4.5-1 and the f ratio in Figure 4.5-2 over different configurations.

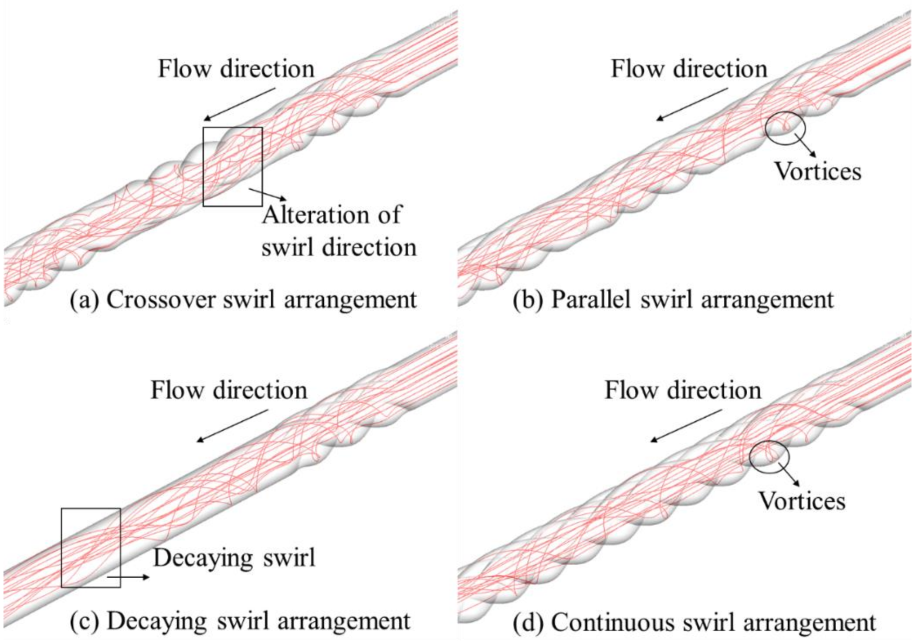

Figure 4.5-4. Streamline view for different tube arrangements at PD8 with the Reynolds number of 16,360.

Previous research has yet to report the difference in heat transfer performance between decaying and continuous swirl flow generated by lobed tubes (Tang et al., 2015, Li et al., 2017). The surface Nu for different tube arrangements at PD8 with a Reynolds number of 16,360 is shown in Figure 4.5-5. For all arrangements, the largest Nu values were consistently located at the entrance section and on the lobed surface of the swirl tube. This phenomenon is attributed to the fluid at the entrance section having a larger temperature difference from the tube wall, which is known as the thermal-entrance effect (Tang et al., 2015). Furthermore, the crossover arrangement exhibits the highest surface Nu because this configuration facilitates improved fluid mixing and generates small-scale vortices. In the case of a decaying swirl flow, the highest surface Nusselt number also occurred at the inlet region on the lobed section and decreased gradually, suggesting the potential benefit of inserting additional swirl tubes in the downstream sections.

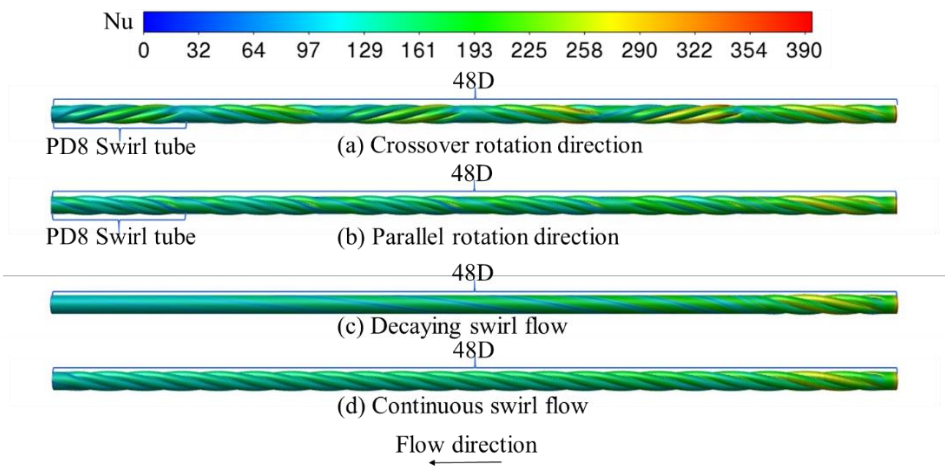

Figure 4.5-5. Local Nu for different tube arrangements at PD8 with the Reynolds number at 16,360.

4.5.3 Regularly-Spaced Swirl Tube

Drawing inspiration from regularly spaced swirl tubes (Wang et al., 2011), this study proposes the implementation of regularly inserted 4-lobed tubes. The configuration of the regularly spaced swirl tube is illustrated in Figure 4.5-6. To incorporate additional swirl tubes systematically, each swirl tube with a distinct PD ratio (4, 6, and 8) was connected to a 100D (2m) long tube. The position of the inserted swirl tube was determined to ensure uniformity in the length at the connected circular tube. A circular tube at 104D (2.08m) was also constructed and utilised as a reference point for subsequent calculations.

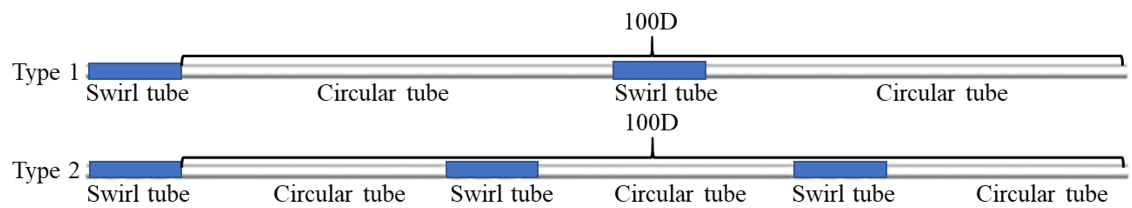

Figure 4.5-6. Arrangement of the regularly-spaced swirl tube

The ratio of the Nu for the regularly-spaced swirl tube is shown in Figure 4.5-7. All swirl tube arrangements exhibited Nusselt number ratios greater than 1. Consistent with previous findings, the Nusselt number ratio increased with a reduction in the Reynolds number and PD ratio. The highest Nu ratio was approximately 1.21 at the lowest Reynolds number for Type 2 PD4. The lowest Nu ratio was observed for Type 1 PD8 at approximately 1.06. An increase in the number of inserted swirl tubes from two to three increased the Nusselt number ratio for all cases, indicating the positive effect of the additional swirl tube.

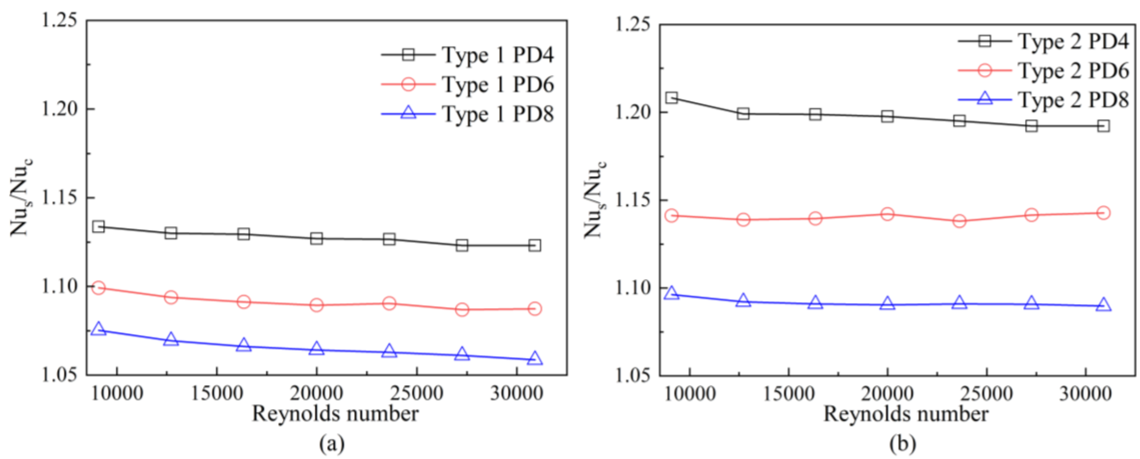

Figure 4.5-7. Nu ratio for regularly-spaced swirl tube.

The ratio of the f for the regularly-spaced swirl tube is shown in Figure 4.5-8. Though all arrangements exhibited a friction factor ratio exceeding 1, the increase in pressure loss was not as significant as 185% suggested by Liu and Sakr (2013). The friction factor ratio increased at higher Reynolds numbers and lower pitch-to-diameter (PD) ratios. Analogous to the Nusselt number ratio variation, the highest friction factor ratio was observed in Type 2 PD4, approximately 1.6, at the largest Reynolds number. Type 1 PD8 yielded the lowest friction factor ratio, approximately 1.15. As anticipated, the insertion of additional swirl tubes and smaller PD ratios resulted in a higher friction loss owing to increased turbulence within the tube. Generally, given this magnitude of pressure drop increment, a regularly-spaced 4-lobed swirl tube can be implemented in existing systems without exceeding the pumping power requirement.

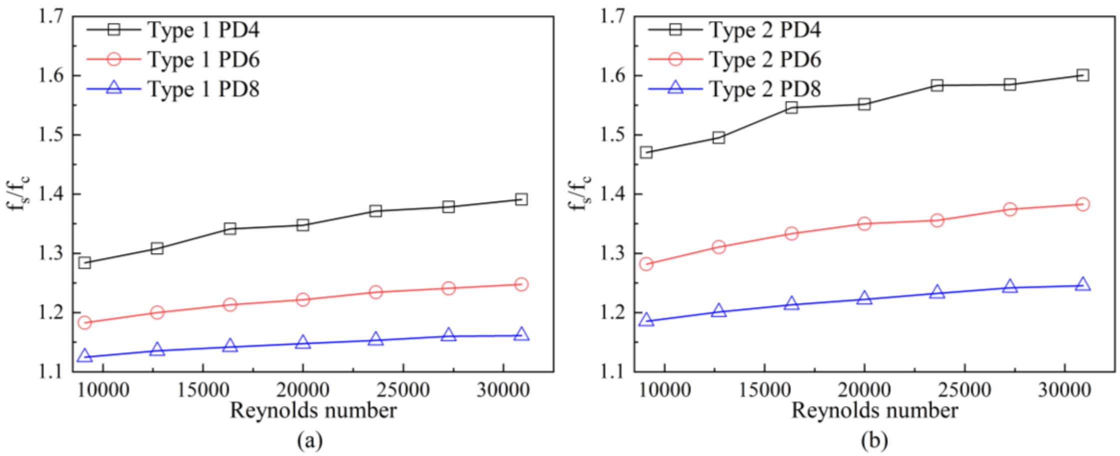

Figure 4.5-8. f ratio for regularly-spaced swirl tube.

The PEC value for the regularly spaced swirl tube is shown in Figure 4.5-9. The PEC value for all arrangements exceeded 1, indicating superior performance compared with that of the circular tube. The maximum PEC value (1.06) was observed for Types 2 PD4 at the lowest Reynolds numbers. Although the insertion of the three swirl tubes resulted in a higher pressure drop, the PEC values for the Type 2 arrangements consistently surpassed those of the Type 1 arrangements. For both types, PD8 exhibited the lowest PEC value among all PD ratios investigated. While the PEC values of PD4 are the highest at low Reynolds numbers, their performance is exceeded by that of PD6 as the Reynolds number increases. This phenomenon is attributed to the dramatic increase in the friction factor for PD4 with the increasing Reynolds number. However, the PEC value remained relatively modest, suggesting potential for further enhancement.

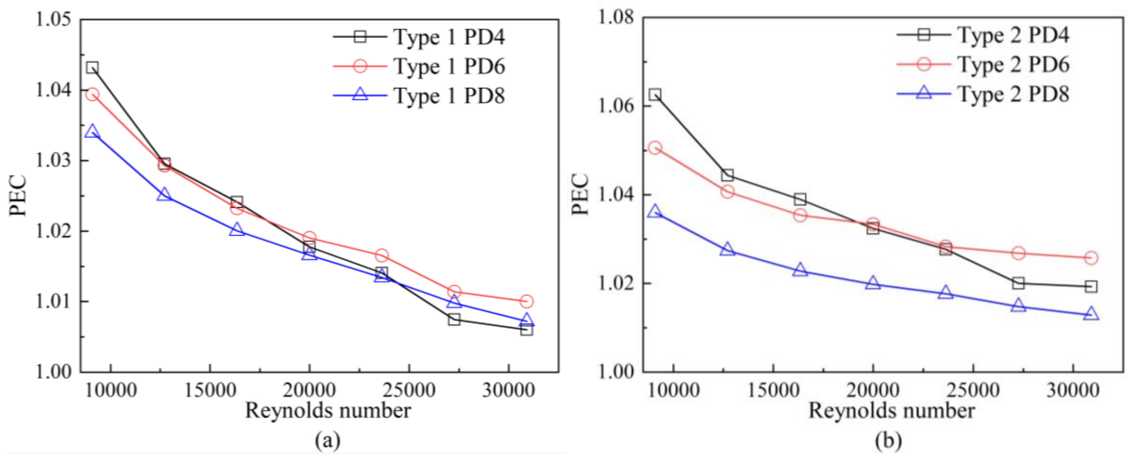

Figure 4.5-9. PEC value for regularly-spaced swirl tube

The surface Nusselt number for the regularly spaced swirl tube is shown in Figure 4.5-10. In contrast to decaying swirl flow, the surface Nusselt number initially decreases due to the swirl decaying effect and subsequently increases after flow through the inserted 4-lobed swirl tube. Furthermore, the highest surface Nusselt number remained in the entrance and lobed regions. Notably, distinct colour bands (indicating differences in the surface Nusselt number) were observed in the decaying section for all tube arrangements. As indicated in previous research (Li et al., 2017), the 4-lobed swirl tube generates four vortical regions within the swirl tube, which rotate downstream of the swirl tube. Consequently, an elevated surface Nusselt number (represented by colour bands) was produced by these vortices.

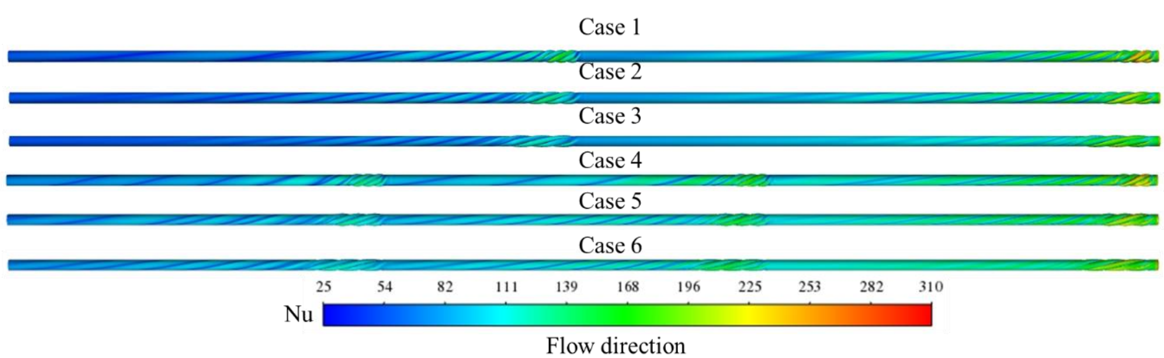

Figure 4.5-10. Surface Nusselt number for regularly-spaced swirl tube.

4.6 Conclusions and Suggestions

- Through simulation, both the heat-transfer coefficient and pressure drop increased with a reduction in the PD ratio of the swirl tubes.
- Although the PD6 'in-swirl' arrangement yielded the highest PEC value at a Reynolds number of 9,000, the overall performance was inferior to that of the circular pipe due to the decaying swirl effect.
- These PEC values can be further increased by reducing the length of the post-swirl circular pipe section.
- The field synergy principle demonstrated mechanism between the difference between the 'in-swirl' and 'ex-swirl' arrangements.
- The thermal enhancement benefit of swirl flow diminished rapidly after leaving the swirl tube outlet. As indicated by the local synergy angle, such enhancement effects dissipated 60–80 tube diameters downstream.
- The crossover arrangement has the largest temperature difference and energy efficiency among all.
- In the numerical results, although the PD4 crossover arrangement exhibited the highest thermal enhancement of 1.11 to 1.09 and pressure drop of 4.81 to 6.07 compared with the circular tube, its PEC value was lower than 1 due to the high-pressure drop.
- At low Reynolds numbers, the PD4 parallel tube exhibited the highest PEC value, ranging from 1.17 to 1. The PD6 decaying tube arrangement exhibited the highest PEC value from 1.04 to 1.03 at higher Reynolds numbers.
- It was observed that small-scale vortices formed within the swirl tube, particularly in the crossover arrangement, which enhanced the mixing and heat-transfer coefficients.
- The regularly spaced swirl tube exhibited a positive effect on the thermal performance, with the highest PEC value of 1.06 corresponding to Type 2 PD4.

The pros and cons of the methods proposed in the above section are listed. The regularly-spaced configuration is considered as the most feasible methods among all. This method can achieve thermal enhancement with modest pressure drop and can be applied to different heat exchanger by welding the circular tube and 4-lobed swirl tube together.

Table 4.6-1. Evaluation of the proposed thermal enhancement methods.

Proposed methods	Advantages	Disadvantages
Decaying configuration	Low-pressure drop Easy to manufacture	Limitation on post-swirl section, low thermal enhancement
Continuous configuration	Higher thermal enhancement	High pressure drop Complexity in geometry
Parallel configuration	Highest PEC value	High pressure drop Complexity in geometry
Crossover configuration	Higher thermal enhancement	Highest pressure drop Complexity in geometry
Regularly-spaced configuration	Modest pressure drop Compensate limitation on post-swirl section	Difficulty in manufacturing

The following aspects represent what could and should have been incorporated into the research:

- The length of the 4-lobed swirl tube was calculated on the basis that a single lobe underwent a 360-degree rotation. The length for difference PD ratio tubes was different, which introduced two parameters (length and PD ratio) on thermal enhancement evaluation. Therefore, instead of fixing rotation degree, the length should have been fixed.

- The fluid properties were assumed to be constant, which may not simulate the reality. Effect of temperature variation on fluid properties should be considered. Instead of using water, other fluid such as air should also be simulated.

- Only single phase flow was considered in the simulation. However, actual heat exchanger involved multiphase flow or phase change such as boiler. This should be considered.

- Though the regularly-spaced method has been proposed and regarded as the most feasible approach thus far, it remains uncertain whether the regularly-spaced 4-lobed swirl tube with a uniform PD ratio represents the combined optimum solution. The present research solely adopts the one-variable-at-a-time approach. In future investigations, a full-factorial research design can be implemented. This design will entail testing all possible combinations of variables, such as diverse swirl tube configurations and various PD ratios. By doing so, it will offer a more comprehensive understanding of the system. Consequently, it has the potential to guide the way towards a combined optimum approach that maximises thermal performance while minimizing pressure drop.

CHAPTER 5: EXPERIMENTAL INVESTIGATION OF THE 4-LOBED SWIRL TUBE

5.1 Introduction

This chapter presents an experimental investigation of the 4-lobed swirl tube. A double-pipe heat exchanger was constructed and a 4-lobed swirl tube with varying PD ratios were fabricated using 3D printing technology. The effect of altering the effective heating length on the heat transfer coefficient was examined to corroborate the simulation results.

5.2 Experimental Methods

5.2.1 Experimental Procedure

A schematic diagram of the experimental rig is shown in Figure 5.2-1. The apparatus comprises a double-pipe heat exchanger with hot and cold water circulation systems supplying hot and cold water to the outer and inner pipes of the heat exchanger, respectively. Flow meters, pressure transducers, and thermal sensors were integrated to measure the flow rate of hot and cold water, the pressure drops across the inner tube side, and the temperature variation along the shell and tube sides. Tap water was used as the fluid in both the tube and shell sides. Throughout the experiments, the ambient temperature was approximately 25°C. The hot water was heated to 65°C using a 10 kW heater and circulated through the shell side. The cold-water temperature was maintained at 23°C using a 10 kW cooler and flowed through the tube side. The flow rate of cold water was regulated to achieve the desired Reynolds number. The test section was enveloped with a layer of insulating material to minimise the heat loss to the surroundings.

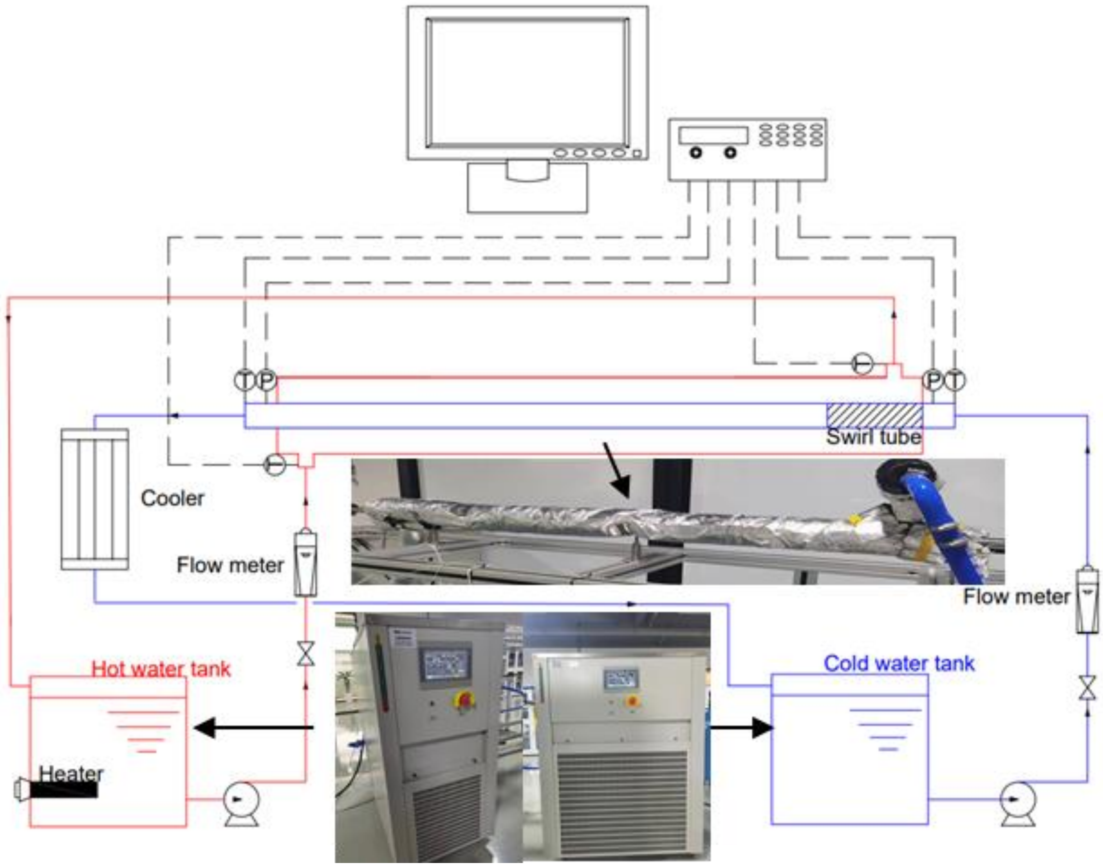

Figure 5.2-1. Schematic diagram of the experimental rig. (T for temperature sensor, P for pressure differential sensor).

To assess the effect of reducing the length of the post-swirl section, the effective length of the double-pipe heat exchanger could be reduced from 2.2m to 1.2m as shown in Figure 5.2-2. The inner tube comprised a 0.2 m circular tube or a 3D-printed swirl generator (0.2 m in length) with a 2 m or 1 m post-swirl circular section. The swirl section was connected via a compression joint to facilitate its easy replacement with a circular tube. The upstream and downstream tube sections were 1 m long and straight to enable full development of the flow boundary layer. The tube inner diameter is 0.02m and these devices were designed and constructed from scratch by the author.

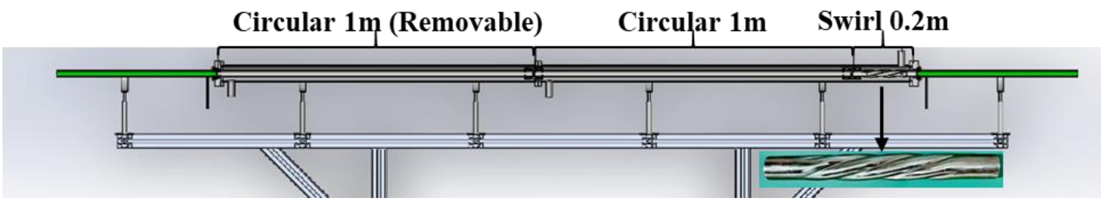

Figure 5.2-2. Pipeline illustration diagram.

A steady state for heat transfer and fluid flow was achieved when the variation in water temperature at the inlet/outlet of the tube/shell sides did not exceed 1% within 2 min and the variation in differential pressure did not exceed 4%. These variations in temperature and pressure were determined after 3 hours of experimentation. The following parameters were recorded: cold and hot water temperatures at the inlet and outlet of the tube and shell side, pressure difference across the entire length of the tube side, and flow rate of cold and hot water. The water temperatures were measured using four calibrated K-type thermocouples with an accuracy of ±0.5°C. The pressure difference was obtained using a differential pressure transducer, PMD55B, with an accuracy of 0.06%. The flow rates of the cold and hot water were measured using an electromagnetic flow meter with an accuracy of ±1%.

The temperature and pressure difference results were collected using a TC-08 data logger with a sampling rate of 20 records/min. In each experimental run, data were recorded when the temperature and pressure readings stabilised. Sampling was continued for 4 min and the final value was calculated as the average of the data collected over this period. The experiment was repeated eight times for both the circular pipe and swirl generator to minimise uncertainties. The maximum deviation for the overall heat transfer coefficient U and pressure difference Δp between each set was 3.5% and 2.6% respectively. Consequently, the experimental results were reproducible within uncertainty ranges. The deviation in the experimental results was primarily attributed to errors in the sensors, geometrical measurements, and heat balance.

5.2.2 4-lobed Swirl Tube Production

The picture of the 3D-printed swirl tubes is shown in Figure 5.2-3.

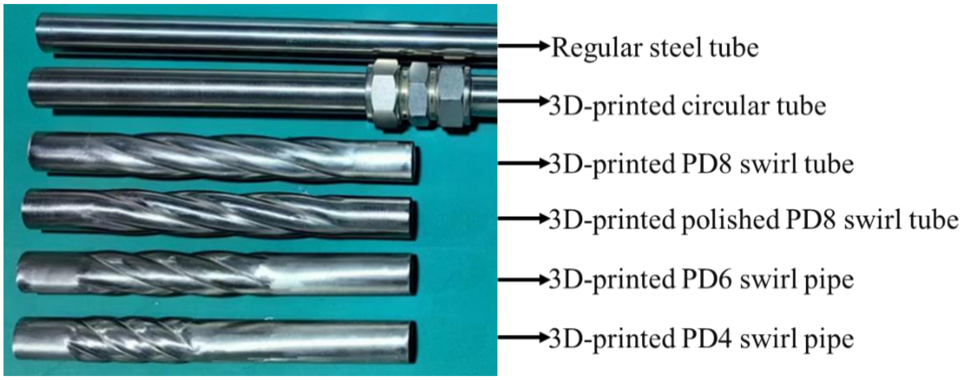

Figure 5.2-3. Schematic of the 3D-printed, swirl tubes.

In the experiments, a standard steel tube was utilised as a benchmark to validate the reliability of the experiment. A swirl tube with a different PD ratio was fabricated using a 3D printing method with steel powder by *Ningbo Allen 3D technology Co., LTD*. The 3D-printed pipe was connected to a steel pipe of identical diameter by using a compression joint to facilitate replacement. The initial length of the PD8 swirl section is $0.16m$ with both ends extended by $0.02m$ into the compression joint. The length of the 3D-printed tubes was consistent with the ease of replacement. Moreover, a 3D-printed circular tube of equivalent length to the swirl tube was also produced to study the effect of both 3D-printing and pipe connection methods. In addition, the average roughness, Ra, of the 3D-printed tube was approximately $12.3\mu m$. In comparison, the Ra for the regular steel tubes in the remaining pipeline is $0.8\mu m$. Therefore, an abrasive flow machining method was used to polish the 3D-printed PD8 swirl tube to achieve the same roughness as the steel tube. This process was conducted by *Suzhoubulaite, LTD*. However, such a polishing method reduces the pipe thickness from $1mm$ to $0.9mm$, which may influence the hydrothermal performance.

5.2.3 Uncertainty Analysis

The uncertainty calculation for an independent parameter φ can be calculated by the following equation (Uhía et al., 2013, Jafari et al., 2017b):

$$\delta\varphi = \sqrt{\sum_{i=1}^{n}(\frac{\delta\varphi}{\delta X_i}\delta X_i)^2} \tag{5.2-1}$$

Where δX_i is the uncertainty of the measured variables and $\delta\varphi$ is the uncertainty of the independent parameters.

For friction factor $f = \frac{\Delta P_i}{(L_i/d_i)(\rho_i u_i^2/2)}$, the uncertainty is calculated by:

$$\frac{\Delta f}{f} = [\left(\frac{\Delta(\Delta P_i)}{\Delta P_i}\right)^2 + \left(\frac{\Delta L_i}{L_i}\right)^2 + \left(\frac{5\Delta d_i}{d_i}\right)^2 + \left(\frac{2\Delta u_i}{u_i}\right)^2]^{1/2} \tag{5.2-2}$$

For overall heat transfer coefficient $U = \frac{Q_{av}}{A_s \Delta T_{LMTD}}$, the uncertainty is calculated by:

$$\frac{\Delta U}{U} = [\left(\frac{\Delta Q_{av}}{Q_{av}}\right)^2 + \left(\frac{\Delta A_s}{A_s}\right)^2 + \left(\frac{\Delta(\Delta T_{LMTD})}{\Delta T_{LMTD}}\right)^2]^{1/2} \tag{5.2-3}$$

The uncertainty of Q_{av}, ΔT_{LMTD} and Δu_i can be calculated with the same procedure. The calculated uncertainty for friction factor f and overall heat transfer coefficient U are 5.5% and 4.7%.

5.3 Results and Discussion

5.3.1 Validation of Experiment Results

A comparison between experimental results and the correlations is presented in Figure 5.3-1. The experiment is repeated 11 times and a two-tailed t-test is conducted. For a two-tailed t-test with a significance level $\alpha = 0.05$, the critical values from the t-distribution table $t_{\alpha/2,df} = 2.228$. Based on the calculation results, the maximum absolute t-test value for Sieder-Tate (2.5-1) and Gnielinski (2.5-2) are 1.6 and 0.48. The values for Petukhov (2.5-3) and Blasius (2.5-4) are 2.10 and 1.52. Therefore, since the maximum absolute t-test values for all the considered correlations are less than the critical value 2.228, it is considered that there is no significant difference between the population mean represented by the sample data and the given theoretical value. The detailed t-test results are shown in Appendix 1.6 Two-tailed t-test. The experimental data demonstrated a general consistency with the correlations. At the lowest Reynolds numbers, the pressure drop results showed relatively higher values compared to the heat transfer results from other correlations. This discrepancy in pressure drop is likely attributable to the connection methods employed.

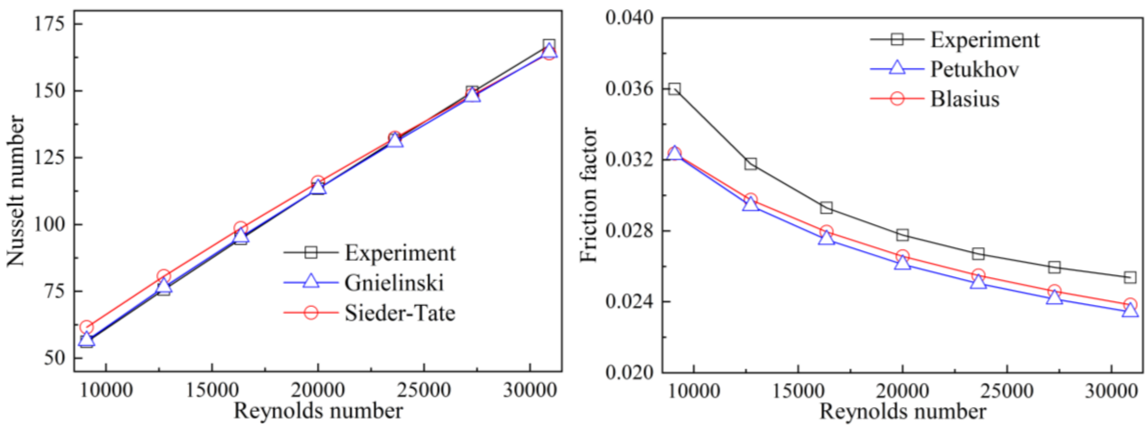

Figure 5.3-1. Comparison between experimental results and correlations for Nusselt number.

5.3.2 Validation of Numerical Results

A comparison of the numerical results with the experimental data for the polished and unpolished pipes for the Nusselt number is shown in Figure 5.3-2. The average deviations between the simulation and experimental results were 5.2% and 2.1% for the PD8 POLISHED and PD8, respectively. Notably, the discrepancy between the simulation and experimental results for the polished tube is greater than that for the unpolished tube. This polishing method also reduced the pipe thickness from $1mm$ to $0.9mm$. The reduction in tube thickness increases the heat transfer coefficient, which is not accounted for in the experimental procedure because the heat transfer coefficient on the shell side and the resistance on the wall are neglected. Given that the single-tube model was adopted during the simulation, the difference in the tube thickness was not incorporated.

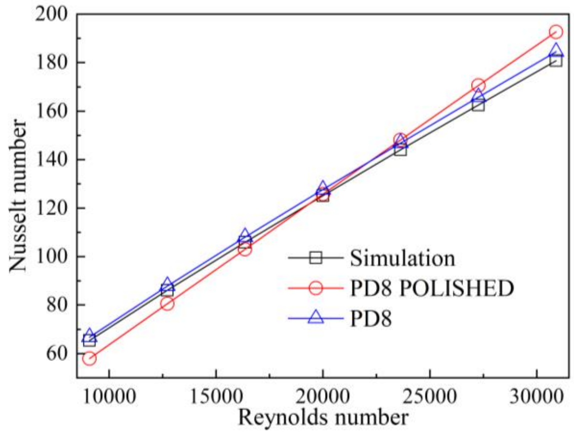

Figure 5.3-2. Comparison of numerical results with experimental data for the Nusselt number.

A comparison of the numerical results with the experimental data for the polished and unpolished pipes in terms of the friction factor is shown in Figure 5.3-3. The average deviations between the simulation and experimental results for the PD8 POLISHED swirl tube are 3.5% and 3.4% for PD8 POLISHED and PD8, respectively. The discrepancy between the simulation and experimental results for the polished tube is comparable to that of the unpolished tube. The minor variation in the pipe thickness may generate flow resistance in the connecting region.

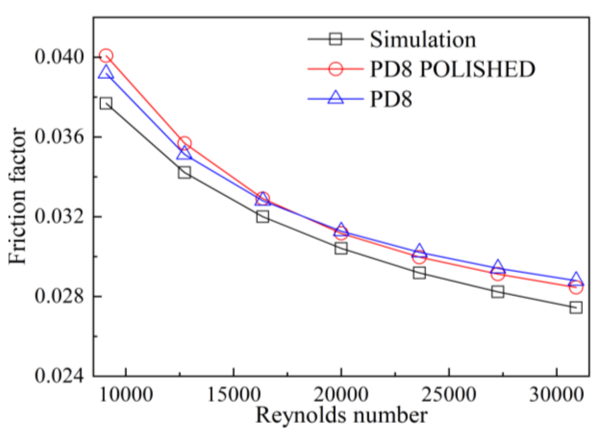

Figure 5.3-3. Comparison of numerical results with experimental data for the friction factor.

Although the surface polishing method did not mitigate the discrepancy between the simulation and experiment, the results obtained from the simulation demonstrated general concordance with the experimental findings. Therefore, to perform a more comprehensive evaluation, a numerical simulation was conducted without considering the roughness condition.

5.3.3 Effect of Different Tube Length

This study examined the impact of reducing the length of the post-swirl circular pipe section on heat transfer. The investigation used a 3D-printed PD8 swirl tube.

Figure 5.3-4 presents the temperature difference between two different tube lengths. By reducing the tube length form 2.2m to 1.2m, the temperature difference between the swirl tube inlet and outlet (ΔT_{swirl}) reduces around 2^{o}. However, the temperature difference between the circular and swirl arrangements increases (ΔT_{swirl}-$\Delta T_{circular}$). These suggest that though the amount of energy transfer decreases when reducing the tube length, the thermal enhancement effect created by the swirl tube becomes more significant.

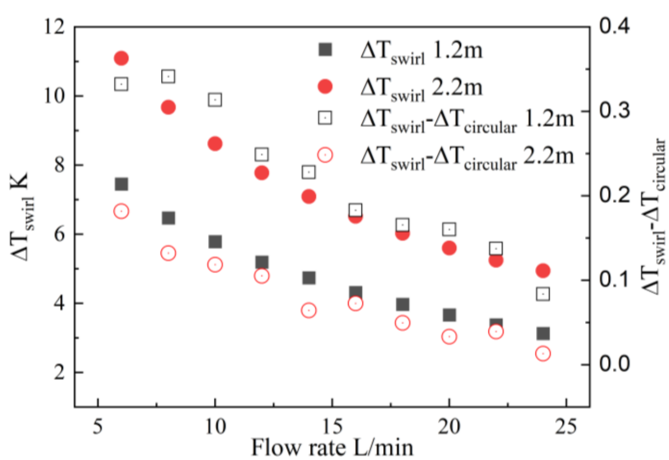

Figure 5.3-4. Temperature difference for different tube length.

Figure 5.3-5illustrates the Nusselt number ratios for swirl generators with varying lengths of post-swirl circular pipe sections. The Nu ratio was higher at around 1.09 for the 1.2m pipe length whereas it was around 1.06 for the 2.2m long section. Therefore, both arrangements increased the thermal performance in comparison to a circular tube.

Although a slight increasing trend was observed for both arrangements, the ratio of Nu_s/Nu_c did not increase significantly over the Reynolds number range examined as the Nu_s/Nu_c for effective lengths 1.2m and 2.2m were 1.085-1.092 and 1.057-1.060, respectively. Moreover, a shorter post-swirl circular section (ie, 1.2m) demonstrated superior thermal enhancement in comparison to the longer 2.2m section.

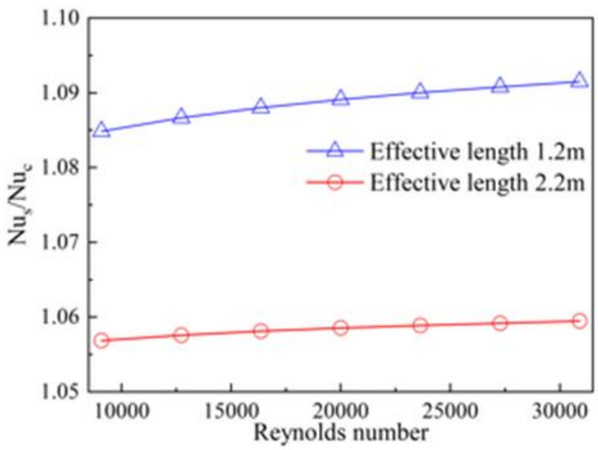

Figure 5.3-5. Performance comparison of two effective tube lengths of 1.2m and 2.2m in terms of Nusselt number.

The friction factor for the swirl generators with different post-swirl circular pipe lengths is shown in Figure 5.3-6. The average f_s/f_c values for the 1.2m and 2.2m tube lengths were 1.13 and 1.09, respectively. Consistent with the results for Nu, reducing the post-swirl circular tube length increased the pumping power, as the shorter length resulted in a higher degree of turbulence in the flow region. Notably, the highest f_s/f_c value was approximately 1.16, which is considerably lower than most of the results for twisted tape (1.85) (Liu and Sakr, 2013).

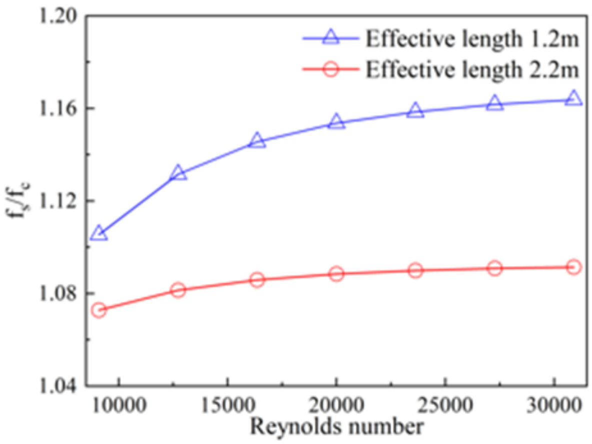

Figure 5.3-6. Performance comparison of two effective tube lengths of 1.2m and 2.2m in terms of Friction factor.

The PEC factor (the ratio of the energy recovered due to heat transfer to the energy consumed due to a higher pressure drop) with different Reynolds numbers is presented in Figure 5.3-7. The average PEC values for the two tube lengths of 1.2m and 2.2m were 1.044 and 1.031, respectively. The PEC values for both arrangements exceeded 1, indicating superior performance compared with that of a circular tube. Increasing the surface roughness of the tube can enhance the overall performance of the heat exchanger. The PEC value also increased upon reduction of the post-swirl tube length, lending support to the concept of the strategic placement of swirl tubes within a system.

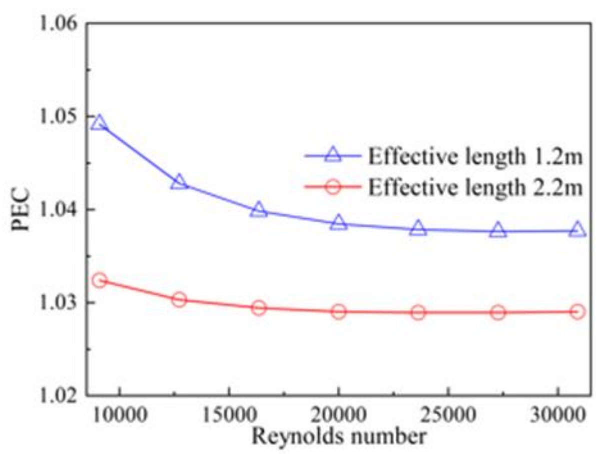

Figure 5.3-7. Performance comparison of two effective tube lengths of 1.2m and 2.2m in terms of PEC.

5.3.4 Effect of PD Ratio

The temperature difference ΔT between various tubes is shown in Figure 5.3-8. Similar to numerical results, a lower PD ratio leads to a higher temperature difference, suggesting a higher thermal efficiency. However, this high thermal efficiency decreases as the flow rate increases. Moreover, the 3D-printed tube exhibits a larger ΔT than the steel tube. This indicates the thermal enhancement effect created by the surface roughness.

Interestingly, the temperature difference for the polished PD8 tube is initially lower than that of the un-polished one. As the flow rate increases, its ΔT surpasses that of the un-polished one. In the previous section, it was demonstrated that the tube-polishing method will reduce both surface roughness and the tube thickness. At lower flow rates, the turbulence is less significant than at higher flow rates. Therefore, the disruption of the thermal boundary layer caused by the surface roughness becomes dominant, so that the ΔT for the polished one is initially lower than that of the un-polished one. As the flow rate increases, the turbulence becomes fully developed, and the effect of the surface roughness is not that significant while a thinner tube thickness promotes more effective heat transfer. As a result, the ΔT for the polished one becomes larger than that of the un-polished one.

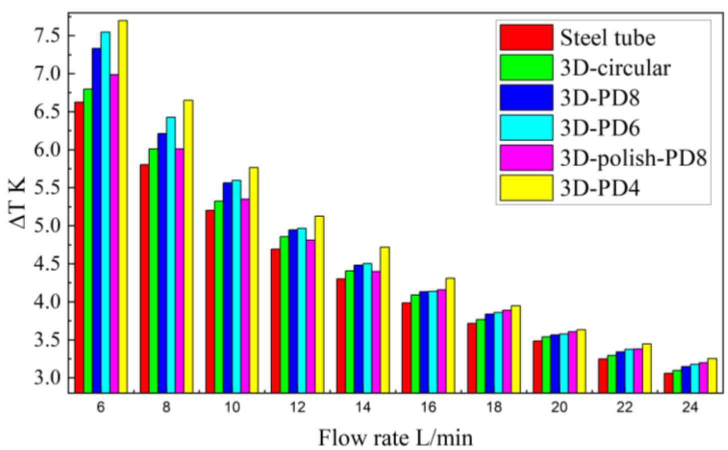

Figure 5.3-8. Temperature difference for various tubes.

Since the effective length 1.2m demonstrates better performance than that of 2.2m, the 1.2m is utilised in further investigations. The experimental results of the Nusselt number ratio for different 3D-printed tubes are shown in Figure 5.3-9. A standard steel tube served as the benchmark for these comparisons. The PD4 swirl tube exhibited the highest Nu ratio across all Reynolds numbers. Notably, the circular tube, which shows a Nu ratio exceeding 1, indicates that the 3D-printed approach and the connecting method enhance heat transfer coefficient relative to the baseline. For the 3D-printed tubes, experimental results reveal that the Nu ratio decreases with increasing Reynolds numbers and PD ratios. In contrast, the Nu ratio of the PD8 polished and circular tubes shows a different pattern, they increase with increasing Reynolds number. Moreover, the Nu ratio of the PD8 polished tube surpasses those of PD8 and PD6 at Reynolds numbers of approximately 20,000. This discrepancy in the PD8 polished tube results is likely attributable to the reduction in tube thickness, as previously noted. Within the investigated Re range, the Nu ratio of the PD4 tube decreases slightly from 1.19 to 1.18, while the circular tube's Nu ratio ranges from 1.01 to 1.06, reflecting its baseline heat transfer performance

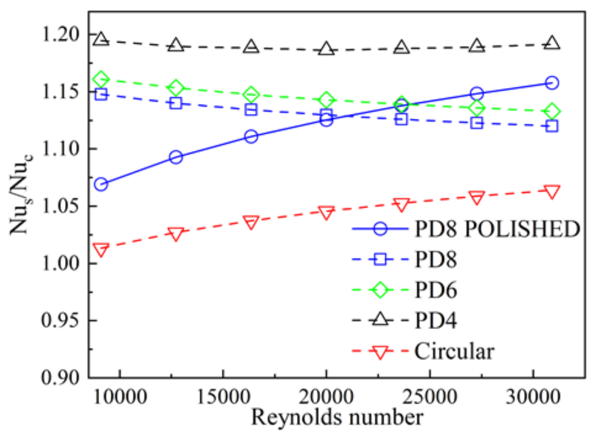

Figure 5.3-9. Experimental results of the Nusselt number ratio for different 3D-printed tubes.

The experimental results of the friction factor ratio for different 3D-printed tubes are shown in Figure 5.3-10. The f ratio for the PD4 tube remained the highest of all tubes, analogous to the Nu ratio. Moreover, the circular tube exhibited a f ratio exceeding 1 due to the surface roughness caused by the 3D-printed method. The f ratio for all tubes demonstrated a tendency to increase with higher Reynolds numbers and a lower PD ratio. Potentially due to the slight difference in pipe thickness, which generates flow resistance in the connecting region, the f ratio for the PD8 polished tube is lower than the unpolished one at higher

Reynolds numbers. However, the f ratio for the PD8 polished tube exceeds that of the PD8 unpolished tube, potentially because of the slight difference in pipe thickness (resulting from polishing), which generates flow resistance, particularly in the connecting region. Future research may consider printing a thicker 4-lobed swirl tube, for instance, with a thickness of around 1.2mm, such that the polished tube would have a thickness of approximately 1mm. The f ratio ranges from 1.23 to 1.29 for the PD4 tube and from 1.08 to 1.14 for the circular tube within the investigated Reynolds numbers.

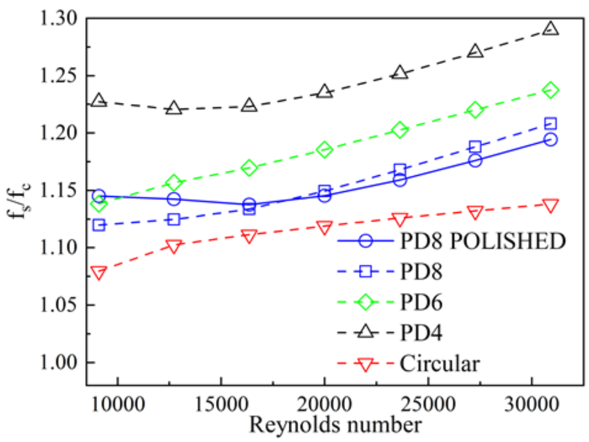

Figure 5.3-10. Experimental results of friction factor ratios for different 3D-printed tubes.

The experimental results obtained through the PEC for different 3D-printed tubes are shown in Figure 5.3-11. The highest PEC value for the decaying arrangement was PD6. Similarly, PD8 exhibited the lowest PEC values in both figures. The rationale for this discrepancy was examined further and the PEC values for all PD ratios of the 3-D printed tubes decreased with increasing Reynolds number, except for the polished specimen. Notably, the PEC value for the circular tube is approximately 1, indicating that the overall influence of the surface roughness and connecting method on the heat exchanger performance is minimal. Further research may consider welding a 3D-printed tube into a regular steel tube to further mitigate this influence. Moreover, the trend for PD8 POLISHED demonstrates an increase with a higher Reynolds number, which differs from the trend observed for the unpolished 3D-printed tubes. This increase in the PEC value may be attributed to the reduction in tube thickness resulting from surface polishing. This disparity will be addressed in subsequent investigations. In general, the PEC values range from 1.12 to 1.09 for the PD4 tube and from 0.99 to 1.02 for the circular tube.

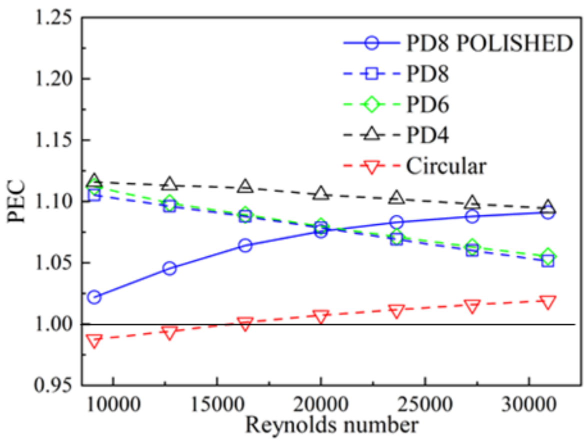

Figure 5.3-11. Experimental results of PEC for different 3D-printed tubes.

5.4 Conclusions and Suggestions

- Experimental results for circular pipes were validated against correlations, and the average difference was 5.3% for Nu and 2.5% for f.
- The temperature difference between each configuration is shown.
- The discrepancy between numerical results and experimental results was 6.1% for Nu and 3.7% for f attributed to increased surface roughness in simulation settings.
- The swirl generator enhanced the overall performance of the heat exchanger. The PD4 decaying swirl tube exhibited the highest PEC value from 1.12 to 1.09 across all configurations, indicating its superior performance in balancing heat transfer enhancement and pressure drop penalty. This outcome differed from the numerical results and might have been attributable to the difference in surface roughness caused by the 3D printing method.
- The 3D-printing method itself increased both thermal enhancement and pressure drop, but its PEC value remains approximately 1, suggesting that although it improves heat transfer to some extent, the increase in pressure drop offsets the benefits to a certain degree, resulting in a marginal overall performance improvement.

- Due to the reduction in wall thickness, the polished tube demonstrated a larger average deviation in the numerical results compared with the unpolished one.

The following aspects represent what could and should have been incorporated into the research:

- Only the decaying swirl flow was investigated in the experimental section. Other configurations such as crossover and regularly-spaced swirl tube should be attempted.
- Different tube inner diameters should be attempted.
- Instead of using the compression joint to connect the tube, the welding method should be attempted to avoid the pressure loss caused by the joint.

CHAPTER 6: INVESTIGATIONS OF SWIRL TUBE IN SOLAR WATER HEATER

6.1 Introduction

Globally, solar thermal energy is a significant source of renewable energy. According to Weiss and Spörk-Dür (2023), projections indicate that by the end of 2022, water solar thermal systems would attain a capacity of 542 GW. This capacity is equivalent to an annual energy saving of 47.48 million tons of oil equivalent. Among the various solar collector designs, flat plate solar collectors (FPSC) and evacuated tube solar collectors (ETCs) are recognised for their simplicity and efficiency. In particular, evacuated tube collectors offer several advantages over flat plate collectors. Notably, they can achieve higher temperatures and demonstrate greater thermal efficiency(Al-Mamun et al., 2023, Sabiha et al., 2015). This has resulted in their predominance in the solar water heater market, with ETCs accounting for 71.7% of solar collector installations in China by 2021 (Weiss and Spörk-Dür, 2023).

As the market for solar water heaters expands, there is an increasing demand for superior solar products. Chopra et al. (2018) analyzed a range of solar collector models, finding that evacuated tube collectors (ETCs) outperform others in efficiency for low to medium-temperature uses. Tabarhoseini et al. (2022) conducted a comprehensive comparison of ETCs and flat plate collectors (FPCs), highlighting ETCs' distinct advantages. Recent studies by Singh and Vardhan (2021) delved into the thermal dynamics of ETCs with helical coiled inserts, revealing that despite a 2.45-fold increase in pressure drop, these ETCs exhibited a thermal efficiency 5.5% higher than their standard counterparts. Gunasekaran et al. (2021) explored the impact of integrating twisted tape inserts within evacuated tubes, noting a 6.8% boost in daily efficiency with a twist ratio of two. O'Neil and Sobhansarbandi (2022) compared the performance of U-pipe and heat pipe ETCs, finding the former to be 13% more efficient. They posited that incorporating MWCNT nanoparticles could further enhance thermal performance. Hemmatian et al. (2024)

evaluated pulsating heat pipe ETCs with phase change materials, achieving a remarkable 42.9% increase in thermal efficiency over traditional models. Zhang et al. (2024) experimented with multi-channel flat tubes in finned ETCs. The experiment achieved an average heat transfer rate of 78.2%, which surpassed that of non-finned versions.

In addition to the above-mentioned improvements to the performance of ETCs, researchers have also explored other methods to enhance thermal efficiency, such as incorporating swirl devices (Seibold et al., 2022). Such a device can induce additional axial recirculation, thereby augmenting mixing and heat transfer (Sheikholeslami et al., 2015). Twisted tapes, for instance, have been effectively utilised in solar water heaters (SWH) to boost their performance (Sadhishkumar and Balusamy, 2014, Jaisankar et al., 2011). Saravanan and Jaisankar (2019) observed an 8.4% improvement in heat transfer rate with the use of v-cut twisted tapes at a ratio of 3, in contrast to a flat plate solar heater. The friction factor also increased by 59.6% when compared with a standard tube. Sundar et al. (2020) examined the impact of Al_2O_3 nanofluid and wire coils. By employing wire coils and a 0.3% nanofluid concentration, they achieved a 64.2% increase in collector efficiency over traditional flat plate collectors. Additionally, they projected a potential reduction in collector costs by 39.3%. Farshad and Sheikholeslami (2019) conducted a numerical study on the heat transfer characteristics of nanofluid in a solar heater with multi-channel twisted tape inserts. Their exergy analysis revealed an enhanced heat transfer rate with an increase in the twist ratio. These results demonstrate the effectiveness of twisted tape inserts in solar water heating (SWH) systems.

Although full-length twisted tapes can significantly increase pressure drop, often by more than 185%, they are also susceptible to fouling issues (Liu and Sakr, 2013). To address this, Wang et al. (2011) introduced regularly spaced, short-length twisted tapes, achieving a notable thermal enhancement factor of 1.079 at a Reynolds number of approximately 10,000. Additionally, the effectiveness of swirl devices like lobed tubes has been explored. Tang et al. (2015) conducted experiments to assess the thermal efficiency of 2-lobed versus 3-lobed pipes. When compared to round pipes, the flow resistance for 2-lobed and 3-lobed swirl tubes increased by factors of 1.08-1.16 and 1.15-1.22, respectively. Notably, the 3-lobed design achieved an overall thermal efficiency that was 5.8% higher than its 2-lobed counterpart. Furthermore, Jafari et al. (2017a) installed a 3-lobed swirl generator at the entrance to a heat exchanger, increasing the flow resistance ratio of between 1.19 and 1.45, and enhancement in overall thermal efficiency ranging from 1.25 to 1.55.

In summary, although twisted tapes can enhance the thermal performance of SWHs, they also tend to increase the pressure drop and are prone to fouling. Given that the 4-lobed swirl tube can also enhance thermal performance and possess fouling cleaning capabilities, the SWH presents a potentially suitable application scenario for the lobed tube. Therefore, the objective of this chapter is to apply 4-lobed swirl generators to enhance the heat transfer coefficient of the SWH while minimising friction loss and to provide guidelines for SWH design. Furthermore, swirl generators and twisted tapes were periodically installed within the SWH to improve thermal efficiency. The thermal performance was evaluated by calculating the Nusselt number, friction factor, and PEC value, and the mechanism was investigated using the field synergy principle. In addition, two ETC setups were procured from commercial suppliers to address this research gap. These rigs were equipped with a copper swirl tube that was fabricated using 3D printing technology. One ETC was modified to include a welded, regularly spaced 4-lobed swirl tube, while the other was fitted with a 3D-printed circular tube for comparative purposes. Throughout the experiment, the inlet and outlet temperatures of the SWH and temperature in the water tank were closely monitored. The thermal performance and pressure losses of both the ETC configurations were thoroughly assessed.

6.2 Simulation Arrangement and Model

Given that the objective of this research is to establish guidelines for the experimental design of the SWH, the geometry of the SWH is simplified to only a single heating tube and absorption plate as given in Figure 6.2-1. Similar simplification can also be seen in Farshad and Sheikholeslami (2019) and Fattahi (2021). The absorption pipes consist of regular circular tubes, tubes with short-length twisted tapes, and 4-lobed swirl tubes, respectively. The geometrical shape of the 4-lobed swirl tube is the same as proposed by Li et al. (2015) while the shape of the twisted tape with a twisted ratio of 5 is constructed as described by Eiamsa-ard and Seemawute (2012). This design simplifies the SWH to isolate the impact of different absorption pipe geometries on its performance. The data from the plain circular tube will be used as a baseline to compare the performance improvements or changes brought about by the tubes with short-length twisted tapes and 4-lobed swirl tubes.

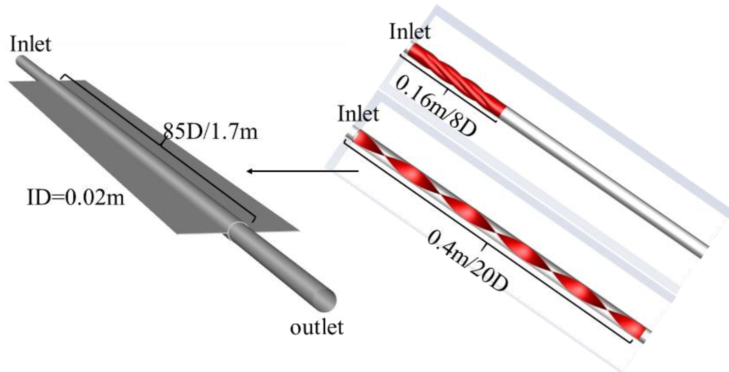

Figure 6.2-1.SHW geometry.

The detailed description for the twisted tape and the swirl tube is shown below:

Table 6.2-1. Detailed description for twisted tape and swirl tube.

Parameter	Twisted tape	Swirl tube
Length	0.4m/20D	0.16m/8D
Specific details	Twisted ratio: 5	Pitch to diameter ratio: 8
	Tape width: 19.5mm	Tube inner diameter: 20mm
	Tape length: 0.8mm	

The effective heat transfer area had a length of 1.7 m, and the inner tube diameter was 0.02 m. To ensure the full development of the flow boundary layer, the inner tube was extended by 0.5 m at both ends. The absorption plate was made of aluminium, and the tube was made of copper. To simulate solar radiation, a continuous solar heat flux of 900 W/m² was applied uniformly to the upper section of the tube and the absorption plates. Adiabatic conditions were set for the bottom and the extended tubes. The water inlet temperature was 293 K, and the inlet velocity ranged from 0.3 m/s to 0.8 m/s. The outlet was configured as a pressure outlet. Water served as the working fluid. Given the relatively small temperature difference (the temperature difference between the inlet and outlet was within 20 K) between the inlet and outlet, the properties of water were assumed to be constant (Tang et al., 2015) due to the small-temperature difference between the inlet and outlet. Table 6.2-2 lists the properties of water, aluminium, and copper.

Table 6.2-2. Material properties.

Material	Density [kg/m^3]	Specific Heat [J/(kg · K)]	Thermal Conductivity [W/(m · K)]	Viscosity [kg/(m · s)]
water	998.2	4182	0.6	0.001
aluminium	2719	871	202.4	-
Copper	8978	381	387.6	-

Table 6.2-3. Geometrical parameters.

geometry	Value [m]
Tube length	2.7m (1.7m+0.5m+0.5m)
Tube diameter	0.02m
Tube and plate thickness	0.001m
Plate width	0.04m

6.3 Mesh Test and Validation

The simulation was conducted using ANSYS FLUENT 2021 R1. A polyhedral mesh is generated by Fluent meshing, as shown in Figure 6.2-2. The following assumptions are made to simplify the simulation: (a) the flow is in a turbulent state, (b) the flow is steady and incompressible, (c) radiation is neglected in the simulation, (d) water properties are assumed to be constant. The SST k-ω model is selected as the turbulence model due to its high accuracy among other models in swirl calculations (Tang et al., 2015). The wall y^+ is approximately 1 for all Reynolds numbers investigated. For pressure-velocity coupling, the SIMPLEC scheme was selected (Zeng and Tao, 2003), while other methods remained as default. The criteria for continuity and energy equations were at 10^{-5} and 10^{-7}. During the calculation, the total outlet pressure and static temperature were used to judge convergence.

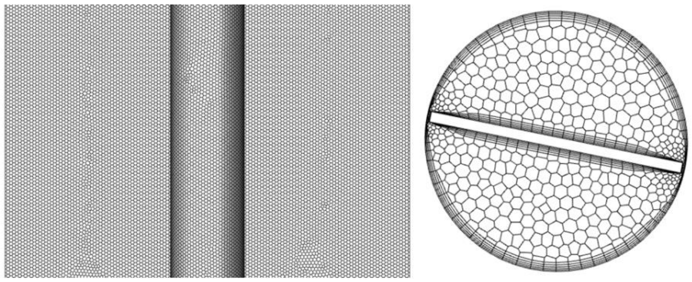

Figure 6.2-2. Mesh overview of the solar water heater inserted with twisted tape.

The mesh density was tested to eliminate errors caused by mesh quantity. Table 6.2-4 shows various mesh densities and their Nu and f results. By increasing the number of cells, both Nu and f converge to a certain value. The dense mesh is used to conduct additional simulations.

Table 6.2-4. Mesh independence test at Re = 7960.

Mesh density	Cell quantity	Nu	f
Coarse	1,176,087	74.9	0.0329
Less dense	2,342,231	72.3	0.0331
Dense	3,508,375	71.9	0.0333
Very dense	4,674,519	71.8	0.0333

The heat flux boundary condition was validated against the experimental results (Eiamsa-ard and Seemawute, 2012) to ensure the reliability of the simulation model. The validation geometry is shown in Figure 6.2-3. To validate the heat flux boundary condition, a specific geometric model was adopted. A single tube with a short-length twisted tape at a twisted ratio of 5 was positioned within a circular tube, as this ratio demonstrated superior thermal performance with a moderate pressure drop compared to full-length twisted tapes. The thermal boundary condition comprised a uniform heat flux in the 50D zone after the twisted tape. The effective length L, was 75D. Both anterior and posterior sections were extended by 0.5m to ensure that the fluid field was fully developed.

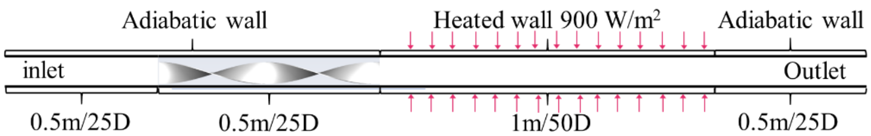

Figure 6.2-3. Condition for verification.

The comparison with experimental results is shown in Figure 6.2-4. The numerical results of the Nusselt number and friction factor were in general agreement with the experimental results. The maximum deviations in the Nusselt number and friction factor were 8.7% and 6.1%, respectively, when the Reynolds number was 5200. The numerical results obtained from the simulations were deemed to be reliable. To enhance the accuracy of the results, further investigations were conducted using Reynolds numbers ranging from 5,970 to 15,920.

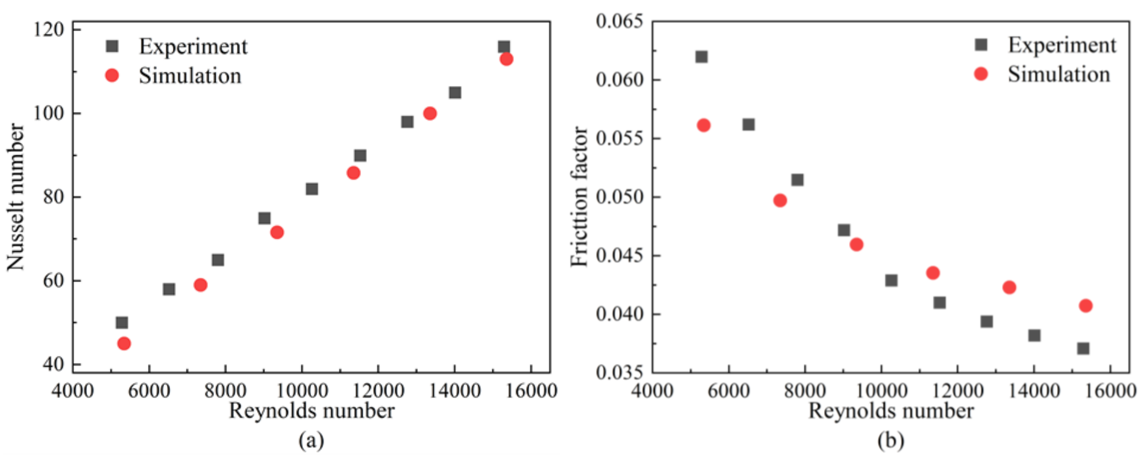

Figure 6.2-4. Comparison with experimental results (a) Validation of Nusselt number. (b) Validation of friction factor (Eiamsa-ard and Seemawute, 2012).

6.4 Numerical Results

6.4.1 SWH Performance

The Nusselt number for different devices is given in Figure 6.4-1. When compared to a circular tube, the insertion of both swirl generators and the presence of a twisted tape within the tube enhanced the heat transfer rate. On average, the Nusselt number for the swirl tube was 2% higher than that of the circular tube. Meanwhile, the Nu for the tube with a twisted tape insertion was 11% higher than that of the circular pipe. This indicates that the twisted tape generates greater turbulence and heat transfer enhancements within the flow compared with swirl generators. This can likely be ascribed to the difference in the effective length of the two devices in contact with the fluid. The twisted tape, with its longer interaction length with the flow, promotes stronger mixing and heat transfer.

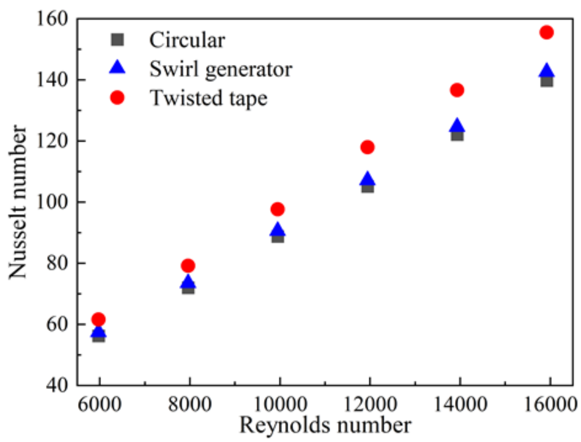

Figure 6.4-1. Comparison of Nusselt number between the twisted tape and swirl generator.

The friction factor for the twisted tape and swirl tube is shown in Figure 6.4-2. Similar to the Nusselt number results, the insertion of both devices led to increased pumping power consumption when compared to the case of a circular tube. On average, the friction factor for the swirl generator increased by 7% and that for the twisted tape increased by 65% relative to the circular configuration. The twisted tape exhibited significantly higher flow resistance compared to the swirl generator. This is because the twisted tape obstructs the fluid movement.

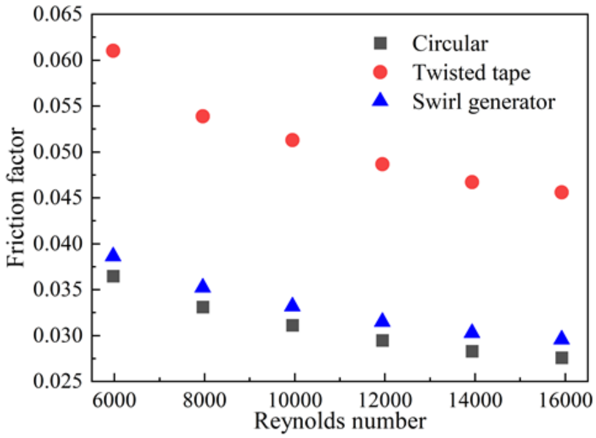

Figure 6.4-2. Comparison of friction factor between twisted tape and swirl generator.

The PEC values for the twisted tape and the swirl tube are shown in Figure 6.4-3. Due to the significant friction loss associated with the twisted tape, the PEC factor of the swirl generator was notably higher than that of the twisted tape. However, within the investigated range of Reynolds numbers, the PEC values of the swirl generators were only slightly greater than 1. This implies that the overall enhancement achieved by the swirl generators was minimal. Therefore, it is necessary to explore alternative modifications, such as regularly-spaced swirl devices, to achieve more substantial thermal enhancement.

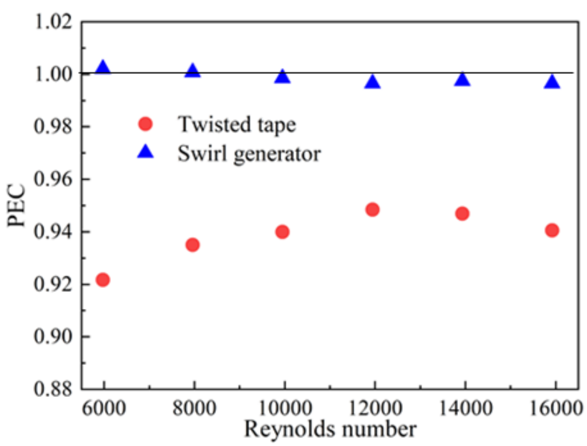

Figure 6.4-3. Comparison of PEC value between the twisted tape and swirl generator.

6.4.2 Flow Behaviour Analysis

The velocity streamline and the turbulence kinetic energy at different locations are shown in Figure 6.4-4. By inserting the swirl tube, a swirl flow is generated, and the highest velocity is observed at the core region within the swirl tube. Similarly, the region with the highest turbulence kinetic energy is also located within the swirl tube, near the centres of the 4-lobed structure. Four regions with the highest turbulence kinetic energy can be observed 10D downstream of the swirl tube exit, which is related to the flow characteristics generated by the swirl tube. Although the velocity streamlines continue to rotate, the turbulence kinetic energy decreases significantly immediately after the exit of the swirl tube. It attains a relatively stable state 20D downstream of the exit.

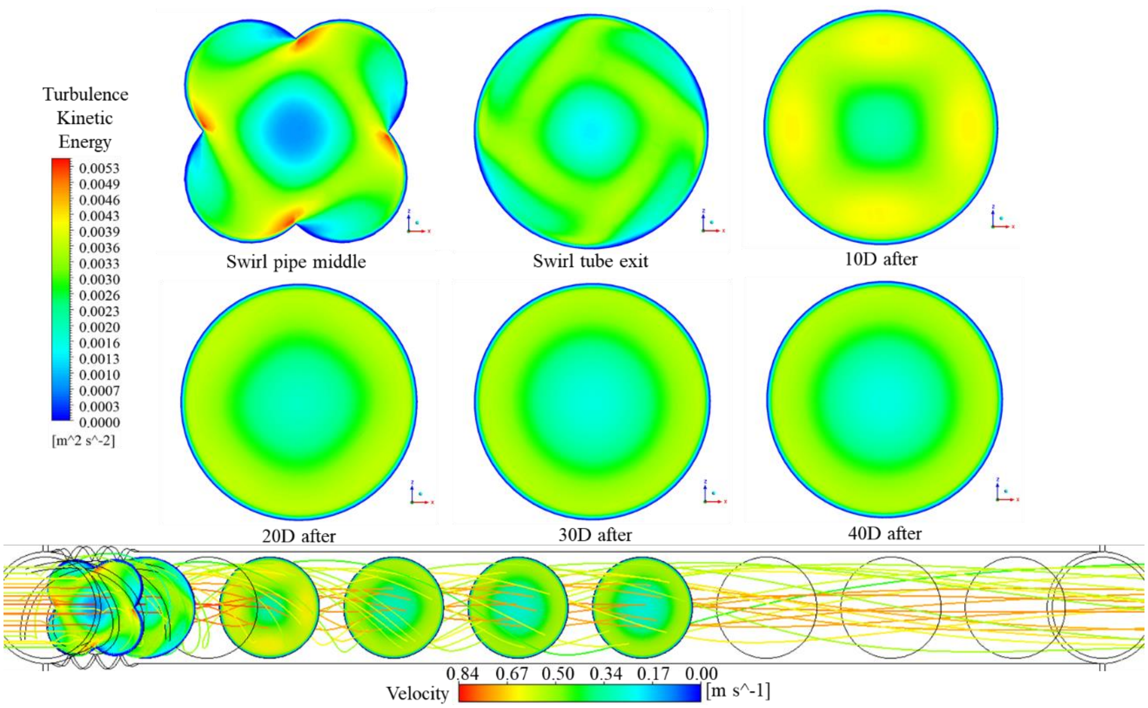

Figure 6.4-4. Velocity streamline and Turbulence Kinetic energy at different locations of the swirl tube.

The velocity streamlines and the turbulence kinetic energy at different locations are shown in Figure 6.4-5. Similar to the observation in the swirl tube, the highest velocity was recorded near the twisted tape. Quantitatively, the magnitude of the velocity near the twisted tape exceeded that near the swirl tube. In contrast to swirl tubes, the highest turbulence kinetic energy was observed in the near-wall region. The turbulence kinetic energy diminishes after the fluid passes the section with the twisted tape because the flow-disrupting effect of the twisted tape is no longer present. The kinetic energy contour stabilises at 40D thereafter, indicating the cessation of the swirl effect, as illustrated in the velocity streamline. The velocity streamlines show a more uniform pattern, consistent with the reduced turbulence kinetic energy, suggesting that the influence of the twisted tape on the flow has dissipated.

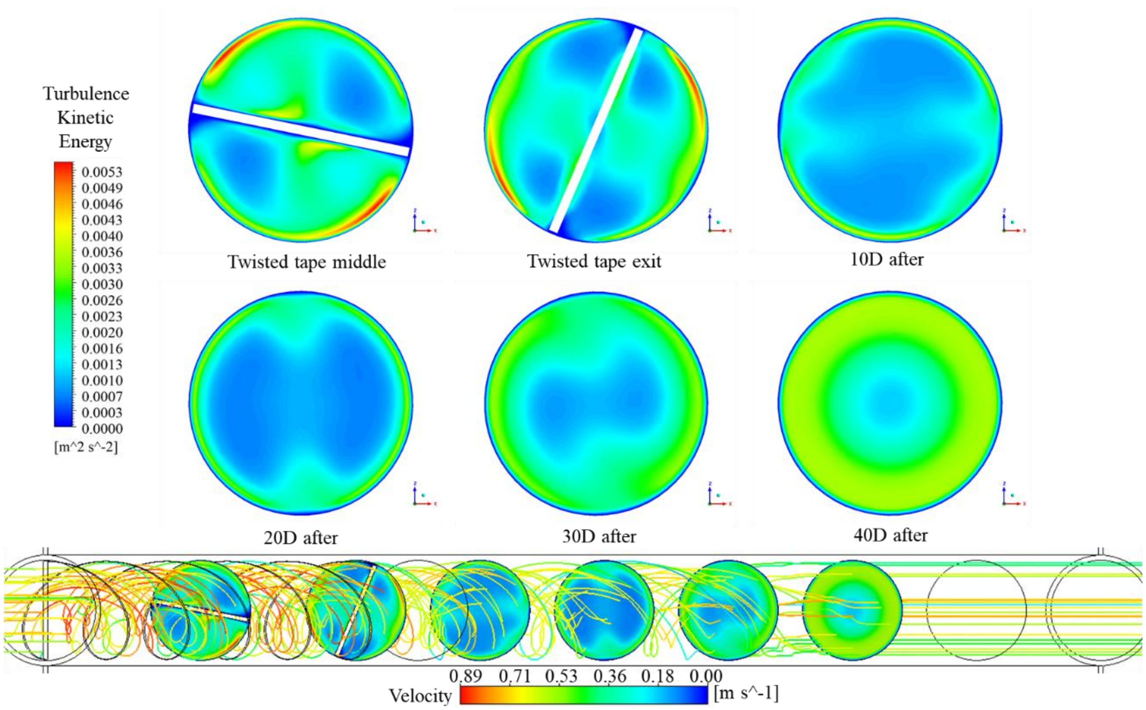

Figure 6.4-5. Velocity streamlines and turbulence kinetic energy at different locations of the Twisted tape.

The cross-sectional view of the temperature isotherm line and the velocity vector is shown in Figure 6.4-6. The tangential velocity vector is normalised to illustrate the fluid field. When a twisted tape is inserted, both the velocity vector and the temperature isotherm line are redistributed along the twist direction of the tape. Furthermore, four distinct vortices that redistribute the temperature and velocity fields were observed in the swirl generator. Additionally, the figure for the twisted tape exhibits a greater number of isotherm lines from the wall to the centre region compared with that of the swirl generator, with the latter's isotherm lines concentrated mainly in the 4-lobed centres. This demonstrates that the disruption caused by the twisted tape to the thermal boundary is more substantial than that of the swirl generator, resulting in a higher heat transfer coefficient.

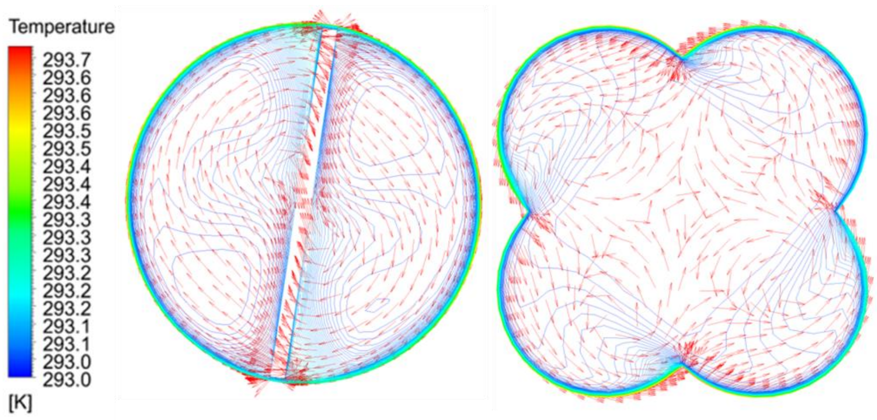

Figure 6.4-6. Velocity vector and isotherm line for two devices at Reynolds number 11940.

The local synergy angle downstream of the two devices is shown in Figure 6.4-7. The local synergy angle of the twisted tape is consistently smaller than that of the swirl tube throughout the tube region. This indicates that the flow with the twisted tape exhibits superior thermal enhancement performance compared to the flow with the swirl generator, which explains the higher Nusselt number observed for the twisted tape in Figure 6.4-1. However, the heat transfer coefficient enhanced by these two devices rapidly diminishes downstream. As both angles increase significantly and stabilise after 50D, further supporting the proposition of regularly positioning a swirl generator. With an extended circular tube and the swirl-decaying effect, the final synergy angle value is expected to be equivalent at the distal end.

Furthermore, the correlations (4.3-1) between the local synergy angle and distance downstream are also fitted. As can be seen, the R^2 values for both were approximately 0.98. As previously noted, the final synergy angle values for both devices should be identical. However, the correlation fails to accurately represent this because the maximum value for the twisted tape is lower than that of the swirl tube. A longer downstream distance might be essential for more accurate correlations. Moreover, the applicability of this correlation to describe the synergy angle variations in swirl-decaying flows generated by other thermal enhancement devices needs further investigation. Also, subsequent research is needed to clarify the significance of these constants in the correlations and their relationship with other factors, such as velocity.

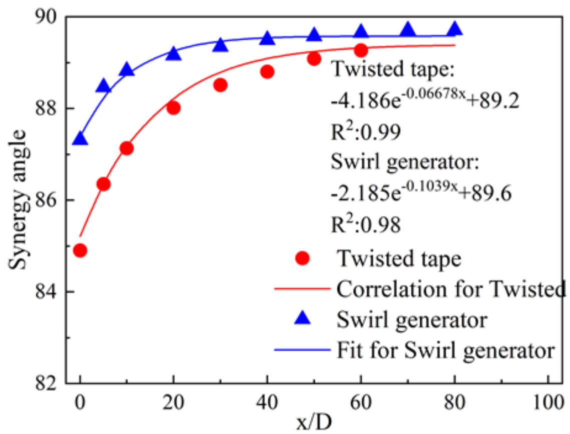

Figure 6.4-7. Synergy angle variations and correlations for two devices at Reynolds number 11940.

6.4.3 Thermal Performance of Regularly Spaced Devices

Regularly spaced configurations for both twisted tapes and swirl generators have been proposed. Both devices were spaced regularly within the 85D absorption pipe. For the twisted tape, the twist ratio remains at 5 while the length of each tape is reduced to 0.16m to maintain consistency with the swirl generators. For the swirl generators, the geometrical conditions were identical to those of the previous configuration. Eight arrangements were constructed. The number of installed swirl devices is increased from 1 to 4, and these devices are equidistantly positioned along the tube region. The arrangements are illustrated in Figure 6.4-8.

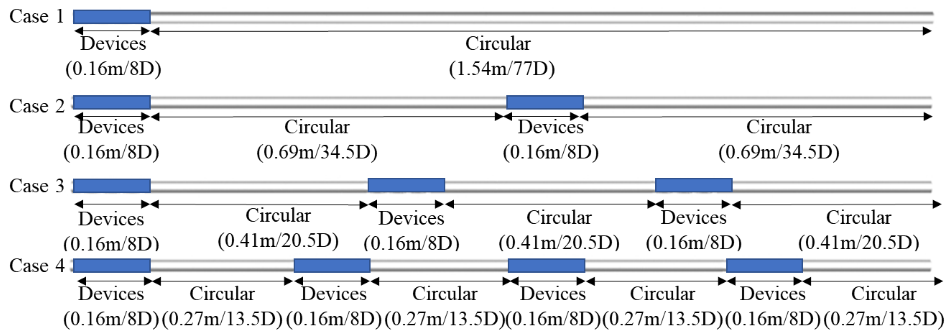

Figure 6.4-8. Arrangements for regularly spaced swirl devices.

6.4.3.1 Regularly-Spaced Twisted Tapes

The Nusselt number for regularly spaced twisted tapes is shown in Figure 6.4-9. Generally, the heat transfer coefficient increased when a higher number of twisted tapes are inserted because the additional twisted tapes introduce turbulence. Comparatively, the thermal enhancement provided by the original twisted tape in Figure 6.4-1 was initially greater than that of Case 1 and Case 2 twisted tapes but was subsequently surpassed by the twisted tapes of Cases 3 and 4. The total length of the inserted twisted tapes for Case 3 and 4 is 0.48m and 0.64m, respectively, which exceeds the length of the original twisted tape (0.4m). As this increase in tape length inevitably generates turbulence, the heat transfer coefficient for Cases 3 and 4 twisted tapes is further enhanced. Consequently, the Nusselt number for the Case 4 twisted tape was 23.6% higher than that of the regular SWH.

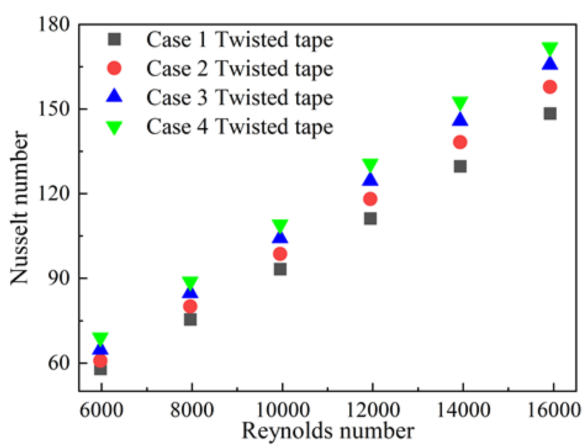

Figure 6.4-9. Nusselt number for regularly-spaced twisted tapes.

The friction factor for regularly spaced twisted tapes is shown in Figure 6.4-10. As the number of twisted tapes increased, the pressure drop increases correspondingly. Analogous to the Nusselt number variation, the friction factor for Cases 1 and 2 twisted tape is lower, whereas for Cases 3 and 4, it is higher than the value for the original twisted tape depicted in Figure 6.4-1. This phenomenon can be attributed to the total length difference between these arrangements, as longer twisted tapes require greater energy to drive the fluid through. Consequently, the friction factor for the Case 4 twisted tape was 203.7% higher than that of the circular tube. Such a substantial increase in pressure loss significantly exceeds the current pumping capacity when this device is implemented in an existing system.

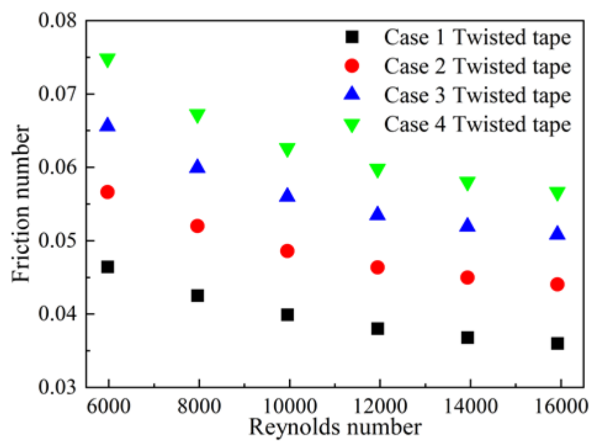

Figure 6.4-10. Friction factor for regularly-spaced twisted tapes.

The PEC values for regularly spaced twisted tape are shown in Figure 6.4-11. The variation in the PEC value does not follow a proportional relationship with the number of twisted tapes, which is different from the trends observed in the previous two figures. Furthermore, the PEC values for all cases first increased as the Reynolds number rose from 6,000 to 12,000 and then decreased significantly, particularly for Case 4. Case 4 demonstrated the highest average PEC at 0.98, whereas Case 2 exhibited the lowest PEC at 0.96. Although all cases displayed a PEC value higher than that of the previous twisted tape, the PEC values for all cases remained below 1, indicating that the energy recovered by the system was lower than the pumping power cost. This phenomenon can be attributed to the high-pressure loss associated with the insertion of twisted tape. In conclusion, regularly spaced twisted tapes do not enhance the solar heater efficiency, and their additional surface may exacerbate the fouling problem. It was pronounced that the PEC values for all cases dropped dramatically at Re of 16,000. The reason for this was that the sensible change in friction factor and Nusselt number caused significant change in PEC.

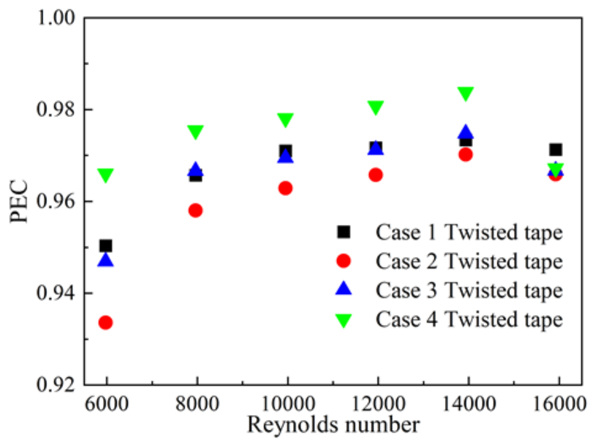

Figure 6.4-11. PEC values for regularly-spaced twisted tapes.

The surface Nusselt number of regularly spaced twisted tapes is shown in Figure 6.4-12. In all cases, the highest Nusselt number was observed at the location of the twisted tape and decreased gradually beyond the twisted tape region owing to the heat-transfer enhancement properties of the twisted tape. The insertion of additional twisted tapes led to an increase in the surface Nusselt number, and this explained the highest Nusselt number observed in Case 4.

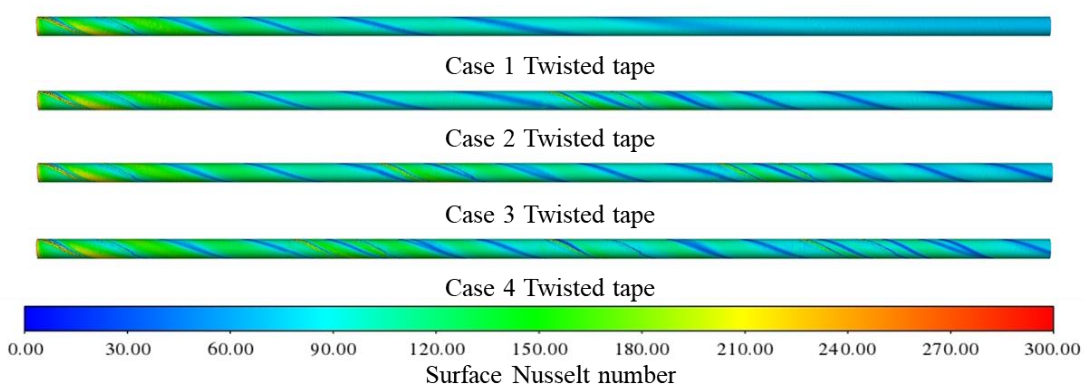

Figure 6.4-12. Surface Nusselt number of regularly spaced twisted tape.

6.4.3.2 Regularly-Spaced Swirl Tube

The following simulations investigate the potential enhancement of solar heater efficiencies through the utilisation of regularly spaced swirl generators.

The Nusselt numbers for various swirl tube configurations are shown in Figure 6.4-13. As the number of inserted swirl generators increases, the thermal efficiency of the solar heater also rises correspondingly. Those inserted swirl generators create additional swirl inside the flow, which helps to maintain a stronger swirling motion and prevent the swirl from decaying rapidly. As a result, the Nusselt number for Case 4 increases by 10% in comparison to the regular circular SWH, which is similar to the result of the twisted tape in Figure 6.4-1. Nevertheless, the number of inserted swirl generators should be carefully considered since the manufacturing and installation processes of the generators can be complex and time-consuming.

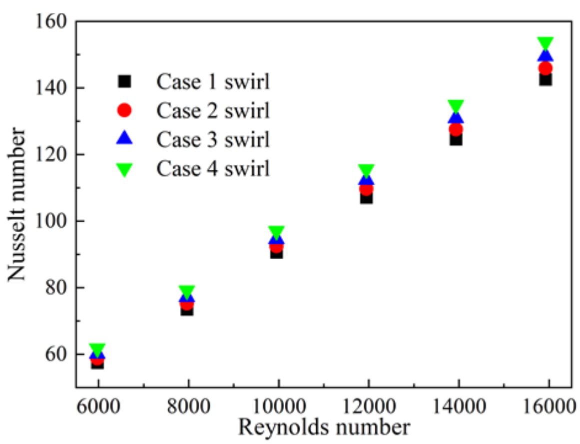

Figure 6.4-13. Nusselt number for regularly-spaced swirl generators.

The friction factor for different cases is given in Figure 6.4-14. Increasing the number of swirl tubes also increases friction losses because these swirl tubes induce greater turbulence within the flow and increase the resistance to fluid passage. Consequently, the pressure drop for the Case 4 swirl tube was approximately 27% higher than that of the circular tube. However, this value is considerably lower than the result for the twisted tape in Case 4 because the swirl tube itself does not create many obstacles for the fluid. When implementing this device in a current system, the pressure loss may not exceed the original pumping capacity.

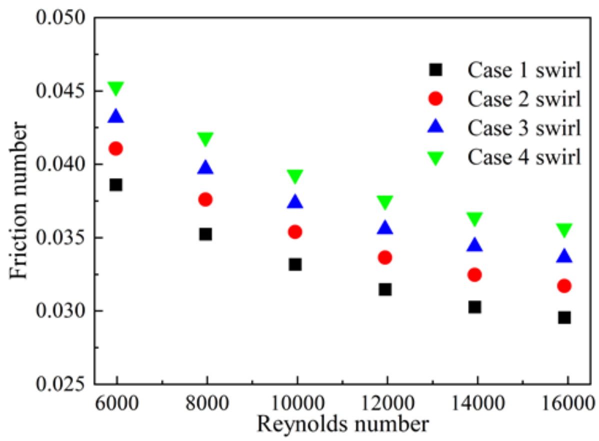

Figure 6.4-14. Friction factor for regularly-spaced swirl generators.

The PEC values for different cases are given in Figure 6.4-15. An increase in the number of swirl generators is associated with an increase in the PEC values. However, the increment from one to two swirl generators did not result in a substantial thermal enhancement. A more significant thermal enhancement was observed when the number increased from two to three and from three to four. Owing to the relatively low friction losses associated with the insertion of swirl generators in a pipe system, the thermal enhancement is not offset, as it is with twisted tapes. The maximum PEC value was observed with the insertion of four swirl generators, which exhibited an average PEC value of 1.5%. Although the overall increment is relatively small, this indicates the feasibility of regularly spaced multiple swirl generators. Furthermore, the generators can mitigate the fouling problem and prevent a decrease in solar water heater efficiency.

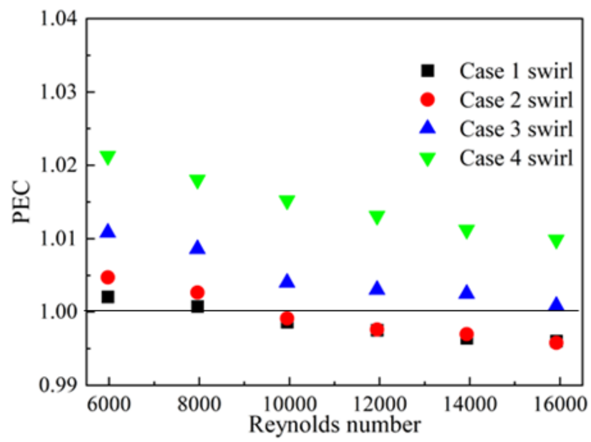

Figure 6.4-15. PEC values for regularly-spaced swirl generators.

The surface Nusselt number of a regularly-spaced swirl tube is shown in Figure 6.4-16. The colour map was adjusted so that it was the same as the one in Figure 6.4-12. Analogous to the twisted tape configuration, the highest Nusselt number was observed at the swirl tube lobes and diminished gradually after the fluid exits the swirl tube. The surface Nusselt number for Case 4 exhibits the highest value because it impedes the decay of the swirl.

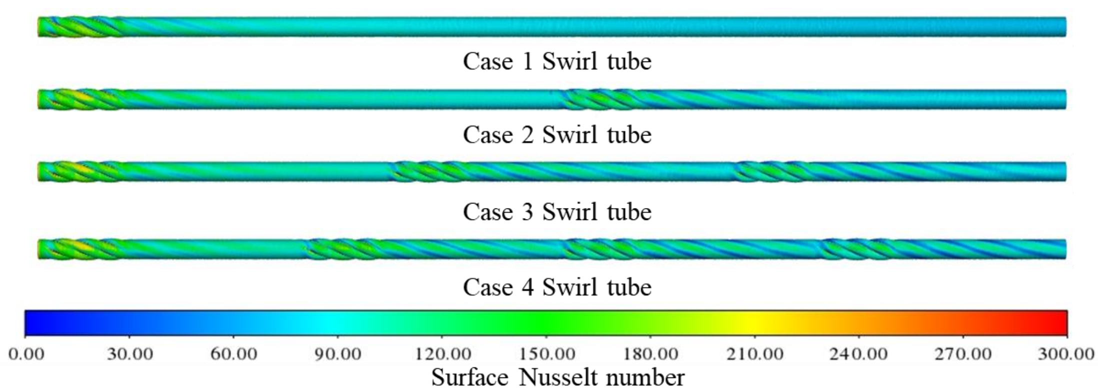

Figure 6.4-16. Surface Nusselt number of regularly spaced swirl tube.

6.4.3.3 Field Synergy Angle for Regularly Spaced Swirl Generators

The synergy angle variation downstream of each swirl tube is depicted in Figure 6.4-17. The synergy angle for each case is presented in separate figures, all of which use the same scale. The insertion of additional swirl generators mitigates the reduction in the local heat transfer rate caused by the swirl decay effect as the local synergy angle is consistently reduced. This indicates the thermal enhancement ability of the additional swirl tube. It was noteworthy that the lowest synergy angle remained constant at approximately 85°, which was attributable to the consistent degree of turbulence generated by the swirl generator. Furthermore, the highest synergy angle exhibits a continuous decrease from 89.9° in Case 1 to 88.9° in Case 4. Thus, the enhancement in the heat transfer coefficient in Figure 6.4-13 can be explained by calculating the local synergy angle.

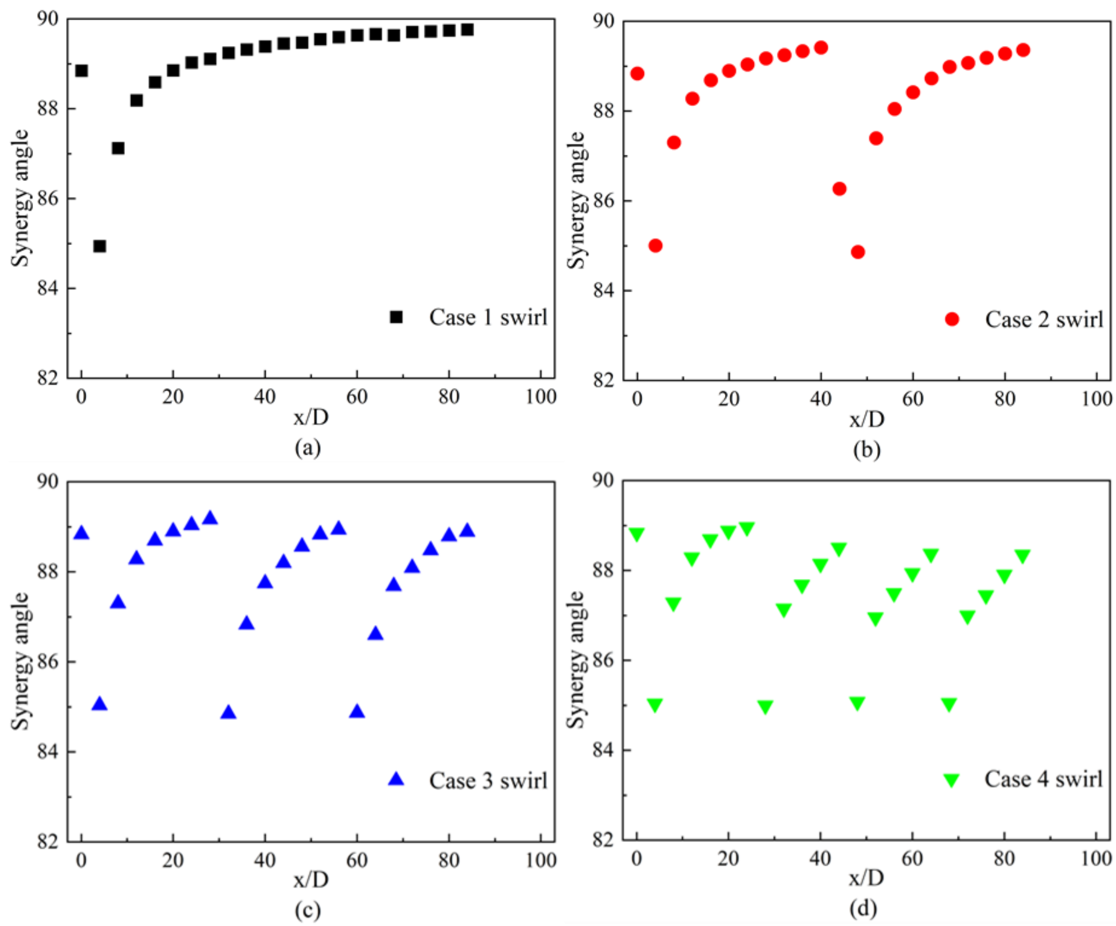

Figure 6.4-17. Synergy angle variation for regularly-spaced swirl generators at Reynolds number 11,940.

6.5 Experimental Method

6.5.1 Experiment Rigs

The evacuated tube solar collector depicted in Figure 6.5-1 comprises two primary components: the inner and outer tubes. The inner U-tube is typically made of copper, while the outer tube is constructed of glass with a vacuum jacket and coated with absorbing materials. An aluminum fin is wrapped around the U-tube to augment the heat transfer surface area.

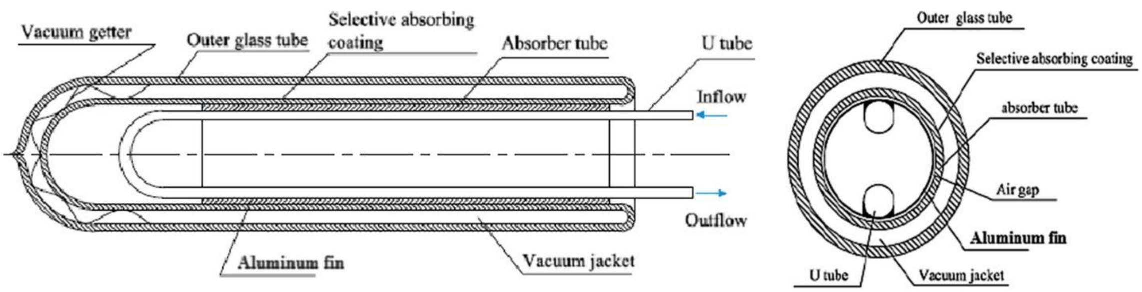

Figure 6.5-1. Demonstration of evacuated tube solar collectors (Ma et al., 2010).

The objective of the experiment was to investigate the impact of swirl tubes on enhancing the efficiency of solar water heaters. The baseline setup consisted of an array of 10 U-shaped riser pipes, each with an effective length of 1.5m. The SWH had an inclination angle of 45 degrees and a width of 1.1m. The U-shaped riser pipes were connected to 32mm diameter copper head pipes. The riser pipes themselves were U-shaped circular copper pipes with an internal diameter of 8mm and a thickness of 0.6mm. The distance between the swirl tube and the U-bend was approximately 160mm. Two sets of experimental rigs were retrofitted from commercially available evacuated tube collectors to assess the performance improvement brought by the incorporating the swirl tube. The evacuated tube collectors were purchased from Haining Futesi New Energy Co., Ltd

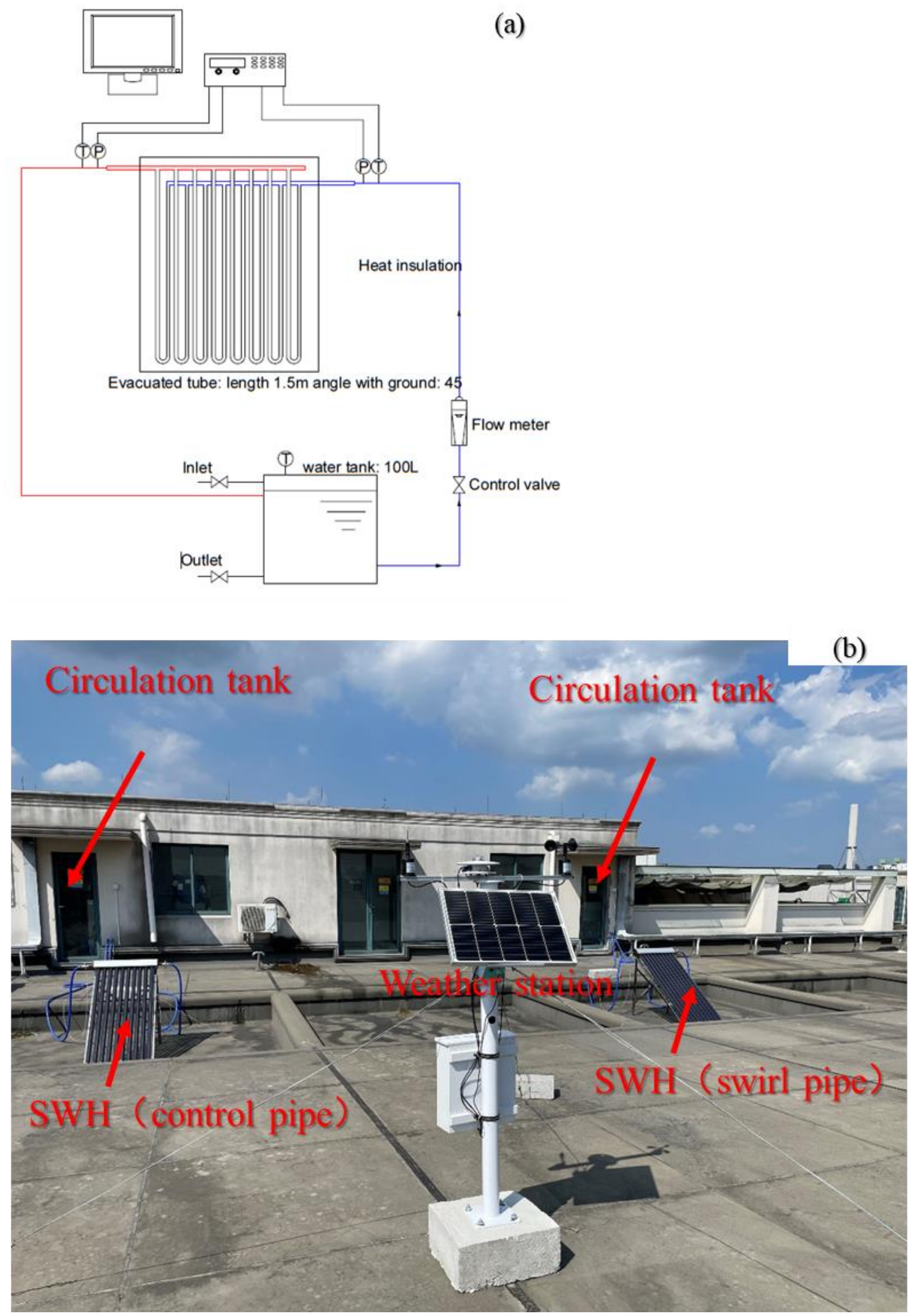

Figure 6.5-2. Experiment rig arrangement.

The SWHs were active, direct heat exchange type, with a circulating pump that could produce a flow rate ranging from 1 to 9L/min to cover both laminar and turbulent flow regimes. The water tanks had a capacity of 50L, and a 2kW cooling unit was installed in the tank. The circulating pump operated from 9:00 am to 3 pm on a sunny day, simulating actual use. During this time, the radiation intensity was the highest. The water temperature was then reduced to approximately 30°C overnight for the next day's experiment.

The experiment was conducted from July to August 2024. Under clear sky conditions, it was conducted on the rooftop of the PMB building at the University of Nottingham Ningbo China, with both SWHs oriented southward. The performance of the two rigs was compared by measuring the inlet and outlet temperatures and pressure drop. Data collection started at 9:30 am when the flow rate had stabilized and ended at 14:30 when the water temperature increment of the SWH was no longer significant. An overview of the retrofitted swirl copper tube is presented in Figure 6.5-3.

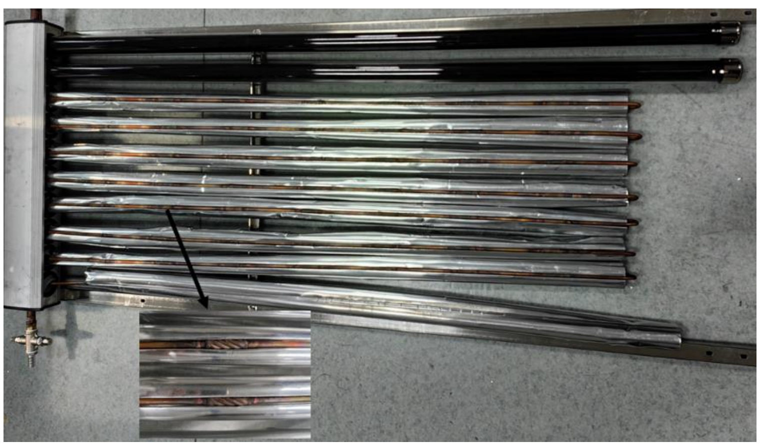

Figure 6.5-3. Overview of the retrofitted swirl copper tube.

The swirl tubes were made with 3D printing technology using copper alloy by the SimpNeed company based in Hangzhou. 14 tubes were required for 1 U-tube as shown in Figure 6.5-4. Initially, 300 3D-printed tubes (150 swirl tubes and 150 circular tubes) were made with a thickness of 0.6mm to maintain consistency with the thickness of the commercial SWH. However, 70% of the 3D-printed tubes had leakage problems during testing due to small gaps between the 3D-printed copper alloy powders. These leakage problems posed a significant challenge to the experiment and needed to be addressed promptly. The formation of such small gaps was because copper had a relatively high reflectivity for the laser energy. The reflection of energy by copper in 3D printing can cause uneven heat distribution, leading to issues like inconsistent melting, voids, and poor surface quality, which caused leaking.

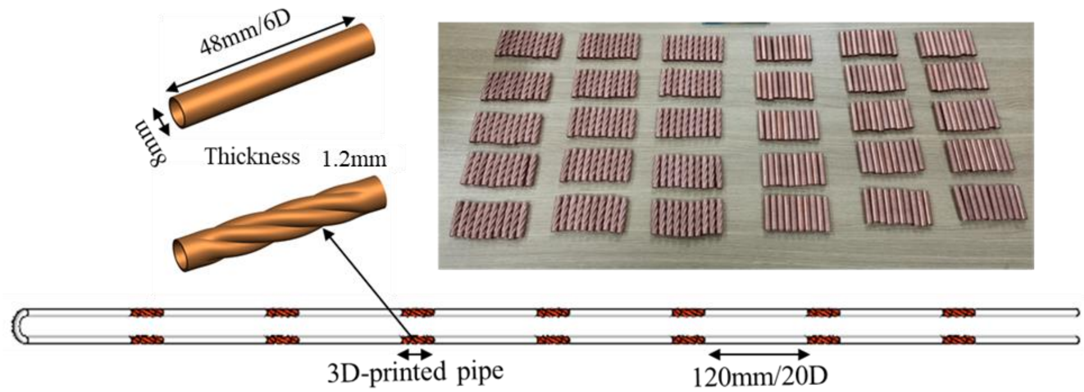

Figure 6.5-4. 3D-printed pipe and pipe arrangement illustration.

It was attempted to heat the 3D-printed tube to 1100 °C under vacuum conditions for 8 hours so that the copper powder could melt and those small gaps could be sealed. However, leakage still occurred during testing after heating the 3D-printed tubes. It was attempted to contact different 3D-printing companies, but no other company was willing to accept the project.

To solve the leaking problem, the thickness of the 3D-printed tube was increased to 1mm. A thicker tube may provide more material to potentially compensate for some of the voids. However, it does not address the root cause of the issue, the uneven heat distribution. Moreover, such an increment in tube thickness will certainly reduce the thermal performance of the SWH. It was unfortunate that no better alternative solution was identified. Therefore, 300 printed pipes (150 swirl tubes and 150 circular tubes) with a diameter of 8mm, a length of 48mm and a thickness of 1mm were made. After testing, 18 swirl tubes and 9 circular tubes were eliminated due to leakage problems.

The eight U-shaped tubes were first cut to 120 mm in length. The entrance and exit of the 3D-printed tube were expanded. This was done so that the cut tube could be welded into the printed tube, preventing leakage and ensuring the welded pipes were straight. Two retrofitted copper tubes were tested under a gauge pressure of 1.2 bar so that leaking would not occur during the experiment.

Temperature measurements were recorded at 30-second intervals. Specifically, the inlet and outlet temperatures were monitored using two PT100 resistance temperature detectors, each with an accuracy of 0.1%. Meanwhile, the pressure drop was measured by a differential pressure transducer with an accuracy of 0.6%. Additionally, the flow rate was measured by an electromagnetic flow meter, which has an accuracy of 0.5%. Finally, the solar intensity was measured by a weather station purchased from Yigu Company based in Wuhan, with an accuracy of 2%.

Table 6.5-1. Summary of the uncertainty of different parameters.

Parameter	Error/uncertainty
Temperature	0.1%
Pressure	0.6%
Solar intensity	2%
Flow rate	0.5%
Thermal efficiency	2.1%
Effective thermal efficiency	2.3%
Energy input from pump	0.8%

The uncertainty of an independent parameter φ can be calculated by the following equation (Uhía et al., 2013, Jafari et al., 2017b):

$$\delta\varphi = \sqrt{\sum_{i=1}^{n} (\frac{\delta\varphi}{\delta X_i}\delta X_i)^2} \tag{6.5-1}$$

where δX_i is the uncertainty of the measured variables and $\delta\varphi$ is the uncertainty of the independent parameters. Based on the calculation the uncertainties for thermal efficiency η, effective thermal efficiency η_{eff} and energy input Q_{pump} are 2.1%, 2.3% and 0.8%.

6.5.2 Data Reduction

To compare the performance, the following parameters are selected to evaluate the performance of each SWH, the following parameters are selected. The Heat transfer rate, friction factor and thermal efficiency should be calculated in each solar water heater.

Thermal efficiency

The thermal efficiency of the solar water heater is calculated with the following equations (Wang et al., 2015):

$$\eta_s = \frac{Q_{heat}}{IA} \tag{6.5-2}$$

Where I is the total solar radiation in W/m^2, A is the heat transfer area in m^2.

This coefficient generally describes the efficiency with which the solar heater absorbs the solar radiation. If the installed swirl tube positively affects the thermal efficiency, its efficiency should be higher than the one with the circular tube.

Effective thermal efficiency

Since the objective is to compare the overall energy balance after installing the swirl generator, it is necessary to consider the mechanical power consumption (Kumar and Layek, 2019).

$$\eta_s{}' = \frac{Q_{heat} - Q_{pump}}{IA} \tag{6.5-3}$$

where Q is the heat transfer rate of the fluid, Q_{pump} is the energy input from pumps.

6.6 Results and Discussions

The relationship between the volumetric flow rate and the Reynolds number regions is shown in Figure 6.6-1. As mentioned previously, the flow rate of this experiment ranged from 1L/min to 9L/min to encompass laminar and turbulent regions. The flow is considered turbulence when the Reynolds number is approximately 4,000 (Wei and Willmarth, 1989). The Reynolds number serves merely as a rough criterion for determining the flow state. In reality, the actual flow state can be influenced by various factors, including pipe roughness and inlet conditions.

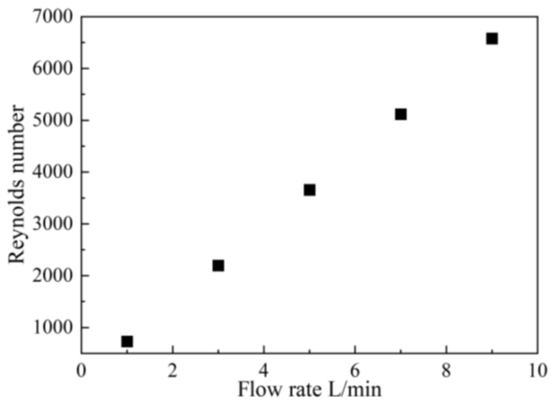

Figure 6.6-1. Relationship between flow rate and Reynolds number.

6.6.1 Pressure drop

The pressure drop variations with different flow rates is shown in Figure 6.6-2. The highest pressure drop is achieved at the highest flow rate. The pressure drop for the swirl SWH is 15% higher than that of the circular one at 9L/min. The pressure drop difference between the swirl and circular SWHs is negligible until turbulent regions, much like the thermal efficiency difference. The difference in pressure drop is again caused by the swirl flow generated by the lobed tube. This pressure drop can be further decreased if the diameter of the printed tube is not expanded for connection.

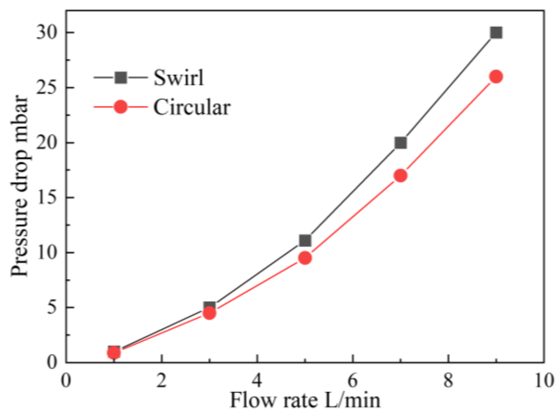

Figure 6.6-2. Pressure drop variations with different flow rates.

6.6.2 Temperature variation

The temperature variation for the two SWHs at 1L/min is shown in Figure 6.6-3. The inlet and the outlet temperature for both are 41 and 45 °C. At 14:30, the outlet temperature is 62.6 °C for swirl and 62.3 °C for circular. The temperature difference between the swirl SWH and the circular SWH is not significant as little difference is observed. This might indicate that the 4-lobed swirl tube has little thermal enhancement ability at a low flow rate.

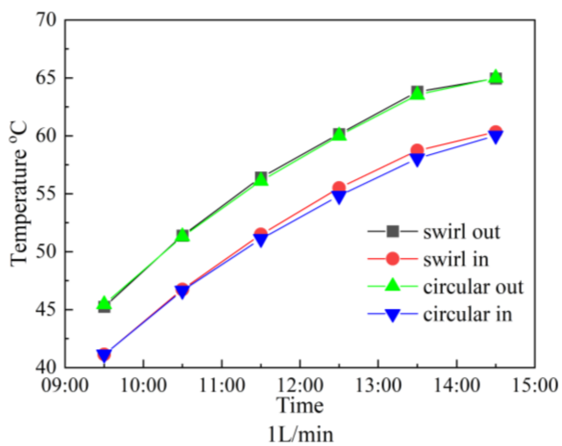

Figure 6.6-3. Temperature variation between two SWHs at 1L/min.

The temperature and thermal efficiency variations at 5L/min is shown in Figure 6.6-4. The inlet and the outlet temperature for both SWHs are adjusted to be the same around 42 and 44 °C at 9:30. At 14:30, the outlet temperature is 63.5 °C for swirl SWH and 61.6 °C for circular SWH. As the flow velocity increase, the temperature difference between the two becomes significant. These results indicate the thermal efficiency of the swirl SWH is higher than that of the circular one due to the swirl effect created by the regularly spaced swirl tube as demonstrated by our previous research (Feng et al., 2023).

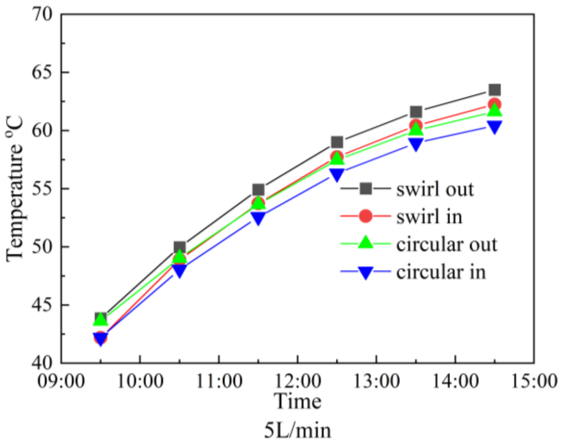

Figure 6.6-4. Temperature variation between two SWHs at 5L/min.

The temperature variations at 9L/min is shown in Figure 6.6-5. The inlet and the outlet temperature for both SWHs are adjusted to be the same around 44 and 45 °C at 9:30. At 14:30, the outlet temperature is 66.8 °C for swirl and 64.8 °C for circular. The temperature rises sharply at first for both rigs and then gradually slows down. Heat can be efficiently transferred because the water temperature in the tanks is initially low. As the water temperature increases, the shrinking temperature difference between the water and the evacuated tube leads to a decrease in efficiency. Due to the swirl effect, the swirl SWH can take away heat more effectively compared with the circular SWH. In addition, the temperature difference between the inlet and outlet of SWHs is lower compared with that at a low flow rate because a lower flow rate allows for a longer heating time.

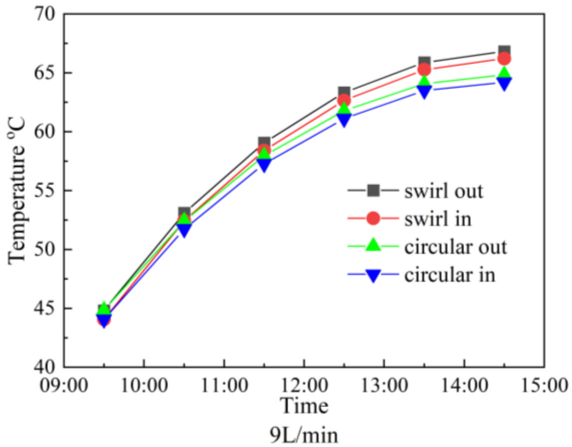

Figure 6.6-5 Temperature variation between the swirl SWH and the circular SWH at a flow rate of 9L/min.

The temperature difference between the swirl inlet and circular inlet is shown in Figure 6.6-6. As the flow rate increases, the temperature difference between the swirl inlet and the circular inlet also exhibits a corresponding rise. This phenomenon clearly demonstrates that the performance of the swirl one surpasses that of the circular one. Although the temperature of the swirl one is higher than that of the circular one at high flow rates, the thermal efficiency of the SWH can be further enhanced. This is because a thinner tube (0.6mm instead of 1mm) allows for better heat transfer, thus potentially increasing the efficiency. The temperature difference at a flow rate of 7L/min is the highest. This might be because the solar intensity at this flow rate is 938W/m^2

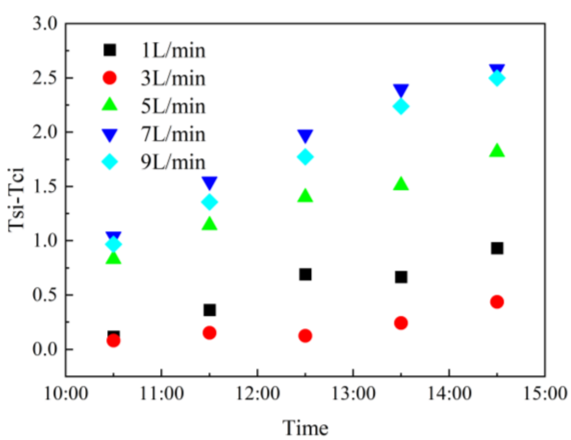

Figure 6.6-6. Temperature difference between the swirl inlet and the circular inlet at different flow rate.

6.6.3 Thermal efficiency

Initially, the temperature difference between the inlet and outlet of the swirl and circular SWHs was used to calculate the thermal efficiency. However, the two temperature differences are not significant since the efficiency between the two SWHs is close. Therefore, the temperature difference in the water tank is used to carry out further calculations.

The efficiency between the two SWHs in 3L/min and 7L/min is shown in Figure 6.6-7. Both figures indicate that the efficiencies at the beginning are the highest due to larger temperature difference. With the increase of temperature, the efficiency decreases. Furthermore, as flow rate increases, the efficiency of the swirl tube surpasses that of the circular tube, which suggests that the swirl tube has a better performance than the circular tube only in the turbulence region.

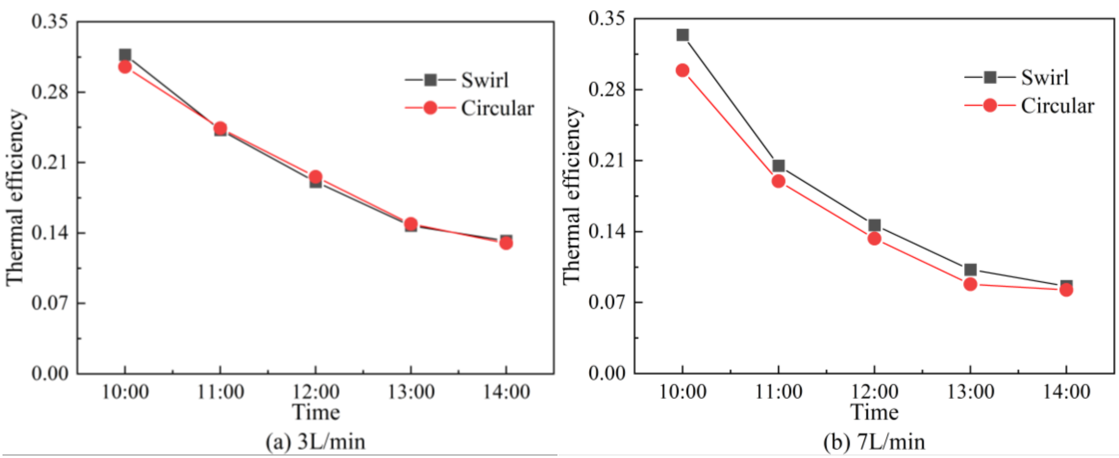

Figure 6.6-7. Efficiency between the two SWHs in 3L/min and 7L/min.

The data collection region's thermal performance at varying flow rates between swirl and circular SWHs is displayed in Figure 6.6-8. For both swirl and circular tubes, the maximum thermal efficiency is approximately 33% at 1L/min In contrast, Singh and Vardhan (2021) can achieve a maximum solar collector efficiency of 70.9%. According to the information provided by the supplier (Haining Futesi New Energy Co., Ltd), the maximum efficiency for the commercial SWH should also be around 70%. Therefore, it is believed that the retrofitting process has a negative effect on the SWH efficiency. The commercialisation of the regularly-spaced swirl tube requires further and deeper effort, especially on the 3-D printing technology for copper.

The efficiency will decrease with the increase of flow rate which may cause by higher heat loss during circulations. Figure 6.6-8 (a) is the effective thermal efficiency that considers the pumping power cost while Figure 6.6-8 (b) is the thermal efficiency that calculate the amount of energy absorbed by the SWH. Since they are almost identical in magnitude, it indicates that the pumping power consumption is relatively small. This is attributable to the relatively low flow velocity, which in turn results in low pumping energy requirements. Additionally, the experiment is carried out at the time when the solar intensity reaches its peak. Given the excellent heat-absorption capacity of the evacuated tube, the energy absorbed by the solar water heater (SWH) is substantially greater than the energy consumed for pumping. Though the efficiencies of both the circular and the swirl SWHs decrease with increasing flow rate, it is noticeable that the efficiency of the swirl SWH increases when the flow rate is in the turbulence region. Moreover, the difference in efficiency between the swirl and circular SWHs is not significant at a low flow rate. On average, the thermal efficiency of the swirl SWH is 3% higher than that of the circular SWH. This suggests that the thermal enhancement ability of the swirl tube is more promising in turbulent regions.

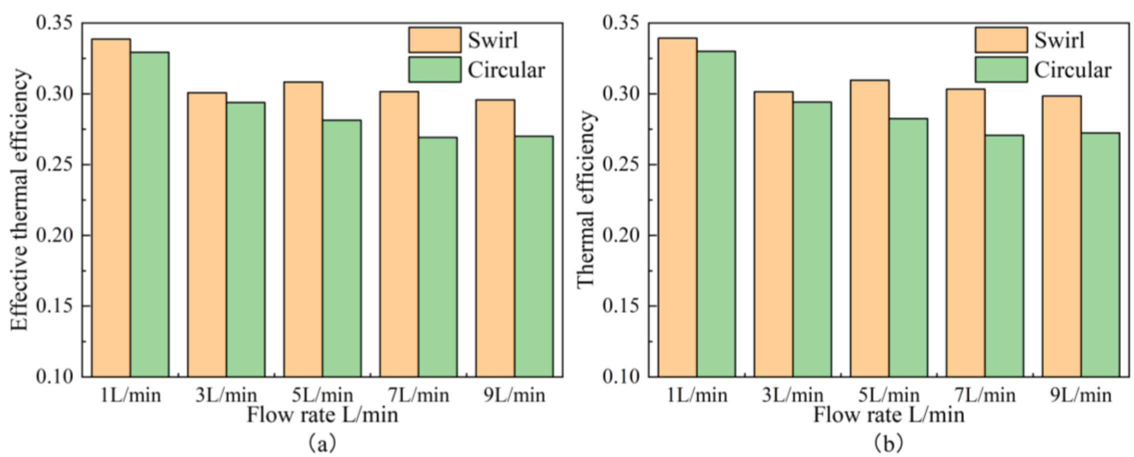

Figure 6.6-8. Thermal efficiency under different flow rate.

6.7 Conclusions

For numerical studies:

- Both devices exhibited lower performance compared to a circular SWH, with twisted tape demonstrating a higher pressure drop penalty (65% compared to a circular tube).
- The field synergy angle indicated that the causes of the poor performance were high friction loss and rapid decay of the swirl flow.
- For the twisted tape, although the heat transfer rate for Cases 3 and 4 increased moderately, its overall performance remained inferior to that of the original circular tube owing to the high flow resistance.
- For swirl generators, the Nusselt number increased by 10% with an increase in the pressure drop by 27%. The highest PEC value was achieved with swirl generators in Case 4, which was approximately 1.02 on average, indicating that the overall performance of the swirl generators (Case 4) was superior to that of the circular solar water heater.

For experimental studies:

- The results indicated that the swirl tube SWH demonstrated superior performance in the turbulent regions, exhibiting approximately 3% higher efficiency than the circular variant.
- The pressure drop observed in the swirl SWH is 15% greater than that in the circular design at the maximum flow rate. However, the energy consumption associated with the pumping power was negligible compared with the heat absorbed by the SWH.
- At the end of the data collection section, the outlet temperature of the swirl design was 2°C higher than that of the circular configuration. Nevertheless, this temperature differential was not obvious at lower flow rates.

CHAPTER 7: CONCLUSION AND FURTHER WORK

7.1 Conclusions

This thesis aims to enhance the thermal efficiency of heat exchangers through the utilisation of a 4-lobed swirl tube. Both experimental and numerical investigations were conducted, encompassing the insertion of a 4-lobed swirl tube in a double-pipe heat exchanger and solar water heater. The following conclusions can be drawn from these investigations:

7.1.1 Numerical Investigation of The 4-lobed Swirl Tube

- The simulation demonstrated that a decrease in the PD ratio of the swirl tubes increased both the heat-transfer coefficient and the pressure drop.
- Due to the decaying swirl effect, the PD6 "in-swirl" arrangement exhibited inferior overall performance compared to the circular pipe, despite achieving the highest PEC value at a Reynolds number of 9,000. Such PEC values can be further enhanced by reducing the length of the post-swirl circular pipe section.
- The disparity in thermal performance between the "in-swirl" and "ex-swirl" arrangements can be effectively elucidated by the field synergy principle.
- The thermal enhancement benefit of the swirl flow diminished rapidly upon exiting the swirl tube. As indicated by the local synergy angle, the swirl enhancement dissipated approximately at 60D downstream.
- The efficiencies between each configuration were tabulated in terms of energy efficiency η_h.
- Despite exhibiting the largest thermal enhancement (1.11 to 1.09) and pressure drop (4.81 to 6.07) in comparison to the circular tube, the PEC value of the PD4 crossover arrangement was less than 1 in the numerical results.
- The PD4 parallel tubes yielded the highest PEC value, ranging from 1.17 to 1 at low Reynolds numbers. At higher Reynolds numbers, the PD6 decaying tube configuration demonstrated the highest PEC value, ranging from 1.04 to 1.03.

- It was observed that the swirl tube generated small-scale vortices, particularly in the crossover configuration, which enhanced the mixing and heat-transfer coefficients.
- Regularly spaced swirl tubes improve thermal performance, with the highest PEC value (1.06 in Types 2).

7.1.2 Experimental Investigation of The 4-lobed Swirl Tube

- The numerical results in Chapter 5 were validated with the experimental results. The average differences of 6.1% for Nu and 3.7% for f were observed when the simulation settings increased the surface roughness value.
- The inlet and outlet temperature difference between different printed tubes were shown and the PD4 has the largest temperature difference.
- Inserting the swirl generator yielded a higher overall performance compared with a regular circular tube. Among all the PD ratios investigated, the PD4 decaying swirl tube exhibited the largest PEC value ranging from 1.12 to 1.09.
- The 3D-printed circular tube demonstrated a higher heat transfer coefficient and higher pressure drop. Therefore, the discrepancy between numerical results and experimental results may be attributed to the surface roughness resulting from the 3D printing methods.
- The polished 3D-printed tube exhibited a larger deviation in the numerical results in comparison with the unpolished one, which can be caused by the reduction in wall thickness and surface roughness.

7.1.3 Investigation of Swirl Generators in a Solar Water Heater

- The insertion of a twisted tape and a 4-lobed swirl tube into the solar water heater both result in a lower overall performance compared to a circular SWH.
- Analysis of the field synergy angle indicated that the rapid decay of the swirl flow was the primary factor contributing to the suboptimal performance of the swirl generators.

- The periodic insertion of twisted tapes and swirl generators led to increased heat transfer coefficients for both devices. However, the PEC value for regularly spaced twisted tapes was lower than that for the circular configuration owing to the high-pressure drop. For swirl generators, a maximum PEC value of 1.02% was achieved when the distance between each swirl tube was 20D (20 times the inner tube diameter).
- In laminar flow, the increase in thermal performance and pressure drop upon insertion of a swirl tube was minimal compared with circular tubes.
- In a turbulent flow, the outlet temperature of the swirl configuration was 2°C higher than that of the circular configuration. The efficiency of the swirl configuration is approximately 3% higher than that of the circular configuration. The pressure-drop penalty of the swirl configuration was 15% higher than that of the circular configuration at the highest flow rate.

7.2 Contribution to Knowledge

This thesis contributes to the knowledge in that:

- A comprehensive literature review was conducted, encompassing the developed thermal enhancement methods and the corresponding numerical and experimental works utilised by previous researchers.

- The thermal performance of various configurations of the 4-lobed swirl tube was investigated, and the superiority of decaying swirl flow in enhancing the thermal performance with a moderate pressure drop was demonstrated. Subsequently, a regularly-spaced 4-lobed swirl tube was proposed and proven to be effective in enhancing the heat-transfer rate.

- The field synergy principle elucidated that the thermal enhancement effect of the swirl flow generated by the swirl tube dissipated at a downstream distance of 60D (60 times the tube's inner diameter) downstream. Correlations between the downstream distance and local synergy angle were proposed. The 3D-printing method was employed to produce a steel 4-lobed swirl tube with PD ratios of 4, 6, and 8. The printed tube was inserted into the heat exchanger and its performance was verified.

- The regularly spaced lobed tube exhibited a higher overall thermal performance than the regularly spaced twisted tape owing to the high-pressure drop caused by the twisted tape. The optimal distance between the lobed tubes was determined to be 20D.

- For the solar water heater, the thermal enhancement effect of the regularly spaced swirl tube was negligible in the laminar flow regime. Consequently, this type of arrangement is only applicable in turbulent regions.

7.3 Further Work

7.3.1 Numerical Work

- This numerical investigation solely examined the thermal performance of 4-lobed swirl tubes. Future research should consider evaluating alternative geometrical shapes and arrangements of the lobed tube that generate decaying swirl flow, such as modifying the ratio between the transition section and swirl section, investigating 3-lobed and 5-lobed configurations, and systematically positioning the lobed tube within a single section.

- The present study utilised only one type of swirl device. Subsequent research could explore various combinations of swirl-flow devices. For instance, the thermal effects of regularly spaced swirl tubes and twisted tapes warrant further investigation.

- This study primarily focused on the heat transfer rate and flow characteristics of the tube side. However, it should be noted that the geometrical configuration of the lobed tube may also have an impact on the performance of the heat exchanger on the shell side, which remains to be explored in future research.

- The field synergy principle has been mainly applied to examine the decaying swirl effect associated with a lobed tube. Further research could apply this principle to investigate the swirl effect related to other swirl devices such as coils and twisted tapes.

- To determine the most optimal geometry and working conditions, a full-factorial research design needs to be carried out. This kind of design has the capability to test every possible combination of variables. For example, it can examine a wide range of swirl tube configurations and different PD ratios.
- Furthermore, to elucidate the performance of swirl SWH at low flow rates, additional studies are necessary to examine the heat transfer mechanism of the lobed tube in laminar regions.

7.3.2 Experimental Work

- A single swirl tube was inserted at the inlet of the heat exchanger using the compression joint method. The thermal enhancement effect of regularly spaced swirl tubes warrants further experimental investigations. As an alternative to a compression joint, a swirl tube may be welded to the heat exchanger.
- The thickness of the 3D-printed tube was 1 mm, whereas that of the commercial SWH copper tube was 0.6 mm. This increased thickness inevitably reduces the heat-transfer efficiency, which represents a compromise in addressing the leakage issue. Furthermore, to facilitate the connection between the printed tube and the commercial copper tube, the inlet and outlet of the printed tubes were expanded owing to the difference in diameter. This disparity resulted in an increased pressure drop. Consequently, it is recommended that future research should focus on advancing the 3D-printing technology to further enhance the thermal efficiency.

REFERENCE

ABE, S., OKAGAKI, Y., SATOU, A. & SIBAMOTO, Y. 2021. A numerical investigation on the heat transfer and turbulence production characteristics induced by a swirl spacer in a single-tube geometry under single-phase flow condition. *Annals of Nuclear Energy,* 159**,** 108321.

ABOU-ZIYAN, H. Z., HELALI, A. H. B. & SELIM, M. Y. E. 2016. Enhancement of forced convection in wide cylindrical annular channel using rotating inner pipe with interrupted helical fins. *International Journal of Heat and Mass Transfer,* 95**,** 996-1007.

AL-MAMUN, M. R., ROY, H., ISLAM, M. S., ALI, M. R., HOSSAIN, M. I., SAAD ALY, M. A., HOSSAIN KHAN, M. Z., MARWANI, H. M., ISLAM, A., HAQUE, E., RAHMAN, M. M. & AWUAL, M. R. 2023. State-of-the-art in solar water heating (SWH) systems for sustainable solar energy utilization: A comprehensive review. *Solar Energy,* 264**,** 111998.

ALONZO-GARCÍA, A., GUTIÉRREZ-TORRES, C. & JIMÉNEZ-BERNAL, J. 2016. Computational Fluid Dynamics in Turbulent Flow Applications.

ANSYS. 2021. Best Practice: RANS Turbulence Modeling in Ansys CFD.

ANSYS, I. 2022. Ansys fluent user's guide, 2022R1. *Ansys Fluent User's Guide*.

ARIYARATNE, C. 2005. Design and optimisation of swirl pipes and transition geometries for slurry transport.

ARJMANDI, H., AMIRI, P. & SAFFARI POUR, M. 2020. Geometric optimization of a double pipe heat exchanger with combined vortex generator and twisted tape: A CFD and response surface methodology (RSM) study. *Thermal Science and Engineering Progress,* 18**,** 100514.

AWAIS, M., ULLAH, N., AHMAD, J., SIKANDAR, F., EHSAN, M. M., SALEHIN, S. & BHUIYAN, A. A. 2021. Heat transfer and pressure drop performance of Nanofluid: A state-of- the-art review. *International Journal of Thermofluids,* 9**,** 100065.

BEJAN, A. & KRAUS, A. D. 2003. *Heat transfer handbook*, John Wiley & Sons.

BERGLES, A. 1998. Techniques to enhance heat transfer. *Handbook of heat transfer,* 3**,** 11.1-11.76.

BEZAATPOUR, M. & GOHARKHAH, M. 2020. Convective heat transfer enhancement in a double pipe mini heat exchanger by magnetic field induced swirling flow. *Applied Thermal Engineering,* 167**,** 114801.

BIEGGER, C., SOTGIU, C. & WEIGAND, B. 2015. Numerical investigation of flow and heat transfer in a swirl tube. *International Journal of Thermal Sciences,* 96**,** 319-330.

BILEN, K., TOKGOZ, N., SOLMAZ, İ. & BALTA, T. 2022. Thermo-hydraulic performance of tube with decaying swirl flow generators. *Applied Thermal Engineering,* 200**,** 117643.

BUCAK, H. & YıLMAZ, F. 2020. The current state on the thermal performance of twisted tapes: A geometrical categorisation approach. *Chemical Engineering and Processing - Process Intensification,* 153**,** 107929.

CHHABRA, R. P. & SHANKAR, V. 2017. *Coulson and Richardson's Chemical Engineering: Volume 1B: Heat and Mass Transfer: Fundamentals and Applications,* San Diego, San Diego: Elsevier Science & Technology.

CHOKPHOEMPHUN, S., PIMSARN, M., THIANPONG, C. & PROMVONGE, P. 2015. Thermal performance of tubular heat exchanger with multiple twisted-tape inserts. *Chinese Journal of Chemical Engineering,* 23**,** 755-762.

CHOPRA, K., TYAGI, V. V., PANDEY, A. K. & SARI, A. 2018. Global advancement on experimental and thermal analysis of evacuated tube collector with and without heat pipe systems and possible applications. *Applied Energy,* 228**,** 351-389.

DAVLETSHIN, I., MIKHEEV, A., MIKHEEV, N. & SHAKIROV, R. 2020. Heat transfer and structure of pulsating flow behind a rib. *International Journal of Heat and Mass Transfer,* 160**,** 120173.

DITTUS, F. & BOELTER, L. 1985. Heat transfer in automobile radiators of the tubular type. *International communications in heat and mass transfer,* 12**,** 3-22.

DU, J. & HONG, Y. 2020. Experimental investigation on thermal-hydraulic characteristics in a traverse rib tube fitted with regularly spaced helical tapes. *International Journal of Heat and Mass Transfer,* 154**,** 119726.

EIAMSA-ARD, P., PIRIYARUNGROJ, N., THIANPONG, C. & EIAMSA-ARD, S. 2014. A case study on thermal performance assessment of a heat exchanger tube equipped with regularly-spaced twisted tapes as swirl generators. *Case Studies in Thermal Engineering,* 3**,** 86-102.

EIAMSA-ARD, S., MARUYAMA, N., HIROTA, M., SKULLONG, S. & PROMTHAISONG, P. 2023. Heat transfer mechanism in ribbed twisted-oval tubes. *International Journal of Thermal Sciences,* 193**,** 108532.

EIAMSA-ARD, S., PETHKOOL, S., THIANPONG, C. & PROMVONGE, P. 2008. Turbulent flow heat transfer and pressure loss in a double pipe heat exchanger with louvered strip inserts. *International Communications in Heat and Mass Transfer,* 35**,** 120-129.

EIAMSA-ARD, S. & SEEMAWUTE, P. 2012. Decaying swirl flow in round tubes with short-length twisted tapes. *International Communications in Heat and Mass Transfer,* 39**,** 649-656.

EIAMSA-ARD, S., YONGSIRI, K., NANAN, K. & THIANPONG, C. 2012. Heat transfer augmentation by helically twisted tapes as swirl and turbulence promoters. *Chemical Engineering and Processing: Process Intensification,* 60**,** 42-48.

EL MAAKOUL, A., EL METOUI, M., BEN ABDELLAH, A., SAADEDDINE, S. & MEZIANE, M. 2017. Numerical investigation of thermohydraulic performance of air to water double-pipe heat exchanger with helical fins. *Applied Thermal Engineering,* 127**,** 127-139.

ELSHAFEI, E. A. M., SAFWAT MOHAMED, M., MANSOUR, H. & SAKR, M. 2008. Experimental study of heat transfer in pulsating turbulent flow in a pipe. *International Journal of Heat and Fluid Flow,* 29**,** 1029-1038.

ESFAHANI, M. R. & LANGURI, E. M. 2017. Exergy analysis of a shell-and-tube heat exchanger using graphene oxide nanofluids. *Experimental Thermal and Fluid Science,* 83**,** 100-106.

FAN, F., QI, C., TANG, J., LIU, Q., WANG, X. & YAN, Y. 2020. A novel thermal efficiency analysis on the thermo-hydraulic performance of nanofluids in an improved heat exchange system under adjustable magnetic field. *Applied Thermal Engineering,* 179**,** 115688.

FARSHAD, S. A. & SHEIKHOLESLAMI, M. 2019. Simulation of exergy loss of nanomaterial through a solar heat exchanger with insertion of multi-channel twisted tape. *Journal of Thermal Analysis and Calorimetry,* 138**,** 795-804.

FATTAHI, A. 2021. Numerical simulation of a solar collector equipped with a twisted tape and containing a hybrid nanofluid. *Sustainable Energy Technologies and Assessments,* 45**,** 101200.

FENG, X., MILES, N. J., LI, G., WANG, Z. & HALL, P. 2023. Numerical investigation of thermal performance of swirl generator in a solar water heater. *Energy proceedings*, 32.

FERNÁNDEZ-SEARA, J., UHÍA, F. J., SIERES, J. & CAMPO, A. 2007. A general review of the Wilson plot method and its modifications to determine convection coefficients in heat exchange devices. *Applied Thermal Engineering,* 27**,** 2745-2757.

FLUENT, A. 2011. Fluent 14.0 user's guide. *ANSYS FLUENT Inc.*

FLUENT, A. 2020. Ansys Fluent theory guide. 2020. *Canonsburg, PA, USA: ANSYS Inc.*

FLUENT, A. 2023. Fluent 14.0 Theory Guide. *ANSYS Inc.*

FOKEER, S. 2006. An investigation of geometrically induced swirl applied to lean phase pneumatic flows.

GANESHALINGAM, J. 2002. *Swirl-induction for improved solid-liquid flow in pipes.* University of Nottingham.

GEORGE, D. D. 2008. Effects of 4-lobe swirl-inducing pipe on pressure drop.

GHASEMIASL, R., HASHEMI, S., ARMAGHANI, T., TAYEBI, T. & POUR, M. S. 2023. Recent Studies on the Forced Convection of Nano-Fluids in Channels and Tubes: A Comprehensive Review. *Experimental Techniques,* 47**,** 47-81.

GNIELINSKI, V. 2013. On heat transfer in tubes. *International Journal of Heat and Mass Transfer,* 63**,** 134-140.

GOSHAYESHI, H. R., GOODARZI, M., SAFAEI, M. R. & DAHARI, M. 2016. Experimental study on the effect of inclination angle on heat transfer enhancement of a ferrofluid in a closed loop oscillating heat pipe under magnetic field. *Experimental Thermal and Fluid Science,* 74**,** 265-270.

GUNASEKARAN, N., MANOJ KUMAR, P., RAJA, S., SHARAVANAN, S., AVINAS, K., AAKASH KANNAN, P. & GOKUL, S. 2021. Investigation on ETC solar water heater using twisted tape inserts. *Materials Today: Proceedings,* 47**,** 5011-5016.

GUNES, S., OZCEYHAN, V. & BUYUKALACA, O. 2010. The experimental investigation of heat transfer and pressure drop in a tube with coiled wire inserts placed separately from the tube wall. *Applied Thermal Engineering,* 30**,** 1719-1725.

GUO, J., XU, M. & CHENG, L. 2010. Numerical investigations of circular tube fitted with helical screw-tape inserts from the viewpoint of field synergy principle. *Chemical Engineering and Processing: Process Intensification,* 49**,** 410-417.

GUO, W., LI, G., ZHENG, Y. & DONG, C. 2020. The effect of flow pulsation on Al2O3 nanofluids heat transfer behavior in a helical coil: A numerical analysis. *Chemical Engineering Research and Design,* 156**,** 76-85.

GUO, Z. Y., LI, D. Y. & WANG, B. X. 1998. A novel concept for convective heat transfer enhancement. *International Journal of Heat and Mass Transfer,* 41**,** 2221-2225.

GUO, Z. Y., TAO, W. Q. & SHAH, R. K. 2005. The field synergy (coordination) principle and its applications in enhancing single phase convective heat transfer. *International Journal of Heat and Mass Transfer,* 48**,** 1797-1807.

GUPTA, M. K. & KAUSHIK, S. C. 2009. Performance evaluation of solar air heater for various artificial roughness geometries based on energy, effective and exergy efficiencies. *Renewable Energy,* 34**,** 465-476.

HANGI, M., RAHBARI, A., WANG, X. & LIPIŃSKI, W. 2022. Hydrothermal characteristics of fluid flow in a circular tube fitted with free rotating axial-turbine-type swirl generators: Design, swirl strength, and performance analyses. *International Journal of Thermal Sciences,* 173**,** 107384.

HASANPOUR, A., FARHADI, M. & SEDIGHI, K. 2014. A review study on twisted tape inserts on turbulent flow heat exchangers: The overall enhancement ratio criteria. *International Communications in Heat and Mass Transfer,* 55**,** 53-62.

HEMMAT ESFE, M., MAZAHERI, H., MIRZAEI, S. S., KASHI, E., KAZEMI, M. & AFRAND, M. 2018. Effects of twisted tapes on thermal performance of tri-lobed tube: An applicable numerical study. *Applied Thermal Engineering,* 144**,** 512-521.

HEMMAT ESFE, M., SAEDODIN, S., MAHIAN, O. & WONGWISES, S. 2014. Heat transfer characteristics and pressure drop of COOH-functionalized DWCNTs/water nanofluid in turbulent flow at low concentrations. *International Journal of Heat and Mass Transfer,* 73**,** 186-194.

HEMMATIAN, A., KARGARSHARIFABAD, H., ABEDINI ESFAHLANI, A., RAHBAR, N. & SHOEIBI, S. 2024. Improving solar still performance with heat pipe/pulsating heat pipe evacuated tube solar collectors and PCM: An experimental and environmental analysis. *Solar Energy,* 269**,** 112371.

HOSSEINIAN, A. & MEGHDADI ISFAHANI, A. H. 2018. Experimental study of heat transfer enhancement due to the surface vibrations in a flexible double pipe heat exchanger. *Heat and Mass Transfer,* 54**,** 1113-1120.

HOSSEINIAN, A., MEGHDADI ISFAHANI, A. H. & SHIRANI, E. 2018. Experimental investigation of surface vibration effects on increasing the stability and heat transfer coeffcient of MWCNTs-water nanofluid in a flexible double pipe heat exchanger. *Experimental Thermal and Fluid Science,* 90**,** 275-285.

HU, Q., QU, X., PENG, W. & WANG, J. 2022. Experimental and numerical investigation of turbulent heat transfer enhancement of an intermediate heat exchanger using corrugated tubes. *International Journal of Heat and Mass Transfer,* 185**,** 122385.

HUANG, F., ZHENG, J., BALEYNAUD, J. M. & LU, J. 2017. Heat recovery potentials and technologies in industrial zones. *Journal of the Energy Institute,* 90**,** 951-961.

IBRAHIM, M. M., ESSA, M. A. & MOSTAFA, N. H. 2019. A computational study of heat transfer analysis for a circular tube with conical ring turbulators. *International Journal of Thermal Sciences,* 137**,** 138-160.

JAFARI, M., DABIRI, S., FARHADI, M. & SEDIGHI, K. 2017a. Effects of a three-lobe swirl generator on the thermal and flow fields in a heat exchanging tube: An experimental and numerical approach. *Energy Conversion and Management,* 148**,** 1358-1371.

JAFARI, M., FARHADI, M. & SEDIGHI, K. 2017b. An experimental study on the effects of a new swirl generator on thermal performance of a circular tube. *International Communications in Heat and Mass Transfer,* 87**,** 277-287.

JAFARI, M., FARHADI, M. & SEDIGHI, K. 2017c. Thermal performance enhancement in a heat exchanging tube via a four-lobe swirl generator: An experimental and numerical approach. *Applied Thermal Engineering,* 124**,** 883-896.

JAISANKAR, S., ANANTH, J., THULASI, S., JAYASUTHAKAR, S. T. & SHEEBA, K. N. 2011. A comprehensive review on solar water heaters. *Renewable and Sustainable Energy Reviews,* 15**,** 3045-3050.

JASAK, H. 1996. Error Analysis and Estimation for the Finite Volume Method With Applications to Fluid Flows. *Direct,* M.

JOULE, J. P. 1861. VIII. On the surface-condensation of steam. *Philosophical transactions of the Royal Society of London***,** 133-160.

KAOOD, A., ABOULMAGD, A., OTHMAN, H. & ELDEGWY, A. 2022. Numerical investigation of the thermal-hydraulic characteristics of turbulent flow in conical tubes with dimples. *Case Studies in Thermal Engineering,* 36**,** 102166.

KEKLIKCIOGLU, O. & OZCEYHAN, V. 2016. Experimental investigation on heat transfer enhancement of a tube with coiled-wire inserts installed with a separation from the tube wall. *International Communications in Heat and Mass Transfer,* 78**,** 88-94.

KEKLIKCIOGLU, O. & OZCEYHAN, V. 2018. A review of heat transfer enhancement methods using coiled wire and twisted tape inserts. *Heat Transfer: Models, Methods And Applications***,** 199-217.

KEKLIKCIOGLU, O. & OZCEYHAN, V. 2021. Thermohydraulic performance evaluation for horizontal tube by using combination of modified coiled wire inserts and graphene nanoplatelet-water nanouids. *International Communications in Heat and Mass Transfer,* 123**,** 105206.

KHOSRAVI-BIZHAEM, H., ABBASSI, A. & ZIVARI RAVAN, A. 2019. Heat transfer enhancement and pressure drop by pulsating flow through helically coiled tube: An experimental study. *Applied Thermal Engineering,* 160**,** 114012.

KONGKAITPAIBOON, V., NANAN, K. & EIAMSA-ARD, S. 2010. Experimental investigation of convective heat transfer and pressure loss in a round tube fitted with circular-ring turbulators. *International Communications in Heat and Mass Transfer,* 37**,** 568-574.

KUMAR, A. & LAYEK, A. 2019. Energetic and exergetic performance evaluation of solar air heater with twisted rib roughness on absorber plate. *Journal of Cleaner Production,* 232**,** 617-628.

KUPPAN, T. 2013. *Heat exchanger design handbook / Kuppan Thulukkanam,* Boca Raton [Fla.], Boca Raton Fla. : CRC Press.

KURTBAŞ, İ., GÜLÇIMEN, F., AKBULUT, A. & BURAN, D. 2009. Heat transfer augmentation by swirl generators inserted into a tube with constant heat flux. *International Communications in Heat and Mass Transfer,* 36**,** 865-871.

LAUNDER, B. E. & SPALDING, D. B. 1972. Lectures in mathematical models of turbulence. *(No Title).*

LÉAL, L., MISCEVIC, M., LAVIEILLE, P., AMOKRANE, M., PIGACHE, F., TOPIN, F., NOGARÈDE, B. & TADRIST, L. 2013. An overview of heat transfer enhancement methods and new perspectives: Focus on active methods using electroactive materials. *International Journal of Heat and Mass Transfer,* 61**,** 505-524.

LI, G. 2016. Investigation of swirl pipe for improving cleaning efficiency in closed processing system.

LI, G., HALL, P., MILES, N. & WU, T. 2015. Improving the efficiency of 'Clean-In-Place' procedures using a four-lobed swirl pipe: A numerical investigation. *Computers & Fluids,* 108**,** 116-128.

LI, G., MILES, N. J., WU, T. & HALL, P. 2017. Large eddy simulation and Reynolds-averaged Navier–Stokes based modelling of geometrically induced swirl flows applied for the better understanding of Clean-In-Place procedures. *Food and Bioproducts Processing,* 104**,** 77-93.

LI, H. & TOMITA, Y. 1994. Characteristics of swirling flow in a circular pipe.

LI, H., WANG, Y., HAN, Y., LI, W., YANG, L., GUO, J., LIU, Y., ZHANG, J., ZHANG, M. & JIANG, F. 2022a. A comprehensive review of heat transfer enhancement and flow characteristics in the concentric pipe heat exchanger. *Powder Technology,* 397**,** 117037.

LI, Q. & XUAN, Y. 2009. Experimental investigation on heat transfer characteristics of magnetic fluid flow around a fine wire under the influence of an external magnetic field. *Experimental Thermal and Fluid Science,* 33**,** 591-596.

LI, X., LIU, S., TANG, S., MO, X., WANG, L. & ZHU, D. 2022b. Analysis of heat transfer characteristics and entransy evaluation of high viscosity fluid in a novel twisted tube. *Applied Thermal Engineering,* 210**,** 118388.

LI, X., WANG, L., FENG, R., WANG, Z., LIU, S. & ZHU, D. 2021. Study on shell side heat transport enhancement of double tube heat exchangers by twisted oval tubes. *International Communications in Heat and Mass Transfer,* 124**,** 105273.

LI, X., ZHU, D., YIN, Y., LIU, S. & MO, X. 2018. Experimental study on heat transfer and pressure drop of twisted oval tube bundle in cross flow. *Experimental Thermal and Fluid Science,* 99**,** 251-258.

LIAW, K. L., KURNIA, J. C., PUTRA, Z. A., AZIZ, M. & SASMITO, A. P. 2023. Enhanced turbulent convective heat transfer in helical twisted Multilobe tubes. *International Journal of Heat and Mass Transfer,* 202**,** 123687.

LIU, B., JIA, M. & LIU, Y. 2024a. Estimation of industrial waste heat recovery potential in China: Based on energy consumption. *Applied Thermal Engineering,* 236**,** 121513.

LIU, K., CAI, B., LI, Q., CHE, X., CAI, W. & FANG, X. 2024b. Multi-objective optimization of twisted tri-lobed tube geometry for enhanced heat transfer and reduced resistance in turbulent flow. *Applied Thermal Engineering,* 247**,** 123064.

LIU, S. & SAKR, M. 2013. A comprehensive review on passive heat transfer enhancements in pipe exchangers. *Renewable and Sustainable Energy Reviews,* 19**,** 64-81.

LUO, A., FANG, H., XIA, J., LIN, B. & JIANG, Y. 2017. Mapping potentials of low-grade industrial waste heat in Northern China. *Resources, Conservation and Recycling,* 125**,** 335-348.

LUO, C. & SONG, K. 2021. Thermal performance enhancement of a double-tube heat exchanger with novel twisted annulus formed by counter-twisted oval tubes. *International Journal of Thermal Sciences,* 164**,** 106892.

MA, L., LU, Z., ZHANG, J. & LIANG, R. 2010. Thermal performance analysis of the glass evacuated tube solar collector with U-tube. *Building and Environment,* 45**,** 1959-1967.

MANGLIK, R. M. 2003. Heat transfer enhancement. *Heat transfer handbook*, 1029-1130.

MARADIYA, C., VADHER, J. & AGARWAL, R. 2018. The heat transfer enhancement techniques and their Thermal Performance Factor. *Beni-Suef University Journal of Basic and Applied Sciences*, 7, 1-21.

MARKETSANDMARKETS. 2024. *Heat Exchanger Market by Type (Shell & Tube, Plate & Frame, Air Cooled), Material (Metal, Alloys, Brazing Clad Materials), End-Use Industry (Chemical, Energy, Hvacr, Food & Beverage, Power, Pulp & Paper), and Region - Global Forecast to 2029* [Online]. https://www.marketsandmarkets.com/Market-Reports/heat-exchanger-market-750.html. [Accessed Feb 21 2025].

MASHOOFI MALEKI, N., AMERI, M. & HAGHIGHI KHOSHKHOO, R. 2023. Experimental study of the thermal-frictional behavior of a horizontal straight tube equipped with a vibrating string turbulators: A novel active method. *Experimental Thermal and Fluid Science*, 140, 110767.

MASUDA, H., EBATA, A. & TERAMAE, K. 1993. Alteration of thermal conductivity and viscosity of liquid by dispersing ultra-fine particles. Dispersion of Al2O3, SiO2 and TiO2 ultra-fine particles.

MCELHINEY, J. E. & PRECKSHOT, G. W. 1977. Heat transfer in the entrance length of a horizontal rotating tube. *International Journal of Heat and Mass Transfer*, 20, 847-854.

MEHTA, B. & KHANDEKAR, S. 2015. Local experimental heat transfer of single-phase pulsating laminar flow in a square mini-channel. *International Journal of Thermal Sciences*, 91, 157-166.

MENTER, F., SECHNER, R. & MATYUSHENKO, A. 2021. Best practice: RANS turbulence modeling in Ansys CFD. *ANSYS Inc.: Canonsburg, PA, USA.*

MENTER, F. R. 1994. Two-equation eddy-viscosity turbulence models for engineering applications. *AIAA Journal*, 32, 1598-1605.

MENTER, F. R., KUNTZ, M. & LANGTRY, R. 2003. Ten years of industrial experience with the SST turbulence model. *Turbulence, heat and mass transfer*, 4, 625-632.

MOECK, E. & MCMORRAN, P. 1977. Dynamic simulation of a reboiler. *IFAC Proceedings Volumes,* 10**,** 513-522.

MORRIS, W. D. & RAHMAT-ABADI, K. F. 1996. Convective heat transfer in rotating ribbed tubes. *International Journal of Heat and Mass Transfer,* 39**,** 2253-2266.

MOUSA, M. H., MILJKOVIC, N. & NAWAZ, K. 2021. Review of heat transfer enhancement techniques for single phase flows. *Renewable and Sustainable Energy Reviews,* 137**,** 110566.

NAKATSUKA, K., JEYADEVAN, B., NEVEU, S. & KOGANEZAWA, H. 2002. The magnetic fluid for heat transfer applications. *Journal of Magnetism and Magnetic Materials,* 252**,** 360-362.

NAKHCHI, M. E., ESFAHANI, J. A. & KIM, K. C. 2020. Numerical study of turbulent flow inside heat exchangers using perforated louvered strip inserts. *International Journal of Heat and Mass Transfer,* 148**,** 119143.

NAPHON, P. & WIRIYASART, S. 2018. Experimental study on laminar pulsating flow and heat transfer of nanofluids in micro-fins tube with magnetic fields. *International Journal of Heat and Mass Transfer,* 118**,** 297-303.

NESBITT, B. 2006. *Handbook of pumps and pumping: Pumping manual international*, Elsevier.

NITSCHE, M. & GBADAMOSI, R. O. 2015. *Heat Exchanger Design Guide: A Practical Guide for Planning, Selecting and Designing of Shell and Tube Exchangers*, Elsevier Science & Technology.

O’NEIL, T. J. E. & SOBHANSARBANDI, S. 2022. Thermal performance investigation of energy storage based U-pipe evacuated tube solar collector: An experimental study. *Sustainable Energy Technologies and Assessments,* 52**,** 102146.

OMIDI, M., FARHADI, M. & JAFARI, M. 2017. A comprehensive review on double pipe heat exchangers. *Applied Thermal Engineering,* 110**,** 1075-1090.

OMIDI, M., RABIENATAJ DARZI, A. A. & FARHADI, M. 2019. Turbulent heat transfer and fluid flow of alumina nanofluid inside three-lobed twisted tube. *Journal of Thermal Analysis and Calorimetry,* 137**,** 1451-1462.

PAK, B. C. & CHO, Y. I. 1998. HYDRODYNAMIC AND HEAT TRANSFER STUDY OF DISPERSED FLUIDS WITH SUBMICRON METALLIC OXIDE PARTICLES. *Experimental Heat Transfer,* 11**,** 151-170.

PETHKOOL, S., EIAMSA-ARD, S., KWANKAOMENG, S. & PROMVONGE, P. 2011. Turbulent heat transfer enhancement in a heat exchanger using helically corrugated tube. *International Communications in Heat and Mass Transfer,* 38**,** 340-347.

PROMVONGE, P. & SKULLONG, S. 2020. Thermo-hydraulic performance in heat exchanger tube with V-shaped winglet vortex generator. *Applied Thermal Engineering,* 164**,** 114424.

QI, C., LIU, M., WANG, G., PAN, Y. & LIANG, L. 2018a. Experimental research on stabilities, thermophysical properties and heat transfer enhancement of nanofluids in heat exchanger systems. *Chinese Journal of Chemical Engineering,* 26**,** 2420-2430.

QI, C., WANG, G., YAN, Y., MEI, S. & LUO, T. 2018b. Effect of rotating twisted tape on thermo-hydraulic performances of nanofluids in heat-exchanger systems. *Energy Conversion and Management,* 166**,** 744-757.

QIU, L., DENG, H., SUN, J., TAO, Z. & TIAN, S. 2013. Pressure drop and heat transfer in rotating smooth square U-duct under high rotation numbers. *International Journal of Heat and Mass Transfer,* 66**,** 543-552.

RAYLOR, B. 1998. Pipe design for improved particle distribution and improved wear.

ROCKLAGE-MARLIANI, G., SCHMIDTS, M. & VASANTA RAM, V. I. 2003. Three-dimensional laser-Doppler velocimeter measurements in swirling turbulent pipe flow. *Flow, Turbulence and Combustion,* 70**,** 43-67.

ROHSENOW, W. M., HARTNETT, J. P. & CHO, Y. I. 1998. *Handbook of heat transfer,* McGraw-Hill New York.

SABIHA, M. A., SAIDUR, R., MEKHILEF, S. & MAHIAN, O. 2015. Progress and latest developments of evacuated tube solar collectors. *Renewable and Sustainable Energy Reviews,* 51**,** 1038-1054.

SADHISHKUMAR, S. & BALUSAMY, T. 2014. Performance improvement in solar water heating systems—A review. *Renewable and Sustainable Energy Reviews,* 37**,** 191-198.

SADIGHI DIZAJI, H., JAFARMADAR, S. & MOBADERSANI, F. 2015. Experimental studies on heat transfer and pressure drop characteristics for new arrangements of corrugated tubes in a double pipe heat exchanger. *International Journal of Thermal Sciences,* 96**,** 211-220.

SAMRUAISIN, P., CHANGCHAROEN, W., THIANPONG, C., CHUWATTANAKUL, V., PIMSARN, M. & EIAMSA-ARD, S. 2018. Influence of regularly spaced quadruple twisted tape elements on thermal enhancement characteristics. *Chemical Engineering and Processing - Process Intensification,* 128**,** 114-123.

SAMRUAISIN, P., KUNLABUD, S., KUNNARAK, K., CHUWATTANAKUL, V. & EIAMSA-ARD, S. 2019. Intensification of convective heat transfer and heat exchanger performance by the combined influence of a twisted tube and twisted tape. *Case Studies in Thermal Engineering,* 14**,** 100489.

SARAVANAN, A. & JAISANKAR, S. 2019. Heat transfer augmentation techniques in forced flow V-trough solar collector equipped with V-cut and square cut twisted tape. *International Journal of Thermal Sciences,* 140**,** 59-70.

SEIBOLD, F., LIGRANI, P. & WEIGAND, B. 2022. Flow and heat transfer in swirl tubes — A review. *International Journal of Heat and Mass Transfer,* 187**,** 122455.

SHEIKHOLESLAMI, M., GORJI-BANDPY, M. & GANJI, D. D. 2015. Review of heat transfer enhancement methods: Focus on passive methods using swirl flow devices. *Renewable and Sustainable Energy Reviews,* 49**,** 444-469.

SHELARE, S. D., AGLAWE, K. R. & BELKHODE, P. N. 2022. A review on twisted tape inserts for enhancing the heat transfer. *Materials Today: Proceedings*, 54**,** 560-565.

SIEDER, E. N. & TATE, G. E. 1936. Heat transfer and pressure drop of liquids in tubes. *Industrial & Engineering Chemistry,* 28**,** 1429-1435.

SIERES, J. & CAMPO, A. 2018. Uncertainty analysis for the experimental estimation of heat transfer correlations combining the Wilson plot method and the Monte Carlo technique. *International Journal of Thermal Sciences,* 129**,** 309-319.

SINGH, I. & VARDHAN, S. 2021. Experimental investigation of an evacuated tube collector solar air heater with helical inserts. *Renewable Energy,* 163**,** 1963-1972.

STEWART, M. 2013. *Heat exchanger equipment field manual [electronic resource] : common operating problems and practical solutions / Maurice Stewart, Oran T. Lewis,* Waltham, Mass., Waltham, Mass. : Gulf Professional Pub.

SUN, Z., ZHANG, K., LI, W., CHEN, Q. & ZHENG, N. 2020. Investigations of the turbulent thermal-hydraulic performance in circular heat exchanger tubes with multiple rectangular winglet vortex generators. *Applied Thermal Engineering,* 168**,** 114838.

SUNDAR, L. S., SINTIE, Y. T., SAID, Z., SINGH, M. K., PUNNAIAH, V. & SOUSA, A. C. M. 2020. Energy, efficiency, economic impact, and heat transfer aspects of solar flat plate collector with Al2O3 nanofluids and wire coil with core rod inserts. *Sustainable Energy Technologies and Assessments,* 40**,** 100772.

SURESH, S., VENKITARAJ, K. P., SELVAKUMAR, P. & CHANDRASEKAR, M. 2012. Effect of Al2O3–Cu/water hybrid nanofluid in heat transfer. *Experimental Thermal and Fluid Science,* 38**,** 54-60.

TABARHOSEINI, S. M., SHEIKHOLESLAMI, M. & SAID, Z. 2022. Recent advances on the evacuated tube solar collector scrutinizing latest innovations in thermal performance improvement involving economic and environmental analysis. *Solar Energy Materials and Solar Cells,* 241**,** 111733.

TAN, X.-H., ZHU, D.-S., ZHOU, G.-Y. & ZENG, L.-D. 2012. Experimental and numerical study of convective heat transfer and fluid flow in twisted oval tubes. *International Journal of Heat and Mass Transfer,* 55**,** 4701-4710.

TAN, X.-H., ZHU, D.-S., ZHOU, G.-Y. & ZENG, L.-D. 2013. Heat transfer and pressure drop performance of twisted oval tube heat exchanger. *Applied Thermal Engineering,* 50**,** 374-383.

TANG, X., DAI, X. & ZHU, D. 2015. Experimental and numerical investigation of convective heat transfer and fluid flow in twisted spiral tube. *International Journal of Heat and Mass Transfer,* 90**,** 523-541.

TAVOUSI, E., PERERA, N., FLYNN, D. & HASAN, R. 2023. Heat transfer and fluid flow characteristics of the passive method in double tube heat exchangers: A critical review. *International Journal of Thermofluids,* 17**,** 100282.

TAYLOR, R. P., HOSNI, M. H. & COLEMAN, H. W. 1990. COMPARISON OF CONSTANT WALL TEMPERATURE AND HEAT FLUX CASES FOR THE TURBULENT ROUGH-WALL BOUNDARY LAYER. *Experimental Heat Transfer,* 3**,** 117-127.

TUNCER, A. D., SÖZEN, A., KHANLARI, A., GÜRBÜZ, E. Y. & VARIYENLI, H. İ. 2021. Upgrading the performance of a new shell and helically coiled heat exchanger by using longitudinal fins. *Applied Thermal Engineering,* 191**,** 116876.

UHÍA, F. J., CAMPO, A. & FERNÁNDEZ-SEARA, J. 2013. Uncertainty analysis for experimental heat transfer data obtained by the Wilson plot method: Application to condensation on horizontal plain tubes. *Thermal Science,* 17**,** 471-487.

WANG, G., ZHANG, Z., WANG, R. & ZHU, Z. 2020. A Review on Heat Transfer of Nanofluids by Applied Electric Field or Magnetic Field. *Nanomaterials,* 10.

WANG, T., ZHANG, Q., SONG, K., ZHANG, K., SU, M. & WU, X. 2022. Thermodynamic characteristics of a novel combination of three-start twisted tube and oval dimples. *Case Studies in Thermal Engineering,* 37**,** 102284.

WANG, Y., HOU, M., DENG, X., LI, L., HUANG, C., HUANG, H., ZHANG, G., CHEN, C. & HUANG, W. 2011. Configuration optimization of regularly spaced short-length twisted tape in a circular tube to enhance turbulent heat transfer using CFD modeling. *Applied Thermal Engineering,* 31**,** 1141-1149.

WANG, Z., YANG, W., QIU, F., ZHANG, X. & ZHAO, X. 2015. Solar water heating: From theory, application, marketing and research. *Renewable and Sustainable Energy Reviews,* 41**,** 68-84.

WEBB, R. 1981. Performance evaluation criteria for use of enhanced heat transfer surfaces in heat exchanger design. *International Journal of Heat and Mass Transfer,* 24**,** 715-726.

WEBB, R. & KIM, N.-H. 2004. *Principles of Enhanced Heat Transfer*.

WEI, T. & WILLMARTH, W. W. 1989. Reynolds-number effects on the structure of a turbulent channel flow. *Journal of Fluid Mechanics,* 204**,** 57-95.

WEISS, W. & SPÖRK-DÜR, M. 2023. *Solar Heat Worldwide* [Online]. Available: https://www.iea-shc.org/solar-heat-worldwide [Accessed 5th March 2024].

WELTY, J. R. 2001. *Fundamentals of momentum, heat, and mass transfer / James R. Welty ... [et al.],* New York, New York : John Wiley & Sons.

WELTY, J. R. 2008. *Fundamentals of momentum, heat, and mass transfer / James R. Welty ... [et al.],* Hoboken, N.J., Hoboken, N.J. : Wiley.

WILCOX, D. C. 2008. Formulation of the k-w Turbulence Model Revisited. *AIAA Journal,* 46**,** 2823-2838.

WU, C.-C., CHEN, C. O.-K., YANG, Y.-T. & HUANG, K.-H. 2018. Numerical simulation of turbulent flow forced convection in a twisted elliptical tube. *International Journal of Thermal Sciences,* 132**,** 199-208.

WU, Z., WANG, L. & SUNDÉN, B. 2013. Pressure drop and convective heat transfer of water and nanofluids in a double-pipe helical heat exchanger. *Applied Thermal Engineering,* 60**,** 266-274.

XIAO, J., HE, S., XIE, G., WANG, S. & ZHANG, Z. 2024. Visualization experiment and thermal-hydraulic behaviour of assembled self-rotating twisted tape in double-pipe heat exchangers. *International Communications in Heat and Mass Transfer,* 155**,** 107456.

XIE, S., GUO, Z., GONG, Y., DONG, C., LIU, J. & REN, L. 2022. Numerical investigation of thermal-hydraulic performance of a heat exchanger tube with helical dimples. *International Journal of Thermal Sciences,* 177**,** 107530.

YANG, S., ZHANG, L. & XU, H. 2011. Experimental study on convective heat transfer and flow resistance characteristics of water flow in twisted elliptical tubes. *Applied Thermal Engineering,* 31**,** 2981-2991.

YE, Q., ZHANG, Y. & WEI, J. 2021. A comprehensive review of pulsating flow on heat transfer enhancement. *Applied Thermal Engineering,* 196**,** 117275.

YU, C., ZHANG, H., WANG, Y., ZENG, M. & GAO, B. 2020. Numerical study on turbulent heat transfer performance of twisted oval tube with different cross sectioned wire coil. *Case Studies in Thermal Engineering,* 22**,** 100759.

YUAN, B., ZHANG, Y., LIU, L., WEI, J. & YANG, Y. 2020. Experimental research on heat transfer enhancement and associated bubble characteristics under high-frequency reciprocating flow. *International Journal of Heat and Mass Transfer,* 146**,** 118825.

YUAN, H., TAN, S., WEN, J. & ZHUANG, N. 2016. Heat transfer of pulsating laminar flow in pipes with wall thermal inertia. *International Journal of Thermal Sciences,* 99**,** 152-160.

ZAMZAMIAN, A., OSKOUIE, S. N., DOOSTHOSEINI, A., JONEIDI, A. & PAZOUKI, M. 2011. Experimental investigation of forced convective heat transfer coefficient in nanofluids of Al2O3/EG and CuO/EG in a double pipe and plate heat exchangers under turbulent flow. *Experimental Thermal and Fluid Science,* 35**,** 495-502.

ZENG, M. & TAO, W. 2003. A comparison study of the convergence characteristics and robustness for four variants of SIMPLE‐family at fine grids. *Engineering Computations*.

ZHANG, C., WANG, D., REN, K., HAN, Y., ZHU, Y., PENG, X., DENG, J. & ZHANG, X. 2016. A comparative review of self-rotating and stationary twisted tape inserts in heat exchanger. *Renewable and Sustainable Energy Reviews,* 53**,** 433-449.

ZHANG, D., DIAO, Y., WANG, Z., PAN, Y., SUN, M., WANG, X., DU, P. & ZHAO, Y. 2024. Thermal performance of two evacuated tube solar collectors with flat heat pipes. *Applied Thermal Engineering,* 241**,** 122366.

ZHANG, S., LU, L. & WANG, Q. 2021. Thermal-hydraulic characteristic of short-length self-rotating twisted tapes in a circular tube. *International Communications in Heat and Mass Transfer,* 122**,** 105157.

ZHAO, X., E, J., ZHANG, Z., CHEN, J., LIAO, G., ZHANG, F., LENG, E., HAN, D. & HU, W. 2020. A review on heat enhancement in thermal energy conversion and management using Field Synergy Principle. *Applied Energy,* 257**,** 113995.

ZOHIR, A. E., ABDEL AZIZ, A. A. & HABIB, M. A. 2011. Heat transfer characteristics in a sudden expansion pipe equipped with swirl generators. *International Journal of Heat and Fluid Flow,* 32**,** 352-361.

APPENDIX

Appendix 1.1 Published Papers

International Communications in Heat and Mass Transfer 156 (2024) 107692

Contents lists available at ScienceDirect

International Communications in Heat and Mass Transfer

journal homepage: www.elsevier.com/locate/ichmt

Enhancing thermal performance of heat exchanger by using different 4-lobed swirl tube arrangements

Xingyu Feng [a,b], Nicholas J. Miles [a,b], Guozhen Li [a,b], Zheng Wang [a,b], Philip Hall [a,b,c,*]

[a] University of Nottingham Ningbo China, Faculty of Science and Engineering, 199 Taikang East Road, Ningbo 315100, Zhejiang, China
[b] Nottingham Ningbo China Beacons of Excellence Research and Innovation Institute, Ningbo 315100, PR China
[c] Zhejiang Provincial Key Laboratory for Carbonaceous Wastes Processing and Process Intensification Research Nottingham Ningbo China Beacons of Excellence Research and Innovation Institute, Ningbo 315100, PR China

ARTICLE INFO

Keywords:
4-lobed tube
3D-printing
Double pipe heat exchanger
Swirl flow
Regular-spaced tube

ABSTRACT

This study numerically and experimentally investigated the thermal performance of a 4-lobed swirl tube. A double-pipe heat exchanger was built using 3D-printed steel tubes with PD ratios ranging from 4, 6 to 8. In addition, a 3D-printed circular pipe was also manufactured to investigate the influence of the 3D-printing method. In the experimental results, the PD4 decaying swirl tube had the highest performance for all PD ratios. The effects of different pitch-to-diameter (PD) ratios and tube arrangements on the swirl pipe were also investigated during simulations. The results reveal that the tube with a smaller PD ratio and crossover arrangement has a larger thermal enhancement and pressure drop. However, in comparison, the decaying arrangement has a relatively higher overall performance since it has a lower pressure drop. The PD6 decaying tube arrangement is the highest, especially at higher Reynolds numbers. Moreover, by showing the streamline within the swirl tube, small-scale vortices are found within the swirl tube, especially in the crossover arrangement. These vortices are formed due to the swirl motion and can enhance mixing and the heat transfer rate. Based on these simulation results, a regular-spaced swirl tube arrangement is proposed and its thermal performance is evaluated. In the experimental results, the PD4 decaying swirl tube gave the highest overall performance from 1.12 to 1.09 across all configurations. In the numerical results, the regularly-spaced swirl tube can further improve the overall performance with moderate pressure drop. Type 2 PD4 has the highest performance value at 1.06.

1. Introduction

Heat exchangers are one of the most important and ubiquitous unit operations in many industrial sectors, where they are used to regulate temperature through either heating or cooling. Lin et al. [1] suggest that waste heat accounts for 26.6 x 10^{18}J and 38% of the total energy from electricity generation, especially in coal-fired thermal power plants in China. Such an amount of waste heat is equivalent to the heat generated by 907 million tons of standard coal. In addition, heat exchangers have been widely utilized in the waste heat recovery process. Thus, any small improvements in the performance of heat exchangers could have a positive and significant influence.

In recent years, researchers have shown increasing interest in applying swirl flow to enhance heat transfer efficiency in shell and tube heat exchangers [2]. Here, the swirl motion of the fluid generates vortices, resulting in increased turbulence near the wall surface and a higher heat transfer coefficient due to the fluid being uniformly mixed [2]. Swirl flow in pipes could also be categorized into two main categories: continuous and decaying swirl flow. With continuous swirl flow, the swirl motion is consistent along the length of the tube, while in decaying swirl flow, the flow is only produced at the inlet of the tube and decays gradually downstream [3].

A common method to generate continuous swirl flow is inserting a twisted tape inside the tube. However, sometimes to accomplish this desired thermal improvement, a great amount of pumping power is needed. For instance, the flow resistance was 185% higher when inserting a full-length twisted tape in comparison to an empty tube [4]. Using this method in current systems might be a challenge to eliminate any benefits of enhanced heat transfer because of the large pressure drop. Continuous swirl flow can also be generated by changing the tube shape. Yang et al. [5] conducted experiments on the effect of pitch and

* Corresponding author at: University of Nottingham Ningbo China, Faculty of Science and Engineering, 199 Taikang East Road, Ningbo 315100, Zhejiang, China.
E-mail address: Philip.HALL@nottingham.edu.cn (P. Hall).

https://doi.org/10.1016/j.icheatmasstransfer.2024.107692

Available online 18 June 2024
0735-1933/© 2024 Published by Elsevier Ltd.

Wiley
International Journal of Energy Research
Volume 2024, Article ID 3927390, 17 pages
https://doi.org/10.1155/2024/3927390

WILEY

Research Article

Optimising the Hydro-Thermal Performance of a Four-Lobed Swirl Tube by Changing the Post-Swirl Pipe Length

Xingyu Feng,[1,2] **Nicholas J. Miles**,[1] **Guozhen Li**,[1,2] **Jiarui Gao**,[1] **Zheng Wang**,[1,2] **and Philip Hall**[1,2]

[1]*Faculty of Science and Engineering, University of Nottingham Ningbo China, 199 Taikang East Road, Ningbo 315100, Zhejiang, China*
[2]*Nottingham Ningbo China Beacons of Excellence Research and Innovation Institute, Ningbo 315100, China*

Correspondence should be addressed to Philip Hall; philip.hall@nottingham.edu.cn

Received 14 March 2024; Revised 30 May 2024; Accepted 24 June 2024

Academic Editor: Mohammadmahdi Abdollahzadehsangroudi

This study explored the heat transfer performance of a decaying swirl flow generated by a four-lobed swirl generator with simulations and experiments. In the experimental studies, the thermal performance of a swirl generator was compared with that of a circular tube, indicating that the printed swirl generator provided better heat transfer performance than the printed circular tube. Further experiments were performed over a range of Reynolds numbers with different lengths of post-swirl, circular pipe to assess the decay of swirl, downstream. Here, for shorter lengths of post-swirl, circular pipe, the thermal improvement was maintained, but this advantage was lost with longer circular pipe runs. In numerical studies, the effect of various pitch-to-diameter (PD) ratios of the swirl pipe, including the actual swirl pipe (*in-swirl*) as a part of the heat exchanger or excluding it (*ex-swirl*), and the effect of different post-swirl section lengths were investigated. The heat transfer rate and pressure drop increased with the reduction of the PD ratio, and the in-swirl arrangements gave higher thermal enhancement and similar pressure loss compared with the ex-swirl arrangements. The PD6 in-swirl arrangement gave the highest thermal enhancement for all the geometries. Applying the swirl intensity and the field synergy principle confirmed these results, showing that any thermal enhancement created by swirl generators disappeared rapidly after exiting the swirl tube. In addition, the field synergy principle was more suited to explain the thermal enhancement effect of the decaying swirl flow instead of swirl intensity. This study demonstrates that by optimising the post-swirl pipe length, overall heat transfer performance can be increased by around 5% with a pressure drop of less than 16%.

1. Introduction

Swirl flow devices, such as twisted tapes, coiled wires, and swirl pipes [1, 2], have been used to enhance the convective heat transfer rate in heat exchangers and have the advantage of being low-cost and easy to install. These devices work on the principle of promoting turbulent flow to improve heat transfer efficiency. However, sometimes it requires a greater amount of pumping power to achieve this desired improvement. For instance, by inserting a full-length twisted tape, the pressure drop was increased by more than 1.85 in comparison to an empty tube [3]. Such a high-pressure drop negates any improved heat transfer benefits when applying these devices in existing systems.

In recent years, various attempts have been made at modifying these swirl flow devices to reduce pressure drops as shown in Figure 1. Eiamsa-ard and Seemawute [4] managed to reduce the friction factor ratio from around 3.2 to 1.7 by shortening the length of the twisted tapes. Such shortened tapes showed a higher heat transfer performance at a Reynolds number of 10,000 than the full-length, twisted tape. Du and Hong [10] proposed the regularly spaced short-length, twisted tape and combined it with a traverse rib tube. Though this combination achieved a hydro-thermal enhancement of 1.00–1.26, the friction factor ratio increased by around 6–15 times. Such a dramatic increase in the flow resistance further raised the requirements for the pumping system. In addition, Masoud Ali et al. [11] inserted an alternate clockwise and counter-

Energy Proceedings
Vol 32, 2023
ISSN 2004-2965

Numerical investigation of thermal performance of swirl generator in a solar water heater

Xingyu Feng[1,2], Nicholas J. Miles[1,2], Guozhen Li[1,2], Zheng Wang[1,2], Philip Hall[1,3*]

[1]University of Nottingham Ningbo China, Faculty of Science and Engineering, 199 Taikang East Road, Ningbo 315100, Zhejiang, China

[2]Nottingham Ningbo China Beacons of Excellence Research and Innovation Institute, Ningbo 315100, PR China

[3]Zhejiang Provincial Key Laboratory for Carbonaceous Wastes Processing and Process Intensification Research
(*Corresponding author: Philip Hall. Email: Philip.HALL@nottingham.edu.cn)

ABSTRACT

This paper presents a numerical investigation of the potential of a 4-lobed swirl generator for enhancing the thermal performance of an active Solar Water Heater (SWH). The hydro-thermal performance of the generator was thoroughly evaluated using the code ANSYS FLUENT 2021 R1, and the results were validated against available experimental data in the literature. The predicted results demonstrated that the proposed swirl generator was capable of giving a higher Performance Evaluation Criteria (PEC) compared to twisted tape as it enhanced the heat transfer at the expense of a much lower pressure loss than the twisted tapes. However, with only one swirl generator, the PEC value for the swirl generator was only slightly higher than 1 and the analysis with the field synergy principle revealed that the thermal enhancement produced only prevails for 30D to 40D downstream. To achieve optimal thermal enhancement in the SWH, strategic placement regimes were examined by regularly placing 2, 3 and 4 swirl generators, respectively, inside the SWH. Simulation results indicated that, with an optimal placement of the swirl generator, the heat transfer coefficient is increased by 9.9% with an extra pressure drop of 26.9% more than a plain circular tube. This increase in heat transfer coefficient can reduce the overall pumping time and, more importantly, can make the SWH more reliable in moderate weather.

Keywords: solar heat exchanger, 4-lobed swirl generator, twisted tape, decaying swirl flow, CFD Ansys fluent, field synergy principle

NONMENCLATURE

Abbreviations

PEC	Performance Evaluation Criteria
SWH	Solar water heater

Symbols

A	Surface area
c_p	Specific heat capacity
D_h	Hydraulic diameter
f	Friction factor
h	Heat transfer coefficient
L	Length of the tube side
Nu	Nusselt number
Δp	Pressure drop
$\dot{Q}$	Heat transfer rate
q_w	Heat flux
T_f	Fluid temperature
T_w	Wall temperature
∇T	Logarithmic mean temperature
$\vec{U}$	Velocity field
u	Fluid velocity
μ	Viscosity
θ	Synergy angle
ρ	Density

1. INTRODUCTION

Solar thermal energy is one of the most important sources of renewable energy. By the end of 2020, the worldwide capacity of water-based solar thermal systems is 500 GW, corresponding to a final energy savings equivalent to 43.6 million tons of oil. Among which, the vast majority of the total capacity in operation

This is a paper for Applied Energy Symposium 2023: Clean Energy towards Carbon Neutrality (CEN2023), April 23-25, 2023, Ningbo, China.

Appendix 1.2 Sample Calculation for Transition Part

The sample calculation at $\gamma = 65$ (deg) or 1.1345 (rad) is given below:

Calculate f and f_1

$$f = \left(\gamma - \frac{1}{2}sin2\gamma\right) = 1.1345 - \frac{1}{2}sin(2 \times 1.1345) = 0.7514$$

$$f_1 = \frac{1}{\sqrt{2}}\left(1 - \frac{1}{tan\gamma}\right) = \frac{1}{\sqrt{2}}\left(1 - \frac{1}{tan1.1345}\right) = 0.3774$$

Calculate the core radius

$$R = R_c\sqrt{\frac{\pi}{4f + 4ff_1{}^2 - 4\sqrt{2}ff_1 + 2}}$$

$$R = 25\sqrt{\frac{\pi}{4 \times 0.7514 + 4 \times 0.7514 \times 0.3774^2 - 4\sqrt{2} \times 0.7514 \times 0.3774 + 2}}$$

$$= 22.6430mm$$

Calculate the lobe radius

$$r^2 = R^2 + f_1{}^2R^2 - \sqrt{2}f_1R^2$$

$$r^2 = 22.643^2 + 0.3774^2 \times 22.643^2 - \sqrt{2} \times 0.3774 \times 22.643^2 = 17.6662^2$$

$$LA_{FD} = \pi R_c{}^2 - \pi R_{cs}{}^2 = \pi \times 25^2 - \pi \times 19.5418^2 = 763.7779mm$$

$$LA_i = \pi R_c{}^2 - \pi R^2 = \pi \times 25^2 - \pi \times 22.6430^2 = 352.7837mm$$

$$\beta = [\frac{\frac{LA_i}{\pi R^2 - LA_i}}{\frac{LA_{FD}}{\pi R^2 - LA_{FD}}}]^{0.5} = [\frac{\frac{352.7837}{\pi \times 22.643^{2^2} - 352.7837}}{\frac{763.7779}{\pi \times 22.643^2 - 763.7779}}]^{0.5} = 0.5577$$

$$\frac{x}{L} = \frac{cos^{-1}(1 - 2\beta)}{\pi} = \frac{cos^{-1}(1 - 2 \times 0.5577)}{\pi} = 0.5368$$

$$Twisted[0, 90°] = \frac{x}{L} \times 90° \times Twisted\ direction = 0.5368 \times 90° \times -1$$

Appendix 1.3 Transition Development of the 4-Lobed Pipe

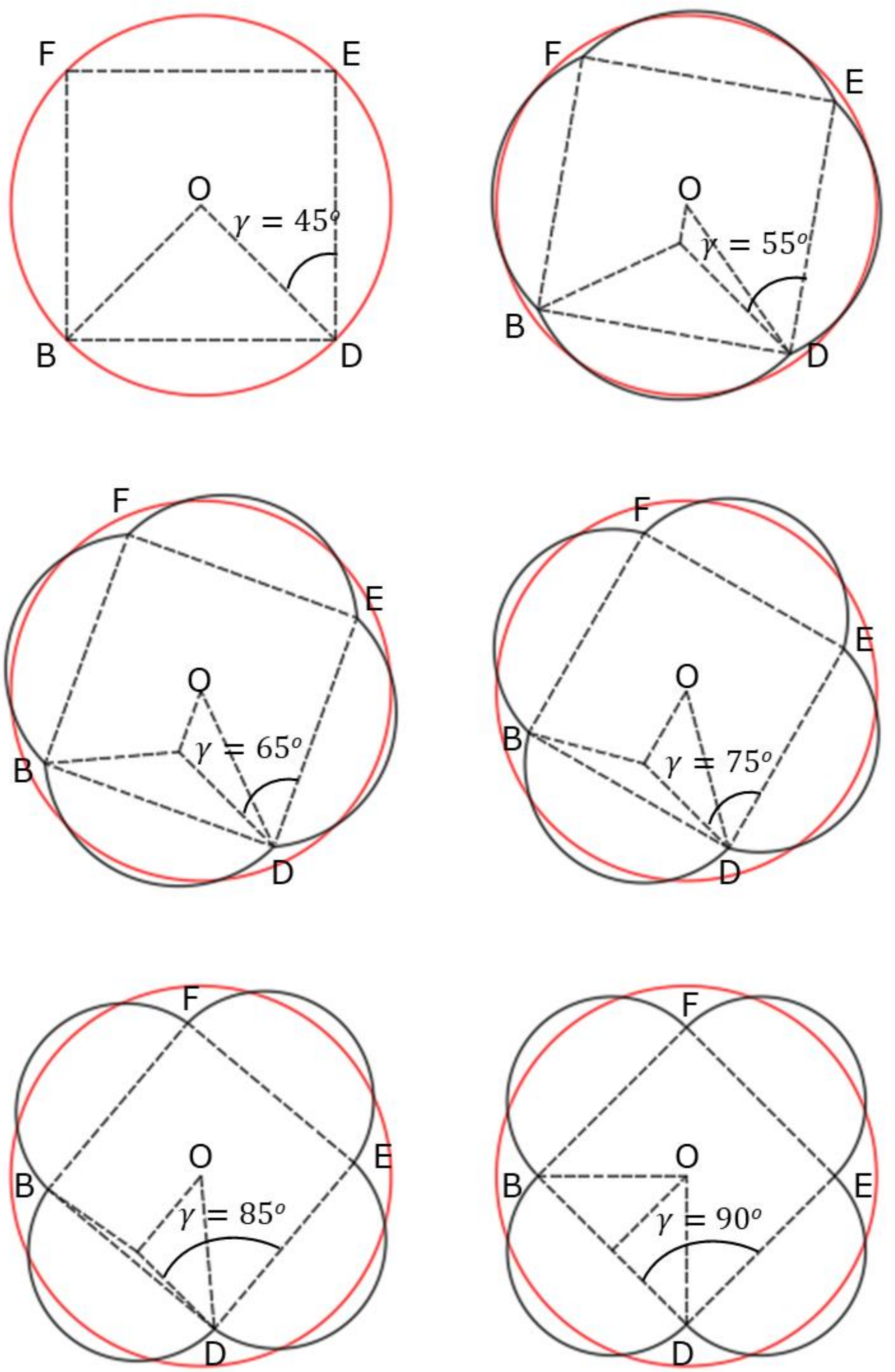

Figure A1. 6 Sections Used in Loft Feature to Create 4-Lobed Transition Pipe.

Appendix 1.4 Table for 4-lobed Swirl Tube.

Table A1. Table for 4-Lobed Swirl Tube.

γ(deg)	*γ(rad)*	f_1	*f*	*R(mm)*	*y(mm)*	*r(mm)*	*β(n=0.5)*	*x/L*	*Twist(t=1)*
45	0.7854	0.0000	0.2854	25.0000	0.0000	25.0000	0.0000	0.0000	0.0000
45.1	0.7871	0.0025	0.2871	24.9881	0.0616	24.9446	0.0387	0.1261	11.3463
46	0.8029	0.0243	0.3032	24.8809	0.6037	24.4578	0.1224	0.2275	20.4775
47	0.8203	0.0477	0.3215	24.7622	1.1816	23.9412	0.1731	0.2732	24.5840
48	0.8378	0.0704	0.3405	24.6437	1.7355	23.4486	0.2120	0.3046	27.4146
49	0.8552	0.0924	0.3601	24.5254	2.2668	22.9785	0.2448	0.3295	29.6567
50	0.8727	0.1138	0.3803	24.4074	2.7769	22.5296	0.2738	0.3506	31.5512
55	0.9599	0.2120	0.4901	23.8194	5.0494	20.5613	0.3883	0.4283	38.5480
60	1.0472	0.2989	0.6142	23.2324	6.9432	18.9692	0.4784	0.4863	43.7627
65	1.1345	0.3774	0.7514	22.6430	8.5450	17.6662	0.5577	0.5368	48.3112
70	1.2217	0.4497	0.9003	22.0479	9.9158	16.5907	0.6323	0.5852	52.6721
75	1.3090	0.5176	1.0590	21.4436	11.1000	15.6978	0.7069	0.6358	57.2206
80	1.3963	0.5824	1.2253	20.8269	12.1301	14.9540	0.7864	0.6941	62.4703
85	1.4835	0.6452	1.3967	20.1942	13.0301	14.3340	0.8786	0.7734	69.6069
86	1.5010	0.6577	1.4314	20.0654	13.1962	14.2230	0.8997	0.7949	71.5373
87	1.5184	0.6700	1.4662	19.9358	13.3580	14.1161	0.9221	0.8200	73.7971
88	1.5359	0.6824	1.5010	19.8054	13.5155	14.0131	0.9461	0.8509	76.5765
89	1.5533	0.6948	1.5359	19.6741	13.6688	13.9138	0.9719	0.8928	80.3554
90	1.5708	0.7071	1.5708	19.5419	13.8182	13.8182	1.0000	1.0000	90.0000

Appendix 1.5 Calculation for Nusselt number from Simulation Results.

The calculation of Nusselt number is based on these two equations in section 2.3.2

$$h = \frac{Q_{heat}}{A(T_w - T_f)}$$

$$Nu = \frac{hD_h}{\lambda}$$

Wall Temperature and Heat Flux

- Once the CFD simulation has converged, extract the wall temperature (T_w), surface area (A) of the tube and the heat flux (Q_{heat}) at the tube wall.
- These three values can be obtained from the simulation results.
- Heat transfer coefficient h can be calculated by (2.3-4)

Fluid Temperature and Thermal Conductivity

- Determine the bulk fluid temperature (T_f). This can be calculated as a volume-weighted average of the fluid temperature in the domain.
- Determine thermal conductivity of the fluid (λ) and the inner diameter of the tube (D_h)

Nusselt number can be calculated by (2.3-8)

The calculation of friction factor is based on this equation in in section 2.3.2

$$f = \frac{\Delta p}{(L/D_h)(\rho u^2/2)}$$

Pressure drop

- Extract the pressure values at the inlet and outlet of the heat transfer area. The pressure drop (Δp) is calculated as the difference between the upstream total pressure and the downstream total pressure.

- Other properties such as length (L), diameter (D_h), density (ρ) and velocity (u)

A user-defined function (UDF) in ANSYS Fluent named DEFINE_EXECUTE_AT_END can be employed to calculate the Nusselt number and friction factor once the simulation converges.

Appendix 1.6 Two-tailed t-test

A sample calculation for friction factor value at flow rate of 6L/min is shown below:

The calculated friction factor data are 0.037231, 0.035544, 0.036067, 0.035912, 0.036207, 0.035834, 0.036184, 0.037059, 0.036397, 0.036556, 0.036300. The theoretical value calculated by the Petukhov (2.5-3) is 0.033889.

1. Calculate the sample mean

$$\bar{x} = \frac{1}{n}\sum_{i=1}^{n} x_i = 0.036299$$

Where n is the sample size and x_i is the i-th sample value.

2. Calculate the sample standard deviation

$$\boldsymbol{s} = \sqrt{\frac{\sum_{i=1}^{n}(x_i - \bar{x})^2}{n-1}} = 0.000503$$

3. Calculate the t-statistic

$$t = \frac{\bar{x} - \mu}{s/\sqrt{n}} = \frac{0.036299 - 0.033889}{0.000503/\sqrt{11}} = 1.44$$

4. Determine the degrees of freedom and the critical value

- The degrees of freedom $df = n - 1 = 10$
- For a two-tailed t-test with a significance level $\alpha = 0.05$, the critical values from the t-distribution table $t_{\alpha/2,df} = 2.228$.
- Since $t = 1.44 < 2.228$, there is not enough evidence to indicate that the population mean drawn form the sample is significantly different from the theoretical value.

Table A2. Two-tailed T-test results under different flow rate.

	6L/min	8L/min	10L/min	12L/min	14L/min	16L/min	18L/min	20L/min	22L/min	24L/min
Sieder-Tate (2.5-1)	1.60883	-0.73330	-0.40132	-0.23853	0.01330	0.14586	0.27536	0.44447	0.55083	0.77829
Gnielinski (2.5-2)	0.25892	-0.17915	-0.08040	-0.06575	0.04053	0.08272	0.14312	0.25257	0.30587	0.48952
Petukhov (2.5-3)	1.44346	0.71854	-0.30435	0.48274	1.43497	1.38810	1.95905	1.14854	2.10365	0.27880
Blasius (2.5-4)	1.52835	0.65376	0.58256	1.13093	1.31761	0.80779	0.61709	0.15960	0.53177	-0.09657

Appendix 1.7 Correlation for Short Length Swirl Tube.

Reynolds number ranges 6,000-30,000

Prandtl number ranges 3-7

$$Nu = a_1 Re^{a_2} Pr^{0.4}$$

Table A3. Nusselt number correlations.

	a_1	a_2
PD4	0.0053	0.970
PD6	0.0098	0.905
PD8	0.0097	0.905
PD8-POLISHED	0.0042	0.990
Steel tube	0.0071	0.925

$$f = a_3 Re^{a_4} + a_5$$

Table A4. Friction factor correlations.

	a_3	a_4	a_5
PD4	85.59	-0.929	0.02496
PD6	7.459	-0.6568	0.0211
PD8	53.02	-0.8917	0.02353
PD8-POLISHED	285.3	-1.068	0.02389
Steel tube	0.5419	-0.3006	-0.0003918